Studies on Magnetic and Electrical Properties of Disordered Carbon

Thesis Submitted to AcSIR
for the Award of the Degree of

DOCTOR OF PHILOSOPHY
In Chemical Sciences

By
Mr. Govind Raj K.
Registration Number: 10CC11J26004

Under the Guidance of
Dr. P. A. Joy

CSIR-National Chemical Laboratory,
Pune - 411008, India.

September 2015

सीएसआयआर–राष्ट्रीय रासायनिक प्रयोगशाला
(वैज्ञानिक तथा औद्योगिक अनुसंधान परिषद)
डॉ. होमी भाभा मार्ग, पुणे – 411 008. भारत
CSIR-NATIONAL CHEMICAL LABORATORY
(Council of Scientific & Industrial Research)
Dr. Homi Bhabha Road, Pune - 411008. India

Certificate

This is to certify that the work incorporated in this Ph.D. thesis entitled ***Studies on Magnetic and Electrical Properties of Disordered Carbon***, submitted by ***Mr. Govind Raj K.*** to Academy of Scientific and Innovative Research (AcSIR) in fulfillment of the requirements for the award of the Degree of ***Doctor of Philosophy in Chemical Sciences***, embodies original research work under my supervision. I further certify that this work has not been submitted to any other University or Institution in part or full for the award of any degree or diploma. Research material obtained from other sources has been duly acknowledged in the thesis. Any text, illustration, table etc., used in the thesis from other sources, have been duly cited and acknowledged.

Govind Raj K
(Student)

Dr. P. A. Joy
(Supervisor)

Date: 26/09/2015
Place: Pune

Communications Channels
NCL Level DID : 2590
NCL Board No. : +91-20-25902000
Four PRI Lines : +91-20-25902000
FAX
Director's Office : +91-20-25902601
COA's Office : +91-20-25902660
SPO's Office : +91 20 25902664
WEBSITE
www.ncl-india.org

...Dedicated to my Parents...

Acknowledgements

This thesis was made possible with the support, encouragement and timely help of many people. I would like to use this pleasant moment as an opportunity to thank all of them.

First and foremost, I sincerely thank my supervisor ***Dr. P. A. Joy*** *for his scientific guidance and support. His unique way of handling students with extreme care, freedom and patience should be mentioned. His passion to do high impact and quality science was worth wondering. I always felt excited by his engineering skills, using which many scientific instruments were assembled in the lab, which was even more precise than the commercially available ones. The constant interactions with Dr. Joy were helpful in developing logical thinking and rigorous data analysis skills. I could not have imagined a better mentor than him.*

I am grateful to the former directors of NCL, Dr. S Sivaram and Dr. Sourav Pal, and the present director, Dr. K. Vijayamohanan, for allowing me to work in this prestigious laboratory. The financial support from CSIR in the form of a research fellowship is also duly acknowledged. I wish to thank Dr. Anilkumar, Chairman, Physical Chemistry Division, for allowing me to use all the divisional facilities. My sincere thanks to all the DAC members, Dr. B. L. V. Prasad, Dr. C. P. Vinod and Dr. K. Krishnamoorthy. They were kind enough to spend their valuable time for the evaluation presentations. The suggestions and the constructive criticisms during these presentations were of great help in shaping my work. All the help that I received from the administrative and other support staff of the different sections of NCL are duly acknowledged.

I was fortunate to have many influential teachers in my student life. I take this opportunity to thank all of them. Thanks to Dr. D. K. Babu, Dr. D. Channe Gowda, Dr. Maria Starwin and Dr. Raghu for their timely help and advice, which made my way to NCL.

Many thanks to my seniors Vijay, Sreeja, Khaja and Pankaj for their support and advice in the initial stages of my work. My labmates Mangesh, Lenin, Bindhu, Ramsundar, Jayaprabha, Manjunath, Anjali, Mohan, Ananth and Arun

were simply great in providing a constructive working atmosphere in the lab. The light moments during lab parties and trips were worth enjoying. Thank you all for making these moments unforgettable. The support which I received from the project students Anju, Guru and Neil helped me in optimizing many of the experiments. I also thank other project students Shibin, Aurelie, Sister Mary, Swetha and Renjith for their company.

I also take this opportunity to thank my friends Hareesh, Sreevishakh, Renjith, Shoy, Gireesh, Anish, Alson, Eldho, Suresh, Sumesh, Rajesh, Bhagesh, Jithesh, Vishal, Sabareesh, Kiran, Vysakh, Sarath and Sunil. The late night discussions, yearly tours and weekend cricket matches with them produced many memorable moments. The company of Manu, Bihag, Anumon, Leena, Soumaya, Anuj, Kethen, Joyashish, Anoop, Raja and Pandy were also helpful.

With all due respect and affection, I would like to thank Achan and Amma, who always supported me by all possible means. I find myself lucky to have them. Both Bittuechi and Deepechi needs to be mentioned for the care, love and support. The way they handled their younger brother was amazing. They always stood by me at difficult times. Thanks to Ajayetten, Vinuetten, Abhiyetten, Akhiyetten, Deepechi and Daniechi for their company and support.

I would like to thank Divya for her constant support, understanding and care. The birth of Meera was special. She made our life more exciting and joyful.

Govind Raj K

Contents

List of Tables

List of Figures

List of Abbreviations

2D VRH: Two-Dimensional Variable Range Hopping

3D VRH: Three-Dimensional Variable Range Hopping

a-C: Amorphous carbon

a-C:H: Hydrogenated amorphous carbon

BET: Brunauer-Emmet-Teller

CCGNR: Chemically Converted Graphene Nanoribbon

CG VRH: Coulomb Gap Variable Range Hopping

CS: Coconut Shell

CNT: Carbon Nanotube

CNF: Carbon Nanofiber

DOS: Density of States

DLC: Diamond-like Carbon

E_F: Fermi Level

FC: Field Cooled

FCM: Field Cooled Magnetization

FWHM: Full Width at Half Maximum

GNR: Graphene Nanoribbon

H: Magnetic Field

H_c: Coercivity

HOPG: Highly Oriented Pyrolytic Graphite

HTT: Heat-treatment Temperature

ICP: Inductively Coupled Plasma

I(D): Intensity of D-peak

I(G): Intensity of G-Peak

IR: Infrared

L_a: In-plane Coherence Length

L_c: Out-of-plane Coherence Length

M: Magnetization

MWNT: Multi-Walled Nanotube

NEXAFS: Near Edge X-ray Absorption Fine Structure

OES: Optical Emission Spectrometry

PDF: Powder Diffraction File

RKKY: Ruderman-Kittel Kasuya-Yosida

SEM: Scanning Electron Microscope

SWNT: Single-Walled Nanotube

SQUID: Superconducting Quantum Interference Device

ta-C: Tetrahedrally bonded amorphous carbon

T_C: Curie Temperature

TEM: Transmission Electron Microscope

TGA: Thermogravimetric Analysis

TK: Tuinstra and Koenig

T_N: Neel Temperature

VRH: Variable Range Hopping

VSM: Vibrating Sample Magnetometer

WL: Weak Localization

XRD: X-ray Diffraction

ZFC: Zero Field Cooled

ZFCM: Zero Field Cooled Magnetization

Abstract

Carbon-based systems are at the center stage of materials science for many years. The disordered forms of carbon, which are structurally in between diamond and graphite, are very important due to their peculiar physical properties and many possible applications. The extent of graphitization in disordered carbon can be tuned by heat-treatment, which can, in turn, give rise to interesting magnetic and electrical properties. Most of the previous studies on disordered carbon systems were performed either on thin film samples or on commercially available specimens whose thermal history is unknown. Similarly, the microstructure of carbon-based systems can be tuned by simple chemical activation technique, which can also modify the physical properties to a different extent.

The present work aims at the systematic study on the evolution of the microstructural, magnetic and electrical properties of disordered carbon derived from a known source. Coconut shell, one of the cheapest and widely used industrial precursor for the preparation of granular and activated carbon, is used as the source of carbon in the present study. The activated carbon derived from coconut shell is presently used for various applications like filters, adsorbents, electrode materials, etc. due to their high specific surface area and porosity. However, until now there are no studies reported on the magnetic and electrical properties of coconut shell derived carbon. The carbon material used for the present study is prepared by the heat-treatment and the chemical activation of coconut shell based carbon. For chemical activation, KOH is used as the activating agent due to the large surface area and microporosity of the KOH activated carbons. Until now the studies on the changes in the structure of activated carbons are limited to the evolution of the pore structure and surface area on activation. The present work aims to study the structural and microstructural changes in heat-treated and KOH activated carbon and to correlate with the magnetic and electrical properties.

Chapter 1 presents a general introduction to different carbon-based systems, magnetism, conduction mechanism in systems with a strong disorder and the weak localization effect. The potential applications of carbon-based materials are

also discussed. A brief description of the structure and properties of different disordered carbon structures is also included in this chapter.

Chapter 2 describes the preparation procedures adopted in preparing the disordered carbon samples for this study. The characterization techniques used in the present work are discussed in detail.

The structural analysis of the heat-treated samples using X-Ray diffraction (XRD) and Raman spectroscopy indicated that those samples heat-treated at lower temperatures (500-700 °C) are highly disordered. However, with an increase in the heat-treatment temperature (HTT) above 800 °C, there is a partial structural arrangement to nanocrystalline graphite. The heat-treated samples, therefore, is an ideal system for studying the evolution of magnetic and electrical properties, with their structural ordering extending from disordered carbon to nanocrystalline graphite. The transmission and scanning electron microscopy (TEM and SEM) images showed no distinct changes in the morphology of heat-treated samples. The results of these structural characterizations of disordered carbon derived from coconut shell are presented in **Chapter 3**.

Chapter 4 presents the studies on the magnetic properties of the heat-treated samples. The heat-treated samples are diamagnetic at room temperature and at low temperatures, they showed ferromagnetic-like characteristics. The effect of impurities on the observed magnetic moment is also discussed. The magnetization values at the highest field applied (60 kOe) decreased sharply for samples heat-treated at relatively lower temperatures, whereas with an increase in HTT, above 800 °C, for the nanocrystalline graphitic samples, the decrease in magnetization is found to be much lower. Temperature dependent magnetization measurements showed a broad magnetic transition around 150 K. A detailed study indicated that the samples have a disordered magnetic state, possibly originating from different types of magnetic interactions at varying strengths.

Chapter 5 includes the studies on the electrical transport properties of heat-treated samples. The temperature variation of electrical resistance, measured in the range 15–300 K, showed that the electrical conduction mechanism of the sam-

ples changes with the extent of structural ordering. The temperature dependent electrical conductivity of the samples with large disorder follows Mott 3D variable range hopping mechanism. However, with an increase in the structural ordering, for samples heat-treated above 800 °C, there is a crossover from strong localization to weak localization, because of which the conductivity becomes less temperature dependent. The changes in the magnetization and conduction mechanism are found to be directly correlating with the changes in the structural characteristics, with an increase in HTT, as evidenced from XRD and Raman spectroscopic studies.

Studies on the KOH activated carbon are discussed in **Chapter 6**. A detailed analysis of the XRD patterns, Raman spectra and TEM images showed that apart from the increase in the surface area and porosity, the activated samples show interesting changes in the microstructure with the development of localized graphitic regions. The in-plane and out-of-plane coherence lengths calculated from XRD is found to vary with the amount of KOH used for activation and the activation temperature. The appearance of two additional peaks at 1625 cm^{-1} (D′) and 2650 cm^{-1} (G′) in the Raman spectra of the activated samples, when compared to the control, showed that the activated samples are graphitized to a much higher extent than the control samples. The electrical conductivity and the magnetic properties of these samples depend on the amount of activating agent used for activation, at a constant HTT. The low-temperature magnetization is observed to follow the changes in the surface area, whereas the coercivity and the electrical conductivity are found to vary with the changes in the microstructure.

The activated carbon sample with the high surface area, prepared by KOH activation is studied for removal of oil spills in water, after making a composite with magnetic iron oxide nanoparticles. This study is included in **Chapter 7**. The magnetic composite material showed good oil removing capacity and the magnetic functionality allowed fast and effective recovery of the material from an oil spill after adsorption, by magnetic separation using a permanent magnet. The composite material showed good temperature stability and can be used in

multiple cycles after proper recycling. Since the coconut shell based activated carbon is cheaper and the process of making the composite is easy and scalable, the overall process is cost effective. Therefore, this technique using the coconut shell based activated carbon - iron oxide composite can be used along with the currently available methods, which may make the process of cleaning oil spills a lot easier and cost effective

Chapter 8 presents the summary of the works discussed in this thesis, which includes the studies on heat-treated carbon, KOH activated carbon and activated carbon - iron oxide composite. A short discussion on the future perspectives is also given at the end.

Chapter 1

Introduction

1.1 Materials science

In recent years, with the development of advanced microscopy techniques, research on nanomaterials with exotic properties, depending on their size and shape, has emerged to the forefront of materials science, revolutionizing science and technology making our life easier and even smarter than before [1,2]. The developments in materials science have played a key role in improving our living standards. The field of materials science deals with the studies on different types of materials in order to understand and engineer their properties [3,4]. Materials science is of multidisciplinary interest and combines the aspects of basic science branches like physics, chemistry and biology to address the most diverse and demanding problems like affordable health care, clean and sustainable energy, global warming, water and air purification, nuclear waste management, fast and low-cost infrastructure development, etc.

The fundamental aim of materials science is to engineer materials suitable for an intended purpose by a careful and precise control of materials composition and processing parameters. From a technological point of view, different materials can be categorized as ceramics, polymers, metals, semiconductors, composites, biomaterials, etc. [4]. The developments in chemistry and physics have aided the growth of materials science tremendously. With new and efficient preparation routes available along with advanced characterization techniques, more and more materials are being discovered, but above that a precise control of structural parameters is made possible, enabling the engineering of materials with desired electrical, magnetic, mechanical, optical and thermal properties [5]. An advanced class of materials called the multifunctional or hybrid materials combine two or more of these properties, making them smart and enabling their usage in applications like information storage, sensors and actuators of different types, energy harvesting and storage, catalysis and several other areas which directly or indirectly affect our day-to-day life [1,4].

The development of information technology has revolutionized our life with the introduction of many smart devices and high-speed computers. However, such

a development was supported by the discovery of new magnetic and electrical materials along with the modifications in of existing ones. The magnetic and electrical materials have numerous applications and are used in nearly every device which we use in our day to day life. Electrical and/or magnetic materials can be found in motors, generators, transformers, loudspeakers, sensors and actuators, data storage devices, electronic reading and writing heads, switches, integrated circuits, different types of light and heat sources, etc. [6,7]. Thus, the widespread demand for electrical and magnetic materials have triggered numerous research works related their structure and properties. The work discussed in this thesis attempts to correlate the structural, electrical and magnetic properties of disordered carbon-based materials.

1.2 Nanomaterials

The prefix "nano" in the word "nanomaterials" means a billionth (10^{-9}). Nanomaterials include a variety of materials like atomic clusters, layered structures, thin films, molecular self-assemblies and all other nanostructured materials of different shapes [8]. The common thread for grouping these various material forms being the nanoscale dimensionality (10^{-9} m), i.e., at least one dimension less than 100 nm, or more typically, less than 50 nm, where the physics and chemistry of such materials are very different from the macroscale properties of the same substance which often results in unique and superior properties [2,8–10]. The history of nanomaterials can be tracked back to the ancient Roman period. Metal and metal oxide nanoparticles, primarily of gold, silver and tin, were used to dye glass articles and fabrics and also as a therapeutic aid in the treatment of arthritis [8,11]. The studies on nanoscale particles gained momentum after the phenomenal work of Michael Faraday on colloidal metals [12]. But an upsurge in practicing the science at nano-level was initiated after the famous enlightening lecture by Nobel laureate Richard P. Feynman at Caltech in the year 1959 [13]. Subsequent developments in understanding and the capability to synthesize, organize and tailor materials at the nanoscale gave birth to a variety of nanomaterials (Table 1.1) in all pos-

Table 1.1: Different types of functional nanomaterials. Taken from reference [9].

Type	Size (approx.)	Materials
Nanocrystals and clusters (quantum dots)	diam. 1–10 nm	Metals, semiconductors, magnetic materials
Other nanoparticles	diam. 1–100 nm	Ceramic oxides
Nanowires	diam. 1–100 nm	Metals, semiconductors sulfides, nitrides
Nanotubes	diam. 1–100 nm	Carbon, layered metal chalcogenides
Nanoporous solids	pore diam. 0.5 -10 nm	Zeolites, phosphates, etc.
2-dimensional arrays (of nanoparticles)	several nm–μm	Metals, semiconductors, magnetic materials
Surfaces and thin films	thickness 1–1000 nm	A variety of materials
3-dimensional structures (superlattices)	several nm in the three dimensions	Metals, semiconductors, magnetic materials

sible morphologies like nanotubes, nanorods, nanowires, nanoribbons, nanocups, nanospheres, nanocubes, nanodots, core-shell nanostructures, etc. which essentially determine their properties.

The unique properties of nanomaterials are primarily due to two different effects called the surface effect and the size effect. For an object of macroscopic dimensions, the surface atoms constitute a negligible proportion of the total number of atoms and will, therefore, play a negligible role in many of the bulk properties of the material except those involving the exchanges at the interface between the object and the surrounding medium like in crystal growth, catalysis, etc. But when the size is reduced to nano dimensions, the surface area-to-volume ratio increases

Table 1.2: Delocalization and confinement in nanostructures. Taken from reference [10].

Quantum structure	Delocalization dimensions	Confinement dimensions
Bulk Conductor	3(x,y,z)	0
Quantum Well	2(x,y)	1(z)
Quantum Wire	1(z)	2(x,y)
Quantum dot	0	3(x,y,z)

exponentially, increasing the specific surface energy which will have an effect on the strain, lattice parameters, local ordering, co-ordination number, phonon density of states, the rate of diffusion, melting point, reactivity, equilibrium shape, etc. and hence determines the physical and chemical properties of the nanostructures. Apart from the surface effect, for very small nanocrystals, there are also quantum confinement effects which change the electronic structure. Hence, with a decrease in size, an electrical conductor becomes more and more resistive, transforming to a semiconducting or insulating state and the optical property changes with a characteristic blue shift in the absorption maxima for quantum dots [14]. Depending on the morphology of the nanostructures, the extent and direction of electron delocalization varies, which in-turn affects the quantum confinement. The delocalization and confinement dimensionalities of quantum nanostructures are presented in Table 1.2.

Some important applications and technologies based on nanomaterials or different nanoarchitectures are nanoelectrochemical sensors, high temperature superconductors, nanotubes and nanoporous materials for gas storage, chips for biochemical assay, nanoelectronics and nanodevices, development of environmental friendly and efficient catalysts, solar cells, light emitting diodes, new lasers, nanosensors, nanocomputers, defect-free electronics for future molecular computers, resonant tunneling devices, spintronics and the linking of biological motors with inorganic nanodevices [1,2,15].

1.3 Electrical properties of materials

Electrical conductivity (σ) is one such property which scales over a wide range depending on the material. For metals, σ lies in the range $\sim 10^4$ to 10^6 Ohm^{-1} cm^{-1}, whereas insulators are non-conducting with $\sigma \leq 10^{-15}$ Ohm^{-1} cm^{-1}. Semiconductors exhibit conductivities less than that of conductors, with $\sim 10^{-5} \leq \sigma \leq 10^{-3}$ Ohm^{-1} cm^{-1} [16]. For a defect free superconducting material, the electrical conductivity reaches infinity below its critical temperature [17]. The electrical properties of metals, semiconductors and insulators are related to their energy band structure. Energy bands are formed by the overlap of individual atomic levels due to the formation of a condensed system on decreasing the interatomic separation, where width of the band is directly related to the overlap integral of the atomic energy levels [18]. The density of states (DOS) is defined as the number of energy states per unit energy and per unit volume [18]. The energy band formed by high-energy orbitals are called conduction band and are generally empty. However, the valence band is formed by occupied molecular orbitals and have lower energy than the conduction band. The highest filled band at absolute zero is known as the Fermi level and the corresponding energy is called the Fermi energy (E_F). According to the free electron model [18,19], for metals, the valence band is partially filled and therefore the electrons in the singly occupied states near E_F can move freely, making the material highly conducting. For insulators, the valence band is completely filled and is separated from the conduction band by a large gap ($\sim$6 eV). Very few electrons are promoted to the conduction band, only when sufficient energy is available to the material, making them non-conducting. Semiconductors have a variable band gap, from 0.5 to 3.0 eV and electrons can be promoted to the conduction band by supplying sufficient energy to the material [18,19].

According to the free electron model, the potential inside a material is assumed to be uniform, but the perturbative effects of lattice vibrations need to be considered in order to explain the electrical conductivity of a material [19]. In addition to local potential fluctuations, due to phonon vibrations, the electronic transport in a material gets further modified considerably by defect-induced scat-

tering and hence is determined by the extent of structural disorder present in the medium [20–22]. A perfectly crystalline semiconducting material has sharp band edges, whereas an amorphous semiconductor has band tails reaching into the gap with a low density of states (DOS) thereby softening the band gap [21]. These tail states are widely separated in energy and are therefore called as localized states. The localized states are separated from the extended states of energy band by an energy level called the mobility edge. The states below the lower mobility edge are localized, while those above it are extended forming a normal band structure. With a change in the random potential induced by disorder, the extended band structure breaks down with the formation of localized states. The E_F then falls in the region of localized states, after crossing the mobility edge from extended to the localized region of the energy band [22]. Since a significant contribution towards the electrical transport properties arises from the extended states, the electrical conductivity of an amorphous material or a defective crystalline material deviates away from that of the corresponding perfectly crystalline material. This kind of emergence of insulating character for a conducting material, with an increase in the disorder or vice-versa, above a critical limit, is called Anderson transition [20,22]. Therefore, an Anderson insulator is associated with localized states of the system, while a metal generally displays diffusive transport associated with delocalized states.

1.3.1 Scaling theory of localization

Scaling theory of localization connects the conductance (G) with the size of the system (L), which characterizes the amount of disorder present [23]. The microscopic length which is of great interest in the localization problem is the mean free path (l) which defines the distance over which the phase of an electron wave function fluctuates by about 2π so that the conduction with negligible resistance due to the scattering of charge carriers, called the ballistic conduction, gives way to a diffusive mechanism while moving through a disordered lattice. The conductance G_0 at this length scale gives a direct measure of disorder at the microscopic level

with small values at large disorder. For ordered materials, with small scattering concentration, electron wave function is extended with large mean free path comparable to atomic spacing. In this context, conventional transport theory, which relies on weak scattering, becomes applicable with large conductivity values which are independent of the scale size (L), provided the system is large enough to have a well-defined mean free path ($L \gg l$) [22]. However, in contrast to this, if the states near the Fermi level are localized, the electronic transport occurs by hopping of charge carriers from an occupied state to an unoccupied state of comparable energy. These localized states, which are very close in energy, are generally very distant in space, so that the hopping probability between these states are exponentially small and the relevant length scale is called as the localization length, ξ. In the presence of disorder above a critical value, the electronic wave function may be profoundly altered and the condition of localization sets in with localization length increasing above the mean free path ($\xi \gg l$). This results in a non-ohmic behavior of conductance, depending on the extent of localization. Considering these factors, the scaling function is constructed as [22]

$$f(g) = d(lng)/d(lnL) \tag{1.1}$$

where, L is the size of the system, g is the conductance (G) of the system expressed in the units of $e^2/\hbar$ and $f(g)$ is the scaling function. Using Equation 1.1, along with the correction for asymptotic forms as well as other perturbative corrections, a scaling conductance function for systems with the different extent of disorder can be formalized to understand the transport properties [22,23].

The localization effect can be observed in disordered materials by measuring the temperature dependence of electrical resistivity [23,24]. With the decrease in the temperature, resistivity increases exponentially, ∼6–8 times in order, indicating an insulating behavior [25]. With considerable ordering, a material may have much lesser room temperature resistivity which remains more or less temperature independent, indicating a crossover from insulating behavior to a metallic state [25]. In the critical regime, the resistivity behavior gets modified with a

$T^{1/2}$ or logarithmic temperature dependence due to the carrier-carrier scattering or a phonon-mediated scattering of charge carriers [22]. At a higher degree of ordering, the resistivity slightly decreases with increasing temperature, showing metallic behavior [25].

1.4 Magnetic materials

The timeline of magnetism begins around 600 BC, with the description of attracting properties of natural magnetite (Fe_3O_4), by Greek philosophers. Most of the fundamental concepts of magnetism and its relation with electricity were discovered during 17^{th} and 18^{th} century through the works of the eminent scientists Hans Christian Oersted, Andre Marie Ampere, Carl Friedrich Gauss, Jean Baptiste Biot, Felix Savart, Michael Faraday and James Clerk Maxwell.

The most important fundamental quantity in magnetism is the magnetic moment (m). The magnetic moment of an electron have contributions emerging from both the spin and the orbital motion. The amount of magnetic moment due to the spin and the orbital motion of an electron in the first Bohr orbit is the same, and is called the Bohr magneton (μ_B), given by Equation 1.2 [26].

$$\mu_B = \frac{eh}{4\pi mc} \tag{1.2}$$

where e is the charge of the electron, h is the Plancks constant, m is the mass of the electron and c is the velocity of light in free space.

For a bar magnet, the magnetic moment is defined as the torque acting on a bar magnet when placed perpendicular to a uniform magnetic field of strength 1 Oe (Oersted) (Equation 1.3) [26].

$$m = (pH\sin\theta)\left(\frac{l}{2}\right) + (pH\sin\theta)\left(\frac{l}{2}\right) = pHl\ \sin\theta \tag{1.3}$$

where, m is the magnetic moment, p is the magnetic pole strength, H is the uniform magnetic field strength, θ is the angle between magnetic filed and the magnet and l is the length of the bar magnet. When, H=1 Oe and θ=90°

$$m = pl \tag{1.4}$$

The unit of magnetic moment (m) is erg/Oe and is known as the electromagnetic unit (emu) of magnetic moment. In order to quantify the magnetic strength or the degree of magnetization of a material, its magnetic moment is presented as the magnetic moment per unit volume (M) given by Equation 1.5 [26].

$$M = \frac{m}{v}\left(\frac{emu}{cm^3}\right) \tag{1.5}$$

where v is the volume of the material. But it is convenient to express the extent of magnetization in terms of the mass of the material due to the advantages that mass is temperature independent and can be measured more accurately than volume. The mass magnetization or specific magnetization (σ) is given by

$$\sigma = \frac{m}{w} = \frac{m}{v\rho} = \frac{M}{\rho}\left(\frac{emu}{g}\right) \tag{1.6}$$

where w is the mass and ρ is the density. Like any other extrinsic property, magnetization can also be expressed per mole, per unit cell, per formula unit, etc. However, depending on the type of the magnetic material, different magnetization behavior are observed at different field strengths and therefore, a magnetic material cannot be characterized completely by knowing the magnitude and sign of M. The quantity which accounts for the magnetic field (H) dependence of M is known as the magnetic susceptibility (χ), which is mathematically expressed as

$$\chi = \frac{M}{H}\left(\frac{emu}{Oe\ cm^3}\right) \tag{1.7}$$

This quantity is also known as volume susceptibility (χ_v) since the magnetic moment per unit volume is used. Susceptibility can also be expressed in many other ways such as mass susceptibility ($\chi_m = \chi_v\rho$, where ρ is the density), atomic susceptibility (χ_A=χ_vA, where A is the atomic weight), molar susceptibility ($\chi_M = \chi_v M'$, where M′ is the molecular weight), etc.

Magnetic induction or total flux density (B) determines the response of a magnetic material towards the applied magnetic field. The relation connecting B and H is

$$B = H + 4\pi M \tag{1.8}$$

$$\frac{B}{H} = 1 + \frac{4\pi M}{H} \tag{1.9}$$

$$\mu = 1 + 4\pi\chi \tag{1.10}$$

$$where, \mu = \frac{B}{H}\left(\frac{gauss}{Oe}\right) \tag{1.11}$$

The ratio of B to H determines how permeable a material is to the magnetic field and is called as magnetic permeability (μ). A material which concentrates a large amount of flux density in its interior has a high permeability.

1.4.1 Types of magnetism

Some materials contain paired electrons in all the shells of their constituent atoms, then the atom as a whole has no net magnetic moment and such materials are called diamagnetic. In these materials, the extra currents generated in the atom by electromagnetic induction when subjected to a magnetic field are always opposite to the direction of the applied field. Therefore, the induced magnetic moments are

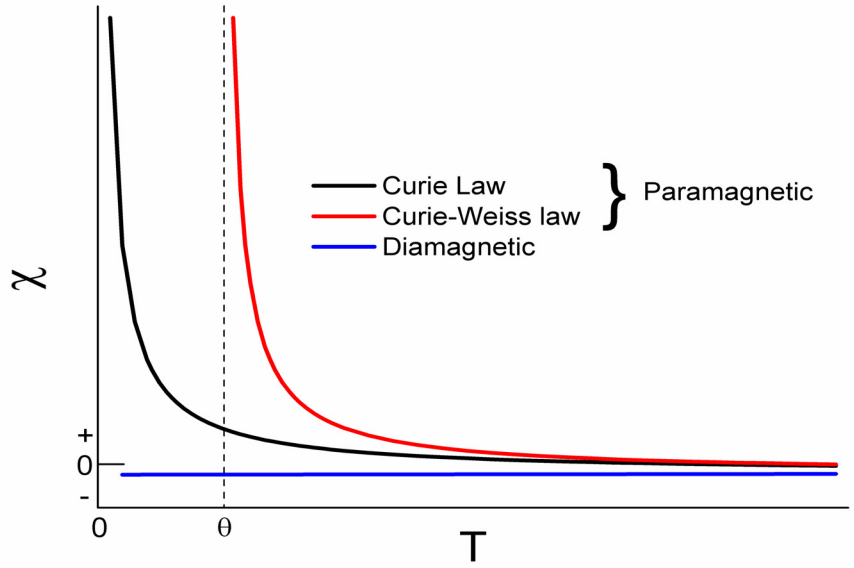

Figure 1.1: Temperature dependence of susceptibility for dia and paramagnetic materials. Taken from reference [26].

directed opposite to the applied field, where the magnitude of this 'negative' moment is directly proportional to the strength of the applied field. This condition was first observed in bismuth and antimony by J. Bergmann in 1778 for which Michael Faraday coined the name diamagnetism in 1845. Atoms with closed shell electronic configuration like inert gases, H_2, N_2, NaCl, covalently bonded carbon, silicon and germanium, most of the organic compounds, superconductors, heavy metals with many core electrons such as mercury, gold, copper, etc. are generally diamagnetic with temperature independent diamagnetic susceptibility (Figure 1.1). The diamagnetism of a molecule can be determined by adding the diamagnetic susceptibility of every atom and bonds in the molecule [27]. The values of the diamagnetic susceptibility of different atoms and bonds are known as Pascal's constants [27]. Diamagnetic materials find applications in delicate magnetic measurements, magnetic field aided alignment of liquid crystals and inorganic materials such as mesoporous silica [28]. Superconductors below their superconducting transition temperature behave as perfect diamagnets repelling the applied field completely and hence is used for magnetic levitation [26].

Unlike diamagnetic materials, the constituent atoms or ions of a paramagnetic

material contain unpaired electrons and therefore has a permanent magnetic moment. But these atomic moments are randomly oriented and dynamic as a result of the thermal agitation. Therefore, the material as a whole shows no or very small net magnetic moment. But in the presence of an applied magnetic field, the individual atomic moments tend to align in the direction of the applied field due to which the net magnetic moment increases with field. A very large net paramagnetic moment can only be achieved at large applied fields and low temperatures which drop back to zero on the removal of the applied field or an increase in the temperature due to the predominance of the randomizing thermal energy over the aligning magnetic field. At normal temperatures, paramagnets show small positive susceptibility in the range of 10^{-3} to 10^{-5} emu g^{-1} Oe^{-1} since only a partial alignment of the atomic moments are possible in an applied magnetic field [26].

The expression for the temperature dependence of paramagnetic susceptibility was formulated by Pierre Curie after a series of experiments, using a large number of substances, over an extended range of temperatures, during 1895. Curie assumed that the individual atomic moments are non-interacting and derived a relation between susceptibility per mole of the material (χ_M) and temperature (T) called the Curie law which is (Figure 1.1) mathematically given as [26]

$$\chi_M = \frac{C}{T} \tag{1.12}$$

where C is the Curie constant per mole. Later, in 1907, Curie law was modified to a more general form by Weiss, called the Curie-Weiss law, considering that the elementary atomic moments do interact among themselves and thereby generating a fictitious internal field called the molecular field (H_m). The molecular field is not a real field and rather is a force which is directly proportional to the magnetization already achieved by the material and is mathematically given as

$$H_m = \gamma M \tag{1.13}$$

where γ is called the molecular field constant. The material when placed in an external magnetic field (H) is therefore affected by both this field and the molecular field. Hence, the total field (H_t) is given by

$$H_t = H + H_m \tag{1.14}$$

Weiss modified the Curie law using these relations to obtain the Curie-Weiss law as

$$\chi_m = \frac{C}{T - \rho C\gamma} = \frac{C}{T - \theta} \tag{1.15}$$

where $\theta = \rho C\gamma$ and is a constant with dimensions of temperature. For interacting atomic moments, θ measures the strength of the interaction since it is directly proportional to γ. The Curie law is thus a special case of Curie-Weiss law with θ=γ=0, when the atomic spins are non-interacting [6,26].

Ferromagnetism is the property by which the atomic moments in certain materials tend to align in a particular direction, in the absence of an external applied field below a certain characteristic temperature called the Curie temperature (T_C). The alignment of moments in a ferromagnetic material is shown in Figure 1.2a. Above T_C, the atomic moments are randomly oriented as in a paramagnetic material and hence a ferromagnetic material behaves as a paramagnet and the susceptibility follows the Curie-Weiss law. The temperature dependence of the inverse susceptibility (χ^{-1}) and saturation magnetization (M_s) of a ferromagnetic material above and below T_C, respectively, is shown in Figure 1.2a. Ferromagnetism is observed in transition metals and their alloys like Fe, Co, Ni, FeNi, CoNi, Cu_2MnAl, etc.

The theory of antiferromagnetism was developed by Neel in the year 1932. He applied Weiss molecular field theory to explain the small positive susceptibility and the peculiar temperature dependence of susceptibility (Figure 1.2b) of an antiferromagnet. In an antiferromagnetic material, individual magnetic moments align in a regular pattern with neighboring moments pointing in opposite

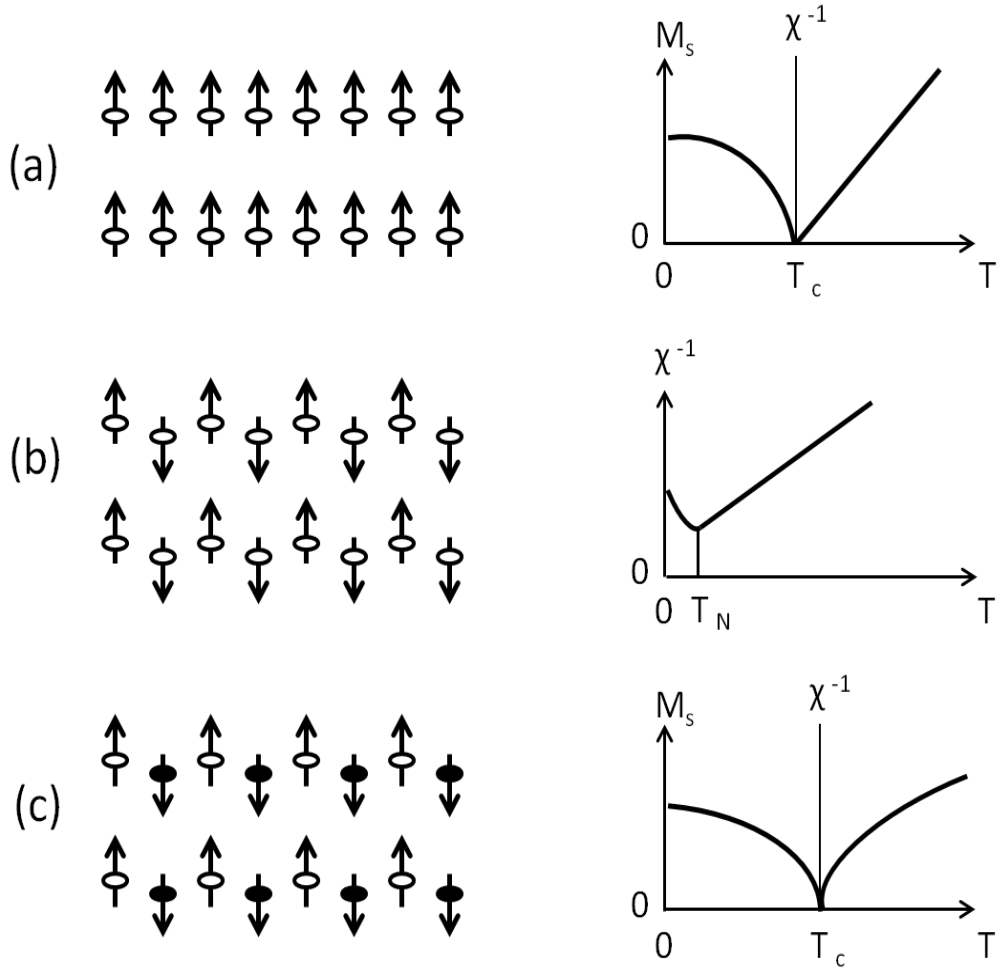

Figure 1.2: Arrangement of moments and temperature dependence of the inverse susceptibility (χ^{-1}) for (a) ferromagnetic, (b) antiferromagnetic and (c) ferrimagnetic materials. The plots (a) and (c) shows temperature dependence of saturation magnetization (M_s) below T_C. Taken from reference [26].

directions (Figure 1.2b). This results in two sublattices with equal and opposite magnetization giving a net zero magnetic moment to the material. The first experimental evidence for antiferromagnetic ordering was obtained during the neutron diffraction experiments on MnO by Shull and Smart in 1949 [29]. Similar to a ferromagnetic material, antiferromagnetic material too behaves as a paramagnet above a certain temperature called the Neel temperature (T_N). Generally, T_N lies far below room temperature so that low-temperature measurements are required to identify an antiferromagnetic material.

Similar to a ferromagnetic material, a ferrimagnetic material also exhibits substantial notable magnetism at room temperature. The arrangement of magnetic moments in a ferrimagnetic material is as shown in Figure 1.2c. A spontaneous magnetic moment arises from the net moment due to the partial cancelation of magnetic moments of the two sublattices. Ferrimagnets also behave as paramagnets above a certain temperature called the Curie temperature (T_C). Due to the presence of spontaneous magnetization, ferrimagnets finds numerous industrial applications similar to the ferromagnets. The most important class among them is ferrites, which are the double oxides of iron and another metal [6,26].

For a magnetic material, the magnetization (M) vs magnetic field (H) curve is typical of that material and is known as the magnetization curve. For a paramagnetic material, M varies linearly with H, with a positive slope (Figure 1.3a). The diamagnetic material has a negative susceptibility with the M decreasing with increase in H (Figure 1.3b). The two important features of magnetization curves of ferromagnetic and ferrimagnetic materials are saturation and hysteresis (Figure 1.3c). Saturation magnetization (M_s) is the constant magnetization that a material attains in the presence of sufficiently high magnetic field. On removing the applied magnetic field, a finite magnetization exists, called the remanent magnetization (M_r). In order to remove M_r, a magnetic field needs to be applied in the opposite direction called the coercive field (H_c). The word hysteresis means "to lag behind" and is used to describe a phenomenon which lags behind its cause. For a magnetic material, hysteresis shows the irreversibility in the magneti-

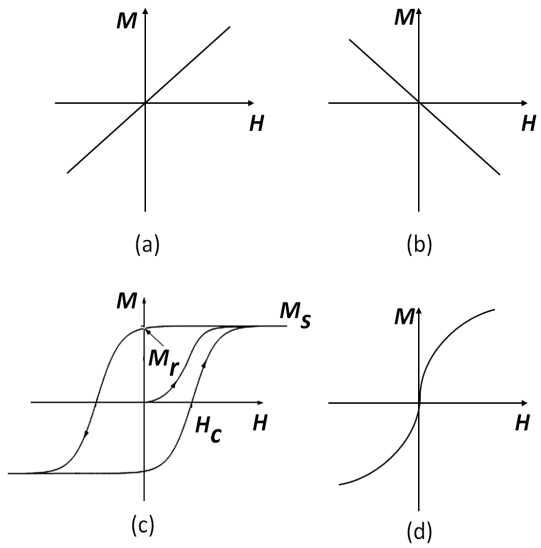

Figure 1.3: Typical M-H curves of (a) paramagnetic, (b) diamagnetic, (c) ferromagnetic/ferrimagnetic and (d) superparamagnetic materials.

zation when the external magnetic field is removed after magnetizing the material to the saturation limit. Different types of magnetism; diamagnetism, paramagnetism, ferromagnetism, ferrimagnetism and antiferromagnetism are observed in magnetic materials which can be determined by measuring their magnetic susceptibility, saturation magnetization and hysteresis behavior [16,26].

The long range ordering of the magnetic moments, in a magnetic material, arise due to the different type of exchange interactions between the atomic moments. The exchange energy (E_{ex}) between the atoms with spins S_i and S_j is given by [26]

$$E_{ex} = -2J \sum S_i.S_j = -2J \sum S_i.S_j \cos\phi \tag{1.16}$$

where, J is a particular integral called the exchange integral, which occurs in the calculation of the exchange effect, and ϕ is the angle between the spins S_i and S_j. If J is positive, E_{ex} is minimum when the spins are parallel (ferromagnetic). However, if J is negative, E_{ex} is minimum when the spins are antiparallel (antiferromagnetic). Therefore, a positive vale of J is the necessary condition for ferromagnetism to occur, whereas, a negative value of J produces the anti-

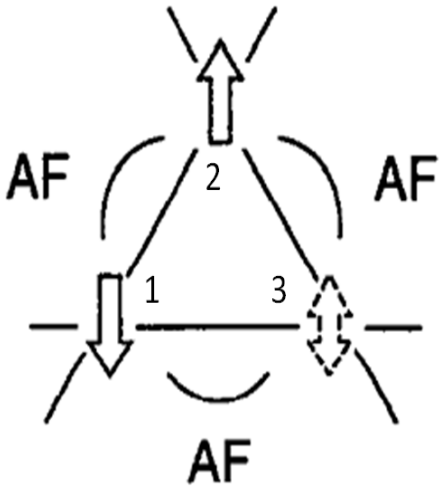

Figure 1.4: A triangular lattice showing frustration among spins due to antiferromagnetic (AF) nearest neighbor interaction.

ferromagnetic arrangement of magnetic moments [26]. There are mainly three mechanisms of magnetic exchange, namely, direct exchange, superexchange and double exchange [26].

The magnitude and sign of the magnetic exchange interaction between two magnetic moments are very sensitive to the distance between them [26]. In some materials, a pair of localized magnetic moments shows a roughly equal probability of having a ferromagnetic or antiferromagnetic interaction through two different paths [30]. As a result of this possibility of a contradictory ordering between two magnetic moments, the moments are said to be frustrated and such systems with frustrated magnetic moments are called as a spin-glass [31]. The frustration in a spin-glass can be visualized by considering an anisotropic triangular lattice with a mixture of an antiferromagnetic nearest neighbor interactions operating in equal strengths (Figure 1.4) [31]. The antiferromagnetic exchange interaction between the magnetic moments makes both the up and down spin arrangement of the third magnetic moment equally probable, thereby making the spin frustrated and affecting the long range spin arrangement of the material. This type of spin frustration can be visualized in crystallographically ordered materials with pyrochlore

or kagome lattices [31]. The spin-glass state can also be observed in disordered materials in which the randomly oriented magnetic moments interact in all three dimensions through the long range Ruderman-Kittel Kasuya-Yosida (RKKY) interactions [32]. A cusp in the temperature dependence of susceptibility, at low temperatures, due to the freezing of the magnetic moments is considered to be the characteristic of a spin-glass [30].

1.4.2 Magnetism in nanomaterials

Magnetic materials have always been in the limelight due to their immense potential applications. Magnetic nanomaterials are more exciting since they exhibit novel magnetic effects owing to the size reduction, extending the possibilities and achievements of bulk magnetic materials [2,9,15]. They are potential candidates for next generation ultrastrong paramagnets and data storage devices with storage capacity extending to terra bit range per square inch [33]. They also find applications in mechanical, electronic and biomedical industry [9]. The properties of an assembly of magnetic nanomaterial depend on the spacial correlation of spins which determines the type and extent of nanoscale exchange coupling. Therefore, magnetic thin films, multilayers, two and three-dimensional arrays or clusters show different magnetic behavior when compared to that of an individual isolated particle and find applications in diverse areas [34]. Another interesting nanomagnetic material is the liquid magnet or ferrofluids and magnetic nanofluids which are formed by dispersing fine magnetic particles in a suitable solvent [35]. A variety of materials can be used with their size typically below 10 nm, such as Fe_3O_4, $BaFe_{12}O_{19}$, Fe, Co and Ni for applications such as coolants, liquid bearings and to monitor magnetic fields and domain configurations [33]. Among the magnetic nanomaterials, magnetic iron oxides such as Fe_3O_4 and γFe_2O_3 are the most widely studied materials due to their stability, biocompatibility, ease of size-controlled synthesis and functionalization. They find applications in the areas involving targeted drug delivery, hyperthermia, ferrofluids, gene separation and magnetic adsorbents [36].

A magnetic nanomaterial exhibits unique magnetic properties when compared to a bulk magnetic material. According to the domain theory of a ferromagnetic material, its demagnetized state has a number of small regions of spin clusters with identical ordering called domains. Therefore, each domain is spontaneously magnetized to the saturation limit but the direction of magnetization is different for different domains so that the net magnetic moment is zero. The reversal in the direction of the magnetic moment of the adjacent domains occurs over a distance involving a few moments and in a gradual manner known as the domain wall or Bloch wall [37]. When the size of a magnetic material is reduced to a size which is less than the size of a domain, then the material will not accommodate a domain wall and so will consist of a single domain. The size limit (D_c) for the formation of a single domain particle can be obtained by considering the interplay between domain wall energy and magnetostatic energy for a magnetic nanoparticle and is given by Equation 1.17.

$$D_c \approx \frac{9(AK_u)^2}{\mu_0 M_s^2} \tag{1.17}$$

where, A is the exchange anisotropy constant and K_u is the uniaxial anisotropy constant, μ_0 is the vacuum permeability and M_s is the saturation magnetization [7]. Typical values for D_c are about 15 nm for Fe, 35 nm for Co, 30 nm for γ-Fe_2O_3 and 750 nm for $SmCo_5$ [38].

For a single domain particle, the anisotropy energy density E is given by the relation [26]

$$E = KV \sin^2 \theta \tag{1.18}$$

where K is the magnetic anisotropy constant, V is the volume of the particle and θ is the angle between the magnetization and the easy axis. Hence, there can be two minima in the anisotropy energy corresponding to magnetization parallel ($\theta = 0$) and antiparallel ($\theta = \pi$) to the easy axis separated by an energy barrier at $\theta =$

$\pi/2$. But for a nanoparticle, KV is very small and hence an energy fluctuation can easily overcome the anisotropy energy and thereby spontaneously reverse the magnetization of a particle from one easy direction to the other even in the absence of an applied field. Therefore, if we consider a distribution of non-interacting single domain particles, having thermal energy $k_B T$, where k_B is the Boltzmann constant and T the temperature, the thermal energy can overcome anisotropy energy barrier when $k_B T \gg KV$. As a result, the system will then behave as a paramagnet with one exception that the individual moment arises from a single domain ferromagnetic particle with many numbers of atomic spins that are ferromagnetically coupled by exchange forces and is therefore called as a superspin and the property is called superparamagnetism. The temperature at which the thermal energy overcome the anisotropy energy barrier is called as the superparamagnetic blocking temperature (T_B). The magnetization curve for a superparamagnetic material below T_B is similar to that of a ferromagnetic or ferrimagnetic material (Figure 1.3c). However, above T_B, the superparamagnetic materials show a magnetization curve with zero coercivity and a non-saturating trend (Figure 1.3d). A dense magnetic nanoparticle sample may show glassy dynamics due to the dipolar and exchange interactions between the particles [39]. Due to the unique magnetic properties, superparamagnetic materials find applications in targeted drug delivery, magnetic hyperthermia, magnetic resonance imaging, ferrofluids, sensors and magnetic adsorbents [6,26].

1.5 Carbon-based materials

1.5.1 Diamond and graphite

The extraordinary ability of the chemical element carbon to combine with itself and other chemical elements in different ways is the basis of organic chemistry and of life. The chemical versatility due to catenation gives rise to a rich and diverse structural forms of solid carbon [40]. The carbon atom has a ground state electronic configuration ls^2, $2s^2$, $2p^2$ and can form hybrid bonds by the promotion

Table 1.3: Some properties of carbon-carbon bonds. Taken from reference [40].

Bond type	Bond order	Bond length (pm)	Mean bond enthalpy (kJ mol^{-1})
$C_{(sp^3)}$-$C_{(sp^3)}$	1	153.0	348
$C_{(Ar)}$-$C_{(Ar)}$	1.5	138.4	518
$C_{(sp^2)}$-$C_{(sp^2)}$	2	132.2	612
$C_{(sp)}$-$C_{(sp)}$	3	118.1	838

*Ar - Aromatic

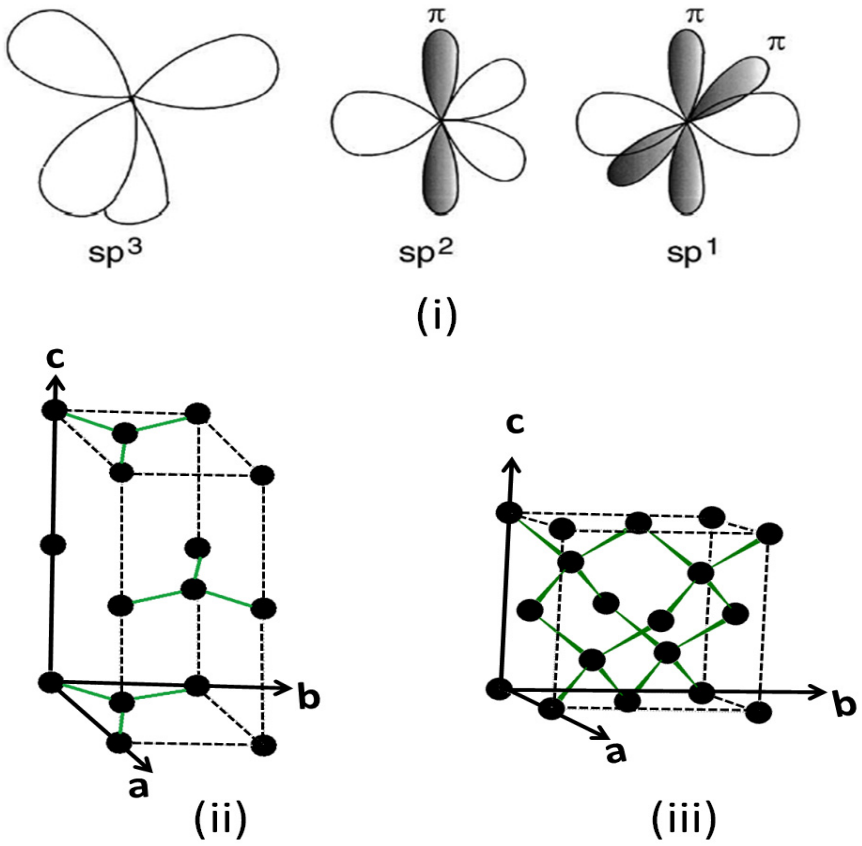

Figure 1.5: (i) sp, sp^2 and sp^3 hybridization in carbon atoms. Unit cell structures of (ii) hexagonal graphite and (iii) cubic diamond.

of electrons followed by hybridization. The emergence of different structural forms on catenation is basically due to the difference in the geometrical arrangement of hybrid orbitals with the sp^3, sp^2 and sp hybridization of carbon atoms (Figure 1.5). Table 1.3 summarizes the variation in the bond order and the mean bond enthalpy for different types of carbon-carbon bonds.

Carbon-based systems exist in both crystalline and amorphous forms. The most common and well-known crystalline allotropes of carbon are cubic diamond and hexagonal graphite (Figure 1.5). Diamond, being a gemstone, is a precious commodity and is also of industrial relevance due to its hardness. Diamond crystallizes in a cubic form with each carbon when linked to four other carbon atoms by means of sp^3 bonds forming a strain-less tetrahedral array of carbon atoms with C-C bond length of 153 pm with a zinc blende type structure [40]. Diamond also exists in the hexagonal form (Lonsdaleite) with a wurtzite crystal structure and a C-C bond length of 152 pm [41]. The crystal density of both types of diamond is 3.52 g cm^{-3}. Natural diamonds are obtained by mining whereas synthetic ones are obtained from graphite after heating it with metals, followed by a high-pressure crystallization (12-15 GPa) at elevated temperatures (1500-2000 K) [42,43]. Graphite, the second well-known allotrope of carbon, has a layered structure and is of huge industrial importance. The basic units of the crystal structure of graphite are the graphene plane or carbon layer plane which is the extended planar hexagonal array of sp^2 hybridized carbon atom having both σ and π bonding. The most common crystal form of graphite is hexagonal (Figure 1.5) and consists of a stack of layer planes in ABAB type stacking sequence [44,45]. Graphite also acquires a rhombohedral structure with ABCABC type stacking of graphene planes and is observed in very small quantities in well-crystallized graphite [45]. The density and in-plane C-C bond distance for both forms of graphite are 2.26 gcm^{-3} and 142 pm, respectively [46]. This observed bond distance is intermediate to that of pure C-C sp^3 and sp^2 bonds (Table 1.3) due to the resonance delocalization of electrons. The large inter-layer distance of 335 pm, when compared to the in-plane C-C bond length, suggests that the π-π interaction

must not be responsible for holding the layers together. Recent scanning probe microscopy images suggested that the π-orbital interaction could be responsible for the weak bonding situation [46,47]. Like diamond, graphite also occurs in nature and synthetic specimens can be prepared by high-temperature treatment of graphitizable carbons, in the range of 3000–3500 °C.

Both diamond and graphite being chemically inert, their structural difference due to different C-C bonding characteristics imparts variations in their physical properties. Table 1.4 presents the differences exhibited by these allotropes in some of the physical properties. Due to its extreme hardness, diamond is used in cutting, drilling, polishing, high-performance bearings, etc. Graphite is the most important synthetic precursor for synthesizing nanocarbon materials and is having much wider applications. Some of the applications include the use as pencil tip, battery electrodes, heat sinks for X-ray anodes, a refractory material in metallurgy and as a dry lubricant [40].

1.5.2 Carbon nanostructures

The discovery of carbon nanomaterials has revolutionized modern science due to their unique chemical and physical properties. Various carbon-based nanostructures are now synthesized in all possible dimensionalities ranging from zero dimension (fullerenes) to three dimension (nanodiamond). One-dimensional structures includes carbon nanotubes (CNTs), carbon nanofibers (CNFs), graphene nanoribbons and diamond nanorods. The two-dimensional carbon structures include graphene and diamond nanoplatelets. The ground breaking discoveries of fullerenes and graphene were recognized by the Nobel prize in chemistry in 1996 and in physics in 2010, respectively.

Fullerenes have the cage structured carbon network with different fixed proportions of sp^3 and sp^2 carbon atoms ranging from 18 atoms to 100 atoms in number and therefore have considerable angle strain [48]. The most popular fullerenes the is one with 60 carbon atoms (Figure 1.6a). Fullerenes can be prepared by different methods like arc vaporization of graphite, laser ablation, resistive heating,

Table 1.4: Properties of diamond and graphite. Taken from reference [49].

Properties	Diamond	Graphite
Density (g/cm^3)	3.515	2.267
Hardness (GPa)	79–102	Soft
Thermal conductivity (W/mK)	2000–2500 (at 25 °C)	($\|$c) 1–6 ($\perp$c) 3000
Refractive index	2.42	($\|$c)2.15 ($\perp$c) 1.8
Magnetic Susceptibility (emu/g)	(-4.5±0.2)x10^{-7}	($\|$c) -30x10^{-6} ($\perp$c) -5xl0^{-7}
Dielectric constant	5.7	($\|$c) 2.6
Resistivity (Ohm m)	$>10^{14}$	($\|$c) 3.28×10^{-2} ($\perp$c) ∼10^{-6}
Carrier Mobility (cm^2/V s)	2200 electrons 1600 holes	($\|$c) 100 electrons 90 holes ($\perp$c) 20000 electrons 15000 holes

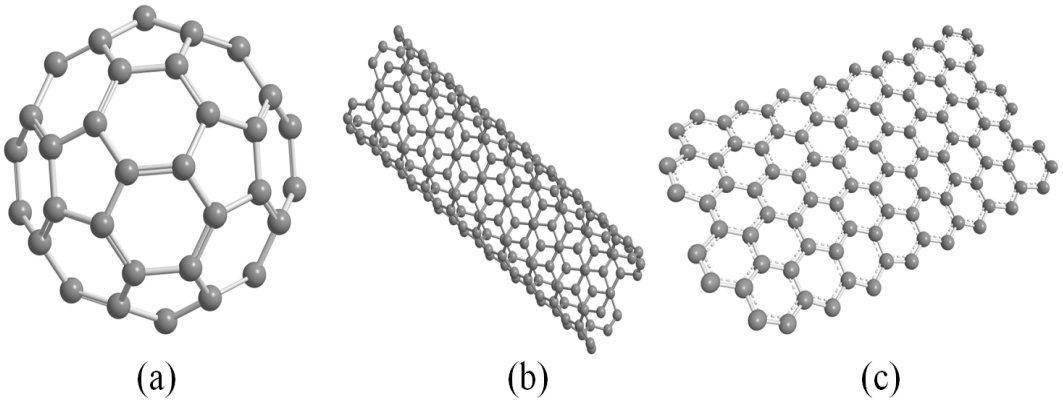

Figure 1.6: Structure of (a) C_{60}, (b) CNT and (c) graphene.

high frequency inductive heating and combustion of benzene-oxygen mixtures in laminar flow flames [50,51]. The C_{60} buckyball has a combination of 12 pentagons and 20 hexagons, forming a spheroid shape with 60 vertices for 60 carbons. Although C_{60} has an alternating system of 60 single and 30 double bonds, there is little π electron delocalization due to its curvature [48,52]. As a result, fullerenes exhibit little aromaticity and instead behave like giant electron-deficient alkene, thereby reacts readily with nucleophiles, bases, reducing agents and radicals [53]. The unusual electronic environment prevailing in C_{60}, their derivatives, polymeric forms, thin films and alkali metal encapsulated structures make them potential catalysts for many organic reactions which are otherwise not feasible [48,54–56]. They also exhibit good hydrogen storage capacity in which hydrogen is stored and released by reversible redox reaction involving carbon-carbon double bond and hydrogen [57,58]. Fullerenes and their derivatives have interesting physical properties like extreme strength, non-linear optical response, unusual electrical and magnetic properties like superconductivity and ferromagnetism [48,59–62].

A CNT can be visualized as rolled hexagonal carbon networks or graphene that are capped by pentagonal carbon rings at both the ends (Figure 1.6b). There are two types of carbon tubes, single-walled (SWNTs) and multi-walled (MWNTs), based on the number of graphene sheets rolled together to give concentrical tubes [63]. The length of CNTs are usually in micrometer, however, their diameter is in nanometers. SWNTs have a smaller diameter in the range

of a few nanometers, whereas MWNTs have a larger diameter of several tens of nanometers. Depending on the directionality in which graphene sheets are rolled, the chirality of CNTs varies, forming zig-zag, armchair or chiral nanotubes [63]. The quantum confinement of electrons perpendicular to the nanotube axis by the graphene wall results in unique physical properties since electrons can now propagate only in one direction, being the nanotube axis. This type of one directional quantum conduction with negligible resistance is not possible in a three dimensional graphite crystal. The density of states near the Fermi level (E_F) is found to depend critically on the chirality of CNTs imparting a metallic property to armchair CNTs and semiconducting property to zig-zag CNTs [64]. Therefore, the physical and chemical properties of CNTs depend on the different structural parameters like inner diameter, outer diameter, the number of walls and the chirality of CNTs [64]. CNTs can be synthesized using a wide variety of processes involving arc-discharge, laser ablation, electrolysis of carbon electrodes, chemical vapour deposition, hydrothermal methods and pyrolysis of hydrocarbons over metal particles [65,66]. Some of the possible applications of CNTs include conductive films, solar cells, fuel cells, supercapacitors, transistors, memories, displays, separation membranes and filters, purification systems, sensors, clothes and drug delivery [67–70].

The latest and most important additions to the nano carbon family which has lead to an explosion of ideas are the two-dimensional structures including graphene (Figure 1.6c) and graphene-related materials like graphene nanoribbons, graphene oxide and reduced graphene oxide [71,72]. Graphene-related systems have been suggested as alternative material for nearly every possible applications [73]. This large demand has triggered the developments in synthetic techniques, doping and functionalization of graphene related systems [74,75].

The most explored aspect of graphene physics is its electronic properties. Electrons propagating through a perfect carbon honeycomb lattice completely loose their effective mass and, as a result, these quasi-particles are described by a Dirac-like equation rather than the Schrödinger equation [76–78]. The theoretical cal-

culations of the energy band structure showed that graphene has geometrically similar valence and conduction bands which intersect at a single point of zero states at the intrinsic Fermi level called the Dirac point, giving graphene a zero-gap semiconducting nature with semi-metallic properties. The two-dimensional quantum confinement leads to some peculiar properties like the quantum Hall effect, Klein tunneling and field effect [78]. Even though graphene is highly flexible, it exhibits huge mechanical strength of 130 Gpa and also can withstand elevated temperatures [79]. Graphene can adhere to metal as well as metal oxide surfaces thereby acting as a hydrophobic coating as well as can act as a protective sheath which effectively reduces corrosion rate to about 20 times [80,81]. Graphene can also be extremely useful in integrated circuits and computer chips due to its high electrical and thermal conductivity (5×10^3 W/mK) along with a negative thermal expansion coefficient owing to the two-dimensionality of out-of-plane phonons [82–84]. The observation of Peltier cooling in metal-graphene junctions is also highly promising while considering high-performance electronics and miniaturization of devices [85]. Strong and flexible transparent conducting graphene films along with graphene quantum dots can find applications in next generation flexible displays along with other numerous optoelectronic, sensor and biomedical applications [73,78].

Apart from these physical properties, graphene and its derivatives like graphene oxide and graphene nanoribbons can exhibit diverse properties due to their unique surface characteristics [86,87]. They can adsorb different atoms or molecules like K, NH_3, NO_2, I_2, etc. on to their surfaces forming donor-acceptor systems similar to graphite [88–91]. Graphene-based systems currently find their use as a support material for catalytically active transition metals [92]. The nanometer scale corrugations in doped or functionalized graphenes as well as in pristine graphene offer further possibilities since they can modify the local environment thereby altering their reactivity. This can enable to perform a wide range of transformations and may offer extraordinary potential in the design of novel catalytic systems, thus making them effective in catalysis [73,93]. The large surface area in the range of

$\sim$2500-3000 m^2/g makes them effective in environmental applications like water treatment. They are also promising candidates for applications in sustainable energy devices like supercapacitor and solar cells [94–96]. Chemical modification or insertion of defects, both intrinsic and extrinsic, in the perfect honeycomb lattice of graphene can perturb the surface energy as well as the energy band structure, increasing the density of states near the Fermi level due to which the properties will be substantially modified and thus open up further possibilities to engineer graphene for many diverse applications [93,97].

1.5.3 Disordered carbon structures

Carbon structures lacking long range order falls under the broad category of disordered carbon. Their bonding characteristics are intermediate between that of diamond and graphite, with the presence of both sp^3 and sp^2 hybridized carbon atoms at variable proportions [98]. The disordered structures having considerably larger proportions of sp^2 hybridized carbon, with a relatively long range of ordering when compared to other disordered carbons are called graphitic carbons [99]. Amorphous carbon (a-C) films can be deposited from carbon containing gases and hydrogenated amorphous carbon (a-C:H) films can be prepared with different proportions of hydrogen, where the hardness of the film is inversely related to the concentration of hydrogen [100,101]. Films with 80-90% of sp^3 carbons are called tetrahedrally-bonded amorphous carbon (ta-C). Hard a-C:H films, known as diamond-like carbon (DLC), are of great interest since their isotropic disordered films without any grain boundaries have chemical inertness, hardness and elastic modulus comparable to that of diamond [102–104].

The ternary phase diagram showing the composition of different disordered carbon forms is shown in Figure 1.7 [105]. The different disordered carbon structures referred in the ternary phase diagram (Figure 1.7) can be synthesized by different techniques like sputtering, pulsed laser deposition, ion-beam deposition, plasma enhanced chemical vapour deposition, etc. using suitable precursors. In addition to these disordered thin films, there are many other carbon forms with

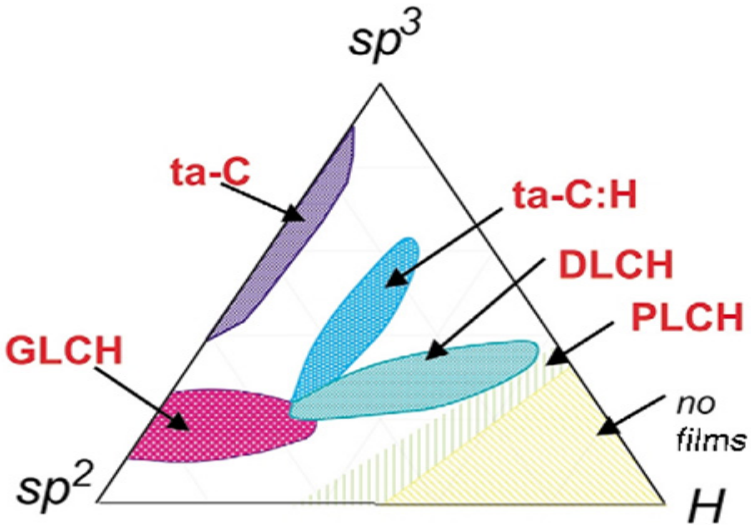

Figure 1.7: Ternary phase diagram of disordered carbon. Taken from reference [105].

disordered graphitic ordering such as soot, chars, glassy carbon and evaporated a-C [106]. These sp^2-rich carbons can be prepared by pyrolysis of suitable precursors or by a high temperature annealing of sp^2-less carbons and falls in the lower left corner of the phase diagram. Top corner contains DLC with 100% sp^3 carbon and the right corner is limited by two hydrocarbon polymers $(CH_2)_n$ and $(CH)_n$ beyond which only molecules form, since structures with interconnecting C-C bond with high hydrogen content are not stable [106].

In general, disordered carbon consists of both sp^3 and sp^2 hybridized carbon atoms distributed in different proportions [107,108]. If we consider a mixed state with a small proportion of sp^3 sites in an sp^2 matrix, one sp^3 site can interact with four hexagonal rings of two different graphite planes due to their tetrahedral geometry. Therefore, a small amount of sp^3 sites in a perfect graphite lattice can completely destroy the ordered arrangement. Such disordered lattice has a considerable amount of structural strain due to the local distortions created by the sp^3 sites [109,110]. With thermal energy being available, the system tries to minimize its lattice energy by forming graphitic clusters by the migration of the sp^3 defects to the sp^2 network. The ease of migration of the sp^3 defects and the resulting clustering depends on the sp^2 to sp^3 ratio, where the energy barrier

decreases with increasing sp^2 fraction.

Disordered carbon materials are classified as graphitizable and non-graphitizable, depending on the structural disorder present in the material. Graphitizable carbon is considerably ordered with low sp^3 content whereas non-graphitizable carbon is highly disordered and has a higher proportion of sp^3 carbon sites [109,111]. Due to the initial difference in the crystallinity, with heat-treatment, graphitizable carbon exhibits much higher structural ordering than non-graphitizable carbon. The lower limit of structural ordering in non-graphitizable carbon, than that in graphitizable carbon, is due to the fact that the structural ordering results from the growth of crystallites already present in the material and not by the formation of new crystallites. The three basic steps involved in the thermally assisted structural enhancement are (i) in-plane crystallite growth, (ii) coalescence of a crystallites along the c-axis and (iii) coalescence of crystallites perpendicular to the c-axis [109]. The first step involves the in-plane growth of small graphitic clusters which starts at relatively lower temperatures (400-600 °C) and proceeds at higher rates with elevation in the temperature. Second and third steps proceed through a thermally activated process which requires much higher temperatures ($\geq$1000 °C for step-ii and $\geq$1500 °C for step-iii). Step-i and step-ii are observed in both types of carbon, whereas step-iii is observed only in graphitizable carbon. It is difficult to induce a perfect graphitic structure by the heat-treatment process, however, the crystallinity can be increased to form a defective graphitic system [112].

The sp^3 and sp^2 carbons give rise to the valence σ and conduction σ^* states separated by a large gap ($\sim$4-6 eV) and the sp^2 carbons form the π and π^* states which occupy the larger gap formed between the σ states. Because of this difference, the sp^3-rich carbon systems have less density of states near the Fermi level, compared to the sp^2-rich systems [107]. The π states formed by the sp^2 carbon atoms are sensitive towards different factors like the sp^3 to sp^2 ratio, their geometrical correlation and clustering of sp^2 carbon atoms [108]. Therefore, these factors determine the energy band structure and the electronic properties which get modified in a

particular system depending on the proportion, clustering or spatial correlation of the sp^2 carbon atoms [49]. The physical properties of different disordered carbon materials depend on the sp^3 to sp^2 ratio, extent and type of clustering of sp^2 phase and presence of heteroatoms. The sp^3 content mainly determines the elastic constants whereas the sp^2 carbon atoms and presence of heteroatoms determine the optical, electronic and mechanical properties [49,113–115]. The possibility of preparing disordered carbon structures with slight modifications in the structural elements, has made them applicable in a variety of fields like magnetic hard disk coatings, wear-protective and antireflective coatings for tribological tools, engine parts, razor blades, corrosion and gas permeation barrier, biomedical coatings for implants, electromechanical and electrochemical systems [105,106,116–120]. Chemically modified disordered carbons, like the fluorinated derivatives, are of special importance due to their low dielectric insulating nature which is useful in improving the switching performance of circuits [121]. The observations of disorder-dependent fluctuations in metal-insulator transitions [25], photoconductivity [122], photoluminescence [123], superconductivity and magnetism [124] are of widespread interest and great significance.

1.5.4 Activated carbon

Activated carbon is obtained by either chemical or physical activation of a carbon-based material and has a large specific surface area (1000–3000 m^2/g) due to the high porosity [125–127]. Carbon-based materials or carbonaceous precursors like organic molecules or polymers can be used for preparing activated carbon by heat-treating at high temperatures (physical activation) in the presence of gases such as O_2, CO_2, etc. [127]. However, the activated carbons produced by the heat-treatment carbonaceous precursor after mixing them with a suitable activating agent such as KOH, NaOH, $ZnCl_2$, H_3PO_4, etc. (chemical activation) have very large surface area and porosity when compared to the physically activated carbons [127]. The surface area and porosity of the activated carbon is also determined by the factors like activation temperature, the amount of activating agent used and

carbonaceous precursor used [128].

Due to the specific large surface area and porous nature, they find applications in water and air purification, gas storage and sequestration, sustainable, environmentally friendly energy storage devices, etc. [126,129–131]. Independent surveys indicated that the demand for activated carbon around the globe can raise by 7.9% every year and is estimated to reach 2.2 million metric ton by 2018 [132]. This increase in demand is mainly due to the recent stringent regulations imposed on the industrial water and air purification standards. With such a huge need, the selection of cheap and easily available organic materials like dead leaves, different nut shells and seeds, husks, wood, sugarcane bagasse, etc., can minimize the production cost and thereby increase the economic viability of activated carbon for large scale applications. Several synthetic precursors like polymers, organic molecules, carbon nanomaterials like graphene, fullerenes, nanotubes, nanofibers, etc. have been used for preparing activated carbonaceous systems [126,133]. These activated carbon-based materials are found to be more efficient and effective for applications in energy storage devices like supercapacitors and battery electrodes after performing a chemical or physical activation [126,134]. H_2 storage is yet another important application which makes activated carbon structures an important candidate while considering sustainable energy solutions [135]. The main criteria that should be met for effective applications in these thrust areas are increased specific surface area and a well-defined pore size distribution with a large number of micropores [136]. But for environmental applications, such as water purification and adsorption of macromolecules like organic dyes, mesoporous carbon is preferred [137].

1.6 Electrical properties of disordered carbon systems

Carbon-based systems like diamond, graphite, nanotubes, fullerenes, graphene, etc. exhibit different electrical properties, from insulating to semiconducting to

superconducting, owing to the difference in the bonding characteristics which in turn determines the energy band structure [138,139]. Any modification in the periodic array of carbon atoms in these structures results in the modification of the band structure which thereby alters the electronic properties [49]. Therefore, the three-dimensional disordered carbon systems, which are structurally in between diamond and graphite, are of particular interest. They can form a wide spectrum of materials (Figure 1.7) with unusual electronic structure and transport properties depending on the nature and the spatial arrangement of sp^3 and sp^2 bonded carbon atoms, when compared to the ordered allotropes [25,49]. Theoretical calculations showed that in a non-graphitic disordered structure with arbitrary sp^2 to sp^3 ratio, the sp^3 sites generate a large gap in the energy band structure, nearly similar to that in diamond ($\sim$5 eV). However, the sp^2 sites, existing as pairs, even-membered rings or chains of sp^2 hybridized carbon atoms, form π states with a smaller gap ($\sim$2 eV), whereas isolated sp^2 sites and odd-membered rings form localized states in the gap giving a finite density of states around the Fermi level for disordered carbons [139,140]. Therefore, in a large band gap formed by σ states, there can be energy intervals formed by localized states known as the mobility gap of an amorphous semiconducting material, where the mobility edge separates the localized states from the extended band tail [24].

In disordered semiconductors with localized states, it is expected that electronic transport basically occurs by hopping of charge carriers through localized π and π^* states in the energy gap, which is mediated by phonons or thermal energy [141]. The specific nature of the hopping conduction in amorphous semiconductors is still a matter of debate and different types of conduction mechanisms, involving hopping of charge carriers, have been proposed. The most widely observed mechanism is the nearest neighbor hopping by thermal activation of charge carriers at high temperatures (Equation 1.19) which involve the jump of charge carriers from one localized state to another localized state or extended states of the energy band with higher energy, utilizing the available thermal energy. Thermally activated hopping conduction is generally observed in highly disordered carbons

like those heat-treated below 800 °C [142,143].

$$\rho(T) = \rho_0 \; exp\left(\frac{E_{hop}}{k_B T}\right) \tag{1.19}$$

where $\rho(T)$ is the pre-exponential factor, $\rho(T)$ is the resistivity at temperature T, E_{hop} is the activation energy for the hopping of charge carriers and k_B is the Boltzmann constant.

Another commonly observed transport mechanism in disordered carbon-based materials is the variable range hopping type conduction near the Fermi level, especially at low temperatures and is given by the Mott's $T^{1/4}$ law (Equation 1.20) [24].

$$\rho(T) = \rho_0 \; exp\left(\frac{T_0}{T}\right)^{1/4} \tag{1.20}$$

where $\rho(T)$ is the temperature dependant resistivity, T is the temperature, ρ_0 is the pre-exponential factor, T_0 is the characteristic Mott temperature which depends on the electronic structure, density of states near the Fermi level and the localization length. The Mott variable range hopping (VRH) model is based on the thermally assisted hopping of charge carriers between the localized states which are far in space but energetically positioned near the Fermi level with comparable energy. However, the power to which the temperature is raised in Equation 1.20 is found to vary depending on the dimensionality of the material. Hence, a more general form of Mott's law (Equation 1.21) is used for describing the variable range hopping conduction, given by

$$\rho(T) = \rho_0 \; exp\left(\frac{T_0}{T}\right)^{\beta} \tag{1.21}$$

where β indicates the dimensionality of the conduction process with $\beta = \frac{1}{d+1}$, for d-dimensional conduction [23,24].

Apart from variable range hopping, many other types of conduction mechanisms are observed at low temperatures in disordered carbons [25,144]. The Coulomb gap (CG) or Efros-Shklovskii (ES) type VRH conduction arises due to the long-range Coulomb interaction between the localized electrons [145]. This interaction breaks down the fundamental assumption of the Mott's theory that the density of states near the Fermi level is constant. It was shown by Efros *et al.* that the density of states near the Fermi level vanish, creating a gap near the Fermi level, called the Coulomb gap (CG), due to the interaction between localized electrons which therefore modifies the conduction mechanism from Mott VRH to CG VRH with β =1/2 (d=1) in Equation 1.21 [145]. A crossover from Mott VRH to CG VRH has been observed in different systems such as disordered carbon films, boron doped carbon and thin films of In_xO_y [25,146,147]. Miyake *et al.* showed that the resistivity curve for sputtered amorphous carbon films deviates from Mott $T^{1/4}$ law and rather has a T^n dependence (Equation 1.22) due to the multiphonon tunneling in this system because of the presence of a weak lattice-carrier coupling in the delocalized π system [148,149].

$$\sigma(T) = \sigma_0 \ (T/T_0)^n \tag{1.22}$$

where $\sigma(T)$ is the conductivity at temperature T, σ_0, A and n are constants [148].

The transport properties of partially ordered materials like the pre-graphitic carbon fibers, defective graphene, etc. are found to be considerably different from those exhibited by a highly disordered material [150]. In these materials, the resistivity exhibits weak temperature dependence, which can be explained only by weak localization mechanisms. More details regarding the weak localization mechanisms are discussed in Chapter 5 (Section 5.5.1).

The fluctuations in the transport properties of disordered carbons, with the extent of ordering, make them particularly interesting due to the scientific and industrial importance of cheap and easily processable semiconducting materials. The density of states near the Fermi level and the extent of localization depend critically not only on the sp^2 to sp^3 ratio but also on the spatial correlation and

clustering of sp^2 sites, disorder, presence of hetero-atoms and sp^3 defects [108]. Changes in the room temperature conductivity and a shift in the conduction mechanism from p-type to n-type were observed after incorporating metallic impurities and hetero-atoms like phosphorous, boron, nitrogen, etc. into the carbon lattice, owing to the increase in the density of states near the Fermi level [151–154].

The disordered carbon obtained by the random inhomogeneous distribution of sp^2 clusters in an sp^3 background are called as graphitic carbons and the random assembly of nano-graphitic sp^2 hybridized carbon domains are termed as nanographites [25]. The thermal or pressure assisted ordering of disordered carbon to a nanographitic phase involves a large increase in the room temperature conductivity with a decrease in the temperature dependence of conductivity below room temperature, indicating an insulator to metal transition with the ordering of graphitic clusters [25,155]. Apart from structurally disordered carbon, this kind of disorder-induced metal-to-insulator, transition called as Anderson transition, has also been observed in many doped semiconductor systems with a compositional disorder like Si:P, $Al_xGa_{1-x}As$ and Ge:Sb [156].

1.7 Magnetism in carbon structures

Diamagnetism has been reported for nearly all carbon-based structures like graphite, diamond, fullerenes, carbon nanotubes and perfectly ordered graphene [157–160]. Diamond has a large diamagnetic susceptibility of -4.5±0.2×10^{-7} emu/g , whereas graphite shows anisotropic diamagnetic susceptibility of about -30×10^{-6} emu/g and -5×l0^{-7} emu/g parallel and perpendicular to c-axis, respectively [161,162].

Further studies showed that the magnetic properties of carbon depend critically on the allotropic modification. Unlike diamagnetic diamond and graphite, in a disordered non-planar carbon lattice containing both sp^2 and sp^3 carbons, spin ordering and magnetic interactions take place [161,163]. This lead to the remarkable development of molecular magnetism [164]. Some of the organic molecules even showed ferromagnetic nature, with a very low T_C (∼1 K) [161]. Due to the enormous interest and large potential applications of lightweight organic ferromag-

nets, many new compounds were synthesized and studied [164]. The accidental discovery of ferromagnetism in the charge transfer complex tetrakis(dimethylamino)-ethylene-C_{60} (TDAE-C_{60}), with T_C = 16 K was a breakthrough in d^0 ferromagnetism [165]. However, there was lot of skepticism about the intrinsic origin of magnetic signals in TDAE-C_{60} but the magnetic measurements made by Suzuki *et al.* [166] and Dunsch *et al.* [167] along with the electron spin resonance experiments by Lappas *et al.* [168] pointed towards the intrinsic origin and demonstrated the existence of an internal magnetic field of about 70 Oe. Later, more doped fullerene systems were studied for their magnetic properties like the cobaltocene doped C_{60} by Mrzel *et al.* [169], who measured a T_C of 19 K, which is higher than that of TADE-C_{60}.

One of the models proposed for making magnetic carbon is the modification of an ordered graphene lattice by substitution of heteroatoms or by the creation of defects using high energy irradiation [170]. The disordered carbon structures include nanodiamond, nanographite, irradiated structures, tetrahedrally bonded nanocarbon or carbon nanofoam, thermally graphitized carbon, reduced graphene oxide, defective graphene, etc. Nanographite is one system which is particularly studied in detail by both experimentalists and theoreticians due to the unique behavior of the π-electron system. Moreover, in nanographites, the electronic structure and the resulting optical, magnetic, transport and thermal properties are completely governed by geometric factors like width, packing, curvature, presence of voids, edge geometry, etc. which give a lot of flexibility in tailoring the properties and also provide novel systems for fundamental study [32,161,171,172]. A graphene layer can be terminated in two different geometries, the zigzag geometry and the armchair geometry (Figure 1.8a) [161]. Energy band calculations showed that unlike the arm chair edges, the zigzag edges have a specific feature with the appearance of a sharp peak in the density of states localized at the Fermi level in the region where the π and π^* bands of a 2D graphite contact each other (Figure 1.8b) [161]. These flat energy bands near the Fermi level can contribute to the paramagnetism by the conduction electrons, called the Pauli paramagnetism or

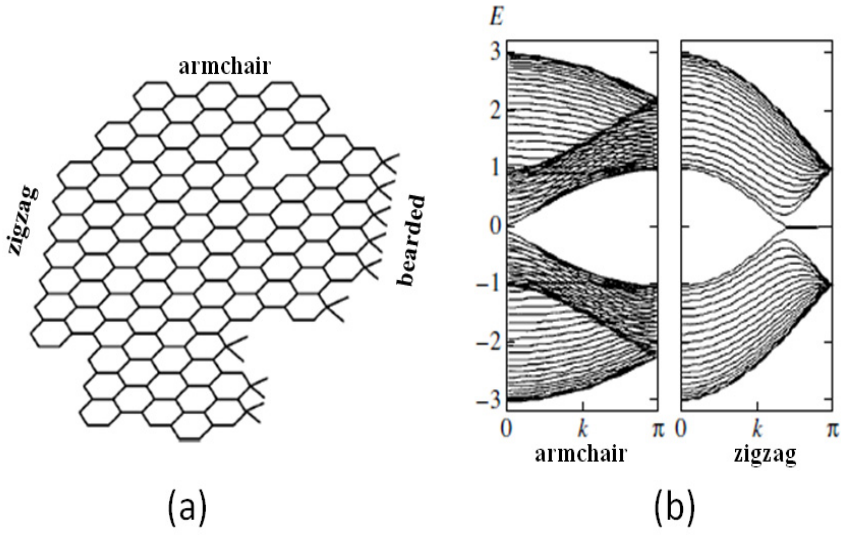

Figure 1.8: (a) Edge geometry and (b) band structure in graphene. Taken from reference [161].

can develop a ferrimagnetic structure whose extent is controlled by the magnitude of the surface deformation caused by the electron–phonon interaction [161,173].

Similarly, the creation of defects in a perfect honeycomb lattice gives rise to a sharp asymmetric peak in the density of states at the Fermi level where the electrons can be easily spin polarized in an applied field to produce a measurable magnetic moment [161,173]. A theoretical study of a graphene ribbon using local spin density calculations showed that the entrapment of hydrogen by dangling bonds at the nanographite perimeter forming bearded edges (Figure 1.8a) can induce a finite magnetization [174]. However, the edge state magnetic moment is fractional, about 0.2 μ_B, deviating from what is expected in the purely localized spin system with a magnetic moment of 1 μ_B [32,175]. The edge state spins for a perfect graphene zigzag edge are arranged in parallel to each other with strong ferromagnetic interactions [176].

Many experimental studies have showed measurable magnetic moments arising from defective carbon materials [170,177–181]. The evolution of disordered spin-glass-like magnetic state during the heat-treatment of amorphous carbon nanofibers was experimentally studied by Shibayama *et al.* [177]. The evolution

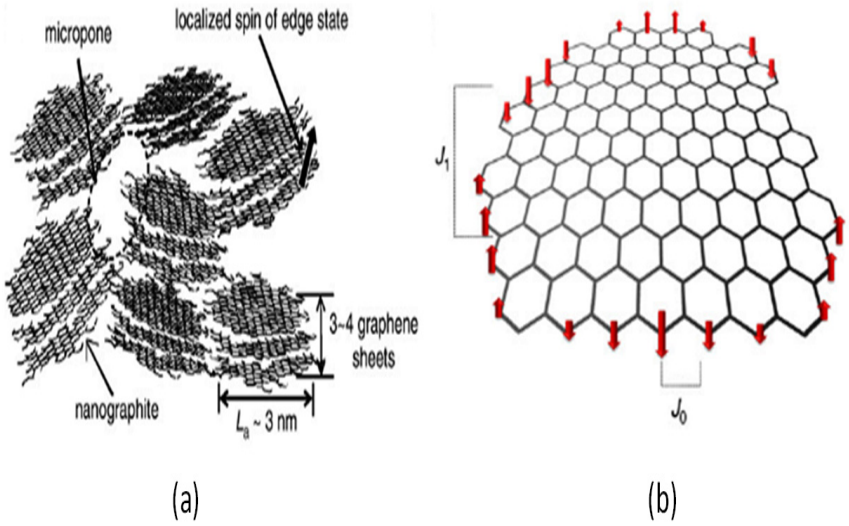

Figure 1.9: Schematic structure of (a) disordered carbon and the structure of an individual (b) nanographene sheet in a nanographite domain along with the spatial distribution of edge-state spins. Taken from reference [32].

of disordered magnetic state suggested complex spin interactions among the localized edge state magnetic moments occurring inside the carbon structure during a graphitic ordering at high temperatures. Amorphous carbon fibers consists of a porous three-dimensional (3D) disordered carbon network of nanographite domains, consisting of a stack of 3–4 nanographene sheets (Figure 1.9a) with the mean in-plane size of about 3 nm [32]. In such a system, different magnetic exchange interactions are predicted (Figure 1.9b). An irregular shaped nanographene sheet has a random distribution of zigzag and armchair edges, among which the spins are arranged ferromagnetically through strong intra zig-zag edge ferromagnetic exchange interactions (J_0) which depend on the edge length and the surrounding environment [176,177]. The spins in a zig-zag edge interact with the spins in the neighboring zig-zag edge through a nanographene analogue of Ruderman-Kittel-Kasuya-Yosida (RKKY) interaction involving an indirect exchange (J_1) mediated by π conduction electrons [6,32]. The J_1 interactions are ten to thousand times weaker than J_0 interactions and they can be (+) ferromagnetic or (-) antiferromagnetic depending on the geometrical relation between the zig-zag edges

considered [32]. The presence of J_0 and J_1 with varying strength develops a finite net magnetic moment with a ferrimagnetic structure in a nanographene sheet [182]. The inter-nanographene sheet magnetic interaction (J_2) in a nanographite domain is antiferromagnetic with intermediate strength. This again brings about a ferrimagnetic structure to nanographite domain since J_2 is operating between the effective magnetic moments in nanographene sheets of different magnitude. Lastly, the inter-domain moments interact through weak antiferromagnetic J_3, forming a ferrimagnetic spin state in ACF [32].

1.8 Materials related to the present work

Disordered Carbon: Carbon is a very versatile element and has been in the center stage for years. There had been significant advances in the science of crystalline carbon whereas the disordered form is still not explored completely due to its versatility. In recent years most of the studies on disordered carbon focused mainly on its surface area and porosity for developing cost effective adsorbents for water and air purification as well as applications like supercapacitor electrodes [137,183]. However, recent experiments on irradiated graphite, nanographite, graphene, reduced graphene oxide, etc. showed that these carbon-only systems can exhibit substantial magnetic response even above room temperature and hence are potential candidates for manufacturing light weight magnets as well as in other applications in the electronic and biomedical industry [170,178,184,185]. The observed magnetism of carbon-based materials depend on edge state spins structure and disorder present in the material [32,177].

Activated Carbon: The structure of different carbon-based materials can be modified by enhancing their surface area and porosity by using different activation methods. Different physical or chemical activation techniques can be used, depending on the application of the material. Activated carbon produced by using activating agents like H_2SO_4, HNO_3, H_3PO_4, $ZnCl_2$, KOH, etc. can have a high surface area with micro/mesopore structure, depending on the activation condition, which makes them attractive as adsorbents, catalytic supports,

supercapacitors, etc. [126,186]

Magnetic carbon composite: Magnetic carbon composites are interesting candidates for water treatment application. A composite of porous carbonaceous material and a nanomagnetic material like Fe_3O_4, Fe_2O_3, Fe, Co_3O_4, Co, Mn_3O_4, etc. with sufficiently high magnetic moment has a major advantage that the magnetic functionality allows the separation of carbon-based adsorbents employed in aqueous system by using an external magnet thereby avoiding the tedious filtration process [187,188]. Many groups around the globe have used this technique for the removal of heavy metal ions and dye molecules from water [187–191].

1.9 Scope of the present work

Most of the previous studies on the magnetic properties of carbon-based materials have been on carbon systems which are near to graphitic ordering. One of the objectives of the present study is to investigate the magnetic properties of more disordered carbon structures and their evolution with structural ordering after preparing bulk disordered carbon samples from a widely used carbon precursor, coconut shell (CS), by simple heat treatment technique. Most of the commercial carbon samples have unknown thermal history and therefore, the correlation of physical properties with the preparation condition is difficult. The choice of CS as the carbon source allows the preparation of disordered carbon with precise control of heat-treatment conditions, which is known to govern the extent of disorder and this may affect the magnetic and electrical properties.

The present study also aims to study the evolution of the electrical properties with the heat treatment-temperature. In most of the reports, the resistivity is thoroughly analyzed only for highly insulating disordered carbon. These materials show large localization and the resistivity increases exponentially with decreasing temperature. However, the electrical properties of a disordered carbon system can vary with the extent of disorder. For disordered carbons, with structural ordering, the resistivity is observed to be less temperature independent. However, for these materials, the conduction mechanism of highly disordered and considerably

ordered carbon specimens has not been satisfactorily explained. The present work attempts to study the changes in the conduction mechanism and the magnetic properties of disordered carbon by systematically analyzing the development in the structural characteristics with heat-treatment.

The CS based activated carbon prepared using KOH has high commercial importance. They are currently employed in water and air filtering units, and studied extensively for applications in electrochemical energy devices, However, the magnetic and electrical properties of KOH activated carbon have not been studied yet, despite of its commercial importance. The present study attempts to correlate the structural evolution and the corresponding changes in the magnetic and electrical properties of the KOH activated carbon. This work is further extended, to the preparation of a cheap highly porous magnetic adsorbent for the removal of oil from oil spills in water bodies. Previous studies using similar magnetic carbon composites, where the carbon is derived from other sources, suffer from the disadvantages like low oil retention, slow response, high cost, etc. The CS based magnetic carbon composite is observed to remove large quantities of oil, instantaneously. The preparation of the material is easy and can be used for preparing large quantities of the material, without any difficulty.

Bibliography

[1] H. Hosono, Y. Mishima, H. Takezoe, H and K. J. MacKenzie, *Nanomaterials: Research Towards Applications* (Elsevier, 2006).

[2] R. W. Kelsall, I. W. Hamley and M. Geoghegan, *Nanoscale Science and Technology* (Wiley, 2005).

[3] B. D. Fahlman, *Materials Chemistry* (Springer, 2011).

[4] H. R. Allcock, *Introduction to Materials Chemistry* (John Wiley & Sons Inc., 2008).

[5] M. A. White, *Physical Properties of Materials* (CRC Press, 2011).

[6] J. M. D. Coey, *Magnetism and Magnetic Materials* (Cambridge University Press, 2010).

[7] R. C. O'handley, *Modern Magnetic Materials: Principles and Applications* (Wiley, 2000).

[8] C. N. R. Rao, G. U. Kulkarni and P. J. Thomas, *Nanocrystals: Synthesis Properties and Applications* (Springer Science & Business Media, 2007).

[9] C. N.R Rao, A. Muller, and K. C. Anthony, *The Chemistry of Nanomaterials: Synthesis, Properties and Applications* (John Wiley & Sons, 2006).

[10] C. P. Poole and F. J. Owens, *Introduction to Nanotechnology* (John Wiley & Sons, 2003).

[11] J. Yacaman, L. Rendon, J. Arenas and M. C. R. Puche, *Science* 273 (1996) 223.

[12] M. Faraday, *Philos. Trans. R. Soc. London* 147 (1857) 145.

[13] K. E. Drexler, *Nanosystems: Molecular Machinery, Manufacturing, and Computation* (Wiley-VCH, 1992)

[14] C. Brechignac, P. Houdy and M. Lahmani, *Nanomaterials and Nanochemistry* (Springer Science & Business Media, 2008).

[15] W. A. Goddard, D. Brenner, S. E. Lyshevski and G. J. Iafrate, *Handbook of Nanoscience, Engineering, and Technology* (CRC press, 2007).

[16] A. R. West, *Solid State Chemistry and its Applications* (John Wiley & Sons, 2013).

[17] T. Terashima, K. Shimura, Y. Bando, Y. Matsuda, A. Fujiyama and S. Komiyama, *Phys. Rev. Lett.* 67 (1991) 1362.

[18] C. Kittel, *Introduction to Solid State Physics* (John Wiley & Sons, 2004).

[19] L. Solymar and D. Walsh, *Electrical Properties of Materials* (Oxford University Press, 2004).

[20] P. W. Anderson, *Phys. Rev.* 109 (1958) 1492.

[21] E. N. Economout and M. H. Cohen, *Phys. Rev. Lett.* 25 (1970) 1445.

[22] P. A. Lee and T. V. Ramakrishnan, *Rev. Mod. Phys.* 57 (1985) 287.

[23] N. F. Mott and E. A. Davis, *Electronic Processes in Non-crystalline Materials* (Clarendon Press, 1979).

[24] N. F. Mott, *Metal-Insulator Transitions* (CRC Press, 1990).

[25] K. Takai, M. Oga, H. Sato, T. Enoki, Y. Ohki, A. Taomoto, K. Suenaga and S. Iijima, *Phys. Rev. B* 67 (2003) 214202.

[26] B. D. Cullity and C. D. Graham, *Introduction to Magnetic Materials* (John Wiley & Sons, 2011).

[27] G. A. Bain and J. F. Berry, *J. Chem. Edu.* 85 (2008) 532.

[28] S. H. Tolbert, A. Firouzi, G. D. Stucky and B. F. Chmelka, *Science* 278 (1997) 264.

[29] C. G. Shull and J. S. Smart, *Phys. Rev.* 76 (1949) 1256.

[30] C. Y. Huang, *J. Magn. Magn. Mater.* 51 (1985) 1.

[31] A. P. Ramirez, *Annu. Rev. Mater. Sci.* 42 (1994) 453.

[32] T. Enoki and K. Takai, *Solid State Commun.* 149 (2009) 1144.

[33] S. D. Bader, *Rev. Mod. Phys.* 78 (2006) 1.

[34] R. Skomski, *J. Phys.: Condens. Matter* 15 (2003) R841.

[35] N. A. Frey, S. Peng, K. Cheng and S. Sun, *Chem. Soc. Rev.* 38 (2009) 2532.

[36] A. H. Lu, E. L. Salabas, and F. Schuth, *Angew. Chem. Int. Ed.* 46 (2007) 1222

[37] F. Bloch, *Z. Physik* 74 (1932) 295.

[38] G. C. Hadjipanayis and G. A. Prinz, *Science and Technology of Nanostructured Materials* (Plenum, 1991)

[39] P. E. Jonsson, arxiv.org/pdf/cond-mat/0310684.

[40] B. Mcenaney, *Carbon Based Materials for Advanced Technology* (Elsevier Science Ltd., 1999).

[41] C. Frondel and U. B. Marvin, *Nature* 214 (1967) 587.

[42] T. Irifune, A. Kurio, S. Sakamoto, T. Inoue and H. Sumiya, *Nature* 421 (2003) 599.

[43] M. Akaishi, H. Kanda and S. Yamaoka, *J. Cryst. Growth* 104 (1990) 578.

[44] P. Trucano and R. Chen, *Nature* 258 (1975) 136.

[45] H. Lipson and A. R. Stokes, *Proc. R. Soc. London, Ser. A* 181 (1942) 101.

[46] B. T. Kelly, *Physics of Graphite* (Applied Science Publishers, 1981).

[47] D. Tominek, S. G. Louie, H. J. Mamin, D. W. Abraham, R. E. Thomson, E. Gam and J. Clarke, *Phys. Rev. B* 35 (1987) 7790.

[48] M. S. Dresselhaus, G. Dresselhaus and P. C. Eklund, *Science of Fullerenes and Carbon Nanotubes* (Elsevier, 1996).

[49] E. Staryga and G.W. Bak, *Diamond Relat. Mater.* 14 (2005) 23.

[50] L. T. Scott, *Angew. Chem. Int. Ed.* 43 (2004) 4994.

[51] C. M. Lieber and C. Chen, *Solid State Phys.* 48 (1994) 109.

[52] S. Liu, Y Lu, M. M. Kappes, J. A. Ibers, *Science* 254 (1991) 408.

[53] A. Hirsch, *Principles of Fullerene Reactivity* (Springer, 1999).

[54] D. M. Guldi and K. D. Asmus, *J. Phys. Chem. A* 101 (1997) 1472.

[55] K. E. Geckeler and S. Samal, *Polym. Int.* 48 (1999) 743.

[56] D. S. Bethune, R. D. Johnson, J. R. Salem, M. S. De Vries and C. S. Yannoni, *Nature* 366 (1993) 123.

[57] M. Yoon, S. Yang, E. Wang and Z. Zhang, *Nano Lett.* 7 (2007) 2578.

[58] O. V. Pupysheva, A. A. Farajian and B. I. Yakobson, *Nano Lett.* 8 (2007) 767.

[59] L. Forro and L. Mihly, *Rep. Prog. Phys.* 64 (2001) 649.

[60] Y. Wang and L. T. Cheng, *J. Phys. Chem.* 96 (1992) 1530.

[61] C. M. Varma, J. Zaanen and K. Raghavachari, *Science* 254 (1991) 989.

[62] T. L. Makarova, K. H. Han, P. Esquinazi, R. R. Da Silva, Y. Kopelevich, I. B. Zakharova and B. Sundqvist, *Carbon* 41 (2003) 1575.

[63] P. J. F. Harris, *Carbon Nanotube Science: Synthesis, Properties and Applications* (Cambridge University Press, 2009).

[64] M. S. Dresselhaus, G. Dresselhaus, P. C. Eklund and A. M. Rao, *Carbon Nanotubes* (Springer, 2000).

[65] H. Dai, *Acc. Chem. Res.* 35 (2002) 1035.

[66] J. Prasek, J. Drbohlavova, J. Chomoucka, J. Hubalek, O. Jasek, V. Adam and R. Kizek, *J. Mater. Chem.* 21 (2011) 15872.

[67] P. M. Ajayan and O. Z. Zhou, *Applications of Carbon Nanotubes* (Springer, 2001).

[68] M. Terrones, *Annu. Rev. Mater.Res.* 33 (2003) 419.

[69] R. H. Baughman, A. A. Zakhidov and W. A. de Heer, *Science* 297 (2002) 787.

[70] Z. Liu, S. Tabakman, K. Welsher and H. Dai, *Nano Res.* 2 (2009) 85.

[71] A. J. Matthew, V. C. Tung and R. B. Kaner, *Chem. Rev.* 110 (2009) 132.

[72] A. K. Geim and K. S. Novoselov, *Nat. Mater.* 6 (2007) 183.

[73] A. K. Geim, *Science* 324 (2009) 1530.

[74] S. Guo and S. Dong, *Chem. Soc. Rev.* 40 (2011) 2644.

[75] V. Georgakilas, M. Otyepka, A. B. Bourlinos, V. Chandra, N. Kim, K. C. Kemp, P. Hobza, R. Zboril, and K. S. Kim, *Chem. Rev.* 112 (2012) 6156.

[76] A. Bostwick, T. Ohta, T. Seyller, K. Horn and E. Rotenberg, *Nat. Phys.* 3 (2006) 36.

[77] T. Enoki and T. Ando, *Physics and Chemistry of Graphene: Graphene to Nanographene.* (CRC Press, 2013).

[78] N. O. Weiss , H. Zhou , L. Liao , Y. Liu , S. Jiang , Y. Huang and X. Duan, *Adv. Mater.* 24 (2012) 5776.

[79] C. Lee , X. Wei , J. W. Kysar and J. Hone , *Science* 321 (2008) 385.

[80] S. Wang , Y. Zhang , N. Abidi and L. Cabrales, *Langmuir* 25 (2009) 11078.

[81] D. Prasai , J. C. Tuberquia , R. R. Harl , G. K. Jennings and K. I. Bolotin, *ACS Nano* 6 (2012) 1102.

[82] A. A. Balandin, S. Ghosh, W. Bao, I. Calizo, D. Teweldebrhan, F. Miao and C. N. Lau, *Nano Lett.* 8 (2008) 902.

[83] Q. Liang, X. Yao, W. Wang, Y. Liu and C. P. Wong, *ACS Nano* 5 (2011) 2392.

[84] K. M. F. Shahil, A. A. Balandin, *Nano Lett.* 12 (2012) 861.

[85] K. L. Grosse, M. H. Bae, F. Lian, E. Pop and W. P. King, *Nat. Nanotechnol.* 6 (2011) 287.

[86] Y. Zhu, S. Murali, W. Cai, X. Li, J. W. Suk, J. R. Potts and R. S. Ruoff, *Adv. Mater.* 22 (2010) 3906.

[87] J. Zhou, M. M. Wu, X. Zhou and Q. Sun, *Appl. Phys. Lett.* 95 (2009) 103108.

[88] Y. H. Zhang, K. G. Zhou, K. F Xie, J. Zeng, H. L. Zhang and Y. Peng, *Nanotechnology* 21 (2010) 065201.

[89] O. Leenaerts, B. Partoens and F. M. Peeters, *Phys. Rev. B* 77 (2008) 125416.

[90] W. Chen, L. Duan and D. Zhu *Environ. Sci. Technol.* 41 (2007) 8295.

[91] J. E. Johns and M. C. Hersam, *Acc. Chem. Res.* 46 (2012) 77.

[92] J. Pyun, *Angew. Chem., Int. Ed.* 50 (2011) 46.

[93] F. Banhart, J. Kotakoski and A. V. Krasheninnikov, *ACS Nano* 5 (2010) 26.

[94] Y. Sun, Q. Wu and G. Shi, *Energy Environ. Sci.* 4 (2011) 1113.

[95] J. D. Roy Mayhew, D. J. Bozym, C. Punckt and I. A. Aksay, *ACS Nano* 4 (2010) 6203.

[96] X. Wang, L. Zhi and K. Mullen, *Nano Lett.* 8 (2008) 323.

[97] R. Romero-Aburto, T. Narayanan, Y. Nagaoka, T. Hasumura, T. M. Mitcham, T. Fukuda, P. J. Cox, R. R. Bouchard, T. Maekawa, D. S. Kumar, S. V. Torti, S. A. Mani and P. M. Ajayan, *Adv. Mater.* 25 (2013) 5632.

[98] M. Theye and V. Paret, *Carbon* 40 (2002) 1153.

[99] P. J. F. Harris, *Crit. Rev. Solid State Mater. Sci.* 30 (2005) 235.

[100] M. Weiler, S. Sattel, T. Giessen, K. Jung, H. Ehrhardt, V. S. Veerasamy, and J. Robertson, *Phys. Rev. B* 53 (1996) 1594.

[101] D. I. Jones and A. D. Stewart, *Philos. Mag. B* 46 (1982) 423.

[102] P. J. Fallon, V. S. Veerasamy, C. A. Davis, J. Robertson, G. A. J. Amaratunga, W. I. Milne and J. Koskinen, *Phys. Rev. B* 48 (1993) 4777.

[103] G. M. Pharr, D. L. Callahan, S. D. McAdams, T. Y. Tsui, S. Anders, A. Anders, J. W. Ager, I. G. Brown, C. S. Bhatia, S. R. P. Silva and J. Robertson ,*Appl. Phys. Lett.* 68 (1996) 779.

[104] F. Li and J. S. Lannin, *Phys. Rev. Lett.* 65 (1990) 1905.

[105] C. Casiraghi, J. Robertson and A. C. Ferrari, *Mater. Today* 10 (2007) 44.

[106] J. Robertson, *Mater. Sci. Eng., R* 37 (2002) 129.

[107] C. W. Chen and J. Robertson, *J. Non-Cryst. Solids* 227 (1998) 602.

[108] J. Robertson, *Prog. Solid State Chem.* 21 (1991) 199.

[109] F. G. Emmerich, *Carbon* 33 (1995) 1709.

[110] R. Gago, M. Vinnichenko, H. U. Jager, A. B. Yu, I. Jimenez, N. Huang, H. Sun and M. F. Maitz, *Phys. Rev. B* 72 (2005) 014120.

[111] A. Oberlin, *Carbon* 22 (1984) 521.

[112] J. Heremans, *Carbon* 23 (1985) 431.

[113] A. Ilie, O. Harel, N. M. J. Conway, T. Yagi, J. Robertson, and W. I. Milne, *J. Appl. Phys.* 87 (2009) 789.

[114] A. C. Ferrari, J. Robertson, M. G. Beghi, C. E. Bottani, R. Ferulano, and R. Pastorelli, *Appl. Phys. Lett.* 75 (1999) 1893.

[115] F. Rouleau and P. G. Martin, *Astrophys. J.* 377 (1991) 526.

[116] N. Boutroy, Y. Pernel, J. M. Rius, F. Auger, H. J. von Bardeleben, J. L. Cantin, F. Abel, A. Zeinert, C. Casiraghi, A. C. Ferrari and J. Robertson, *Diamond Relat. Mater.* 15 (2006) 921.

[117] A. K. Gangopadhyay, P. A. Willermet, M. A. Tamor and W. C. Vassell, *Tribol. Int.* 30 (1997) 9.

[118] G. Dearnaley and J. H. Arps, *Surf. Coat. Technol.* 200 (2005) 2518.

[119] E. Frackowiak and F. Beguin, *Carbon* 39 (2001) 937.

[120] L. L. Zhang and X. S. Zhao, *Chem. Soc. Rev.* 38 (2009) 2520.

[121] A. Grill, *Diamond Relat. Mater.* 10 (2001) 234.

[122] G. A. J. Amaratunga, V. S. Veerasamy, W. I. Milne, C. A. Davis, S. R. P. Silva and H. S. MacKenzie, *Appl. Phys. Lett.* 63 (1993) 370.

[123] I. Felner and E. Prilutskiy, *J. Supercond. Nov. Magn.* 25 (2012) 2547.

[124] A. V. Rode, E. G. Gamaly, A. G. Christy, J. G. F. Gerald, S. T. Hyde, R. G. Elliman, B. Luther-Davies, A. I. Veinger, J. Androulakis and J. Giapintzakis, *Phys. Rev. B* 70 (2004) 054407.

[125] S. H. Yoon, S. Lim, Y. Song, Y. Ota, W. Qiao, A. Tanaka and I. Mochida, *Carbon* 42 (2004) 1723.

[126] J. Wang and S. Kaskel, *J. Mater. Chem.* 22 (2012) 23710.

[127] J. A. Agullo, B. C. Moore, D. C. Amoros and A. L. Solano, *Carbon* 42 (2004) 1367.

[128] Z. Hu and M. P. Srinivasan, *Microporous Mesoporous Mater.* 27 (1999) 11.

[129] C. Brasquet and P. Le-Cloirec, *Carbon* 35 (1997) 1307.

[130] T. Otowa, R. Tanibata and M. Itoh, *Gas Sep. Purif.* 7 (1993) 241.

[131] J. P. M. Lozar, M. Kunowsky, F. S. Garcia, J.D. Carruthers and A. L. Solano, *Energy Environ. Sci.* 5 (2012) 9833.

[132] *http://www.marketresearch.com/Freedonia-Group-Inc-v1247/Activated-Carbon-8194058/.*

[133] O. Ioannidou and A. Zabaniotou, *Renewable and Sustainable Energy Rev.* 11 (2007) 1966.

[134] Y. Zhu, S. Murali, M. D. Stoller, K. J. Ganesh, W. Cai, P. J. Ferreira and A. Pirkle, *Science* 332 (2011) 1537.

[135] H. Wang, Q. Gao and J. Hu, *J. Am. Chem. Soc.* 131 (2009) 7016.

[136] J. Chmiola, G. Yushin, Y. Gogotsi, C. Portet, P. Simon and P. L. Taberna, *Science* 313 (2006) 1760.

[137] H. Tamai, T. Kakii, Y. Hirota, T. Kumamoto and H. Yasuda, *Chem. Mater.* 8 (1996) 454.

[138] P. Delhaes, *Carbon Based Solids and Materials* (John Wiley & Sons, 2013).

[139] J. Robertson and E. P. Oreilly, *Phys. Rev. B* 35 (1987) 2946.

[140] N. A. Marks, D. R. McKenzie, B. A. Pailthorpe, M. Bernasconi, and M. Parrinello, *Phys. Rev. Lett.* 76 (1996) 768.

[141] J. Robertson, *Adv. Phys.* 35 (1986) 317.

[142] F. Carmona, P. Delhaes, G. Keryer and J. P. Manceau, *Solid State Commun.* 14 (1974) 1183.

[143] D. Dasgupta, F. Demichelis and A. Tagliaferro, *Philos. Mag. B* 63 (1991) 1255.

[144] K. Sreedhar and P. A. Joy, *Solid State Commun.* 99 (1996) 589.

[145] A. L. Efros and B. I. Shklovskii, *J. Phys. C: Solid State Phys.* 8 (1975) L49.

[146] P. Vishwakarma and S. Subramanyam, *J. Appl. Phys.* 100 (2006) 113702.

[147] R. Rosenbaum, *Phys. Rev. B* 44 (1991) 3599.

[148] K. Shimakawa and K. Miyake, *Phys. Rev. Lett.* 61 (1988) 994.

[149] K. Shimakawa and K. Miyake, *Phys. Rev. B* 39 (1989) 7578.

[150] V. Bayot, L. Piraux, J.P. Michenaud, and J.P. Issi, *Phys. Rev. B* 40 (1989) 3514.

[151] J. J. Hauser, *J. Non-crystalline Solids* 23 (1977) 21.

[152] G. A. J. Amaratunga, V. S Veerasamy, C. A. Davis, W. I. Milne, D. R. McKenzie, J. Yuan and M. Weiler, *J. Non-crystalline Solids* 164 (1993) 1119.

[153] V. S. Veerasamy, J. Yuan, G. A. J. Amaratunga, W. I. Milne, K. W. R. Gilkes, M. Weiler, and L. M. Brown, *Phys. Rev. B* 48 (1993) 17954.

[154] D. I. Jones, and A. D. Stewarat, *Phil. Mag. B* 46 (1982) 423.

[155] A. W. P. Fung, M. S. Dresselhaus and M. Endo, *Phys. Rev. B* 48 (1993) 14953.

[156] B. Kramert and A. MacKinnont, *Rep. Prog. Phys.* S6 (1993) 1469.

[157] N. Ganguli and K. S. Krishnan, *Proc. R. Soc. London, Ser. A* 177 (1941) 168.

[158] S. Hudgens, M. Kastner and H. Fritzsche, *Phys. Rev. Lett.* 33 (1974) 1552.

[159] R. C. Haddon, L. F. Schneemeyer, J. V. Waszczak, S. H. Glarum, R. Tycko, G. Dabbagh, A. R. Kortan, A. J. Muller, A. M. Mujsce, M. J. Rosseinsky, S. M. Zahurak, A. V. Makhija, F. A. Thiel, K. Raghavachari, E. Cockayne and V. Elser, *Nature* 350 (1991) 46.

[160] M. Sepioni, R. R. Nair, S. Rablen, J. Narayanan, F. Tuna, R. Winpenny, A. K. Geim and I. V. Grigorieva, *Phys. Rev. Lett.* 105 (2010) 207205

[161] T. L. Makarova, *Semiconductors* 38 (2004) 615.

[162] T. Makarova and F. Palacio, *Carbon Based Magnetism: An Overview of the Magnetism of Metal Free Carbon-Based Compounds and Materials* (Elsevier, 2006).

[163] H. M. McConnell, *J. Chem. Phys.* 39 (1963) 1910.

[164] D. Gatteschi, *Adv. Mater.* 6 (1994) 635.

[165] P. M. Allemand, K. C. Kishan, A. Koch, F. Wudl, K. Holczer, S. Donovan, G. Grner and J. D. Thompson, *Science* 253 (1991) 301.

[166] A. Suzuki, T.Suzuki, R.J. Whitehead and Y. Maruyama, *Chem. Phys. Lett.* 223 (1994) 517.

[167] L. Dunsch, D. Eckert, J. Frhner, A. Bartl and K.H. Muller, *J. Appl. Phys.* 81 (1997) 4611.

[168] A. Lappas, K. Prassides, K. Vavekis, D. Arcon, R. Blinc, P. Cevc, A. Amato, R. Feyerherm, F. N. Gygax and A. Schenck, *Science* 24 (1995) 1799.

[169] A. Mrzel, A. Omerzu, P. Umek, D. Mihailovic, Z. Jaglicic and Z. Trontelj, *Chem. Phys. Lett.* 298 (1998) 329.

[170] S. Talapatra, P. G. Ganesan, T. Kim, R. Vajtai, M. Huang, M. Shima, G. Ramanath, D. Srivastava, S. C. Deevi and P. M. Ajayan, *Phys. Rev. Lett.* 95 (2005) 097201.

[171] K. Wakabayashi and M. Sigrist, *Phys. Rev. Lett.* 84 (2000) 3390.

[172] C. W. Chiu, M. F. Lin, and F. L. Shyu, *Physica E* 11 (2001) 356.

[173] M. Fujita, K. Wakabayashi, K. Nakada, and K. Kusakabe, *J. Phys. Soc. Japan* 65 (1996) 1920.

[174] K. Kusakabe and M. Maruyama, *Phys. Rev. B* 67 (2003) 092406.

[175] D. Jiang and S. Dai, *J. Phys. Chem. A* 112 (2008) 332.

[176] K. Wakabayashi, M. Sigrist and M. Fujita, *J. Phys. Soc. Japan* 67 (1998) 2089.

[177] Y. Shibayama, H. Sato, T. Enoki and M. Endo, *Phys. Rev. Lett.* 84 (2000) 1744.

[178] Y. Wang, P. Pochet, C. A. Jenkins, E. Arenholz, G. Bukalis, S. Gemming, M. Helm, and S. Zhou, *Phys. Rev. B* 90 (2014) 214435.

[179] Y. Liu, N. Tang, X. Wan, Q. Feng, M. Li, Q. Xu, F. Liu and Y. Du, *Sci. Rep.* 3 (2013) 2566.

[180] S. Qin, X. Guo, Y. Cao, Z. Ni and Q. Xu, *Carbon* 78 (2014) 559.

[181] C. N. R. Rao, H. S. S. R. Matte, K. S. Subrahmanyam and U. Maitra, *Chem. Sci.* 3 (2012) 45.

[182] V. L. J. Joly, K. Takahara, K. Takai, K. Sugihara, T. Enoki, M. Koshino and H. Tanaka. *Phys. Rev. Lett.* 81 (2010) 115408.

[183] P. Simon and Y. Gogotsi, *Nat. Mater.* 7 (2008) 845.

[184] Y. Wang, Y. Huang, Y. Song, X. Zhang, Y. Ma, J. Liang and Y. Chen, *Nano Lett.* 9 (2009) 220.

[185] K. Bagani, A. Bhattacharya, J. Kaur, A. Rai Chowdhury, B. Ghosh, M. Sardar and S. Banerjee, *J. Appl. Phys.* 115 (2014) 023902.

[186] A. M. Puziy, O. I. Poddubnaya, A. M. Alonso, F. S. Garcia and J. M. D. Tascon, *Carbon* 40 (2002) 1493.

[187] M. Zhu and G. Diao, *Nanoscale* 3 (2011) 2748.

[188] L. C.A. Oliveira, R. V. R. A. Rios, J. D. Fabris, V. Garg, K. Sapag and R. M. Lago, *Carbon* 40 (2002) 2177.

[189] C. S. Castro, M. C. Guerreiro, M. Goncalves, L. C.A. Oliveira and A. S. Anastacio, *J. Hazard. Mater.* 164 (2009) 609.

[190] L. Tang, Y. Cai, G. Yang, Y. Liu, G. Zeng, Y. Zhou, S. Li, J. Wang, S. Zhang, Y. Fang and Y. He, *Appl. Surf. Sci.* 314 (2014) 746.

[191] L. Zhou, Y. Shao, J. Liu, Z. Ye, H. Zhang, J. Ma, Y. Jia, W. Gao and Y. Li, *ACS Appl. Mater. Interfaces* 6 (2014) 7275.

Chapter 2

Experimental methods

2.1 Introduction

This chapter describes the experimental methods used for the preparation of carbon-based materials and characterization techniques employed for their structural analysis and other physical property measurements. For the preparation of disordered carbon, a simple pyrolysis technique was used. Activated carbon was prepared through liquid state activation techniques with different activating agents like HNO_3, H_2SO_4, KOH, etc. Nanocrystalline Fe_3O_4 was prepared through co-precipitation technique. Different instrumental techniques like X-ray diffraction, Raman spectroscopy, Infrared spectroscopy, Inductively coupled plasma-optical emission spectrometry, SQUID vibrating sample magnetometer, etc. were used for characterizing the materials.

2.2 Methods of synthesis

2.2.1 Preparation of disordered carbon

Many methods are available for the preparation of carbon-based materials. Deposition methods like ion-beam deposition, pulsed laser deposition, chemical vapour deposition, laser ablation, sputtering, etc. have been used for producing disordered carbon films [1,2]. The composition of the disordered carbon films prepared by these methods mainly depends on the target material, chemical environment used for deposition and substrate temperature [1,2]. Nanostructured carbonaceous materials can be prepared from any organic matter or molecular precursors by their pyrolysis under an inert atmosphere or limited supply of air [3,4]. The general method used for the synthesis of two dimensional carbon nanomaterials, including graphene, proceeds through chemical routes involving the oxidation-exfoliation of graphite to graphene oxide, followed by its reduction [5–8]. Carbon fibers with varying crystallinity can be prepared by pyrolysis of fibers formed after spinning polyacrylonitrile, petroleum pitch, etc. [5,9]. Carbon nanostructures with different geometries can be prepared through hydrothermal methods from various molecular precursors after adding suitable structure directing agents [5,10,11].

The industrial large scale production of carbon is through pyrolysis of some suitable carbon-rich, ash-free materials like polymers, wood, nutshells, coal tar, cellulose fiber, etc. [3,12–14]. The main advantage of the bioresources is that their usage makes the preparation step cost effective and hence industrially viable. Several articles are available in the literature which reports the use of a variety of bioresources as precursors for preparing carbon [3,13,14]. The advantage of the combustion process is that samples can be produced in bulk quantities within a small time. On thermal treatment, initially, the moisture along with the volatile contents in the precursor gets removed from the precursor followed by carbonization. Generally, an agricultural waste or any other locally available bioresource can be used as the precursor for the preparation of carbon [3,15]. The texture and properties of the carbon, thus produced, depend on the precursor as well as the processing parameters such as pyrolysis temperature, time and use of activating agents during pyrolysis [3,16]. The carbonaceous materials thus produced have different porosity, surface area, crystallinity, surface functionalities, etc. which induce a difference in their reactivities as well as other physical properties [3,17–20].

2.2.2 Methods for preparing activated carbon

Many different precursors have been used for preparing activated carbon with an eye on developing low coast adsorbents, fillers, porous electrodes, etc. which include agricultural wastes such as wheat, corn straw, olive stones, bagasse, sunflower shell, pinecone, olive residues, eucalyptus maculata, sugar cane bagasse, almond shells, peach stones, grape seeds, straw, apricot stones, cotton stalk, cherry stones, peanut hull, coconut shells, rice hulls, corn cob, corn hulls, hazelnut shells, pecan shells, rice husks, rice straw and neem leaves [3,4,21–28]. Activated carbon can be prepared either by a physical activation or a chemical activation. Physical activation is a two-step process which involves the carbonization of a suitable precursor followed by the activation of the resulting carbon at elevated temperatures ($\geq$800 °C) in the presence of a suitable oxidizing gas such as CO_2, steam, air or their mixtures. Usage of CO_2 allows better control on the microstructure of the

activated carbon and hence is used widely [29,30]. Various bioresources like corn cob, rice husk, oak, rice straw, rice hulls, peanut hulls, almond shells, etc. have been used for preparing activated carbon after physically activating using these oxidizing agents [3]. In the chemical activation process, the two steps are carried out either simultaneously or one after the other. The precursor material can be mixed with the chemical activating agents such as KOH, NaOH, K_2CO_3 H_3PO_4, $ZnCl_2$ etc. and heated to a high temperature to obtain chemically activated carbon [31–34]. In a second approach, the precursor can be carbonized first and then the pre-treated carbon is chemically activated in a similar manner as discussed. Chemical activation offers several advantages over physical activation. It can be performed at a much lower temperature than for physical activation and therefore consumes less amount of energy. The chemically activated carbon has large surface area and superior porosity when compared to their physically activated counterparts. Therefore, the chemically activated carbon finds applications as adsorbents and filters whereas physically activated carbons are generally used as fillers.

Chemical activation is used in many studies on the adsorption properties of activated carbon prepared from bioresources like corn cob, olive seeds, rice husks, rice straw, pecan shells, peanut hulls, apricot stones and almond shells [3]. Among these activating agents, KOH is found to be better since it produces micro/mesoporous activated carbons with a large surface area at relatively low activation temperatures [35,36]. The porosity and surface area of activated carbon can be tuned by controlling the amount of activating agent used and the activation temperature [35,36]. In a typical procedure, a weighed amount of a precursor material or pre-treated carbon is mixed with the desired amount of the activating agent by solid state mixing or liquid state impregnation followed by drying. Liquid state impregnation has the advantage that the distribution of the activating agent in the parent system is more homogeneous. The mixture containing the pretreated carbon and the activating agent is then transferred to a high temperature tubular furnace and heated to the desired temperature under an inert atmosphere to obtain activated carbon.

2.2.3 Synthesis of iron oxide nanoparticles

Different methods used for the preparation of iron oxide nanoparticles are co-precipitation, sol-gel, hydrothermal/solvothermal, auto-combustion, microemulsion, templated and biomimetic syntheses. In present work, co-precipitation technique was used for the synthesis of Fe_3O_4 nanoparticles.

In a co-precipitation reaction, the soluble metal salts in the form of nitrates, chlorides, sulphates, etc, are precipitated as sparingly soluble species such as the corresponding oxides, hydroxides, oxalates and carbonates under conditions of supersaturation on the addition of a suitable precipitating agent [37,38]. The hydroxides, oxalates and carbonates can be converted to the respective metal oxides by calcination at a suitable temperature. Since the supersaturation conditions, which lead to precipitation, generally occur as a result of some chemical reaction. For the synthesis of iron oxide nanoparticles, the iron (III) and iron (II) salts are co-precipitated in a suitable basic media. This method can yield large quantities of nanoparticles, depending on the reaction conditions.

The particle size distribution varies with all those factors which determine the reaction rate such as rate of reactant addition, stirring rate, the concentration of reactants, temperature, etc. The theory of co-precipitation reaction includes three major steps namely nucleation, growth and agglomeration [37]. Nucleation involves the formation of large amounts of very small sparingly soluble particles as a result of supersaturation. The detailed mechanisms involved in the growth and agglomeration steps which control the size and morphology of the nanoparticles are well described in the literature [37]. The growth of nanoparticles can be arrested either by capping the nanoparticles with a suitable surfactant and then utilizing the steric repulsion between the capped nanoparticles or by the electrostatic or Van-der Waals repulsion resulting from the chemisorption of charged species like H^+ and OH^- [37,38]. Interestingly, the metal oxide nanoparticles formed after calcination of precipitated oxalate, hydroxide or carbonate retain their morphology through a process called topotatical growth which increases the diversity of this technique.

2.2.4 Preparation of materials used in the present study

For the present study, the disordered carbon is prepared by a simple heat-treatment process. The precursor material for the preparation of carbon, dry coconut shell (CS), is crushed into small pieces and introduced into a horizontal tubular furnace. The furnace is then heated to the desired temperature, under flowing nitrogen atmosphere. A detailed description of the sample preparation and the heat-treatment program used are given in Chapter 3 (Section 3.2).

The disordered carbon obtained after heat-treatment is activated by using KOH to prepare the KOH activated samples. For KOH activation, the disordered carbon is impregnated with the required amount of KOH by treating the sample with a KOH solution. This solution is then dried, which then formed a slurry. The slurry is heat-treated at the required activation temperature. The detailed description is given in Chapter 6 (Section 6.3).

The activated carbon - iron oxide composite is prepared by *in situ* co-precipitation method. For comparing results, the carbon material is activated by two different methods, a liquid state activation by using H_2SO_4–HNO_3 mixture and by the KOH activation after impregnating carbon with KOH, followed by heating at a high temperature. The composite is then prepared by adding ammonia to a solution containing the activated carbon and Fe^{2+}/Fe^{3+} ions. The detailed description of preparation of the composite is given in Chapter 7 (Section 7.2)

2.3 Characterization and measurement techniques

2.3.1 X-ray diffraction

X-rays occupy the region between gamma and ultraviolet rays in the electromagnetic spectrum. X-ray diffraction (XRD) experiment which uses X-rays of wavelength in the range 0.5-2.5 Å is one of the most fundamental characterization technique for both bulk and nanocrystalline solid materials [39]. When X-rays pass through the periodic array of atoms, they get diffracted, the constructive interference of diffracted rays occurs only when the condition given by Bragg's

law (Equation 2.1) is satisfied [39,40].

$$n\lambda = 2d\ \sin\theta \tag{2.1}$$

where λ is the wavelength of X-rays, d is the spacing between two adjacent lattice planes in the crystal and θ is the diffraction angle. Therefore, X-ray of a fixed wavelength, when interacts with a particular material, gets diffracted at some specific angles belonging to a set of planes and satisfying the Bragg's law. This allows the structural determination of a specific material by analyzing its XRD pattern.

For nanocrystalline materials, XRD peak width increases with decreasing crystallite size since the destructive interference is not complete when the number of planes becomes limited in the case of a nanomaterial [40,41]. The average crystallite size of a nanomaterial can be determined from the peak width by using the Scherrer formula (Equation 2.2).

$$t = \frac{K\lambda}{B\cos\theta} \tag{2.2}$$

where t is the crystallite size in Å, λ is the X-ray wavelength in Å, B is the width of diffraction peak (full width at half maximum, FWHM), θ is the Bragg angle and K is a constant which depends on the shape of the crystallite, which is generally taken as 0.9, assuming spherical geometry [41]. For determining the in-plane dimension of two-dimensional materials like graphene, K=1.84 is used [41,42]. Before substituting the value of B in Equation 2.2, an instrumental correction becomes necessary since the latter also contributes to the width of the XRD peak [40]. B is corrected for instrumental broadening by using the formula

$$B^2 = B_M^2 - B_S^2$$

where B_M is the measured peak width and B_S is the instrumental contributions to the line broadening obtained by using a standard bulk material.

In the present work X-ray studies were performed on a Phillips Xpert Pro diffractometer using Cu Kα radiation (1.5418 Å) filtered using nickel filter. Most of the diffraction experiments were carried out at a scan rate of 0.5 °/minute.

2.3.2 Transmission electron microscopy

Transmission electron microscopy uses high energy electrons for imaging materials at nanometer scale [43,44]. In a transmission electron microscope (TEM) the electrons are accelerated to velocity approaching speed of light using a high potential field (100-1000 kV) due to which their de Broglie wavelength decreases far below the wavelength of light and thereby increasing the penetration power of electrons and enhancing the resolution to Å level [39]. TEM uses an array of electromagnetic lenses to focus the electron beam on to the sample and then to the detection system like a photographic plate or a CCD camera [44]. The electron optical column is maintained under high vacuum conditions. TEM imaging can be done either in a bright field mode or a dark field mode [43]. In the bright field mode, only direct beams from the objective lens pass through the projection lens and get displayed as the image. Here thick areas, crystalline areas and regions having heavy atoms appear dark. In the dark field mode, the direct beam is blocked and diffracted beams from the objective lens are allowed to pass through the projection lens. The diffracted beam carries more information such as defects, crystallite size, stacking faults, etc. since they interact with the sample much more when compared to the direct beam. High resolution TEM (HR-TEM) is an advanced version of TEM which uses the transmitted and the scattered electron beams to create an interference image with better contrast.

TEM experiments in the present study was performed on a model FEI, TECNAI G^2TF30 transmission electron microscope. TEM analysis requires unique sample preparation. Initially, the powder sample was dispersed in a suitable solvent with low boiling point like isopropanol and then carefully drop coated on to a carbon and polymeric film coated copper grids for analysis. The coated samples were then allowed to dry for overnight before performing the analysis.

2.3.3 Scanning electron microscopy

Scanning electron microscopy (SEM) is one of the widely used tool for studying the microstructure and morphology of materials by high resolution surface imaging with unique three-dimensional characteristics [45]. The instrumentation and electronics of SEM is very much similar to that of a TEM with the presence of an electron gun, focusing electromagnetic lenses, high vacuum column and the software. However, in SEM, the accelerating potential is much lower than that in a TEM and hence the penetrating power of electrons is substantially reduced. The imaging proceeds by the scanning of a sample's surface by an electron beam with a spot diameter of nearly 1 nm. The SEM beam thus focused to a fine point on the sample then scans the area under investigation line by line over the sample's surface in a rectangular raster pattern. The intensities of various signals created by interactions between the electron beam and the specimen are measured and then mapped as variations in brightness with the help of software to produce SEM images [45]. Images with higher magnification can be obtained by reducing the size or the area scanned on the material. SEM, unlike TEM, does not require any special sample preparation and the only requirement is that the sample must be able to withstand the vacuum of the chamber and bombardment by the electron beam. Non-conducting samples require a fine coating of conducting materials like gold or silver because the bombarded electrons tend to accumulate on the sample's surface thereby developing unwanted potential difference.

The microstructure analysis of the carbon pellets was carried using a FEI Quanta 200 3D ESEM. The samples were fixed on to the disc holder by using carbon tapes before inserting into the SEM sample chamber for imaging.

2.3.4 Raman spectroscopy

Raman spectroscopy is one of the most widely used nondestructive tools for the characterization of materials. At the experimental level, Raman spectroscopy offers much versatility so that samples ranging from ceramic oxides, polymers, organic molecules, bacteria or other micro-organisms, etc. in any physical state can

be analyzed instantaneously without any special sample preparation. In Raman spectroscopy, the sample is irradiated by intense laser beams in the ultraviolet or visible region (ν_0) and the scattered light is observed in a back scattering geometry. The scattered radiation can be broadly of two types, the Rayleigh scattering and the Raman Scattering. In Rayleigh scattering, the scattered rays have the same frequency (ν_0) as the incident radiation, whereas in Raman scattering the scattered rays have either lower (ν_0-ν_m) or higher frequency (ν_0+ν_m) when compared to the incident radiation. Here ν_m denotes the vibrational frequency of the molecule. The (ν_0-ν_m) and (ν_0+ν_m) lines are known as Stokes and anti-Stokes lines, respectively. Hence, in Raman spectroscopy, we measure the vibrational frequency of different bonds in a material in terms of the shift in the frequency ($\nu_0 \pm \nu_m$) of the incident radiation. The main condition for showing Raman activity is that the vibrational transition should proceed with a change in polarizability. Detailed description of the theory of Raman spectroscopy is available in several text books [46,47].

Raman spectroscopy is one of the fundamental and the most sensitive characterization tool for crystalline, nanocrystalline and disordered carbon. The in-plane (L_a) as well as out-of-plane (L_c) coherence lengths and the inter-layer spacing of carbon affect the Raman spectrum of carbon-based materials. The most common Raman lines for a carbon-only material are located around 1500–1630 cm^{-1} and 1355 cm^{-1} and are designated as G- and D-peaks (Figure 2.1), respectively [48–50]. For perfectly crystalline graphite, D-peak is absent and G-peak due to the in-plane bond stretching motion of sp^2 hybridized carbon pairs occurs with E_{2g} symmetry around 1580 cm^{-1} [50]. It is important to note that this mode has nothing to do with six membered rings and emerges in the presence of sp^2 carbon pairs irrespective of whether they are aromatic or olefinic. The D-peak is a breathing mode of A_{1g} symmetry involving phonons near the K-zone boundary and emerges in the presence of disorder with its intensity related to the number of disordered six membered rings [50]. Therefore, the G-peak to D-peak intensity ratio, *I(D)/I(G)*, characterizes the extend of disorder and therefore is a measure of the in-plane coherence length. For disordered carbon, L_a is related to the intensity ratio by

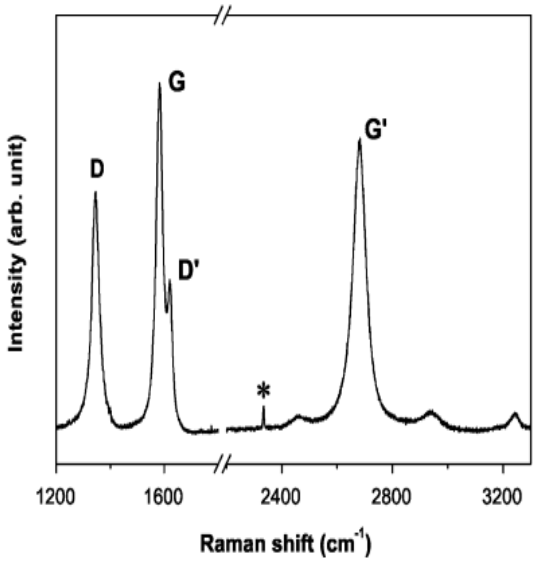

Figure 2.1: Raman spectrum of a nanographite sample recorded with laser excitation wavelength of 515 nm, showing the main Raman features. The peak marked with ∗ comes from the Raman mode of N_2 gas. Taken from reference [51].

the Tuinstra and Koenig (TK) equation (Equation 2.3) [48].

$$\frac{I_D}{I_G} = \frac{C(\lambda)}{L_a} \tag{2.3}$$

For nanocrystalline carbon, the above relation gets modified (Equation 2.4) and *I(D)/I(G)* is directly related to L_a^2 [50].

$$\frac{I_D}{I_G} = \frac{C'(\lambda)}{L_a^2} \tag{2.4}$$

Where $C(\lambda)$and $C'(\lambda)$ are constants which depend on the energy of the incident laser. Other important Raman features that are observed in carbon systems with micro or even nanosized graphitic regions are the D′-peak and G′-peak which are positioned around 1625 cm^{-1} and 2650 cm^{-1} (Figure 2.1), respectively [50]. The D- and D′-peaks emerge due to the breakage of crystal symmetry in the presence of disorder which activates certain vibrational modes which are otherwise forbidden in a perfect sp^2 lattice [51,52]. The symmetry allowed G′-peak corresponds to

the overtone of the D-peak and appears in the second-order Raman spectra of crystalline graphite. The G′-peak is very sensitive to the stacking order of the graphene sheets along the c-axis [52,53]. The Raman spectral changes associated with different types of carbonaceous materials and with an increase in the disorder in a perfect graphitic lattice are well documented in the literature [50,52,53].

For present study Raman spectra were recorded on a Horiba JY labraman HR 800 micro Raman spectrometer using 633 nm He-Ne laser.

2.3.5 Infrared spectroscopy

Infrared (IR) spectroscopy is a fingerprint technique and is used to identify the functional groups and bonding characteristics in molecules and bulk materials. This technique probes the vibrational frequency of bonds by irradiating with the entire range of infrared radiation. The necessary criteria that have to be satisfied for a certain bond vibration to be IR active is that the vibration should be associated with a change in the dipole moment [46]. Therefore, when a sample is irradiated with IR radiation, the IR energy in resonance with the bond vibration energy is absorbed if the above criteria is satisfied and the remaining part is transmitted. The IR spectroscopy allows the calculation of parameters like bond length and force constant from the observed vibrational frequency [46]. Fourier transform infrared spectrometers (FT-IR) are widely used currently since spectra can be obtained instantaneously. This is possible because FT-IR spectrometers allow simultaneous recording of the whole spectrum with the help of computers whereas conventional ones scans from one end of the spectrum to the other end thereby spending most of the time in recording unwanted background noise.

In the present work, the IR studies were carried out using a Bruker Tensor-27 FT-IR spectrometer in the frequency range 400 to 4000 cm^{-1} after properly mixing the sample with spectroscopic grade KBr and pressing to thin pellets. All samples studied were made moisture free by placing under an IR lamp for 15 minutes before recording the spectra.

2.3.6 Thermogravimetric analysis

Thermal analysis techniques include a wide variety of techniques which measures a property of a material as a function of temperature [54]. Thermogravimetry (TG) involves the measurement of the change in the weight of a sample with an increase in temperature. Using this technique, a wide variety of samples like inorganic materials, metals, polymers, ceramics, glasses, organic molecules, composites, etc. can be analyzed in different gas atmospheres like nitrogen, argon, helium, air and vacuum [55]. In dynamic thermogravimetry, the temperature sweep is controlled at a particular linear rate depending on the material under investigation. The weight change is continuously measured using a thermobalance whose sensitivity must be in accordance with the mass of the sample used and the expected mass changes. The thermogravimetric curve shows the change in weight as a function of temperature corresponding to the events like dehydration, desorption, vaporization, decomposition, reactions like oxidation or reduction, melting and sublimation. Therefore, thermogravimetric analysis (TGA) can be used for the study of reactions as well as in material characterization and testing [55].

In the present study, TGA was used to monitor the carbonization process of the precursor material. A Seiko 32 thermal analyzer was used to measure the weight change after heating upto 1173 K under the nitrogen atmosphere at a heating rate of 10 K/min.

2.3.7 Inductively coupled plasma - optical emission spectrometry

Inductively coupled plasma-optical emission spectrometry (ICP-OES) is one of the most powerful and accurate method for the determination of elements when present is trace amounts [56]. In this technique, the sample needs to be supplied in liquid or gaseous form and hence solid samples have to be either digested in concentrated acids or the element in consideration needs to be extracted using proper extraction technique. The main part of an ICP instrument is an assembly of three concentric fused silica tubes known as the torch. The torch is surrounded

by a water cooled copper coil, generally with two or three turns and connected to a radio frequency generator called the load coil [57]. Argon flows through all the three silica tubes at different flow rates and serves different purposes like the formation of stable plasma core with a temperature of $\sim$ 10,000 K and sample entry to the plasma. The outer argon flow maintains and positions the plasma with respect to the outer walls and the induction coil. The analyte is introduced through the central tube to the plasma core using argon gas as the carrier after converting the sample solution to an aerosol using a nebulizer. The argon flow through the silica tube in the middle is used for lifting the plasma position slightly, if needed, and also for diluting the inner gas flow when organic solvents are present [57].

The aerosol thus introduced to the plasma gets vaporized instantaneously thereby converting the analyte elements to free gaseous atoms. Further, the gaseous atoms get excited within the plasma by collisional excitation and often get converted to excited ions due to the high temperature inside the plasma. The excited atoms and ions then relax to the ground state by emission of photons with characteristic wavelengths depending on the energy level distribution of that species. This enables the identification of the element whose quantitative determination then becomes easy since the total number of photons emitted during the relaxation process is directly proportional to the number of excited species. For analyzing the emission from excited species, an optical emission spectroscope with high resolving power is used. A detailed description of the instrumentation and theory can be found in the literature [57]. ICP has the capacity of analyzing multiple elements simultaneously with high accuracy and precession. The system can be completely automated and has a detection limit of 0.1–100 ng/mL for most of the elements. Moreover, the low background emission with negligible chemical interference, along with all these advantages makes the system highly useful for trace detection of elements.

For the current study, ICP-OES was performed using a Spectro Arcos FH-12 analyzer and standard samples were prepared from ICP multi-element standard solution from Merck chemicals.

2.3.8 Surface area measurements

In this method, a dried and degassed sample is subjected to a nitrogen environment at different pressures. The surface area of a given material is determined by using the theory developed by Stephen Brunauer, P.H. Emmet and Edward Teller (BET method) to describe multilayer adsorption of gases on solid surfaces [58]. The main assumptions of the theory are [59],

1) The solid surface is homogeneous where adsorption occurs only on well defined sites.
2) There is no lateral interaction between the molecules.
3) The uppermost layer is in equilibrium with the gas phase.
4) Desorption process is homogeneous and is kinetically limited and hence heat of adsorption needs to be provided for the desorption for the first molecular layer.
5) The heat of adsorption for the first layer is the same as that for a solid sample surface.
6) Higher layers are assumed to be condensed species. Therefore, their heat of adsorption is equal to heat of liquefaction.
7) At saturation pressure, the number of layers becomes infinite.

Brunauer-Emmett-Teller (BET) equation (Equation 2.5) for calculating the number of nitrogen molecules required to form a single layer on the adsorbent surface, known as the monolayer capacity of the material, is given by [58],

$$\frac{P}{v(P_0 - P)} = \frac{1}{Cv_m} + \frac{(C-1)P}{Cv_m P_0} \tag{2.5}$$

where P is the adsorption equilibrium pressure, P_0 is saturation vapour pressure of the adsorbate at the experimental temperature, v is the volume of N_2 adsorbed at a pressure P, v_m is the volume of adsorbate required for monolayer coverage, C is a constant that is related to the heat of adsorption and liquefaction. The BET equation allows us to plot a straight line with $P/(P_0\text{-}P)$ against P/P_0 having slope

$s = (C-1)/(v_m C)$ and intercept $i = 1/(v_m C)$. The monolayer capacity (V_m) can be calculated by solving the equations for slope and intercept and then can be related to the total surface area (SA) in square meter by using the Equation 2.6 [58].

$$SA = \frac{v_m\ N}{22414} A_m \times 10^{-20}\ \ (m^2) \tag{2.6}$$

where N is the Avogadro number and A_m is the area of cross section of the adsorbate molecule. The specific surface area of the solid material can be then obtained by dividing the total surface area by mass of the solid and is expressed in m^2/g. The pore volume and pore size distribution are calculated by using the adsorption isotherms according to which the material can be classified as macroporous (pore diameter above 50 nm), mesoporous (pore diameter 2–50 nm) or microporous (pore diameter less than 2 nm) materials.

In the present work, surface area and porosity measurements were performed by nitrogen adsorption technique using a Quantachrome Quadrasorb automatic volumetric instrument.

2.3.9 Magnetic measurements

The magnetization of a sample can be measured by using a vibrating sample magnetometer (VSM), where the sample is vibrated in a uniform magnetic field producing a voltage in the pickup coils located near the sample [60]. The voltage developed in these coils is directly proportional to the magnetic moment of the vibrating sample. The sensitivity of the measurement can be enhanced by using advanced detection systems like superconducting quantum interference device (SQUID) instead of conventional copper coils. SQUID uses the property of Josephson junction; a small insulating gap between two superconductors. When connected in a circuit, the measuring current flows through the ring by tunneling of electrons through the insulating gap [61]. SQUID assembly has a superconducting ring with two Josephson junctions. When a change in magnetic flux is

brought about, it generates a voltage and a current in the ring which gets added and subtracted to the measuring current at two Josephson junctions. This induces a resistance change and a voltage across the superconducting loop. The SQUID assembly thus becomes highly sensitive since it can determine the change in electric current, even corresponding to a single electron change, thereby giving a field sensitivity of 2×10^{-15} Tm^2 [61]. Magnetization (M) of samples can be measured as a function of magnetic filed (H) or temperature (T) and time (t), both in the presence or absence of a magnetic filed depending on the required information [60].

Magnetization measurement of samples discussed in this work was performed on a Quantum Design MPMS 7T SQUID-VSM. The magnetic susceptibility was calibrated by using a standard sample of palladium metal, with weight susceptibility (χ_g) of 5.25 $\times10^{-6}$ cm^{3}g^{-1} at 298 K. The system has a sensitivity of 10^{-8} emu at zero magnetic field and can operate from 1.8 K to 400 K. Temperature calibration and oxygen contamination inside the sample chamber were checked by using a standard indium sample with superconducting transition temperature of 3.4 K. The instrument used can operate at high magnetic fields up to 70 kOe (7 T), which is attained by an electromagnet with superconducting coils.

The magnet and the SQUID detection coil are placed in an ever-cool liquid helium dewar to maintain the critical temperature of the superconductors. For measurements involving temperature sweep, the temperature was increased at 2 K/min for both zero field cooled (ZFC) and field cooled (FC) measurements. For ZFC measurement, initially the sample is cooled at 20 K/min from 300 K to 1.8 K in the absence of field. After reaching 1.8 K a sufficiently low field, depending on the magnetic moment of the sample, is applied and magnetization is recorded as a function of increasing temperature. FC measurement is also similar to ZFC measurement, with one marked difference that the cooling is performed under a small magnetic field. Magnetic measurement is then performed in the same field. For M versus H measurements, the magnetic field was increased or decreased at the rate of 250 Oe/min in the respective quadrants.

2.3.10 Electrical resistance measurements

Resistance measurements were performed by the four probe method as described by Van der Pauw [62]. This method allows the measurement of resistance and Hall effect for any arbitrary shaped flat samples. The important criteria that have to be satisfied for measurements on arbitrary shaped discs without knowing the current pattern are

1) The contacts should be at the circumference of the sample.
2) The contacts should be sufficiently small (point contacts).
2) The sample must have homogeneous thickness.
3) The sample should not have isolated holes.

Detailed description of the theory of Van der Pauw method is given in the literature [62]. Figure 2.2 shows a schematic diagram of the four probe connection on an arbitrarily shaped sample, where the resistivity can be calculated by the following relation (Equation 2.7)

$$\rho = \frac{\pi d}{ln2} \frac{(R_{AB,CD} + R_{BC,DA})}{2} f\left(\frac{R_{AB,CD}}{R_{BC,DA}}\right) \tag{2.7}$$

$R_{AB,CD}$ is defined as the potential difference V_D-V_C between the contacts D and C per unit current through the contacts A and B when current enters the sample through the contact A and leaves through the contact B. Similarly, the resistance $R_{BC,DA}$ is defined. f is a function of the resistance ratio $R_{AB,CD}/R_{BC,DA}$ and satisfies the relation given by Equation 2.8. d is the sample thickness in cm.

$$\frac{R_{AB,CD} - R_{BC,DA}}{R_{AB,CD} + R_{BC,DA}} = f \; arccosh\left\{exp\frac{(ln2/f)}{2}\right\} \tag{2.8}$$

For low-temperature measurement, the sample was mounted on a closed cycle cryostat from APD cryogenics. The temperature was controlled by a digital temperature controller model 9650 by Scientific instruments. An additional temperature sensor (DT 400 Si diode, Lakeshore Cryotronics) was placed near to the

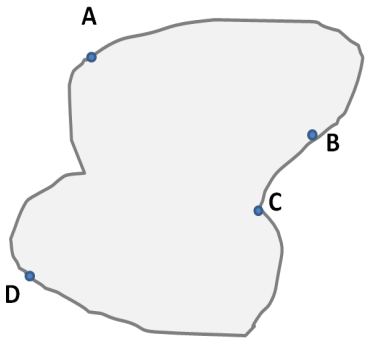

Figure 2.2: A sample having arbitrary shape connected with four probes (A,B,C and D) at the circumference for Van der Pauw measurement.

sample inside the cryostat to avoid temperature errors during low-temperature measurements. A Keithley 220 constant current source with current input range 10^{-9}–10^{-3} A was used as the input source. A Keithley 196 multimeter and Keithley 6517A model electrometer were used for the voltage measurements depending on the resistance offered by the sample. The measurement was carried out during cooling at a rate of 2 K/min and the data was continuously recorded with the help of an IBM computer.

Bibliography

[1] J. Robertson, *Prog. Solid State Chem.* 21 (1991) 199.

[2] K. Takai, M. Oga, H. Sato, T. Enoki, Y. Ohki, A. Taomoto, K. Suenaga and S. Iijima, *Phys. Rev. B* 67 (2003) 214202.

[3] O. Ioannidou and A. Zabaniotou, *Renewable Sustainable Energy Rev.* 11 (2007) 1966.

[4] H. H. Acma, S. Yaman and S. Kucukbayrak, *Energy Convers. Manage.* 47 (2006) 1004.

[5] T. N. Hoheisel, S. Schrettl, R. Szilluweit and H. Frauenrath, *Angew. Chem. Int. Ed.* 49 (2010) 6496.

[6] W. S. Hummers and R. E. Offeman, *J. Am. Chem. Soc.* 80 (1958) 1339.

[7] D. C. Marcano, D. V. Kosynkin, J. M. Berlin, A. Sinitskii, Z. Sun, A. Slesarev, L. B. Alemany, W. Lu and J. M. Tour, *ACS Nano* 4 (2010) 4806.

[8] D. R. Dreyer, S. Park, C. W. Bielawski and R. S. Ruoff, *Chem. Soc. Rev.* 39 (2010) 228.

[9] M. L. Minus and S. Kumar, *J. Min. Met. Mater. Soc.* 57 (2005) 52.

[10] S. H. Yu, X. Cui, L. Li, K. Li, B. Yu, M. Antonietti and H. Coelfen, *Adv. Mater.* 16 (2004) 1636.

[11] H. S. Qian, S. H. Yu, L. Luo, J. Gong, L. Fei and X. Liu, *Chem. Mater.* 18 (2006) 2102.

[12] M. Jagtoyen, M.Thwaites, J.Stencel, B.Mcenaney and F.Derbyshire, *Carbon* 30 (1992) 1089.

[13] Y. Guo and D. A. Rockstraw, *Carbon* 44 (2006) 1464.

[14] W. M. A. W. Daud and W. S. W. Ali, *Bioresour. Technol.* 93 (2004) 63.

[15] A. G. Pandolfo, M. A. Amoli and J. S. Killingley, *Carbon* 32 (1994) 1015.

[16] M. J. Prauchner and F. R. Reinoso, *Microporous Mesoporous Mater.* 152 (2012) 163.

[17] J. Laine and S. Yunes, *Carbon* 30 (1992) 601.

[18] B. D. Epstein, E. D. Molle, and J. S. Mattson, *Carbon* 9 (1971) 609.

[19] Y. Xie and P. M. A. Sherwood, *Chem. Mater.* 2 (1990) 293.

[20] A. Marcilla, , S. Garcia, M. Asensio and J. A. Conesa, *Carbon* 38 (2000) 429.

[21] D. Savova, E. Apak, E. Ekinci, F. Yardim, N. Petrov, T. Budinova, M. Razvigorova and V. Minkova, *Biomass Bioenergy* 21 (2001) 133.

[22] A. Aygun, S. Y. Karakasb and I. Duman, *Microporous Mesoporous Mater.* 66 (2003) 189.

[23] B. S. Girgis, S. S. Yunis and A. M. Soliman, *Mater. Lett.* 57 (2002) 164.

[24] B. S. Girgis and M. F. Ishak, *Mater. Lett.* 39 (1999) 107.

[25] W. Su, L. Zhou and Y. Zhou, *Carbon* 41 (2003) 861.

[26] W. T. Tsai, C. Y. Chang and S. L. Lee, *Bioresource Technol.* 64 (1998) 211.

[27] N. Yalcyn and V. Sevinc, *Carbon* 38 (2000) 1943.

[28] M. Biswal, A. Banerjee, M. Deo and S. Ogale, *Energy Environ. Sci.* 6 (2013) 1249.

[29] T. Zhang, W. P. Walawender, L. T. Fan, M. Fan, D. Daugaard and R. C. Brown, *Chem. Eng. J.* 105 (2004) 53.

[30] M. M. Sabio, M. T. Gonzalez, F. R. Reinoso and A. S. Escribano,*Carbon* 34 (1996) 505.

[31] M. Kitano, K. Arai, A. Kodama, T. Kousaka, K. Nakajima, S. Hayashi and M. Hara, *Catal. Lett.* 131 (2009) 242.

[32] Y. Guo and D. A. Rockstraw, *Microporous Mesoporous Mater.* 100 (2007) 12.

[33] M. A. L. Rodenas, D. C. Amoros and A. L. Solano, *Carbon* 41 (2003) 267.

[34] J. Hayashi, A. Kazehaya, K. Muroyama and A. P. Watkinson, *Carbon* 38 (2000) 1873.

[35] J. Romanos, M. Beckner, T. Rash, L. Firlej, B. Kuchta, P. Yu, G. Suppes, C. Wexler and P. Pfeifer, *Nanotechnology* 23 (2012) 015401.

[36] T. Otowa, R. Tanibata and M. ltoh, *Gas Sep. Purif.* 7 (1993) 241.

[37] I. M. Kolthoff, *J. Phys. Chem.* 36 (1932) 860.

[38] W. Wu, Q. He and C. Jiang, *Nano Res. Lett.* 3 (2008) 397.

[39] A. R. West, *Solid State Chemistry and its Applications* (John Wiley & Sons, 2013).

[40] B. D. Cullity and S. R. Stock, *Elements of X-ray Diffraction* (Pearson, 2001).

[41] A. L. Patterson, *Phys. Rev.* 56 (1939) 978.

[42] J. Biscoe and B. E. Warren, *J. Appl. Phys.* 13 (1942) 364.

[43] D. B. Williams and C. B. Carter, *The Transmission Electron Microscope* (Springer, 1996).

[44] L. Reimer and H. Kohl, *Transmission Electron Microscopy: Physics of Image Formation* (Springer, 2008).

[45] W. Zhou, R. Apkarian, Z. L. Wang and D. Joy, *Fundamentals of Scanning Electron Microscopy (SEM)* (Springer, 2007).

[46] C. N. Banwell and E. M. McCash, *Fundamentals of Molecular Spectroscopy* (McGraw-Hill, 1994).

[47] J. R. Ferraro, *Introductory Raman Spectroscopy* (Academic press, 2003).

[48] F. Tuinstra and J. L. Koening, *J. Chem. Phys.* 53 (1970) 1126.

[49] L. G. Cancado, K. Takai, T. Enoki, M. Endo, Y. A. Kim, H. Mizusaki, A. Jorio, L. N. Coelho, R. M. Paniago and M. A. Pimenta, *Appl. Phys. Lett.* 88 (2006) 163106.

[50] A. C. Ferrari and J. Robertson, *Phys. Rev. B.* 61 (2000) 14095.

[51] M. A. Pimenta, G. Dresselhaus, M. S. Dresselhaus, L. G. Cancado, A. Jorio and R. Saito, *Phys. Chem. Chem. Phys.* 9 (2007) 1276.

[52] P. Lespade, R. Al-Jishi, M. S. Dresselhaus, *Carbon* 20 (1982) 427.

[53] H. Wilhelm, M. Lelausian, E. McRae, B. Humbert, *J. Appl. Phys.* 84 (1998) 6552.

[54] D. Skoog, D. West, F. L. Holler and S. Crouch, *Fundamentals of Analytical Chemistry* (Cengage Learning, 2013).

[55] J. D. Menczel and R. P. Bruce, *Thermal Analysis of Polymers: Fundamentals and Applications* (John Wiley & Sons, 2014).

[56] J. Cazes, *Analytical Instrumentation Handbook* (CRC Press, 2004).

[57] A. J. Bard, J. D. Debad, J. K. Leland, G. B. Sigal, J. L. Wilbur, J. N. Wohlsatdter and R. A. Meyers, *Encyclopedia of Analytical Chemistry: Applications, Theory and Instrumentation* (John Wiley & Sons, 2000).

[58] J. Rouquerol, R. Francoise, P. Llewellyn, G. Maurin and K. S. W. Sing, *Adsorption by Powders and Porous Solids: Principles, Methodology and Applications* (Academic press, 2013).

[59] K. S. W. Sing, *Adv. Colloid Interface Sci.* 76 (1998) 3.

[60] B. D. Cullity and C. D. Graham, *Introduction to Magnetic Materials* (John Wiley & Sons, 2011).

[61] Y. S. Greenberg, *Rev. Mod. Phys.* 70 (1998) 175.

[62] L. J. Van der Pauw, *Philips Res. Rep.* 13 (1958) 1.

Chapter 3

Preparation and characterization of disordered carbon

3.1 Introduction

The unique properties of disordered carbons, which can be considered to be in between that of diamond and graphite, are known to depend on their microstructure [1]. The microstructure of disordered carbons can be varied over a wide range by proper heat-treatments [1,2]. During heat-treatment, the mixed sp^2/sp^3 phase, which has a considerable structural strain, relaxes to a thermodynamically stable structure which contains rings and chains of sp^2 hybridized carbon atoms forming graphitic clusters in an amorphous background [3–6]. The extent of graphitic ordering depends on the heat energy available for the migration of the sp^2 carbon atoms. The graphitic ordering is mainly brought about by the clustering of the sp^2 carbon atoms, since the conversion of sp^3 to sp^2 carbon atoms is limited to much higher heat-treatment temperatures (≥ 1300 °C) owing to the greater energy needed to break an sp^3 bond [2,3,5].

For the present study, dried coconut shell (CS) collected from Calicut district of Kerala, is used as the precursor material. CS was selected as the carbon source because of its relevance as a prime industrial precursor for the production of granular activated carbon due to the ease of availability and low ash content on pyrolysis [7,8]. The dried coconut shell can be crushed into pieces of suitable size, and can be pyrolyzed under selected conditions to obtain the desired carbon sample. Pyrolysis above 500 °C is known to remove most of the volatile matter and a further increase in the temperature results in an increase in the surface area and porosity by gasification of carbon by forming CO or CO_2 depending on the availability of oxygen in the pyrolyzing environment [3,9,10].

Preparation of compact carbon pellets from powders, for different studies, using conventional methods like mechanical pressing, is a difficult and time consuming task, considering that the carbon grains remain loosely bound even after applying a large pressure. The electrical properties of the carbon pellets thus produced may get modified due to the ineffective sintering of the carbon grains. A solid piece of CS on pyrolysis readily produces well-sintered hard carbon pellets, which is, therefore, an additional advantage of the current precursor for the studies on the

electrical properties of the disordered carbon [11].

Even though CS-based carbons have been used for various applications, there are no detailed and systematic studies reported on the development of the microstructure of these materials during the heat-treatment. Thus, different characterization studies have been performed on carbon samples derived from CS by heat-treatment at different temperatures to compare the microstructures. The disordered carbon samples are characterized mainly by powder X-ray diffraction and Raman spectroscopy. X-ray diffraction is used to calculate the in-pane (L_a) and out-of-plane (L_c) coherence lengths of the material, respectively, from the (100) and (002) diffraction peaks, which are directly related to the degree of crystallinity [12]. The changes in the Raman spectral parameters are analyzed to track and identify the extent of order/disorder present in the heat-treated samples, based on the 3-stage model proposed by Ferrari and Robertson [13].

3.2 Preparation of disordered carbon

3.2.1 Thermogravimetric analysis of the precursor

All nutshells, including CS, are known to contain a large portion of volatile matter including oil [14]. Therefore, a careful choice of the pyrolysis temperature is required in order to remove all the volatile matter so that the observed properties necessarily correspond to carbon microstructure. Thus, thermogravimetric analysis (TGA) was performed on dry CS, under N_2 atmosphere, to fix the minimum pyrolysis temperature. Figure 3.1 shows the TGA curve of dry CS used for the preparation of disordered carbon. The decrease in the weight of dry CS occurs at almost the same temperature (230 °C) with a total weight loss of ∼80 %, as reported previously [14]. However, there is a minor disagreement between the extent of final weight loss, which might be arising due to the difference in the composition of CS, collected from different regions around the globe [14,15]. Initial 6% weight loss observed below 100 °C in the TGA curve of CS corresponds to the removal of moisture from the material and the sharp weight loss at ∼300 °C corresponds

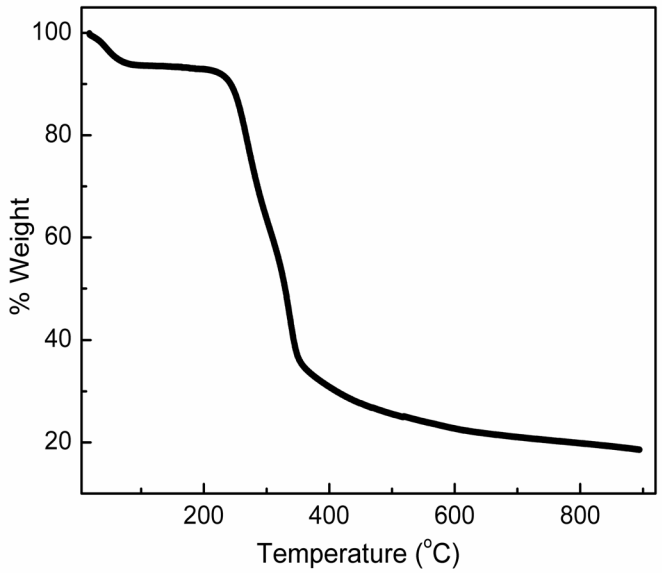

Figure 3.1: TGA curve of dry coconut shell.

to the removal of bound organic species and thus indicating the carbonization of CS [16]. After CS is transformed to carbon, the effect of heating above ∼350 °C is mainly to rearrange from amorphous state to more stable graphitic structure by removal of various hetero-elements and oxygen-containing surface functional groups like acid, alcohol, etc., formed during carbonization [17].

Based on the TGA results, the minimum pyrolysis temperature for the current study is fixed as 500 °C, since the weight loss above this temperature is almost linear and very small compared to the drastic changes at lower temperatures.

3.2.2 Heat-treatments

For preparing different disordered carbon samples, dry CS was crushed in to small rectangular pieces (∼10 mm x 10 mm) and heat-treated at different temperatures, in the range 500 °C to 1000 °C in a horizontal programmable tubular furnace under flowing nitrogen atmosphere.

The temperature programs used for the heat-treatment are summarized in Table 3.1. The desired final heat-treatment temperature (HTT) was reached through

Table 3.1: Temperature programs used for the heat-treatment.

Sample code	T_1 (°C)	t_1 (Min.)	T_2 (°C)	t_2 (Min.)	T_3 (°C)	t_3 (Min.)	T_4 (°C)
HT500	150	60	350	90	500	240	30
HT600	200	60	400	90	600	240	30
HT700	250	60	500	90	700	240	30
HT800	250	60	550	90	800	240	30
HT900	300	60	600	90	900	240	30
HT1000	300	60	650	90	1000	240	30

three steps. The first step involved heating from room temperature to a desired temperature (T_1), at a heating rate of 5 °C/min. This temperature was then maintained for 60 minutes (t_1). The temperature of the furnace was then further increased to T_2 at a rate of 5 °C/min, and then maintained at this temperature for 90 minutes (t_2). The temperature was then increased to the desired final temperature, T_3. The carbon sample was kept at T_3 for 4 hours (t_3) and then the furnace was cooled to room temperature (T_4) at a rate of 10 °C/min. Part of the carbon pellet obtained after heat-treatment was crushed and powdered using an agate mortar and pestle, for characterization and other studies.

The carbon powders obtained after crushing the heat-treated pellets are labeled as HTxxx, where xxx is the heat-treatment temperature (Table 3.1). The heat-treated samples were further treated with conc. HCl (Merck, 37%) at 80 °C for 4 hours, at 100 °C, and all the acid-treated samples were recovered by filtration and washed several times using double distilled water. The acid solution was analyzed for metal contents using inductively coupled plasma - optical emission spectroscopy (ICP-OES). The acid-treated powder samples are labeled as HTxxxA.

3.3 Characterization of disordered carbon

3.3.1 Determination of trace elements

The cultivation of coconut tree requires the supply of many nutrients, whose intake occurs naturally from a fertile soil. The primary nutrients include potassium, nitrogen and phosphorous [18]. There are many other secondary nutrients which help in the growth of the plant which includes magnesium, chlorine, calcium, sulphur and sodium [18]. Apart from the primary and secondary nutrients, depending on the mineral content of the soil, many other micronutrients like iron, copper, zinc, etc. are also absorbed by the plant [18]. These nutrients mainly exist in the plant as inorganic compounds and organometallic complexes, which play a vital role in different stages of the plant growth [18,19].

Pyrolysis of CS is a complex procedure and during pyrolysis in an inert atmosphere, the trace amounts of elements present in complex form, may produce inorganic phases and will remain embedded in the carbon matrix [20,21]. These trace amounts of inorganic compounds can play a crucial role in modifying many of the physical properties of the carbon samples. Especially, the studies on the magnetic properties of the resulting carbon need special attention and precise determination of the amount of magnetic impurities, if any, is required. The compounds formed may be magnetic, including ferromagnetic elements, due to the reducing atmosphere during pyrolysis. The highly sensitive instruments like SQUID magnetometer can pick up the small magnetic moments of the impurities present in the carbon material. Quantitative determination of metal impurities in the acid extract of the heat-treated samples was performed by ICP-OES, after calibrating with a multi-element standard solution from Merck chemicals. The results showed that several metal ions are present in the heat-treated carbon samples and extracted into the acid solution, which are detected from the ICP analysis. These include salts of ferromagnetic metals Fe, Co and Ni. The result of the quantitative analysis is summarized in Table 3.2. The ICP analysis required large quantities of the heat-treated samples and hence more than one coconut shell was used for the

Table 3.2: Concentration of metal ion impurities (ppm) present in the heat-treated carbon samples.

Sample code	Al	B	Ca	Co	Fe	K	Mg	Na	Ni
HT500 to HT1000	210	94	350	20	70	620	11	276	24
HT500A	11	3	30	4	6	26	< 1	14	5
HT500AA	5	< 1	6	< 1	< 1	5	< 1	< 1	< 1

acid extraction process. Minor variations can be expected in the mineral content of different shells used for the sample preparation and therefore, Table 3.2 shows the average concentration of the metal ion impurities. The concentrations of the metal ion impurities are found to be considerably reduced in HT500A (sample washed using acid after pyrolysis), when compared to that in HT500. To verify the efficiency of the acid extraction process, HT500A was again treated with concentrated hydrochloric acid under similar conditions (HT500AA) as that of HT500 and the extract was subjected to ICP analysis. The concentrations of the metal ion impurities and especially the magnetic metal impurities are found to be negligible after the second acid extraction process.

3.3.2 Surface area analysis

The surface area and porosity of the heat-treated samples were measured by nitrogen adsorption method. As described in Section 2.3.8, the heat-treated samples were first ground to fine powders and loaded into the nitrogen adsorption chamber of the instrument after degassing. Figure 3.2 shows the pore size distribution and surface area (inset of Figure 3.2) of the heat-treated samples. HT500 has a small number of $\sim$7 Å wide pores. With increasing HTT, no significant increase in the pore size distribution is observed up to HTT=700 °C. However, for HTT above 700 °C, a large increase in the number of sub-nanometer pores is observed. Thus, samples HT800, HT900 and HT1000 are comparatively more porous than those heat-treated at lower temperatures. A similar trend is observed in the surface

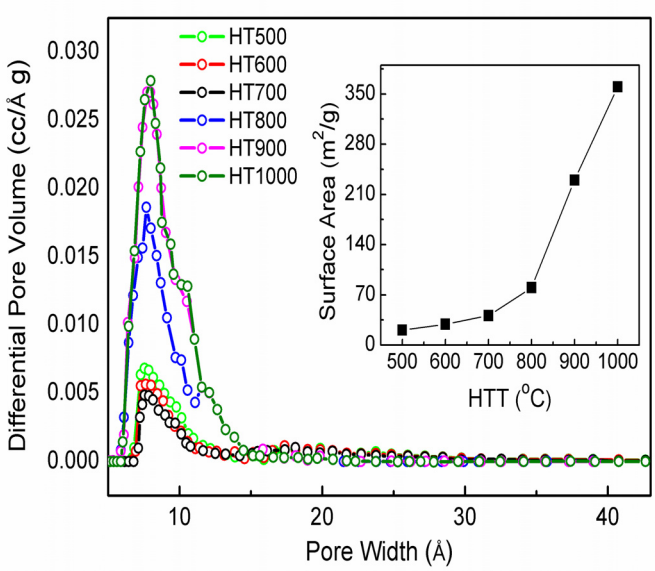

Figure 3.2: Pore size distribution in carbon samples heat-treated from 500 °C to 1000 °C. Inset shows the surface area as a function of HTT. Solid lines are guide to the eyes.

area with HTT. Samples HT500, HT600 and HT700 have low surface area (< 60 m^2/g) owing to the poor porosity compared to those heat-treated above 700 °C. A large increase in the surface area is observed for samples heat-treated above 800 °C, and this is mainly due to the increase in the number of sub-nanometer sized pores. However, it should be noted that the surface area and pore width of the heat-treated samples are much smaller when compared to the activated carbon samples prepared from CS (> 500 m^2/g) reported in the literature [10,22]. This indicates that the trace amounts of metal compounds found to be present in the CS are not acting as activating agents and therefore their presence do not affect the evolution of the surface area and porosity of the heat-treated carbons.

3.3.3 Scanning electron microscopy

Figure 3.3 shows the SEM images of the different heat-treated carbons. The carbon samples consist of granular carbon with porous carbon grains. HT500 consists of smaller pores, and the pores are widened with increasing heat-treatment temperature. This is in agreement with the development in the surface area and porosity observed after surface area measurement. Apart from the small changes

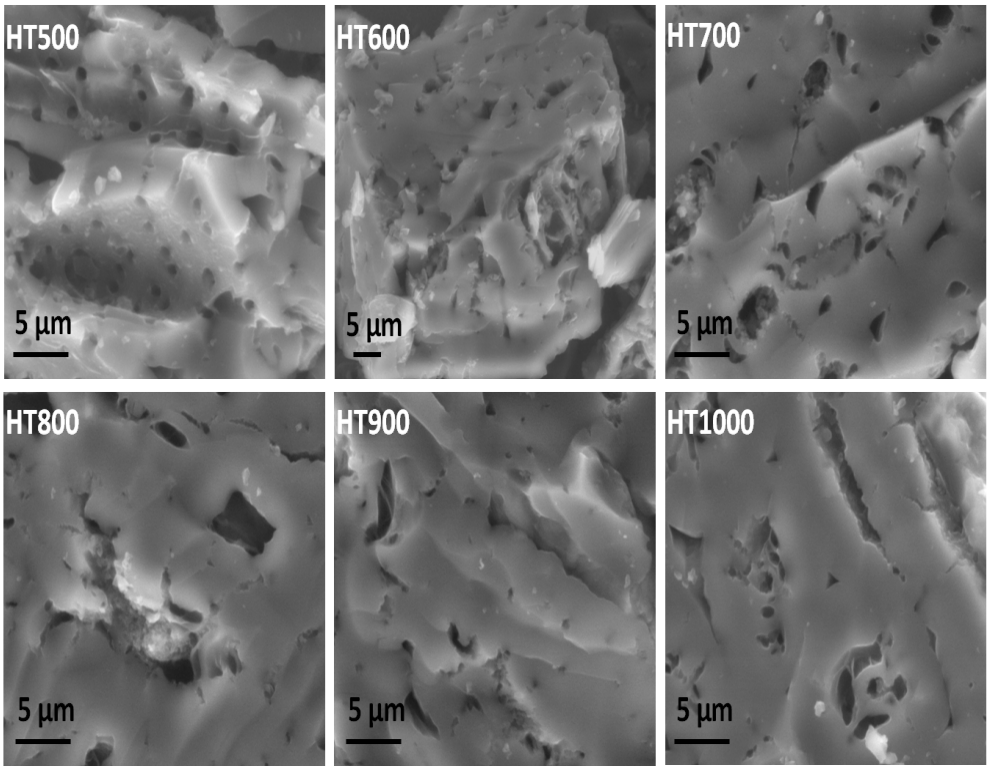

Figure 3.3: SEM images of the heat-treated carbon samples.

in the porosity, there is not much difference in the morphology of the heat-treated samples. The small difference in the porosity is not likely to produce any considerable effect on the physical properties (such as electrical and magnetic properties) of the heat-treated samples.

3.3.4 Transmission electron microscopy

The TEM images of the powdered samples, heat-treated at the lowest (500 °C) and the highest (1000 °C) temperatures, along with their corresponding acid-treated samples, are shown in Figure 3.4. All the four samples contain arbitrarily shaped carbon particles. The sizes of the particles are also comparable, in the micrometer range. This indicates that the morphology and size of the particles in the carbon powders are not affected either by the heat-treatment process or by the acid-treatment process.

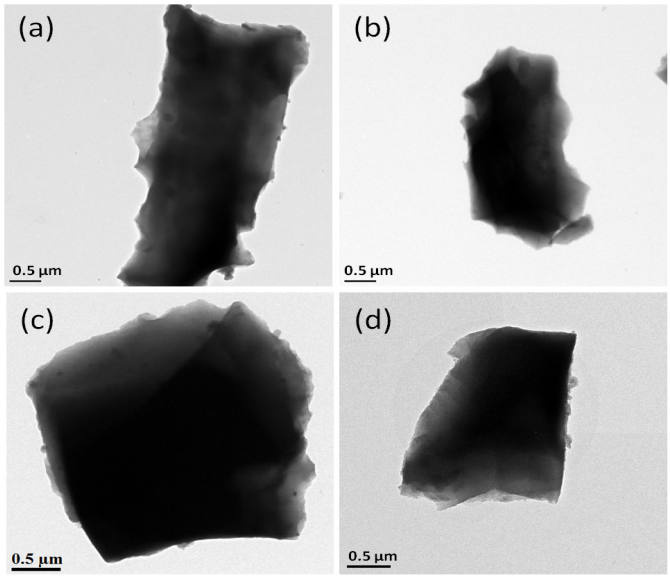

Figure 3.4: TEM images of (a) HT500, (b) HT500A, (c) HT1000 and (d) HT1000A.

3.3.5 X-ray diffraction

The structural analysis of the heat-treated samples was done by powder XRD in order to obtain more insights on the structural changes, if any, after the heat-treatment at different temperatures. Biscoe and Warren, in their theory of random lattices, pointed out that the observation of peaks of type (*00l*) and (*hk0*), with the absence of the general (*hkl*) reflections, in the XRD pattern of disordered carbon, is due to the disordered structure with random orientation of roughly parallel graphitic layers [12]. The powder samples with parallel layer groups of graphene layers, which are nearly equidistant with an orientational disorder, give a comparatively sharp reflection of the type (*00l*) and a diffuse reflection of the type (*hk0*). The powder XRD patterns of the heat-treated samples (Figure 3.5) consist of two broad peaks, an intense peak at $\sim$23° (2θ) and a less intense peak at $\sim$44° (2θ), which correspond to the (*002*) and (*100*) Bragg reflections, respectively, representing the out-of-plane and in-plane coherence lengths of disordered carbon [12]. The in-plane (L_a) and out-of-plane (L_c) coherence lengths are calculated from the widths of the (*100*) and (*002*) peaks, respectively, using the Scherrer type equation, $L = K\lambda/Bcos\theta$, with two different values of the constant K for

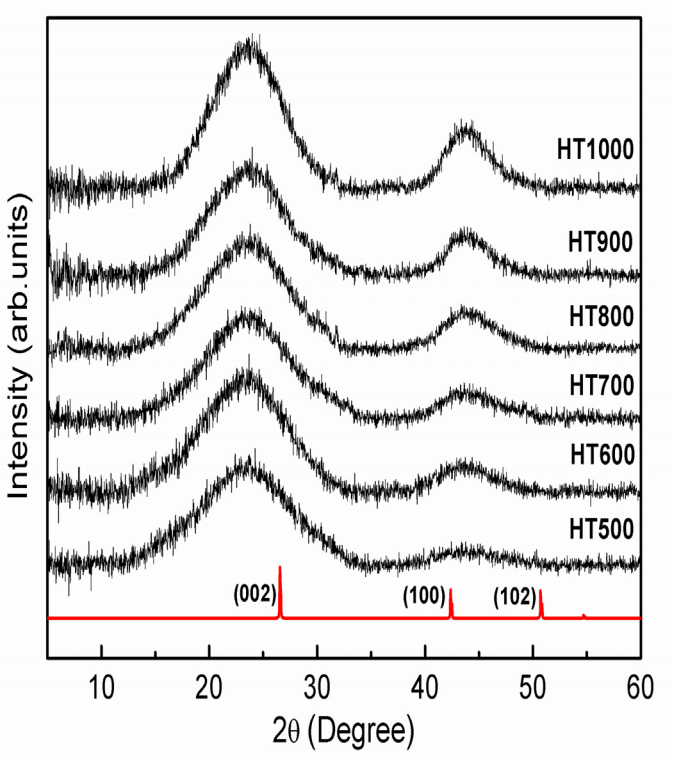

Figure 3.5: Powder XRD patterns of the heat-treated carbon samples along with the simulated (red) pattern for graphite (PDF#752078).

calculating L_a (K=1.84) and L_c (K=0.89), as reported in the literature [12,23]. B (in radians) is the full width at half maximum (FWHM) and λ is the wavelength of X-rays. The B values in radian are obtained by converting the corresponding values in degree by multiplying with the factor $\pi/180$ after correcting for instrumental contributions as discussed in Section 2.3.1. Table 3.3 gives the (*002*) and (*100*) peak positions and the corresponding B values. With the increase in HTT from 500 to 1000 °C, both the (*002*) and (*100*) peaks become less broad indicating the transformation to a more ordered structure [12]. Correspondingly, L_a is found to increase from ∼15 to ∼20 Å, and L_c increases from ∼12 to ∼16 Å (Figure 3.6).

Murty *et al.* had suggested that the nucleation and growth of new crystallites, as observed in metals, does not generally occur in pure disordered carbons and therefore, the increase in the coherence lengths on heat-treatment is due to the growth of crystallites that already exists in disordered carbon [24]. The ordering

*Table 3.3: (002) and (100) peak positions and their full width at half maximum (*B*) observed in the XRD patterns of the heat-treated carbons.*

Sample code	(*002*) peak		(*100*) peak	
	2θ	B	2θ	B
	(Degree)	(Radian)	(Degree)	(Radian)
HT500	23.5	0.120	43.7	0.200
HT600	23.6	0.108	43.8	0.187
HT700	23.6	0.103	43.8	0.180
HT800	23.7	0.100	43.8	0.175
HT900	23.7	0.090	43.8	0.163
HT1000	23.8	0.088	43.8	0.151

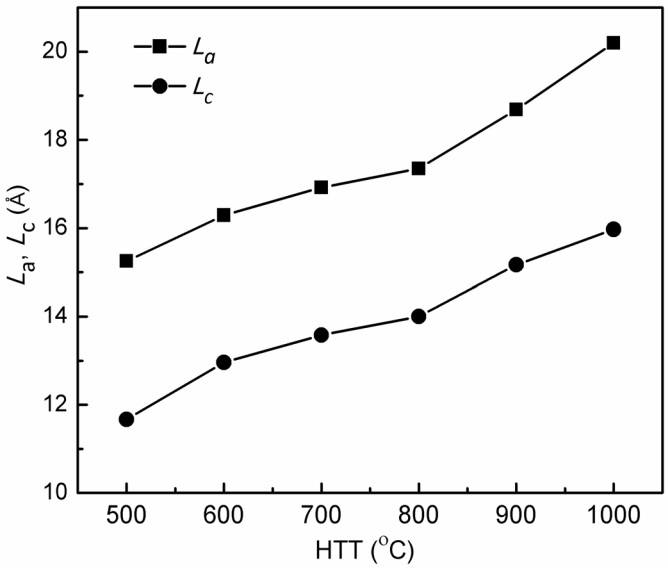

Figure 3.6: Changes in L_a and L_c with HTT.

of disordered carbon can be ascribed to three different phenomena; (i) the in-plane crystallite growth, (ii) coalescence of crystallites along the c-axis and (iii) the coalescence of crystallites along the a-axis [3]. The in-plane crystallite growth occurs at comparatively low temperatures (∼400 °C) due to which only L_a increased with little change in L_c. The coalescence of crystallites along the c-axis occurs by the stacking of graphene planes, which has moderate activation energy and therefore occurs at intermediate temperatures (500–1000 °C). However, the coalescence along the a-axis in a side-wise manner, due to its large activation energy, requires much higher temperatures ($\geqslant$ 1100 °C) [3].

The activation energies for all the three processes can vary depending on the extent of disorder present in the material. A large increase in the coherence length can be expected in carbon structures with less disorder than those with a larger extent of disorder and are called as graphitizable and non-graphitizable carbons, respectively [3,25]. A small increase in the values of L_a and L_c with HTT, below 500 °C, is reported for both non-graphitizable and graphitizable carbons. But in the present study, the low magnitude of the coherence lengths even after heat-treatment at 1000 °C suggested that the heat-treated samples belong to non-graphitizable carbons [3].

In the present case, since the thermally induced graphitization process occurs by the growth of graphitic domains from amorphous carbon, the overall structure should be containing small graphitic clusters embedded in an amorphous background. Since the XRD pattern has contributions from both the graphitic clusters and amorphous regions, the coherence lengths calculated from the XRD data are average values. Therefore, the actual dimension of the graphitic cluster could be larger than the calculated values (Figure 3.6) considering that they are localized in an amorphous background [3,25]. However, the changes in the extent of graphitization with HTT must be the same as shown in Figure 3.6, since the extent of graphitization varies directly with the average cluster dimensions.

3.3.6 Raman spectroscopy

The first order Raman spectra of diamond consists of a single prominent line at ∼1332 cm^{-1} corresponding to the triply degenerate optical phonons in the zone center [26]. For pure crystalline graphite, the Raman peaks appear at 1557 cm^{-1}, 2746 cm^{-1} and 3246 cm^{-1}, known as the G-peak, G′-peak or 2D-peak and 2G-peak, respectively [27]. The G-peak is characteristic of a material with sp^2 carbon atoms without being specific to hexagonal rings. The D-peak in the graphitic carbon emerges only in the presence of disorder and hence perfectly crystalline graphite will show only a sharp G-peak due to sp^2 carbon atoms.

Depending on the crystallinity of a disordered carbon system, the G-peak position can vary over a wide range, nearly from 1510 cm^{-1} to 1600 cm^{-1} [28]. The D-peak to G-peak intensity ratio, $I(D)/I(G)$, is one of the most important Raman parameters for disordered carbon and is used to determine the in-plane coherence length. In disordered carbon, the intensity of the G-peak and its position are determined by the number of sp^2 carbon atoms and the extent of clustering, whereas the intensity of the D-peak is determined by the presence of disordered hexagons and the broadening of the D-peak is related to the presence of non-aromatic carbon clusters containing five or seven membered rings [28]. Therefore, as the number of disordered hexagons increases, the intensity of D-peak increases above that of the G-peak and vice-versa. In the absence of disordered hexagons, as in the case of crystalline graphite, where the hexagons are completely ordered, the D-peak is generally absent and a sharp G-peak is observed at 1575 cm^{-1}. Generally, in amorphous carbons, while analyzing the G- and D-peak components, peak intensity ratio is preferred over the integrated intensity ratio since the integrated intensity is related to non-aromatic carbon clusters with five or seven membered rings [28].

The Raman spectra of the heat-treated samples consist of two peaks due to graphitic G-peak at ∼1575 cm^{-1} corresponding to the in-plane bond stretching motion of sp^2 carbon atoms and the disorder-induced D-peak at ∼1335 cm^{-1} (Figure 3.7). For all the heat-treated samples, the D-peak width is found to be

approximately double than that of the G-peak, suggesting that these samples are much different from the disordered graphite for which the D- and G-peak widths are almost comparable [29]. Raman spectra of the heat-treated carbon samples are analyzed according to the three-stage model of graphitization proposed by Ferrari and Robertson [28].

3.4 The three-stage model for graphitization

According to the three-stage model, the changes in the characteristics of the Raman G- and D- peaks during the ordering or disordering of a disordered carbon phase to a perfectly crystalline system or vice-versa can be broadly classified into three stages as shown in Figure 3.8 [28]. The different stages are classified based on the changes in the $I(D)/I(G)$ ratio. In the model, the boundary of stage-1 is between perfectly crystalline graphite and nanocrystalline graphite, where the $I(D)/I(G)$ ratio (0–2) as well as the G-peak position (1580–1600 cm^{-1}) increases continuously due to the changes in the vibrational density of states during the conversion from monocrystalline to polycrystalline graphite [28,30]. Further disorder in the nanocrystalline graphite induces a different trend for both the Raman spectral parameters. Both parameters steadily decrease due to the insertion of sp^3 defects, resulting in amorphous carbon structure ($\sim$20% sp^3) and this region is classified under stage-2. In this region, the structure consists of disordered hexagons as well as non-hexagonal rings owing to the bond angle and bond-bending disorder induced due to the insertion of sp^3 defects [28,31].

With more and more sp^3 defects being inserted into the carbon structure, the extent of sp^2 clustering decreases and eventually reaches a stage where sp^2 dimers are embedded in sp^3 matrix [28,31,32]. In this region, with the increase in the sp^3 content, the G-peak position increases while the $I(D)/I(G)$ ratio shows a small decrease characterizing stage-3. The in-plane coherence length of samples occupying in stage-2 and stage-3 is observed to be $L_a < 20$ Å [28]. Since $L_a < 20$ Å in stage-2, for considerably disordered systems, $I(D)/I(G)$ ratio does not follow the Tuinstra-Koenig (TK) relation, $(I(D)/I(G) \propto L_a^{-1}$, which was previously

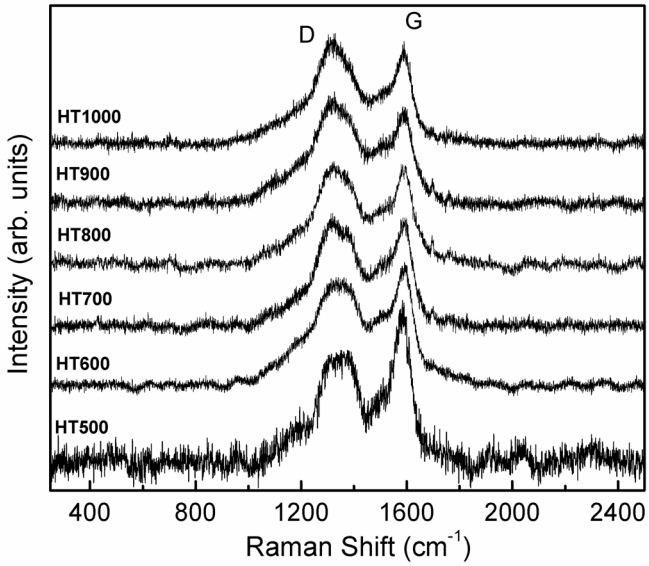

Figure 3.7: Raman spectra of the different heat-treated samples.

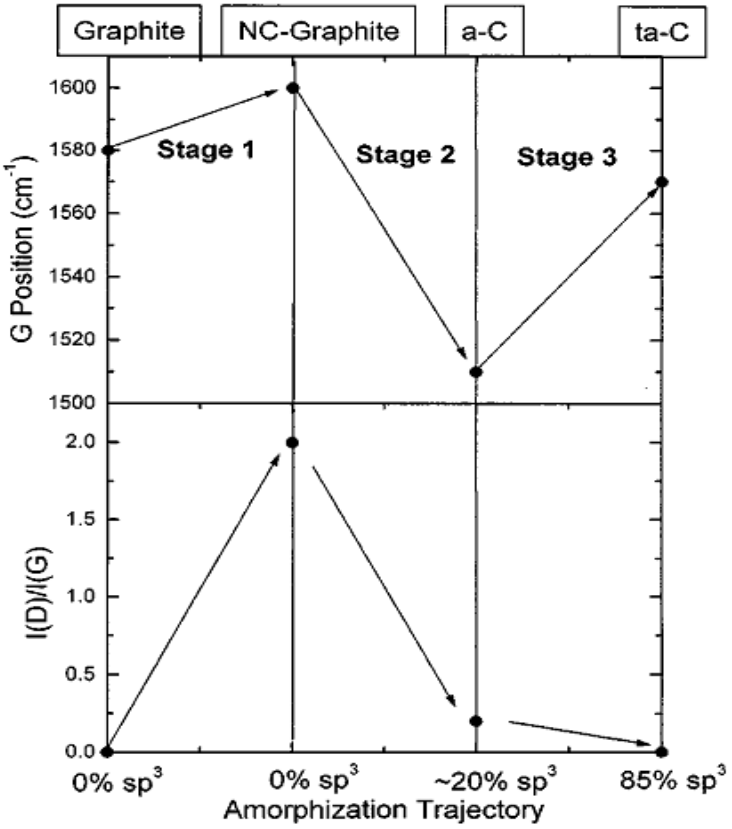

Figure 3.8: Changes in the Raman parameters during disordering of graphite, taken from reference [28].

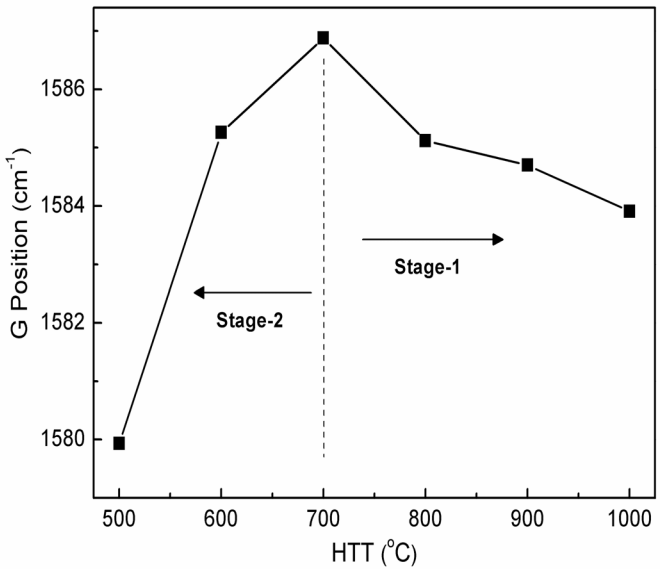

Figure 3.9: Variation of the Raman G-peak position as a function of heat-treatment temperature.

found to be valid for different ordered carbonaceous materials [33]. However, in stage-2, the $I(D)/I(G)$ ratio varies directly with ${L_a}^2$ and reversal in dependency of $I(D)/I(G)$ on L_a is not abrupt, but occurs through a broad maxima [28,33,34].

3.5 Changes in the Raman spectral characteristics with heat-treatment

In the present study, since we consider the graphitization process from disordered carbon, the Raman spectral characteristics are expected to show a reverse trend, with increasing heat-treatment temperature, that is a transition from stage-3 to stage-1 through stage-2. The variations of the G-peak position and the $I(D)/I(G)$ ratio, as a function of HTT, are shown in Figure 3.9 and Figure 3.10, respectively. For the heat-treated samples, the Raman G-peak position (Figure 3.9) initially increases sharply with increase in the heat-treatment temperature from 500 to 700 °C and then decreases slowly with increase in HTT after reaching a maximum value for HTT = 700 °C. This indicates that the samples HT500 and HT600 fall under stage-2, which consists of disordered carbon. On increasing the HTT above

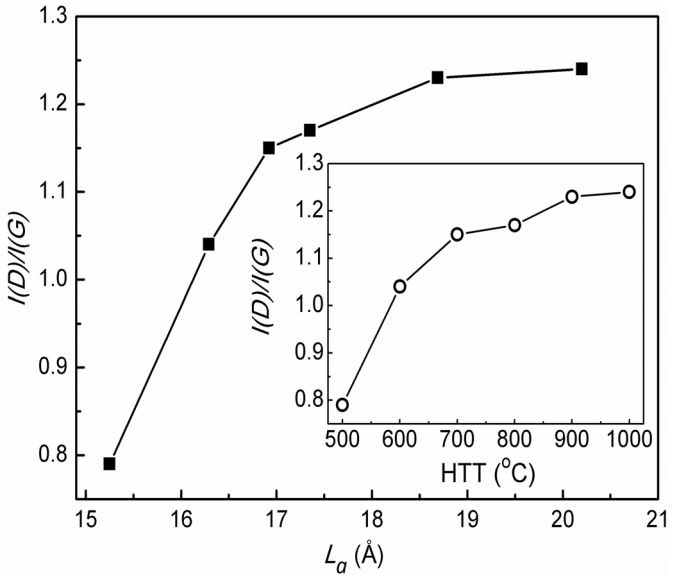

Figure 3.10: Variation of the $I(D)/I(G)$ ratio as a function of L_a. Inset shows the variation of $I(D)/I(G)$ as a function of HTT.

700 °C, there is considerable ordering by the formation of graphitic clusters in a disordered background. The structural relaxation to a graphitic phase resulting from the ordering of the hexagons, induced by thermal energy, shifts the G-peak position, which follows the stage-1 behavior [3,28]. Similarly, the $I(D)/I(G)$ ratio (Figure 3.10) initially increases sharply as L_a is increased and reaches a broad maximum at higher L_a values close to 20 Å, corresponding to HT1000 (Figure 3.10 inset), which is characteristic of a crossover from stage-2 to stage-1. These observations indicate the transition from amorphous carbon to nanocrystalline graphite. Thus, the present CS-derived carbon samples are in the boarder region separating the two carbon forms and hence does not obey the TK relation and/or the modified relation for stage-2, with $I(D)/I(G) \propto L_a^2$. The enhancement in the values of L_a and L_c (Figure 3.6) with HTT also occurs in a particular manner, with a larger increase from HT500 to HT600, which then becomes gradual and further increases above HT800. This shows that the extent of graphitization is much higher in stage-1 (HT800 to HT1000) when compared to stage-2 (HT500 to HT700) and therefore supports the observed changes in the Raman spectral characteristics.

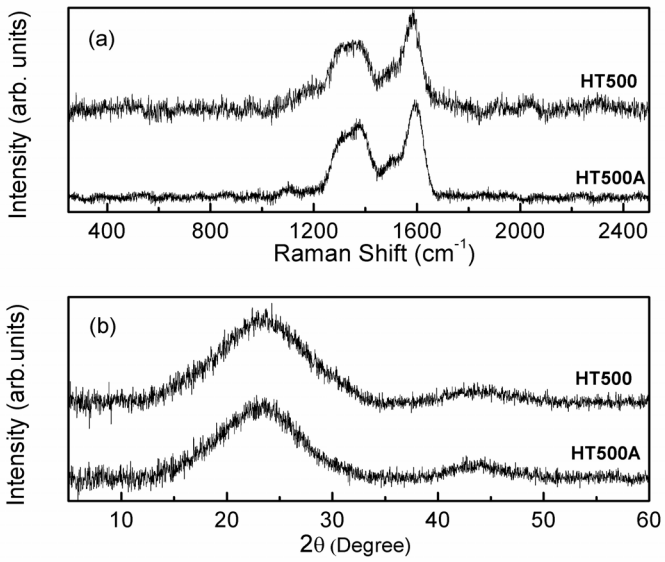

Figure 3.11: Comparison of the (a) Raman spectra and (b) XRD patterns of HT500 and HT500A.

3.6 Effect of acid-treatment on the carbon structure

The effect of acid-treatment on the microstructure of the disordered carbon was checked by comparing the Raman spectra and XRD patterns of HT500 and HT500A (Figure 3.11). The $I(D)/I(G)$ ratio does not show any considerable variation after the acid-treatment (0.80 for HT500A) when compared to that of HT500 (0.79). The G-peak position of HT500A, however, showed a small shift of 9 cm^{-1} towards the high energy region when compared to that of HT500 (Figure 3.9), after acid-treatment. Since the $I(D)/I(G)$ ratio does not show any variation, the shift in the G-peak position cannot be arising from the changes in the extent of graphitization. Therefore, the shift in the G-peak position could be arising from the modifications in the in-plane bond stretching vibrations of sp^2 carbon atoms after the acid-treatment. This indicates that the acid-treatment is chemically modifying the edge termination and dangling bonds in the carbon structure, in a similar manner as observed from the near-edge X-ray absorption fine structure (NEXAFS) studies on fluorinated activated carbon fibers [35]. The L_a (15.3 Å) and L_c (11.7

Å) values of HT500A, calculated from the XRD pattern, is more or less the same as that of HT500 (Figure 3.6). The coherence lengths being similar, XRD data shows that there is no change in the extent of graphitization on acid-treatment and therefore, supports the observations from the Raman spectra.

The comparison of the Raman spectra and the XRD patterns of HT500 and HT500A, therefore, indicates that the acid-treatment is limited to the extraction of impurities from the carbon and minor chemical modifications. It is clear that the acid-treatment is not bringing about any changes in the extent of graphitization. Therefore, the changes in the extent of graphitization observed after heat-treatment of carbon samples may hold for the corresponding acid-treated samples also.

3.7 Sample-to-sample variation and effect of heat-treatment atmosphere

CS being a natural resource, the composition and microstructure of each CS used for the heat-treatment need not be exactly similar. This difference can lead to sample-to-sample variations in the microstructure of the heat-treated carbons. To identify the extent to which the carbon structure can vary depending on the precursor, XRD and Raman studies were performed after heat-treating three different shells under nitrogen (sample codes: CN-1, CN-2 and CN-3), argon (sample code: CAr) and helium (sample code: CHe) atmospheres at 1000 °C, with the same heat-treatment program given in Table 3.1. The samples heat-treated at 1000 °C were used for studying the sample-to-sample variation and effect of gas atmosphere, since a high degree of graphitization can be brought about at this HTT, which makes the comparisons more reliable. It is expected that a similar or comparable variation in the microstructure is possible among the carbon samples heat-treated at the same HTT (HTT$\leq$1000 °C).

The XRD patterns (Figure 3.12) and the Raman spectra (Figure 3.13) of CN-1, CN-2 and CN-3 are first compared to identify the sample-to-sample variations

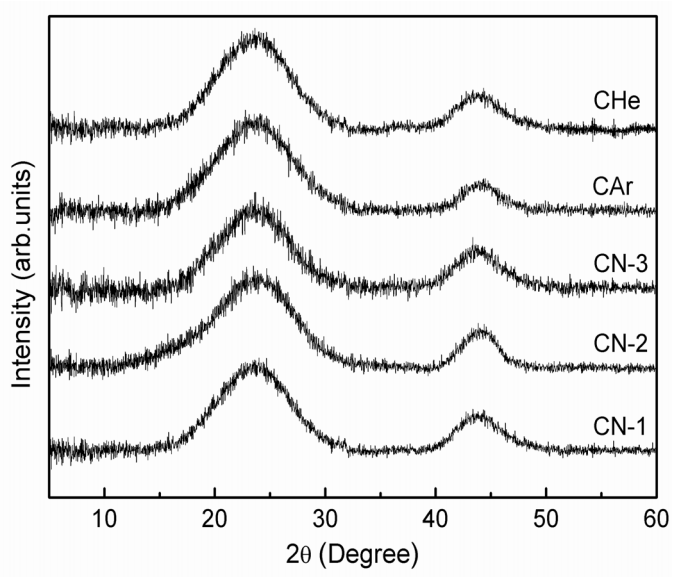

Figure 3.12: Comparison of the XRD patterns of carbon samples derived by heat-treatment at 1000 °C in nitrogen atmosphere (CN-1, CN-2 and CN-3), argon atmosphere (CAr) and helium atmosphere (CHe).

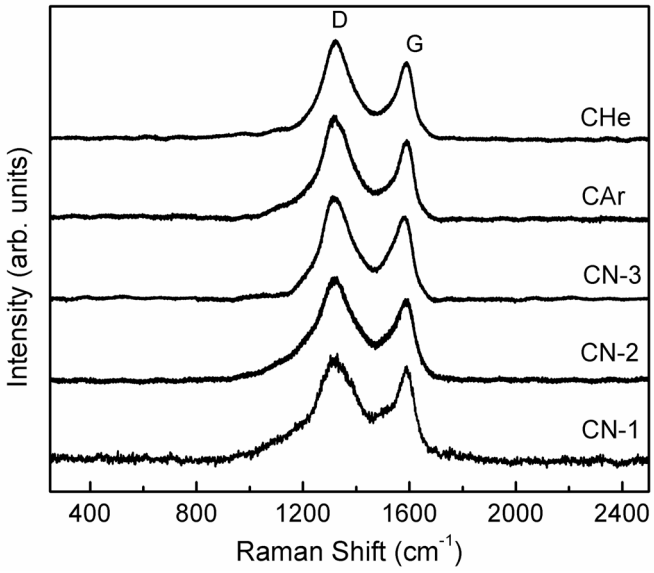

Figure 3.13: Comparison of the Raman spectra of carbon samples derived by heat-treatment at 1000 °C in nitrogen atmosphere (CN-1, CN-2 and CN-3), argon atmosphere (CAr) and helium atmosphere (CHe).

Table 3.4: Coherence lengths and Raman spectral parameters derived from Figure 3.12 and Figure 3.13, respectively.

Sample code	L_a (Å)	L_c (Å)	$I(D)/I(G)$	G-Peak (cm^{-1})
CN-1	20.2	15.2	1.23	1583
CN-2	20.5	15.2	1.25	1584
CN-3	21.1	15.1	1.24	1584
CAr	20.5	15.1	1.23	1586
CHe	21.3	15.2	1.33	1585

in the microstructure on heat-treating three different pieces of CS from different shells (Table 3.4). For these samples, both L_a and L_c values vary only over a very small range, indicating that there could be a small sample-to-sample variation in the extent of graphitization even when the heat-treatment conditions are invariant. This variation could be arising from the difference in the porosity, volatile matter content, mineral content, etc. of the precursor used, which is beyond control while using a natural precursor like CS. However, the $I(D)/I(G)$ ratio and the Raman G-peak position are more or less the same, suggesting that the density and type of defects in individual clusters are almost similar. Switching the heat-treatment atmosphere from nitrogen to argon does not produce any notable change in these parameters. However, when helium is used instead of nitrogen or argon, a small increase in the $I(D)/I(G)$ ratio is observed.

This could be due to the higher thermal conductivity of helium (157 mW/mK for helium compared to 18 mW/mK for argon and 26 mW/mK for nitrogen, at 300 °C and 0.1 MPa pressure) [36], which provides a slightly better efficiency for the heat-treatment process inducing a better and uniform graphitization at 1000 °C. The heat-treatment at different temperatures under argon and helium atmospheres were not attempted since the microstructure of the samples heat-treated at 1000 °C in these gas atmospheres were not significantly different from those obtained

by heat-treatment under nitrogen atmosphere, at the same temperature.

3.8 Conclusions

The evolution of the structural characteristics of disordered carbon samples prepared from coconut shell, on varying the heat-treatment temperature, is studied and discussed. A quantitative determination of the trace metal content by ICP-OES showed the presence of different metal ions in the acid extract. Acid-treatment of heat-treated samples is effective enough in removing most of the impurities embedded in the samples. The porosity and surface area continuously increases with an increase in the heat-treatment temperature. The magnitude of the surface area in the heat-treated samples is too low when compared to that of the chemically activated carbon. SEM and TEM studies did not show any notable difference in the morphology among the samples heat-treated at different temperatures or among the heat-treated and acid-treated samples. The in-plane and out-of-plane coherence lengths calculated from the XRD peak widths showed a regular increase with increasing HTT. The increase in the coherence length with increase in the heat-treatment temperature from 500 °C to 1000 °C showed evidence for ordering of carbon from nanocrystalline graphitic domains in an amorphous background. A near-graphitic ordering is assumed to take place since the coherence lengths are much smaller than those observed for graphitizable carbons. This was established by Raman spectroscopy studies. The variations in the intensity of Raman D-peak and G-peak ratio, $I(D)/I(G)$, and the Raman G-peak position showed evidence for a structural transition from disordered carbon to nanocrystalline graphite as the heat-treatment temperature is increased above 800 °C. The samples heat-treated in the temperature region 800-1000 °C belong to the diffuse boundary region separating the disordered carbon and nanocrystalline graphite and therefore are particularly interesting. The different hybridization characteristics and the extent of clustering of graphitic regions in these samples are expected to result in interesting physical properties. Coconut shell being a natural source, it is not possible to produce carbon samples with exactly similar

microstructural properties even after heat-treating them under similar conditions. However, this variation can be neglected since the Raman and XRD spectra of three carbon samples heat-treated at 1000 °C, under nitrogen atmosphere, were almost comparable. The gas atmosphere in which heat-treatment is carried out did not affect the microstructure much.

Bibliography

[1] M. Theye and V. Paret, *Carbon* 40 (2002) 1153.

[2] K. Takai, M. Oga, H. Sato, T. Enoki, Y. Ohki, A. Taomoto, K. Suenaga and S. Iijima, *Phys. Rev. B* 67 (2003) 214202.

[3] F. G. Emmerich, *Carbon* 33 (1995) 1709.

[4] J. Heremans, *Carbon* 23 (1985) 431.

[5] E. Staryga and G.W. Bak, *Diamond Relat. Mater.* 14 (2005) 23.

[6] R. Gago, M. Vinnichenko, H. U. Jager, A. B. Yu, I. Jimenez, N. Huang, H. Sun and M. F. Maitz, *Phys. Rev. B* 72 (2005) 014120.

[7] http://coconutboard.nic.in/charcoal.htm

[8] http://www.activatedcarbon.com/products/coconut/

[9] J. Romanos, M. Beckner, T. Rash, L. Firlej, B. Kuchta, P. Yu, G. Suppes, C. Wexler and P. Pfeifer, *Nanotechnology* 23 (2012) 015401.

[10] Z. Hu and M. P. Srinivasan, *Microporous Mesoporous Mater.* 27 (1999) 11.

[11] W. M. Daud, M. Badri and H. Mansor, *J. Appl. Phys.* 67 (1990) 1915.

[12] J. Biscoe and B. E. Warren, *J. Appl. Phys.* 13 (1942) 364.

[13] A. C. Ferrari and J. Robertson, *Phys Rev B* 61 (2000) 14095.

[14] A. J. Tsamba, W. Yang, W. Blasiak, *Fuel Process. Technol.* 87 (2006) 523.

[15] S. Bandyopadhyay, R. Chowdhury and G. K. Biswas, *Can. J. Chem. Eng.* 77 (1999) 1028.

[16] Z. Hu, M. P. Srinivasan and Y. Ni, *Carbon* 39 (2001) 877.

[17] A. Oberlin, *Carbon* 22 (1984) 521.

[18] http://www.agritech.tnau.ac.in/expert_system/ coconut/coconut/coconut_nutrie_management.html#eon

[19] F. S. Chapin, *Ann Rev. Ecol. Syst.* 11 (1980) 233.

[20] R. Child and S. Ramanat, *J. Am. Chem. Soc.* 60 (1938) 1506.

[21] G. Afrane and O. W. Achaw, *Bioresour. Technol.* 99 (2008) 6678.

[22] O. Ioannidou and A. Zabaniotou, *Renewable Sustainable Energy Rev.* 11 (2007) 1966.

[23] N. Iwashita N, C. R. Park, H. Fujimoto, M. Shiraishi and M. Inagaki, *Carbon* 42 (2004) 701.

[24] H. N. Murty, D. L. Biederman and E. A. Heintz, *Carbon* 7 (1969) 667.

[25] J. Robertson and E. P. Oreilly, *Phys. Rev. B* 35 (1987) 2946.

[26] S. A. Soolin and A. K. Ramdas, *Phys. Rev. B* 1 (1970) 1687.

[27] Y. Wang, D. C. Alsmeyer and R. L. McCreery, *Chem. Mater* 2 (1990) 557.

[28] A. C. Ferrari and J. Robertson, *Phys. Rev. B* 61 (2000) 14095.

[29] A. C. Ferrari, *Solid State Commun.* 143 (2007) 47.

[30] P. Lespade, R. Al-Jishi and M. S. Dresselhaus, *Carbon* 20 (1982) 427.

[31] T. Kohler, T. Frauenheim and G. Jungnickel, *Phys. Rev. B* 52 (1995) 11837.

[32] U. Stephan, T. Frauenheim, P. Blaudeck and J. Jungnickel, *Phys. Rev. B* 50 (1994) 1489.

[33] F. Tuinstra and J. L. Koening, *J. Chem. Phys.* 53 (1970) 1126.

[34] L. G. Cancado, K. Takai, T. Enoki, M. Endo, Y. A. Kim, H. Mizusaki, A. Jorio, L. N. Coelho, R. M. Paniago and M. A. Pimenta, *Appl. Phys. Lett.* 88 (2006) 163106.

[35] M. Kiguchi, K. Takai, V. L. J. Joly, T. Enoki, R. Sumii and K. Amemiya, *Phys. Rev. B.* 84 (2011) 045421.

[36] N. B. Vargaftik, *Handbook of Thermal Conductivity of Liquids and Gases* (CRC Press, 1993).

Chapter 4

Magnetic properties of disordered carbon

4.1 Introduction

The discovery of magnetism in organic free radicals triggered the exploration of magnetic properties of different organic molecules and carbon-based systems like fullerenes and carbon nanotubes which were otherwise considered to be non-magnetic due to the absence of *d* electrons [1]. Different nitrogen and oxygen containing organic radicals have been studied for their magnetic properties and many theoretical models were constructed to explain the spin-exchange in these radicals [1–3]. Pyrolytic carbons with different proportions of sp^3 and sp^2 hybridized carbon atoms have also been studied for their magnetic properties after preparing from different organic precursors [1].

The magnetic properties observed in carbon-based materials have been ascribed to the electronic properties arising from different factors including mixed sp^2-sp^3 sites, peculiar edge geometry, dangling bonds, the presence of heteroatoms, guest molecules and pores [4–8]. The experimentally observed magnetic characteristics are found to be in good agreement with the theoretical predictions [9,10]. The importance of defects and dangling bonds in developing a magnetic state in non-magnetic crystalline carbon systems, such as diamond and graphite, was established through high-energy irradiation experiments using proton, neutron, ^{15}N and ^{12}C [11–13]. The extinction of ferromagnetism and development of diamagnetic character in highly oriented pyrolytic graphite (HOPG), after annealing at very high temperatures, due to the increase in the grain size and reduction of edge states, point towards the importance of graphene edges, grain boundaries, defects and/or vacancies [14]. Shibayama *et al.* observed the development of a disordered magnetic state, like a spin-glass state, in heat-treated carbon system near the insulator to metal transition region which also pointed towards the mixed sp^3-sp^2 state in developing magnetic interactions [15].

Studies on the magnetic properties of the ordered low-dimensional carbon systems, including graphene, reduced graphene oxide, graphene nanoribbons, chemically modified graphene and graphene dots, are reported recently [16–22]. A recent experimental and theoretical study on the magnetic properties of graphene oxide

pointed towards the crucial role of unpaired spins on the carbon radicals, due to the presence of epoxy groups, in determining the magnetic properties [18]. The main issue related to the magnetization measurements of carbon samples is that their properties are highly sensitive to the microstructure and chemical functionalities.

Studies on graphene oxide based systems by different research groups have shown contrasting results due to the minor variations in the carbon structures [18–20]. The contribution of Fe, Co and Ni metallic impurities as well as their compounds towards the observed magnetic signal has been analyzed in detail [23]. From the absence of any correlation between the measured magnetic moment and the concentration of magnetic impurities present, the role of impurity phases towards the magnetic properties of carbon has been ruled out [13,23–25]. Moreover, magnetic force microscopy has also provided supplementary evidence for the development of magnetic moments in carbon-based materials when irradiated with high energy radiations [26].

Even though there are many reports on the magnetic properties of different carbon-based systems, including pyrolyzed carbon, only limited systematic studies are available in the literature on the effect of heat-treatment induced graphitization on the magnetic properties of carbon systems [14,15]. The development of disordered magnetism in thin films of nanographitic carbon, at the insulator to metal transition regime, in heat-treated samples, as reported by Shibayama *et al.* [15], is of great interest since it described a new class of inherent magnetic state in carbon-based materials. Since most of the recent studies on the magnetic properties of carbon-based materials are concentrated on ordered graphene-based systems and thin film samples [13,15,18,26], the effect of heat-treatment on the magnetic properties of bulk disordered carbon is still left unexplored.

The structural characterization of the different heat-treated carbon samples, as discussed in Chapter 3, showed that they belong to the crossover region be-

tween disordered carbon and nanocrystalline graphite. Since disorder and dangling bonds are the main contributors towards the magnetic properties of disordered carbon, the highly disordered carbons obtained by the pyrolysis of coconut shell are used to study the evolution of the magnetic properties as a function of the extent of graphitization. Similar attempt for systematically studying the evolution of the magnetic properties of bulk disordered carbon prepared from a natural source, whose thermal history is completely known, is not reported in the literature.

4.2 Experimental Methods

The carbon pellets obtained after heat-treatment (Section 3.2) were crushed and powdered using an agate mortar and pestle and samples in the powdered form were used for the magnetic measurements. The samples heat-treated at different temperatures (xxx °C) are labeled as HTxxx (Table 3.1, Chapter 3). Hereafter, this set of samples will be collectively referred to as the heat-treated samples. The heat-treated samples were further treated with conc. HCl, as described in Chapter 3, to remove any metal impurities and labeled as HTxxxA.

To check the efficiency of the extraction process, HT500A obtained after washing HT500 with acid was again subjected to acid-treatment and analyzed for impurities and this sample is labeled as HT500AA. Magnetization measurements, as a function of magnetic field, were performed up to a field of 60 kOe (6 T). Magnetization as a function of temperature was measured from 2 K to 300 K, under both field cooled (FC) and zero field cooled (ZFC) protocols, after applying a magnetic field of 10 kOe (1 T). The magnetization of the carbon samples derived after heat-treating CS belonging to the different batches was measured and compared. The effect of heat-treatment atmosphere in modifying the magnetic properties was also investigated by comparing the magnetization of samples heat-treated under different gas atmospheres.

4.3 Changes in the magnetization with heat-treatment temperature

The heat-treated samples are diamagnetic at 300 K with their magnetic moment decreasing with increasing applied magnetic field (Figure 4.1). However, at 2 K, all the carbon samples (Figure 4.2) showed 'S'-shaped magnetization curves. This type of magnetization curve is explained by using the Brillouin function given by Equation 4.1 [27–31].

$$\frac{M}{M_0} = \frac{2J+1}{2J}\coth\left(\frac{2J+1}{2J}\right)a' - \frac{1}{2J}\coth\frac{a'}{2J} \tag{4.1}$$

$$a' = \frac{\mu_H H}{k_B T}$$

where M is the magnetic moment at a particular field H, M_0 is the saturation magnetization, J is the total angular momentum quantum number, μ_H is the maximum magnitude of each magnetic moment, k_B is the Boltzmann constant and T is the temperature [27].

In a condensed electronic system, the angular momenta of various orbits with different orientation combine vectorially to give the resultant orbital angular momentum. This is characterized by the total orbital angular momentum L. Similarly, the individual electron spin momenta combine to give the resultant spin momentum, described by the total spin S. The total angular momentum is then the sum of L and S ($J = L + S$). For a system with non-interacting spins, there will not be any orbital angular momentum contribution (L=0) to the moment, and therefore, the contribution to the total angular momentum becomes equal to the total spin (J=S=1/2) [27]. Hence, the Brillouin type M-H curve (Equation 4.1) with J=1/2, indicates the presence of a non-interacting spin system. A nearly good fit to the Brillouin function (Equation 4.1, J=1/2) in Figure 4.3 to the measured M-H curves of different heat-treated samples points towards the non-interacting nature of the magnetic moments in these samples.

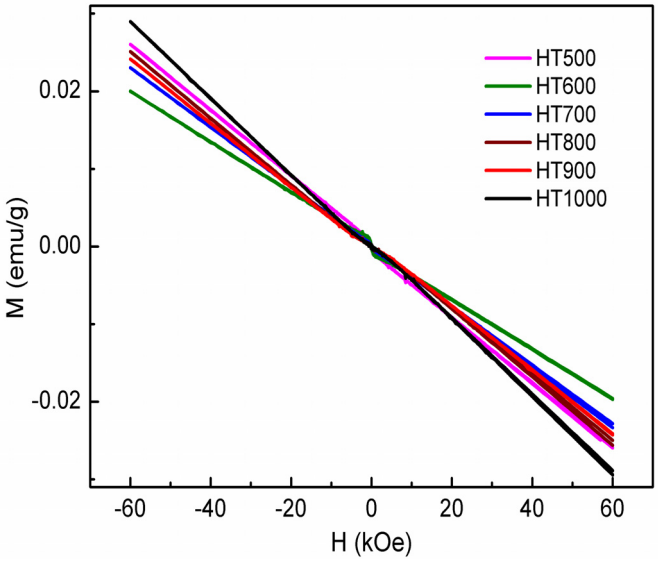

Figure 4.1: Magnetization curves of the heat-treated samples measured at 300 K.

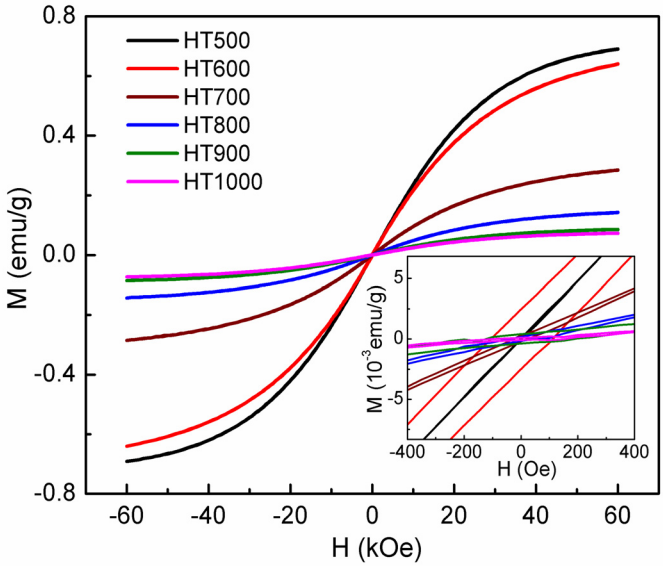

Figure 4.2: Magnetization curves of the heat-treated samples measured at 2 K. Inset: Enlarged curves showing magnetic hysteresis.

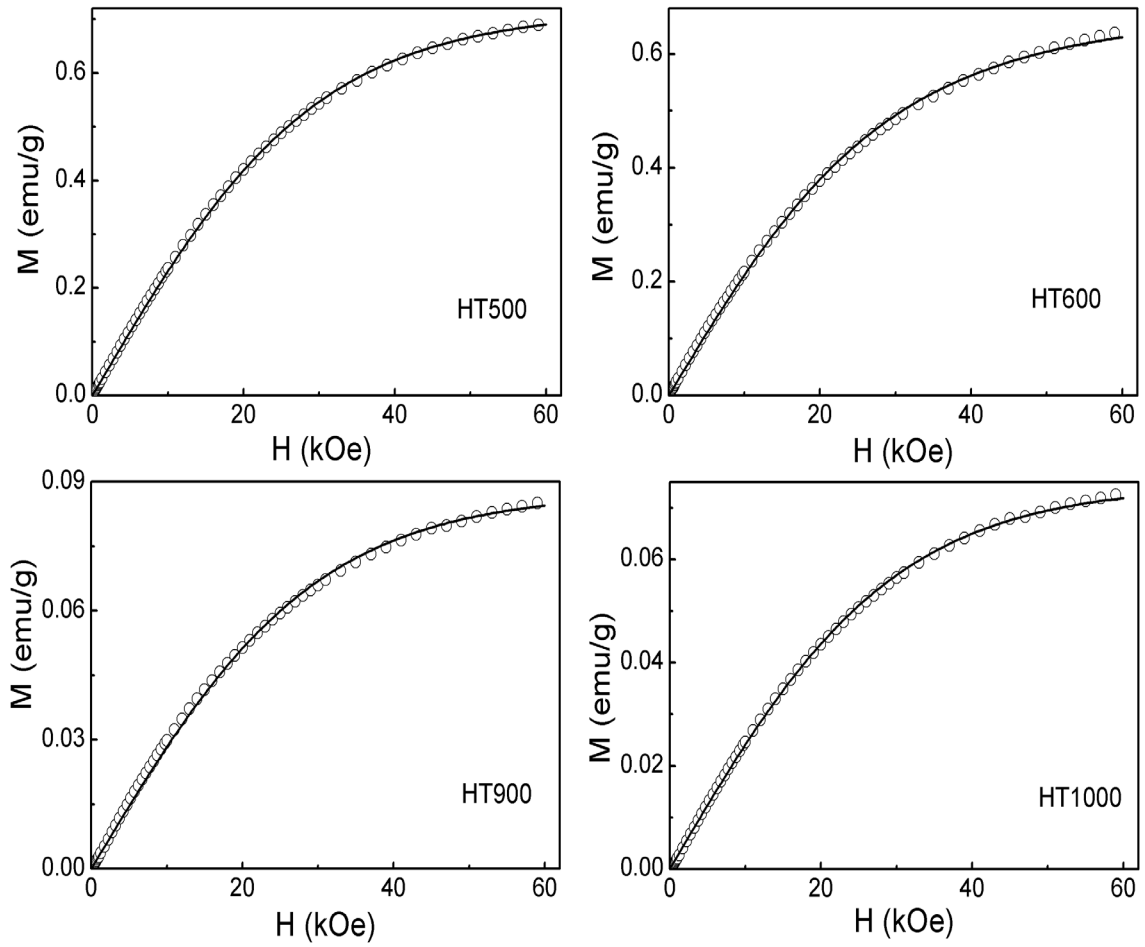

Figure 4.3: Fit of initial magnetization curves of HT500, HT600, HT900 and HT1000 using Brillouin function with J=1/2.

Similar non-saturating magnetization curves, even at very high magnetic fields, were previously reported for carbon systems like disordered carbon films [30,31], potassium and bromine adsorbed graphene sheets [32] and graphene nanoribbons [21]. However, the magnetization curves in the present case show significant coercivity (Figure 4.2), which indicates that the observed magnetism cannot be explained by localized electron spins and the samples are not simply paramagnetic. In a disordered carbon structure, different type of magnetic exchange interactions are possible between the edge-state spins of nanographitic domains, as discussed in Chapter 1 (Section 1.7). At the same time, a paramagnetic contribution can also originate from the free spins and isolated defects. Since the magnetization curves of the heat-treated samples, measured at 2 K, show significant coercivity along with a relatively good fit to the Brillouin function with J=1/2, it is likely that the paramagnetic contribution from the free spins is dominating over the ferromagnetic/feriimagnetic contributions from the nanographitic domains. More details which rule out the paramagnetic nature of the disordered carbon samples are discussed in Section 4.7.

Elemental (ICP) analysis of the heat-treated samples (Table 3.2, Chapter 3) showed the presence of various metal ion impurities, including Fe, Co and Ni. The concentrations of Fe, Co and Ni present in the heat-treated samples are shown in Table 4.1. To quantify the maximum possible contribution from impurities towards the measured mass magnetization, the contribution to the magnetization from the ferromagnetic elements Fe, Co and Ni was calculated using their concentration obtained from ICP-OES and standard mass magnetization values for bulk ferromagnetic Fe (221.9 emu/g), Co (162.5 emu/g) and Ni (57.50 emu/g) at 0 K [27]. For the heat-treated samples, Fe, Co, and Ni concentration varied from 66 ppm to 78 ppm, 19 ppm to 22 ppm, and 19 ppm to 28 ppm, respectively. The ICP analysis required large quantities of the samples and hence more than one coconut shell was used for the sample preparation, by heat-treatment at a particular temperature. Therefore, the variation in the concentration of metal impurities in different heat-treated samples might be due to the difference in the

Table 4.1: The measured magnetization values at 60 kOe (M_{6T}), the concentration of Fe, Co and Ni present in the heat-treated samples and the calculated maximum possible contribution of these metals towards magnetization (M_{Calc}).

Sample	M_{6T}	Co	Fe	Ni	M_{Calc}
	emu/g	ppm	ppm	ppm	emu/g
HT500	0.69	20	70	26	0.0173
HT600	0.64	19	73	22	0.0173
HT700	0.29	19	69	22	0.0167
HT800	0.14	23	79	19	0.0170
HT900	0.08	19	66	26	0.0164
HT1000	0.07	20	73	27	0.0178

mineral content of each shell used for sample preparation. However, even after considering the extreme case, where it is assumed that all of these elements are present in their elemental form and behave as bulk ferromagnetic metals at 0 K, their contribution towards magnetization is in the range 0.016–0.018 emu/g of carbon. Table 4.1 clearly shows that the measured magnetization at 60 kOe is comparatively much larger for samples heat-treated at the lower temperatures (HT500 to HT700) when compared to those heat-treated at the higher temperatures (HT800 to HT1000). Thus, for the higher HTT samples, even though the measured moment is still larger than the calculated value of ∼0.02 emu/g, the difference between the observed and the calculated values are much smaller when compared to that of the lower HTT samples.

4.4 Sample-to-sample variation and effect of heat-treatment atmosphere

Controlled heat-treatment of ordered molecular precursors can be used to produce high quality graphene [33]. However, the extent of graphitization in carbon-based

materials heat-treated at a particular temperature may depend on the precursor used. CS produced highly disordered carbon, as evidenced by the XRD and Raman spectral characteristics of the heat-treated samples, as discussed in Chapter 3. The XRD and Raman studies on the extent of structural order/disorder in CS heat-treated carbon prepared from different pieces of CS (Section 3.4) heat-treated under nitrogen (sample code: CN-1, CN-2 and CN-3) atmosphere, argon (sample code: CAr) atmosphere and helium (sample code: CHe) atmosphere showed that small variations in the coherence lengths can be expected, irrespective of the heat-treatment atmosphere, even though the HTT is kept constant. The Raman spectral parameters like *I(D)/I(G)* and G-peak position of CN-1, CN-2, CN-3, CAr and CHe were almost the same, however, the coherence lengths L_a and L_c showed some variations (Table 3.4, Chapter 3). The nearly same *I(D)/I(G)* ratios and G-peak positions for these samples suggested that the graphitic clustering effects are similar. To check for the sample-to-sample variation in the magnetic properties, if any, the room temperature and low-temperature magnetization of three different batches of CS-derived carbon obtained after heat-treatment at 500 °C and 800 °C in nitrogen atmosphere are compared. These heat-treatment temperatures were selected because the low-temperature magnetization of these samples are higher when compared to those heat-treated at 1000 °C. The 500 °C heat-treated samples, which showed the highest magnetization at 2 K are diamagnetic at room temperature, with the magnetic moment decreasing with increasing magnetic field (Figure 4.4). The magnetization curves of CN-1, CN-2 and CN-3 at 300 K are similar to that of the HT500 measured at the same temperature (Figure 4.1), with comparable magnetization at 60 kOe. However, the carbon samples heat-treated in argon, helium and argon-hydrogen (sample code: CArH) mixture (96.5% argon and 3.5% hydrogen) show some deviations in the diamagnetic susceptibility when compared to the carbon samples heat-treated in the nitrogen atmosphere.

The magnetization curves of the three different carbon samples, heat-treated at 500 and 800 °C, under nitrogen atmospheres, measured at 2 K, are shown in Figure 4.5. All the three samples show similar characteristics; S-type magnetiza-

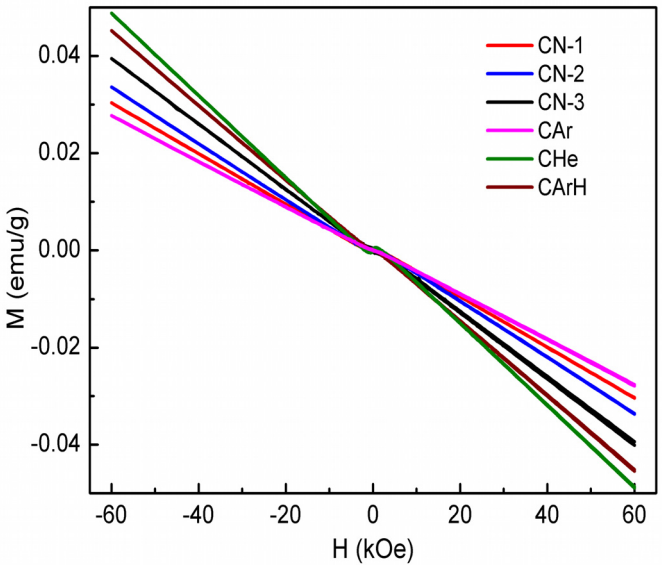

Figure 4.4: Magnetization curves (at 300 K) of carbon samples derived from CS after heat-treatment at 500 °C under nitrogen (CN-1, CN-2 and CN-3), argon (CAr), helium (CHe) and argon-hydrogen (CArH) mixture.

tion curves with similar saturation trend and comparable magnetic moments. The magnetization at 60 kOe for the three samples CN-1, CN-2 and CN-3, heat-treated at 500 °C is obtained as 0.62, 0.69 and 0.74 emu/g, respectively. The average value of the magnetization is 0.68 emu/g. Similar variation in the magnitude of magnetization is observed for the sample heat-treated at 800 °C also. For the three samples, the magnetization at 60 kOe is obtained as 0.16, 0.14 and 0.13 emu/g, respectively, and the average value of magnetization is 0.145 emu/g. Thus, it may be considered that the magnetization at 60 kOe may vary within ±10%. This sample-to-sample variation could be arising from the small differences expected in the amount of volatile matter and the different organic matters of each CS used for heat-treatment and the associated small changes in the microstructure, dangling bonds, edge state, etc.

Further, to identify the effect of the pyrolysing gas atmosphere, CS was heat-treated at 500 °C under nitrogen, argon, helium and argon-hydrogen mixture in a similar manner as described in Chapter 3. The magnetization curves measured at 2 K (Figure 4.6) for these samples also have similar shape and saturation trend with

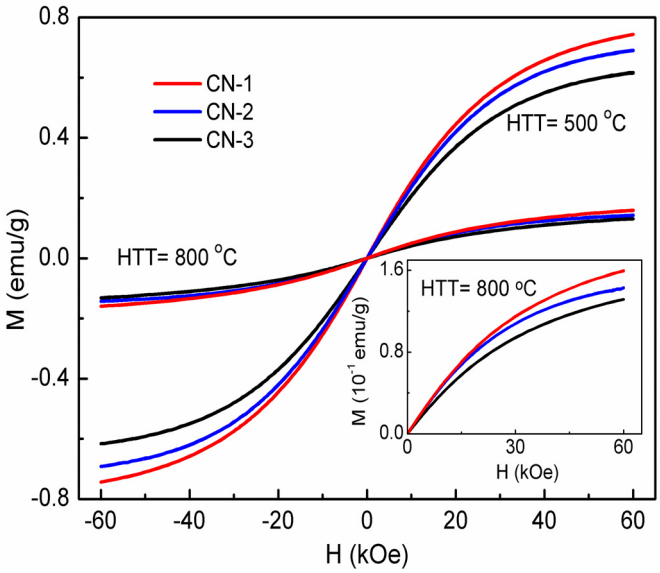

Figure 4.5: Magnetization curves (at 2 K) of carbon samples derived from three different batches (CN-1, CN-2 and CN-3) of CS after heat-treatment at 500 °C and 800 °C under nitrogen atmosphere. Inset shows the enlarged view of the initial magnetization curves of the samples heat-treated at 800 °C

their magnetization at 60 kOe falling in the expected range due to the sample-to-sample variations. However, the samples heat-treated under argon-hydrogen and helium atmospheres show much lower magnetization than the samples heat-treated under argon and nitrogen. This is likely to be due to the increase in the graphitization for the samples heat-treated at 500 °C under argon-hydrogen and helium atmospheres owing to the better thermal conductivity of hydrogen (187 mW/mK at 300 °C and 0.1 MPa) and helium (157 mW/mK at 300 °C and 0.1 MPa) when compared to that of argon (18 mW/mK at 300 °C and 0.1 MPa) and nitrogen (26 mW/mK at 300 °C and 0.1 MPa) [34]. The gases with higher thermal conductivity can induce better graphitization in the carbon samples by uniform and fast heating. More importantly, the sample heat-treated under argon-hydrogen atmosphere is diamagnetic at room temperature and shows a magnetization curve similar to that of the samples heat-treated under other gases, at 2 K. Considering that the relatively lower magnetization of CHe is likely to be due to the better graphitization, the extent of variation in the magnetization of CN-1, CAr and CArH, for

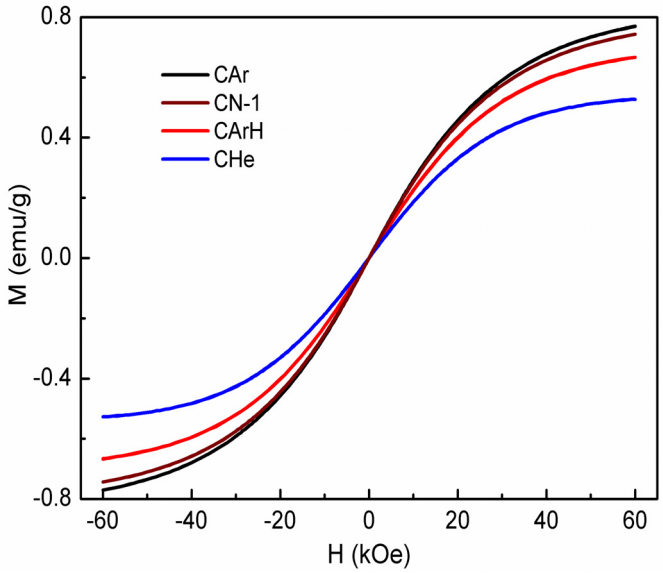

Figure 4.6: Magnetization curves (at 2 K) of samples heat-treated at 500 °C under argon (CAr), nitrogen (CN-1), argon-hydrogen mixture (CArH) and helium (CHe) gas atmospheres.

which the graphitization is similar, is calculated. For CN-1, CAr and CArH, the magnetization, at 60 kOe, is obtained as 0.74, 0.77 and 0.67 emu/g, respectively and the average value of magnetization is 0.723 emu/g. Thus, the magnetization at 60 kOe may be considered to be varying by ±7%, which is nearly in the same range as that of sample-to-sample variation. This indicates that the inorganic minerals present in CS are not getting reduced to any of the ferromagnetic metal (Fe, Co and Ni) during heat-treatment under the reducing argon-hydrogen atmosphere. Since the magnetic characteristics are comparable for samples prepared from different pieces of CS (sample-to-sample variation) and only similar variation is observed for samples heat-treated under different gas atmospheres, further studies on the effect of graphitization on the temperature variation of magnetization are limited to the samples heat-treated from 500 to 1000 °C under nitrogen atmosphere.

The diamagnetic response of the heat-treated samples, at room temperature (Figure 4.4), points towards the intrinsic origin of their magnetic properties. The highest impurity contribution towards magnetic moments of the heat-treated car-

bon generally comes from ferromagnetic metals due to their high mass magnetization values when compared to other magnetic compounds like metal oxides or carbides [27]. Among the different heat-treatment atmospheres used in this study, the mixture of argon and hydrogen can reduce the different metal salts present in carbon to the respective metals. In such a case, heat-treatment under argon-hydrogen mixture should produce disordered carbon with a substantially high magnetic moment, if magnetic metal impurities are present. However, in the present case, similar magnetization values are observed for CS heat-treated under the reducing argon-hydrogen atmosphere and those heat-treated under nitrogen, argon and helium. This shows that considerable amounts of magnetic metal salts or metals are not present in CS which can mask the magnetic properties of the heat-treated carbon by their contribution to the magnetization.

4.5 Magnetic measurements on acid-treated samples

In order to rule out the contribution of magnetic metal impurities as the origin of ferromagnetism in the heat-treated samples, the samples are treated with conc. HCl (detailed procedure is given in Chapter 3). After acid-treatment, the concentrations of Fe, Co and Ni are found to be too low (< 1 ppm), which indicates that the metal impurities are leached out of the samples as soluble chlorides during the acid-treatment. The magnetization of the acid-treated samples when measured as a function of applied magnetic field (Figure 4.7) also showed similar curves as that of the original heat-treated samples. However, the magnetization at 60 kOe is found to be relatively lower than that of the corresponding heat-treated samples and the magnetic hysteresis remained even after the acid-treatment. Thus, the contribution of impurity towards magnetization is calculated using (Table 4.1), assuming that the impurity is in the form of bulk ferromagnetic metals. The calculated values are 3% and 28% of the measured values for HT500 and HT1000, respectively, even though nearly the same amounts of ferromagnetic impurities are

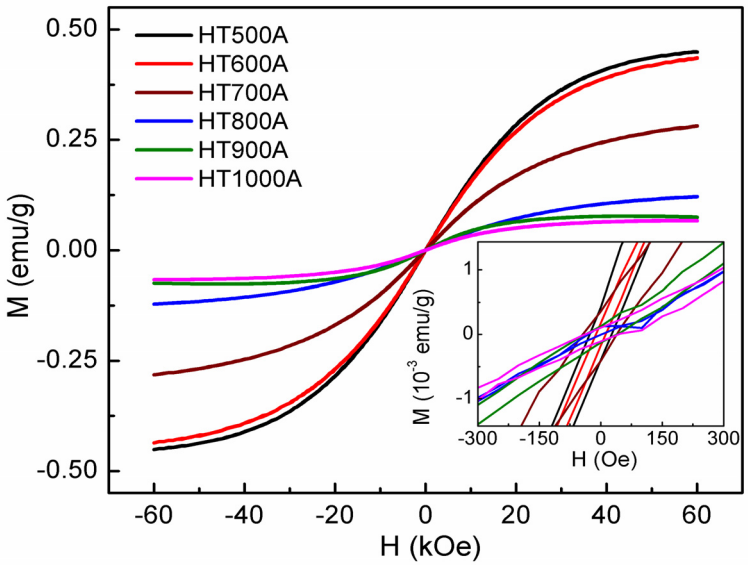

Figure 4.7: Magnetization curves of acid-treated samples measured at 2 K. Inset: Enlarged curves showing magnetic hysteresis.

present in both samples. Thus, it is possible that the observed ferromagnetism in the heat-treated samples is due to the intrinsic contribution from edge states and dangling bonds and the reduced magnetization after acid-treatment is due to the changes in the local structure.

It has been reported that in the case of thermally induced graphitization, the effect of HTT on amorphous carbon samples is to develop thermodynamically more stable nanocrystalline graphitic structure through the heat-treatment induced migration of the sp^3 defects which tend to extend the π-conjugated areas at the expense of strain energy [35,36]. This relaxation to a graphitic structure with increase in HTT causes the reduction of edge states and dangling bonds in the system which are otherwise contributing to the magnetic behavior of disordered carbons [37,38]. Thus, for the higher HTT samples, since the edge states contributing to magnetism being considerably reduced and the samples being more graphitic, there is a large reduction in the magnetization. The mass magnetization corresponding to the amount of ferromagnetic impurities is also found to be too low ($\sim$0.002 emu/g) to account for the observed magnetization values at 60 kOe. Therefore, the magnetic impurities cannot be responsible for the magnetic

properties of these samples.

The magnetization curves with Brillouin type saturating trend observed for both the heat-treated and the acid-treated samples indicate that they are more related to a superparamagnetic-like disordered magnetic behavior, similar to that observed previously in graphene nanoribbons [21]. The coercivity of the heat-treated and acid-treated samples might be arising from the spin blockade in random direction due to local magnetic anisotropy. In a carbon-based system, the structural defects, small inhomogeneities in the graphitic cluster, orientation disorder, different edge terminating groups, etc. can contribute towards the local magnetic anisotropy [39].

4.6 Role of microstructure

The variation of the magnetization at 60 kOe for the different heat-treated samples, as a function of HTT, is shown in Figure 4.8. Here, the magnetization at the highest field of measurement (60 kOe) decreases with increasing HTT, following a specific trend. Initially, there is a small decrease in the magnetization when HTT is increased from 500 to 600 °C. As HTT is increased to 700 °C and further to 800 °C, the magnetization decreases sharply. However, with the elevation of HTT above 800 °C, the magnetization does not vary much and shows a saturating trend. This peculiar nature of decrease in the low-temperature magnetization can be directly correlated with the changes in coherence lengths, L_a and L_c, as discussed in Chapter 3 (Figure 3.6) and the variation in the intensity ratios of the D and G Raman bands, *I(D)/I(G)* (Figure 3.10, Chapter 3), with HTT. This indicates that the variation in the magnetization at 60 kOe follows the changes in the carbon microstructure on heat-treatment. The decreasing magnetization with increasing HTT for the present coconut shell based disordered carbon is similar to the previous report on nanographite based carbon materials, where the results are explained in terms of disordered magnetism caused by random strengths of inter-nano-graphite antiferromagnetic interactions mediated by π-conduction carriers [15].

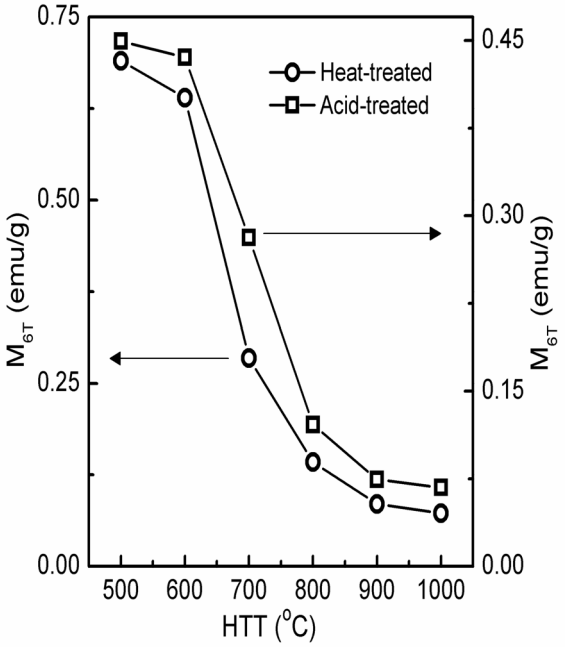

Figure 4.8: Magnetization measured at 60 kOe (M_{6T}) of heat-treated and acid-treated samples as a function of HTT. Solid lines are guides to the eyes.

The samples heat-treated at 500 °C, 600 °C and 700 °C showed gradual ordering of amorphous carbon with a small increase in the coherence length, as discussed in Chapter 3 (Section 3.3.5). In this region, samples being more disordered, and to induce a small increase in L_a requires removal of defects in large numbers which can lead to a large decrease in the magnetization. As HTT increases to 700 °C, *I(D)/I(G)* ratio increases beyond unity (Figure 3.10, Chapter 3) showing the ordering of amorphous carbon to nanocrystalline graphite. Heat-treatment beyond 800 °C induces much more rapid increase in L_a giving a clear indication that there is a fast relaxation to nanocrystalline graphite in this region, where a diamagnetic contribution from aromatic carbon clusters also starts to develop due to which both the absolute value and the variation in the magnetization are much less for samples heat-treated above 800 °C.

Magnetization measurements on the acid-treated samples at 2 K (Figure 4.7) indicated that the magnetization curves have similar shape and saturation trends as that of the heat-treated samples. The magnetization of all the acid-treated sam-

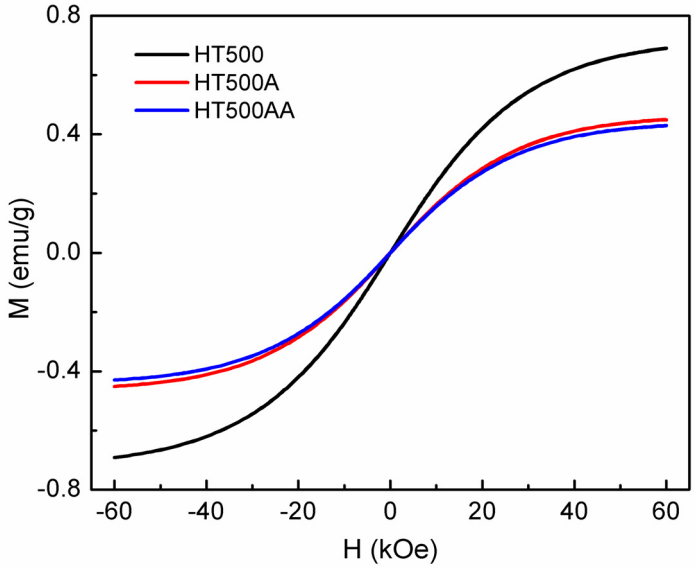

Figure 4.9: Magnetization of HT500 before and after two consecutive acid-treatments.

ples are lower than that of the corresponding heat-treated samples (Figure 4.2). However, the variation in the magnetization at 60 kOe from HT500A to HT1000A are similar to that observed for heat-treated samples, as a function of HTT (Figure 4.8). Similar to the heat-treated samples, the acid-treated samples also show a small coercivity.

As mentioned, the magnetization of all the samples decreased after treating with the acid. As shown in Figure 4.9, after the first acid-treatment, magnetization of HT500 is decreased by 0.24 emu/g. However, the second acid-treatment on HT500A reduced the magnetization only by 0.02 emu/g. This indicates that impurity phases are not contributing to the magnetization after the first acid-treatment, if it is assumed that the difference in the magnetization after the first acid-treatment is contributed by ferromagnetic impurities. However, assuming that the impurities are present in the ferromagnetic state, the maximum possible contribution to magnetization from the ferromagnetic impurities which was leached out from the respective samples is only 0.02 emu/g. Since HT500 is having the highest degree of disorder, the large decrease in the magnetization after first acid-treatment can be due to the suppression of magnetic contribution from magnetic π-edge states due to the chemical modification and stabilization of the

dangling bonds by hydrogen or chlorine atom. This decreases the localized spin concentration, similar to the effect of fluorination on activated carbon fibres as reported by Kiguchi *et al.* [8]. As discussed in Chapter 3, the graphitization at higher HTT is brought about by the thermally assisted growth and coalescence of individual clusters [35]. During this growth process, therefore, the number of edge states corresponding to the graphic zig-zag edges and dangling bonds in the amorphous background gets reduced. Hence, the acid-treatment of higher HTT samples cannot be effective in bringing down the magnetic moment by chemical modification of edge states and dangling bonds, when compared to that of lower HTT samples. Thus, acid-treatment of lower HTT samples decreases the magnetization to a larger extent while for higher HTT samples, the acid-treatment cannot decrease the magnetization in a similar manner, thereby causing this large difference.

4.7 Temperature variation of magnetization

Temperature variation of magnetization of all the samples (heat-treated and acid-treated samples) were measured in the temperature range 2–300 K in a magnetic field of 10 kOe (1 T) to gain more insight in to the magnetic nature of the samples. The zero field cooled (ZFC) and field cooled (FC) magnetization curves, measured in an applied field of 10 kOe, showed different behavior for the heat-treated and acid-treated samples, as shown in Figure 4.10. The ZFC and FC magnetization curves of the heat-treated samples HT500 and HT1000 as well as the acid-treated samples HT500A and HT1000A (samples with the highest and lowest magnetization at 2 K, Figure 4.2 and Figure 4.7) are shown in Figure 4.10. Insets in the figures show the enlarged portions in the temperature range 75 to 225 K to show the difference between the FC and ZFC magnetization curves very clearly. For all the heat-treated samples, an increase in the magnetization is observed below 200 K with a broad hump around 150 K, indicating a magnetic-like transition, which is more pronounced in the FC curve than in the ZFC curve as shown in the insets of Figure 4.10.

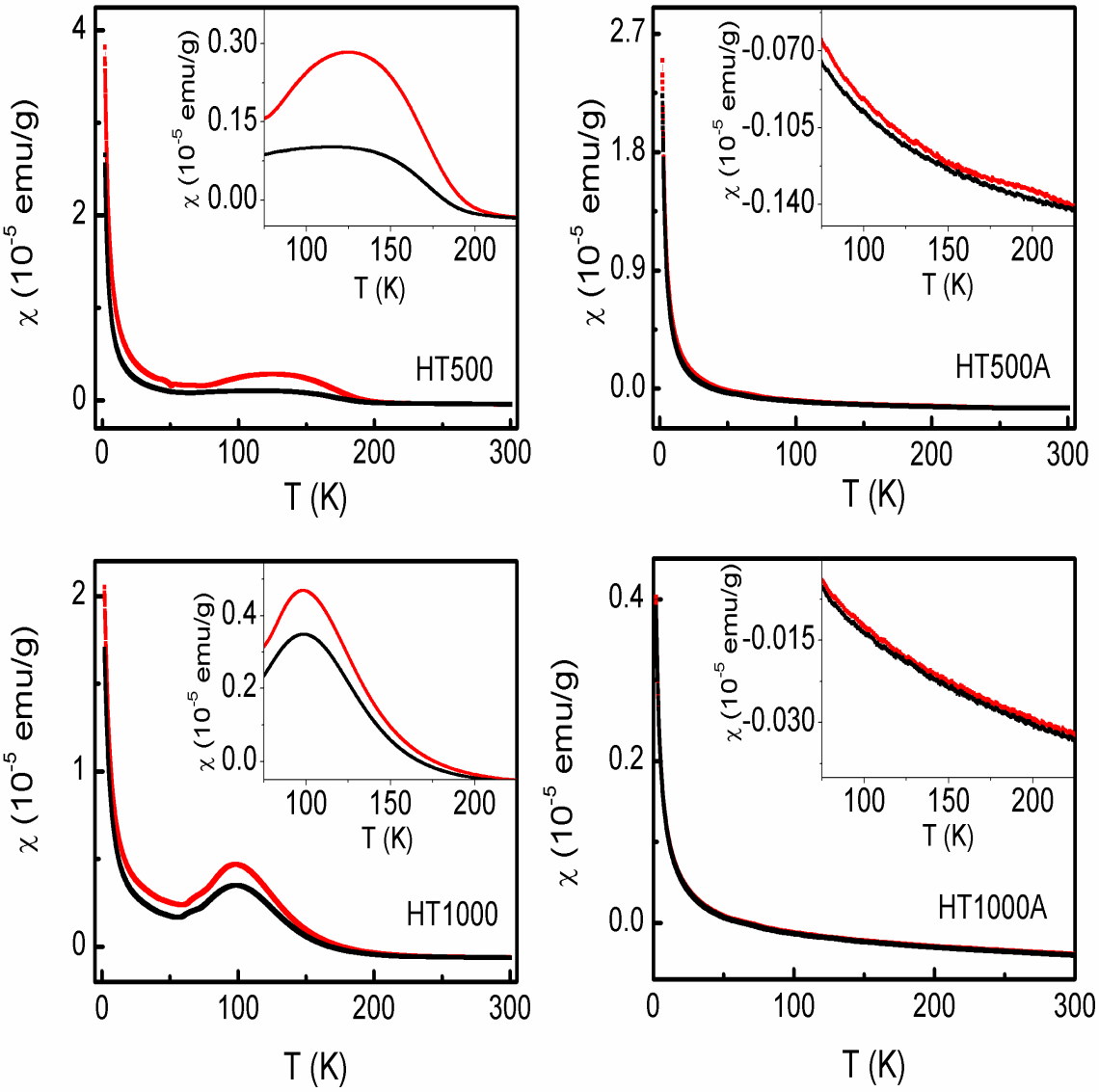

Figure 4.10: ZFC (black) and FC (red) curves for HT500, HT500A, HT1000 and HT1000A. Insets show the zoomed curves in the temperature region where a hump is observed in the magnetization curves.

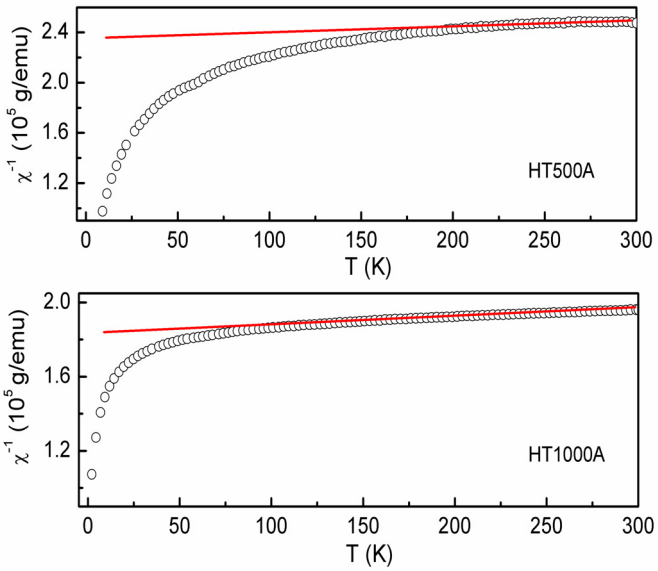

Figure 4.11: The inverse susceptibility versus temperature plots of HT500A and HT1000A, showing deviation from Curie behavior.

Figure 4.11 shows the χ^{-1} versus T plots of the ZFC curves of HT500A and HT1000A, for which the ZFC magnetization increased continuingly with a decrease in the temperature. For a paramagnet, the plot of χ^{-1} versus temperature should be a straight line [27]. However, for the acid-treated samples, HT500A and HT1000A, the magnetization does not fall on a straight line when χ^{-1} is plotted as a function of temperature. Thus, the Curie-Weiss behavior (Equation 1.15) further confirms that the carbon samples are not simply paramagnetic even though the magnetization curves, measured at 2 K, fits relatively well to the Brillouin function with J=1/2 (Figure 4.3).

The magnetic transition observed in acid-treated samples can originate due to the complex magnetic interactions which compete among themselves forming a spin-glass state or low dimensionality of the magnetic system, as reported for different carbon-based systems [15,21,29,40,41]. However, after the acid-treatment process, for all the samples, the broad transition and the humps are disappeared completely. The spin-glass-like disordered state can originate from the competing ferromagnetic and antiferromagnetic interactions or due to the complex dipolar interactions in a concentrated assembly of magnetic nanoparticles [42]. In a

spin-glass-like system, the FC magnetization (FCM) curve diverges from the ZFC magnetization (ZFCM) curve below a certain temperature, when measured as a function of temperature [15,21,42].

To rule out any impurity effect and to confirm the intrinsic origin of a spin glass like disordered magnetic state in the heat-treated carbon samples, the acid-treated sample HT500A, for which the hump is disappeared after acid treatment, was subjected to a further heat-treatment at 500 °C followed by another acid-treatment, and again another heat-treatment. Thus, the heat and acid treatments were repeated in multiple cycles. FCM and ZFCM curves of the different heat and acid treated samples are shown in Figure 4.12. HT500A (Figure 4.12b) heat-treated again at 500 °C (Figure 4.12c) under identical conditions as in the case of HT500 shows identical features in the magnetization curves as that of HT500 (Figure 4.12a). The nature of the FCM and ZFCM curves are similar to that of HT500 (Figure 4.12a), showing the magnetic transition below 200 K and the broad hump between 100 and 200 K (Figure 4.12c). The magnetic transition and the hump disappear on further acid-treatment (Figure 4.12d), and again reappear on heat-treatment at 500 °C (Figure 4.12e). As the contribution from magnetic impurities is found to be negligible in the samples after the first acid-treatment itself (Table 3.2, Chapter 3), it is clear that the magnetic transition-like feature and the broad hump are due to the magnetic contribution from carbon and not from any other impurities. Figure 4.13 shows the magnetization curves of the corresponding acid and heat-treated HT500 samples, measured at 2 K. It is observed that the magnitude of magnetization at low temperatures is reduced after the acid-treatment and then increased again after the heat-treatment and the trend is repeated for further acid and heat-treatments. As evident from the inset of Figure 4.13, the coercivity continuously increases after each treatment. The highest coercivity of 280 Oe is obtained for the final sample after two subsequent acid-treatments and each followed by further heat-treatment. This suggests that the microstructural changes produced during consecutive acid/heat-treatment, including the edge reconstruction, inhomogeneous distribution of graphitic cluster size

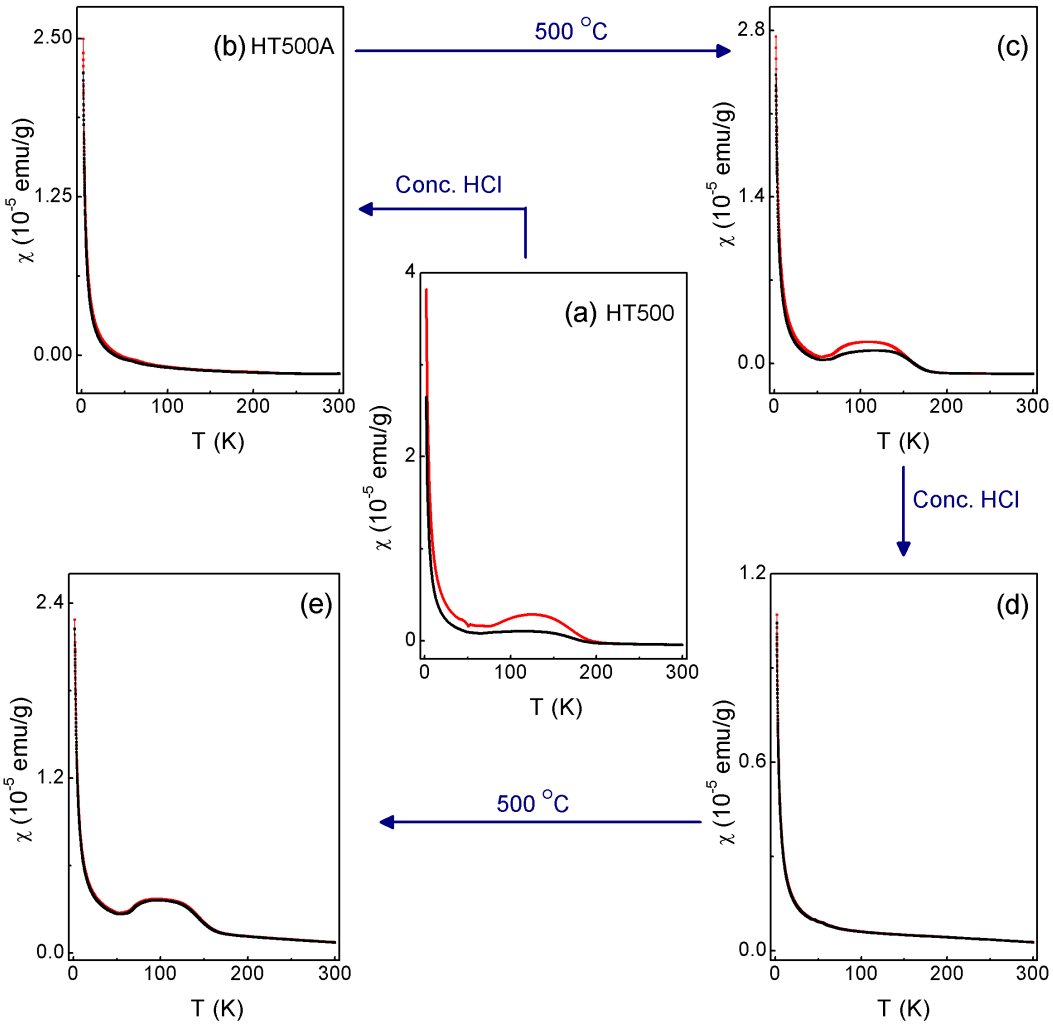

Figure 4.12: ZFC (black) and FC (red) curves of (a) HT500 and (b) HT500A. The changes in the ZFC and FC curves of (c) HT500A after reheating at 500 °C under identical conditions as in the case of HT500, (d) reheated sample after a second acid-treatment and (e) after reheating the second acid-treated sample at 500 °C under identical conditions as for previous samples.

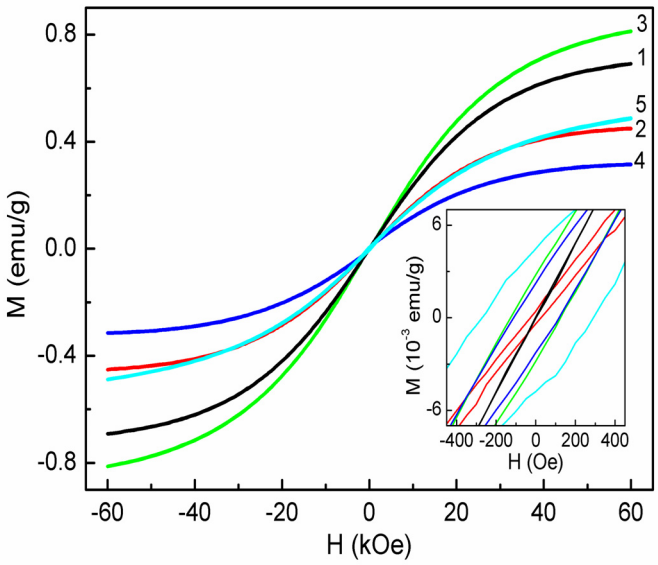

Figure 4.13: Magnetization curves of HT500 after repeated heat and acid-treatments, measured at 2K. (1) HT500, (2) HT500A, (3) HT500A heat-treated at 500 °C, (4) sample 3 acid-treated, and (5) sample 4 heat-treated at 500 °C. Inset: enlarged curves showing magnetic hysteresis.

and changes in the distribution of different functional groups could be responsible for the continuous increase in the coercivity [39].

The results show that the magnetic characteristics are highly reproducible after heat/acid-treatment under identical conditions. As the contribution from magnetic impurities is found to be negligible in the samples after the first acid-treatment itself, it is clear that the magnetic transition and the hump are due to the magnetic contribution from carbon and not from any other impurities. The contrast in the ZFC-FC magnetization behavior among the heat-treated and the acid-treated carbon samples is quite similar to the observations made on graphene nanoribbons (GNRs) and chemically converted graphene nanoribbons (CCGNRs) [21]. GNRs showed field cooling effect which was absent in CCGNRs which was ascribed to the edge reconstruction involved during the chemical treatment. Our experiments clearly prove that spin-glass type disordered magnetism exists even in carbon structures with low crystallinity. Also, the results show the critical dependency of edge states towards magnetic interactions in disordered carbon.

These observations also support the assumptions made related to the changes in the nature of the magnetization curves upon acid-treatments on heat-treated samples.

4.8 Conclusions

Magnetic measurements on disordered carbon samples heat-treated from 500 to 1000 °C showed diamagnetic behavior at RT whereas a ferromagnetic-like magnetization curves are observed at 2 K with significant coercivity. At 2 K, The magnetization at 60 kOe decreased with increasing heat-treatment temperature. The calculated maximum possible magnetic contribution from the ferromagnetic metal impurities showed that the concentrations of metal from impurities are too low to account for the observed magnetization. The heat-treated samples, on further acid-treatment, also showed similar magnetization curves at 2 K, with a small decrease in the magnetization. The decrease in the magnetization after acid-treatment and the maximum possible magnetic contribution from the impurities extracted during the acid-treatment process are not comparable. A detailed analysis showed that the extent of decrease in the magnetization after acid-treatment is different for higher HTT and lower HTT samples, even though the same amount of metal impurities are present in all the samples, which also pointed towards the intrinsic origin of magnetic properties in the heat-treated samples. Further, the variation of magnetization with HTT is found to be perfectly correlating with the changes in the carbon structure. The Raman *I(D)/I(G)* ratio and the G-peak position as well as the coherence lengths calculated from XRD data showed a structural transition from disordered carbon to nanocrystalline graphite when HTT increases above 800 °C. Therefore, the decrease in the magnetization with an increase in HTT can be ascribed to the reduction of edge states and dangling bonds along with the development of graphitic clusters with a diamagnetic response.

The magnetic measurement of three different batches of CS heat-treated at similar conditions showed that the magnetic properties of these samples are not exactly same, as expected, due to the small variations in the composition and

texture of CS. Considering this sample-to-sample variation (±10%), the magnetization of samples prepared by changing the heat-treatment atmosphere is also varying in the same range (±7%) and therefore can be neglected. Moreover, the sample heat-treated under reducing conditions (in argon-hydrogen atmosphere) did not produce any considerable changes in the magnetization, confirming that ferromagnetic metals are not formed during the heat-treatment. The FC and ZFC magnetic measurements of heat-treated samples showed a broad hump below 150 K, which vanished after the acid-treatment, due to the chemical modification of edge states and dangling bonds on acid-treatment. Proof for this is obtained from studies on repeated heat/acid-treatment of the initially acid-treated sample. Thus, the present study shows that a disordered magnetic state with random strengths, previously observed in nanographite and graphene nanoribbons, also exists in amorphous carbon with different extent of graphitization. This observation in amorphous carbon can trigger further work to understand the magnetism in detail due to the large possibilities in preparing magnetic amorphous carbon with different microstructures.

Bibliography

[1] T. L. Makarova, *Semiconductors* 38 (2004) 615.

[2] H. M. McConnell, *J. Chem. Phys.* 39 (1963) 1910.

[3] Y. Nakazawa, M. Tamura, N. Shirakawa, D. Shiomi, M. Takahashi, M. Kinoshita and M. Ishikawa, *Phys. Rev. B* 46 (1992) 8906.

[4] T. Enoki and K. Takai,*Solid State Commun.* 149 (2009) 1144.

[5] K. Takahara, S. Hao, H. Tanaka, T. Kadono, M. Hara, K. Takai and T. Enoki *Phys. Rev. B* 82 (2010) 121417.

[6] K. Takai, T. Suzuki and T. Enoki, *Phys. Rev. B* 81 (2010) 205420.

[7] D. W. Boukhvalov, S. Moehlecke, R. R. da Silva and Y. Kopelevich, *Phys. Rev. B* 83 (2011) 233408.

[8] M. Kiguchi, K. Takai, V. L. J. Joly, T. Enoki, R. Sumii and K. Amemiya, *Phys. Rev. B.* 84 (2011) 045421.

[9] O. V. Yazyev and L. Helm, *Phys. Rev. B* 75 (2007) 125408.

[10] J. O. Sofo, G. Usaj, P. S. Cornaglia, A. M. Suarez, A. D. H. Nieves and C. A. Balseiro, *Phys. Rev. B* 85 (2012) 115405.

[11] P. Esquinazi, D. Spemann, R. Hohne, A. Setzer, K. H. Han and T. Butz, *Phys. Rev. Lett.* 91 (2003) 227201.

[12] Y. Wang, P. Pochet, C. A. Jenkins, E. Arenholz, G. Bukalis, S. Gemming, M. Helm and S. Zhou, *Phys. Rev. B* 90 (2014) 214435.

[13] S. Talapatra, P. G. Ganesan, T. Kim, R. Vajtai, M. Huang, M. Shima, G. Ramanath, D. Srivastava, S. C. Deevi and P. M. Ajayan, *Phys. Rev. Lett.* 95 (2005) 097201.

[14] X. Miao, S. Tongay and A. F. Hebard, *Carbon* 50 (2012) 1614.

[15] Y. Shibayama, H. Sato and T. Enoki, *Phys. Rev. Lett.* 84 (2000) 1744.

[16] Y. Wang, Y. Huang, Y. Song, X. Zhang, Y. Ma, J. Liang and Y. Chen, *Nano Lett.* 9 (2009) 221.

[17] S. Qin, X. Guo, Y. Cao, Z. Ni and Q. Xu, *Carbon* 78 (2014) 559.

[18] D. Lee, J. Seo, X. Zhu, J. M. Cole and H. Su, *Appl. Phys. Lett.* 106 (2015) 172402.

[19] G. Khurana, N. Kumar, R. K. Kotnala, T. Nautiyal and K. S. Katiyar, *Nanoscale* 5 (2013) 3346.

[20] T. Tang, F. Liu, Y. Liu, X. Li, Q. Xu, Q. Feng, N. Tang and Y. Du, *Appl. Phys. Lett.* 104 (2014) 123104.

[21] S. S. Rao, S. N. Jammalamadaka, A. Stesmans, V. V. Moshchalkov, J. V. Tol, D. V. Kosynkin, A. H. Duque and J. M. Tour, *Nano Lett.* 12 (2012) 1210.

[22] A. K. Swain, D. Li and D. Bahadur, *Carbon* 57 (2013) 346.

[23] A. V. Rode, E. G. Gamaly, A. G. Christy, J. G. F. Gerald, S. T. Hyde, R. G. Elliman1 B. L. Davies, A. I. Veinger, J. Androulakis and J. Giapintzakis, *Phys. Rev. B.* 70 (2004) 054407.

[24] J. M. D. Coey, M. Venkatesan, C. B. Fitzgerald, A. P. Douvalis and I. S. Sanders, *Nature* 420 (2002) 156.

[25] S. Ma, J. H. Xia, V.V. S. S. Srikanth, A. X. Sun, T. Staedler, X. Jiang, A. F. Yang and Z. D. Zhang, *Appl. Phys. lett.* 95 (2009) 263105.

[26] K. H. Han, D. Spemann, P. Esquinazi, R. Hhne, V. Riede and T. Butz, *Adv. Mater.* 15 (2003) 1719.

[27] B. D. Cullity and C. D. Graham, *Introduction to Magnetic Materials* (John Wiley & Sons, 2011).

[28] R. R. Nair, M. Sepioni, I-Ling Tsai, O. Lehtinen, J. Keinonen, A. V. Krasheninnikov, T. Thomson, A. K. Geim and I. V. Grigorieva, *Nat. Phys.* 8 (2012) 199.

[29] J. Cernak, G. Helgesen, A. T. Skjeltorp, J. Kovac, J. Voltr and E. Cizmar, *Phys. Rev. B* 87 (2013) 014434.

[30] R. Hohne, K. H. Han, P. Esquinazi, A. Setzer, H. Semmelhack, D. Spemann and T. Butz, *J. Magn. Magn. Mater.* 272 (2004) E839.

[31] K. Takai, M. Oga, T. Enoki and A. Taomoto, *Diamond Relat. Mater.* 13 (2004) 1469.

[32] K. Takai, T. Suzuki, T. Enoki, H. Nishihara and T. Kyotani, *Phys. Rev. B* 81 (2010) 205420.

[33] A. Golzhauser, *Angew. Chem., Int. Ed.* 51 (2012) 10936.

[34] N. B. Vargaftik, *Handbook of Thermal Conductivity of Liquids and Gases* (CRC Press, 1993).

[35] F. G. Emmerich, *Carbon* 33 (1995) 1709.

[36] K. Takai, M. Oga, H. Sato, T. Enoki, Y. Ohki, A. Taomoto, K. Suenaga and S. Iijima, *Phys. Rev. B* 67 (2003) 214202.

[37] V. L. J. Joly, M. Kiguchi, S. J. Hao, K. Takai, T. Enoki, R. Sumii, K. Amemiya, H. Muramatsu, T. Hayashi, Y. A. Kim, M. Endo, J. C. Delgado, F. L. Urias, A. B. Mendez, H. Terrones, M. Terrones and M. S. Dresselhaus, *Phys. Rev. B* 81 (2010) 245428.

[38] K. Takai, M. Oga, T. Enoki and A. T. Aomoto, *Diamond Relat. Mater.* 13 (2004) 1469.

[39] K. Bagani, A. Bhattacharya, J. Kaur, A. Rai Chowdhury, B. Ghosh, M. Sardar and S. Banerjee, *J. Appl. Phys.* 115 (2014) 023902.

[40] A. W. Mombru, H. Pardo, R. Faccio, O. F. de Lima, E. R. Leite, G. Zanelatto, A. J. C. Lanfredi, C. A. Cardoso and F. M. A. Moreira, *Phys. Rev. B* 71 (2005) 100404.

[41] D. Areon, Z. Jaglieie, A. Zorko, A. V. Rode, A. G. Christy, N. R. Madsen, E. G. Gamaly and B. L. Davies, *Phys. Rev. B* 74 (2006) 014438.

[42] K. Binder, A. P. Young, *Rev. Mod. Phys.* 58 (1986) 801.

Chapter 5

Electrical properties of disordered carbon

5.1 Introduction

As described in Chapter 3, the investigations based on XRD and Raman spectroscopy have shown that the extent of disorder in the heat-treated carbon, obtained after the pyrolysis of CS at different HTT, changes continuously from that of disordered carbon to nanocrystalline graphite. Such pre-graphitic systems with varying crystallinity contain chains, rings and clusters of benzenoid networks embedded in an sp^3 matrix [1]. These structures are reported to exhibit different electronic properties due to the contribution of these networks towards the energy band structure [2,3]. As already mentioned in Chapter 1 (Section 1.6), the sp^3 sites in the sp^2/sp^3 mixed clusters mainly govern the generation of a large band gap, almost in the same range as that of diamond (∼4-6 eV). Theoretical calculations showed that the pairs, even-membered rings and chains of sp^2-carbon atoms form π-states with a smaller gap (∼2 eV), whereas the isolated sp^2 sites and odd-membered rings of sp^2 carbon atoms form localized states in the gap [1,4,5]. A pre-graphitic disordered carbon containing all these contributions thus have a finite density of states around the Fermi level, depending on the extent of graphitization [1,4]. Therefore, disordered carbon systems show large deviations in the electronic transport properties when compared to that of the ordered allotropes [2,3,6].

In a crystalline material, the electrons are delocalized in an extended energy band structure [7]. Structural disorder in such an ordered material results in the smearing out of the band edge towards the gap to form localized tail states, where the extended states are separated from the localized states by the mobility edge. For systems with large disorder, the Fermi level falls in the localized regime, making the samples insulating, and with a decrease in the disorder, the mobility edge approaches the Fermi level. Further structural ordering pushes the mobility edge above the Fermi level, which then falls in the extended region of the energy band, and such materials show metallic properties [7–9]. In a variety of insulating and highly disordered carbon systems, the experimental results indicated that electronic transport near room temperature is controlled by hopping conduction

between the π and π^* levels [10]. However, there is a lack of agreement about the specific nature of the hopping conduction in different carbon systems studied [2,3,11–13].

Several transport models have been suggested for explaining the temperature dependence of resistivity such as the thermally activated hopping conduction (Equation 5.1) [11], Mott variable range hopping (Equation 5.2 and Equation 5.3 with β=1/3 or 1/2) [2,7,8], coulomb-gap variable range hopping (Equation 5.3, β=1/2) [12] and multiphonon tunneling (Equation 5.4) [13], as discussed in Chapter 1 (Section 1.7). The equations describing these conduction mechanisms are

$$\rho(T) = \rho_0 \; exp\left(\frac{E_{hop}}{k_B T}\right) \tag{5.1}$$

$$\rho(T) = \rho_0 \; exp\left(\frac{T_0}{T}\right)^{1/4} \tag{5.2}$$

$$\rho(T) = \rho_0 \; exp\left(\frac{T_0}{T}\right)^{\beta} \tag{5.3}$$

$$\sigma(T) = \sigma_0 \; (T/T_0)^n \tag{5.4}$$

Where $\rho(T)$ and $\sigma(T)$ are the resistivity and conductivity, respectively, at temperature T. E_{hop} is the activation energy for hopping conduction, k_B is the Boltzmann constant, ρ_0 and σ_0 are the pre-exponential factors, T_0 is the characteristic Mott temperature. β in Equation 5.3 indicates the dimensionality of the conduction process, and is given by $\beta = \frac{1}{d+1}$, for d dimensional conduction. The parameters emph$sigma_0$, A and n in Equation 5.4 are constants for a particular system [13].

Less disordered carbon systems have much lower room temperature resistivity when compared to the systems with large disorder, with a weak temperature dependence of resistivity [2]. In such materials, the weak temperature dependence

of resistivity is explained based on the columbic interactions in the presence of disorder and two dimensional weak localization (2D WL) [14,15].

Another effect which modifies the conduction mechanism is the Kondo-type scattering of the conduction electrons by magnetic impurities when present in a conducting non-magnetic lattice [16]. The magnetic impurities in a non-magnetic lattice flips the complementary electron spins to a different extent, thereby scattering the two complementary electron waves asymmetrically. This effect, in turn, destroy their phase coherence and results in a destructive interference leading to a small increase in resistivity at low temperatures [16]. Kondo effect has been experimentally verified in many different systems such as graphene with Co adatoms [17], defective graphene [18], $Yb_3Os_4Ge_{13}$ [19] and $UCo_{0.5}Sb_2$ [20]. The defect induced magnetic moments in He^+ irradiated graphene have been shown to couple strongly to conduction electrons in graphene, resulting in the Kondo effect [18].

The modification of the hopping conduction with HTT in the insulating regime of the insulator-metal (I-M) transition has been studied in disordered carbon films and amorphous carbon fibers [2,3]. However, the changes in the conduction mechanism with graphitization towards the metallic side of the I-M transition are not addressed so far. The heat-treated disordered carbon samples, described in Chapter 3, can be an ideal system for studying the changes in the conduction mechanism with the extent of graphitization. The crossover from stage-2 to stage-1, with HTT, confirmed the ordering of disordered carbon structure to nanocrystalline graphite. In this regime, since the extent of graphitization is much higher, the conduction mechanism can get modified due to the carrier interactions in the presence of weak disorder or due to the weak magnetic moment induced by the edge state spins of isolated graphitic clusters. The present Chapter focuses on the changes in the conduction mechanism with graphitization in the critical region of the I-M transition.

5.2 Experimental methods

The disordered carbon pellets used for the electrical measurements were obtained by pyrolysis of CS as discussed in Chapter 3 (Section 3.2.2). The flat faces of the heat-treated pellets (typical size 10 mm x 5 mm x 1 mm) were smoothened by using a fine emery paper (C-600) and then treated with conc.HCl (Merck, 37%), followed by washing with double distilled water to remove any impurities. These pellets labeled as HTxxx, where xxx is the heat-treatment temperature (Table 3.1, Chapter 3), were used for electrical resistance measurements using the Van der Pauw geometry, as discussed in Chapter 2 (Section 2.3.10). The resistance was measured as a function of temperature, by cooling from 298 K to 15 K, using a closed cycle cryostat. A temperature sensor was placed near the sample to ensure the exactness of the sample temperature. The current input (10^{-9}–10^{-3} A) was optimized for each sample depending on its resistivity.

5.3 Room temperature resistivity

The room temperature resistivity (ρ_{298K}) shows large changes with HTT as shown in Figure 5.1. HT500 has very large ρ_{298K} (7200 Ohm cm) when compared to the samples heat-treated at higher temperatures. The ρ_{298K} of HT600 (440 Ohm cm) is about 15 times lower when compared to that of HT500, which again decreases by four orders of magnitude on increasing the HTT to 700 °C. ρ_{298K} of HT800 is reduced by a factor of ten when compared to that of HT700 and on further increase in HTT, for HT900 and HT1000, the ρ_{298K} shows a nearly saturating trend with much smaller decrease. The low-temperature to room temperature resistivity ratio (ρ_{15K}/ρ_{298K}) also shows a similar trend (Figure 5.2). The sample HT500 was found to be highly insulating (Figure 5.1) and thus, the resistivity measurements could not be performed at low temperatures. Here, the decrease in ρ_{298K} and especially ρ_{15K}/ρ_{298K}, which is a measure of the extent of disorder present in the system follow a specific trend, with a decrease of one order of magnitude when HTT increases from 500 to 600 °C, followed by five orders of

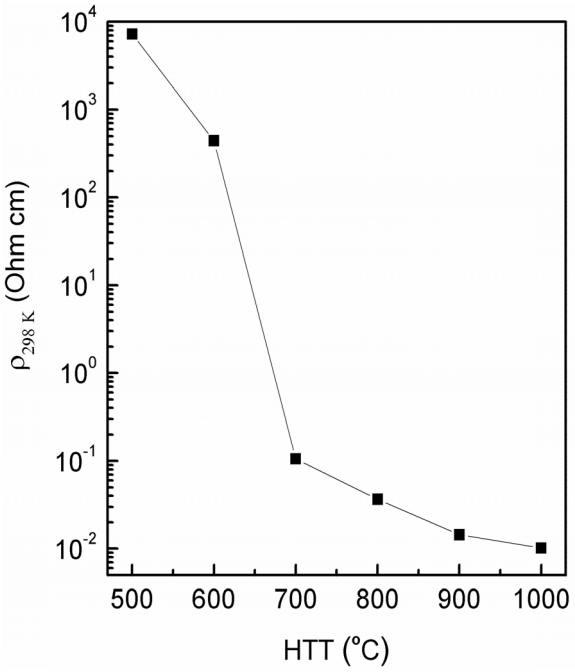

Figure 5.1: Variation of room temperature resistivity with HTT. Solid line is guide to the eyes.

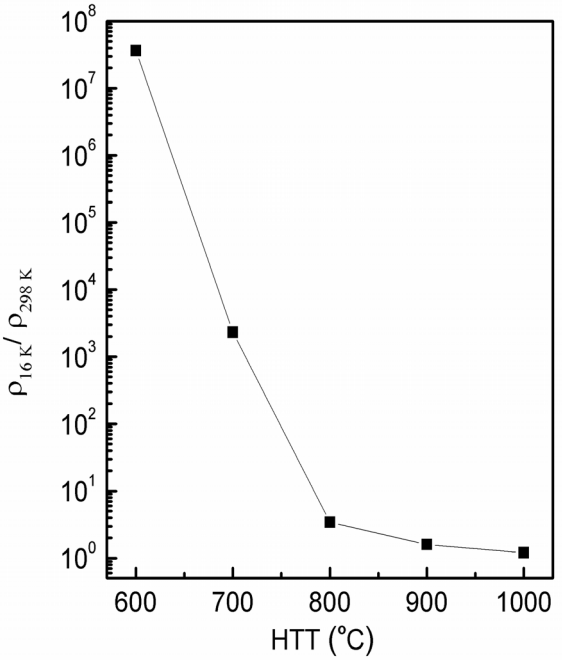

Figure 5.2: Low-temperature to room temperature (ρ_{15K}/ρ_{298K}) resistivity ratio with HTT. Solid line is guide to the eyes.

magnitude decrease when HTT is increased from 600 to 700 °C and three orders of magnitude decrease from HTT 700 to 800 °C, followed by a gradual decrease. The changes in ρ_{298K} and ρ_{15K}/ρ_{298K} with the increase in the HTT can be correlated to the extent of graphitization. Both these parameters follow the changes in L_a and L_c (Figure 3.6, Chapter 3) and the Raman G-peak position (Figure 3.9, Chapter 3). The large drop in ρ_{298K} and ρ_{15K}/ρ_{298K} occurs where the coherence lengths are small, where the G-peak position falls under stage-2. The gradual decrease in both the parameters are observed when the coherence length increases more steeply, where the G-peak position falls under stage-1.

5.4 Temperature variation of resistivity

The resistivity curves (ρ-T) of the samples heat-treated from 600 to 1000 °C, as a function of temperature, are shown in Figure 5.3. For all the samples, the resistivity increases with decreasing temperature. The lower HTT samples (HT600 and HT700) show large increase in the resistivity on lowering the temperature, whereas for higher HTT samples (HT800, HT900, and HT1000), the resistivity curves show only a weak temperature dependence.

In disordered electronic systems with a large degree of disorder, the localization length, ξ, is small due to the localization of conduction electrons in a small length scale, since the benzenoid networks of conduction electrons are too small with wide spatial separation [6]. The strong localization effect in disordered carbon is reflected directly in the ρ-T curves, with an exponential increase in the resistivity as the temperature is decreased [2]. In heat-treated disordered carbon, the disorder depends not only on the concentration of the sp^3 defects but also on the degree of clustering of the sp^2 carbon atoms [2]. Thus, in strongly disordered systems, ξ becomes comparable to the benzenoid cluster size whereas in weakly disordered systems, ξ can be much larger, exceeding the distance that an electron travels before it encounters a scattering center or comparable to the actual size of the sample [6,21]. This decrease in the defect induced scattering of conduction electrons results in a weak temperature dependence of the ρ-T curve [16,22], as

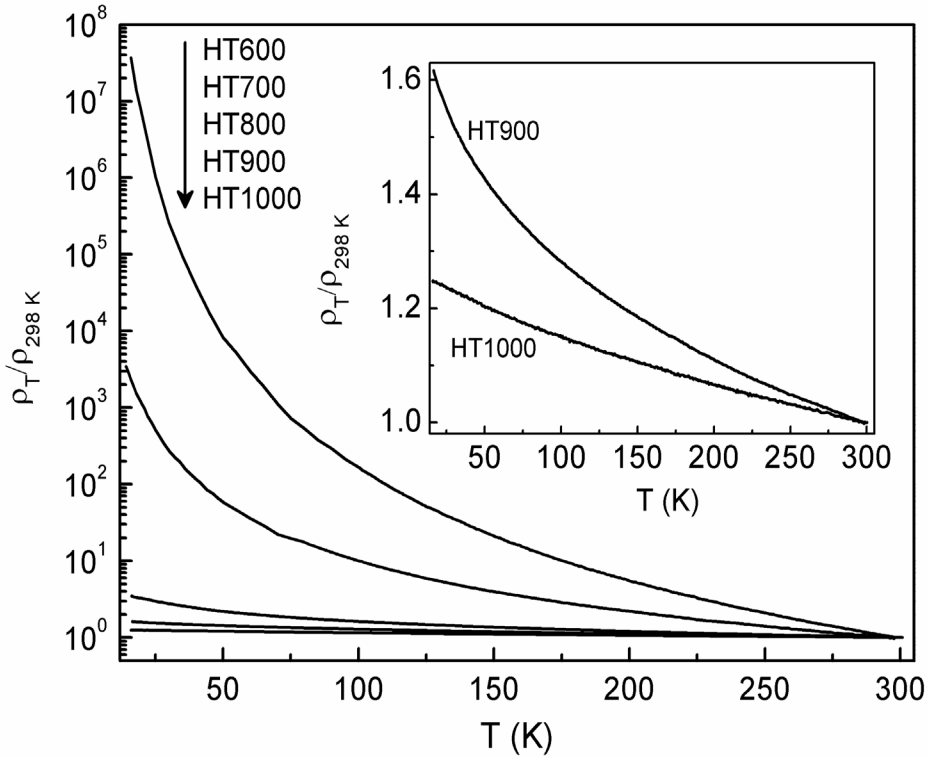

Figure 5.3: Temperature variation of resistivity of different heat-treated samples.

observed for HT800, HT900 and HT1000 (Figure 5.3). The changes in the ρ-T behavior indicate the crossover from insulating to conducting regime. The nearly temperature independent ρ-T behavior of HT1000 shows that the sample is in the critical regime, being more towards the metallic side. The negative value of $\mathrm{d}\rho/dT$ at higher HTT should be arising from the randomness in the nanographitic cluster size and spatial correlation [2]. Similar changes in the room temperature resistivity as well as the low-temperature to room temperature resistivity ratio, with an increase in the heat-treatment temperature, have been observed in amorphous carbon fibers and non-graphitic disordered carbon films prepared by pulsed laser deposition [2,23]. This has been interpreted as a direct consequence of the decrease in the disorder-induced scattering of charge carriers, owing to the development of percolation pathways consisting of delocalized benzenoid networks with elevation in the structural regularity.

5.5 Localization effect in highly disordered carbon

Strong localization effects are shown by systems with a large disorder [2,11]. In these systems, the low-temperature electrical transport properties are generally governed by activated hopping (Equation 5.1) or variable range hopping of charge carriers (Equation 5.2 and Equation 5.3 with $\beta = 1/3$ or $1/2$). Activated hopping conduction has been observed in highly disordered systems like phosphorous or boron doped amorphous carbon films, sputtered amorphous carbon films heat-treated at 400 °C [10,24]. In more ordered structures like epitaxial CrN films, boron carbide, PbSe quantum dots, etc., variable range hopping conduction, with different exponents (Equation 5.3) is observed [25–27]. Carbon systems with a large disorder, such as those belonging to stage-2, are also expected to show either activated hopping or variable range hopping conduction at low temperatures since the charge carriers are extremely localized due to the small cluster size [6].

Figure 5.4 shows the plot of $ln\rho$ against $1/T$ for the sample HT600. The non-linear variation shows that the activated hopping mechanism is not valid. Therefore, the carrier transport in these materials is expected to occur through three-dimensional variable range hopping (3D VRH) mechanism due to the randomness in the conduction pathways. Hence, the ρ-T data of the different samples are analyzed according to the Mott 3D VRH type conduction mechanism (Equation 5.2). The experimental data of HT600 and HT700 are found to fit well to the Mott 3D VRH model (Figure 5.5), as expected for highly disordered materials. However, for HT800, the experimental data diverges from the Mott 3D VRH law, at low temperatures (below 110 K), which is likely to be due to the modification of the conduction mechanism with structural ordering.

The value of T_0 extracted after least-squares fit to the experimental data to Equation 5.2 for HT600, HT700 and HT800 shows a continuous decrease with increasing HTT (Table 5.1). The ρ_0 values are in good agreement with those obtained for non-crystalline carbon heat-treated at similar temperatures [11]. The

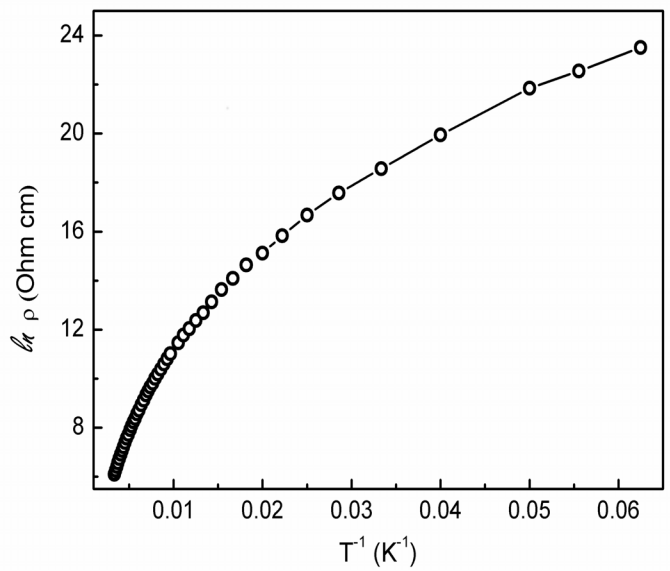

Figure 5.4: Plot of ln ρ against 1/T for HT600.

decrease in the Mott characteristic temperature, T_0, indicates that the mobility edge is approaching the Fermi level (E_F) with increasing HTT due to the associated structural ordering. T_0 is related to the localization length, ξ, and the density of states near the Fermi level, $N(E_F)$, through the relation shown in Equation 5.5 and these are important parameters which indicate the extent of localization in a disordered electronic system [28].

$$\xi = \left[\frac{k_B T_0 N(E_F)}{18}\right]^{-\frac{1}{3}} \tag{5.5}$$

In highly disordered carbon, where the charge carriers are extremely localized, the localization length can be taken as the effective coherence length or the graphitic cluster size calculated from the XRD data [6]. Therefore, the values of $N(E_F)$ are calculated using Equation 5.5, after substituting the values of L_a (Figure 3.6, Chapter 3) calculated from XRD (Table 3.3, Chapter 3) data, for ξ. The increase in $N(E_F)$ with HTT (Table 5.1) is consistent with the evolution of band structure in disordered carbon by the introduction of localized states near the Fermi level due to the thermal energy assisted clustering of sp^2 carbon atoms at the expense of the strain energy [29,30].

Due to the decrease in the structural disorder, a divergence from the 3D VRH

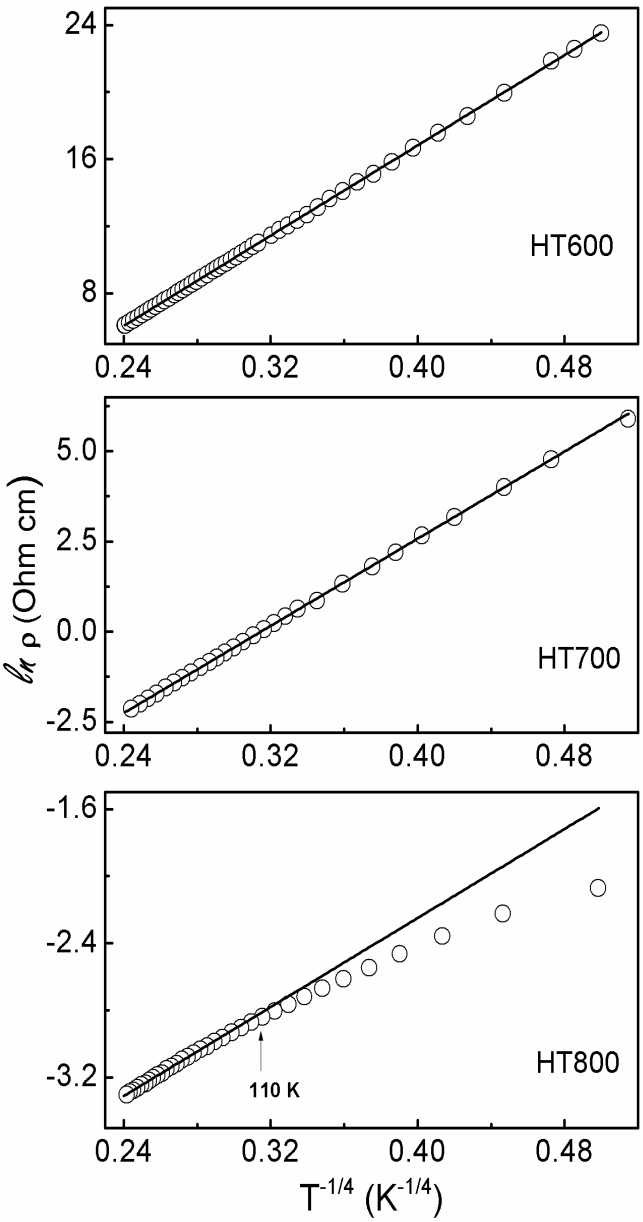

Figure 5.5: Fit (solid line) to the experimental data (open circles) using the Mott 3D VRH law (Equation 5.2). Some points in the experimental data are skipped for clarity.

Table 5.1: T_0 and ρ_0 values obtained from fitting the experimental data to 3D VRH law and values of N(E_F) calculated using Equation 5.5.

Sample code	ρ_0 (Ohm cm)	T_0 (K)	N(E_F) ($eV^{-1}cm^{-3}$)
HT600	4.1×10^{-5}	2×10^{7}	10^{18}
HT700	7.5×10^{-4}	8×10^{5}	10^{19}
HT800	7.4×10^{-3}	2×10^{3}	10^{22}

law, with a modification of the conduction mechanism to the Coulomb gap VRH (CG VRH) law (Equation 5.3 with $\beta = 1/2$), has been reported previously in heat-treated non-graphitic disordered carbon films and boron-doped carbon [2,31]. This crossover from 3D VRH to CG VRH is due to the steep increase in the localization length with decrease in the disorder, which becomes comparable to the mean hopping length due to the elevation in the carrier density and increase in the mean free path [31]. However, in the present case, such a cross over to CG VRH (Equation 5.3 with $\beta = 1/2$) or even to a Mott 2D VRH (d = 2, $\beta = 1/3$ in Equation 5.3) mechanism was not observed for HT800 or for other higher HTT samples. The deviation from Mott 3D VRH law for HT800, along with the weak temperature dependence of resistivity observed for HT800, HT900 and HT1000, is indicative of a change in the insulating character and emergence of a semiconducting nature with the increase in the extent of graphitization. Even though the heat-treatment in the temperature range 1000–1500 °C cannot induce a complete in-plane ordering, as reported [29], similar weak temperature dependence of the resistivity, previously observed in disordered carbon film, was analyzed based on the Drude model for the 2D graphene π-band after considering an orientation disorder in graphene layers [2]. Similar kind of resistivity anomaly was observed in pre-graphitic carbon and this has been ascribed to the two possible factors, a small mean free path owing to the coulomb interaction in the presence of disorder

or the two-dimensional weak localization (2D WL) [14–16,32]. Therefore, the resistivity data of HT800, HT900 and HT1000 have been analyzed based on these two models, as discussed in the following section.

5.5.1 Structural ordering and weak localization effect

During the conduction of electrons through a disordered material, the scattered electrons have two types of lifetimes, the elastic lifetime (τ_0) in the eigenstate of momentum and the inelastic lifetime (τ_i) in the eigenstate of energy [14,16]. At low temperatures, $\tau_i \gg \tau_0$, and therefore, the inelastic events contribute more towards the conduction process. The inelastic lifetime is related to temperature as $1/\tau_i \propto T^p$, where T is the temperature and p is a constant which can vary from 0.5 to 1.5. Therefore, in order to explain the modification in the temperature dependence of resistivity due to this inelastic carrier scattering, a correction factor (T^p) needs to be applied in the equation describing the resistivity curves [22,33]. In disordered materials, the modification in the low-temperature resistivity due to the inelastic carrier-carrier and carrier-phonon interactions is given by Equation 5.6

$$\sigma(T) = \sigma_0 + AT^p \tag{5.6}$$

The second term in Equation 5.6 accounts for the carrier-carrier and carrier-phonon interactions. A $T^{1/2}$ dependence of conductivity ($p = 0.5$ in Equation 5.6) is observed for disordered systems if the scattering process is dominated by carrier-carrier interactions [14]. However, if the carrier-phonon interactions dominate, the value of the exponent increases above 0.5, typically in the range 0.75 to 1.5, depending on the relative variation in the phonon wavelength and the system dimensionality determined by the extent of disorder [22]. The resistivity curve of HT800 exhibits good agreement with Equation 5.6, as shown in Figure 5.6. The fitting parameters obtained are $\sigma_0 = 0.64$ Ohm^{-1}cm^{-1}, $A = 2.05$ and $p = 0.45$. Since $T^{1/2}$ dependence of conductivity is characteristic of inelastic scattering by charge carrier interactions, the value of p closer to 0.5 for HT800 suggests that

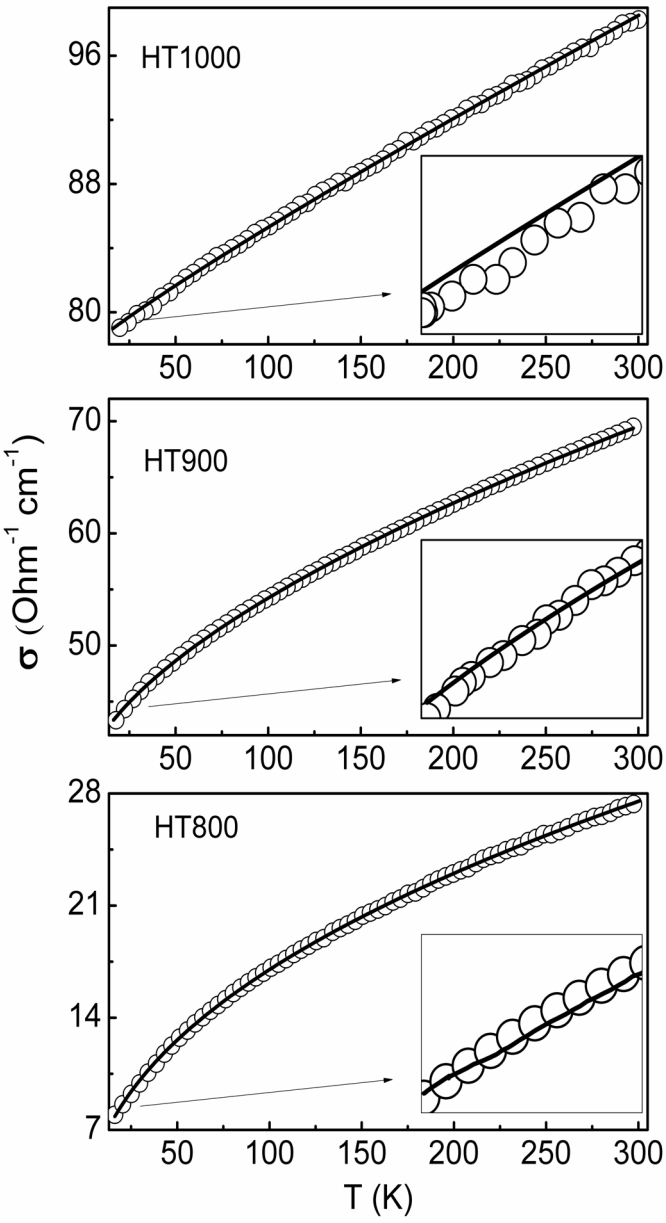

Figure 5.6: Fit (solid line) to the experimental data (open circles) using Equation 5.6. The insets show the data below 35 K. Some points in the experimental data are skipped for clarity.

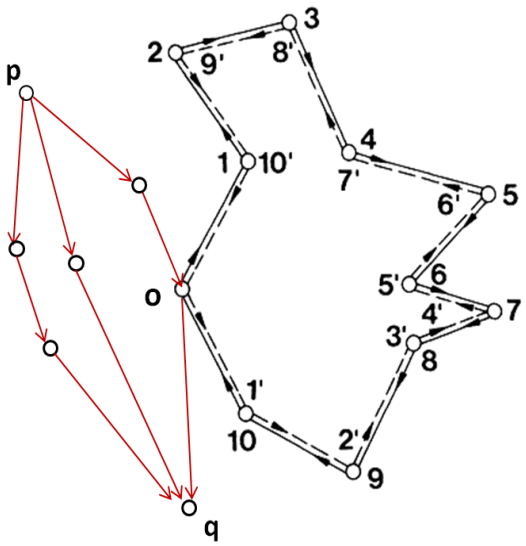

Figure 5.7: The diffusion pathways of the conduction electron in a disordered system (red line). The loop formations due to quantum diffusion are shown in black (solid and dashed lines). Taken from reference [35].

the carrier-carrier interaction dominates at initial stages of graphitization [14]. As HTT is increased to 900 and 1000 °C, Equation 5.6 remains valid for nearly in the entire high-temperature region, but a small deviation is observed at very low temperatures, with the conductivity being slightly lower than the fitted value (insets in Figure 5.6) and the difference increases with increasing HTT.

The 2D WL mechanism has been observed to be operative in considerably ordered pre-graphitic carbon systems as well as in mechanically exfoliated graphene flakes [15,34]. 2D WL originates when the probability of elastic scattering of charge carriers by static defects is larger than the inelastic scattering due to carrier-phonon or carrier-carrier interactions [15]. The elastic scattering of charge carriers by random defects produces a coherent backscattering. The localization effect due to the coherent backscattering is shown in Figure 5.7. The electronic transport from point 'p' to 'q' can occur through multiple defect-induced diffusion pathways (red lines), the conduction path given through points p–o–q in Figure 5.7 is one such pathway. At any instant there can be an additional pathway originating from point 'o', which returns back to the same point forming a loop (thick black line) as

shown by o–1–2–...-8–9–10–o because in the case of quantum diffusion, the probability to return to the origin is much higher than in classical diffusion since the amplitudes add coherently [35]. For classical diffusion process, the probability of a reverse pathway (black dotted line) o–1′–2′–...–8′–9′–10′–o is exactly equal to that of the direct pathway. The total probability is then the sum of each of these two probabilities. It can also be shown that this intensity is twice as large in the case of quantum diffusion when compared to classical diffusion problem [35]. Now the electron tends to remain at point 'o', as a localized electron, rather than getting transmitted through the medium and hence this process is assumed to a precursor to localization, known as weak localization [35]. This coherent backscattering due to elastic scattering by random defects is common to any wave propagating through a disordered media and has been experimentally observed during the passage of light through disordered media like polymer solutions [36]. In the case of graphene flakes, both the inherent structural defects and the graphene edges can act as scattering centers [34].

The 2D WL in graphitic clusters has also been identified to produce a very small decrease in the conductivity (increase in resistivity) at low temperatures, since the elastic scattering increases as the temperature decreases. Therefore, the temperature dependence of conductivity has to be corrected by adding an additional logarithmic temperature dependent term in Equation 5.6. The modified relation is given as Equation 5.7 [14,32].

$$\sigma(T) = \sigma_0 + AT^p + BlnT \tag{5.7}$$

On using Equation 5.7, which includes the logarithmic correction term for weak localization interpretation, the fitted curves exactly follow the experimental data in the entire measured temperature range for both HT900 and HT1000 as shown in Figure 5.8 (a,b). The fitting parameters obtained for the σ-T curves of HT800, HT900 and HT1000 using Equation 5.6 and Equation 5.7 are listed in Table 5.2.

Figures 5.8(c) and (d) show the temperature dependent contribution of each term in Equation 5.7 towards the conductivity of HT900 and HT1000, respectively.

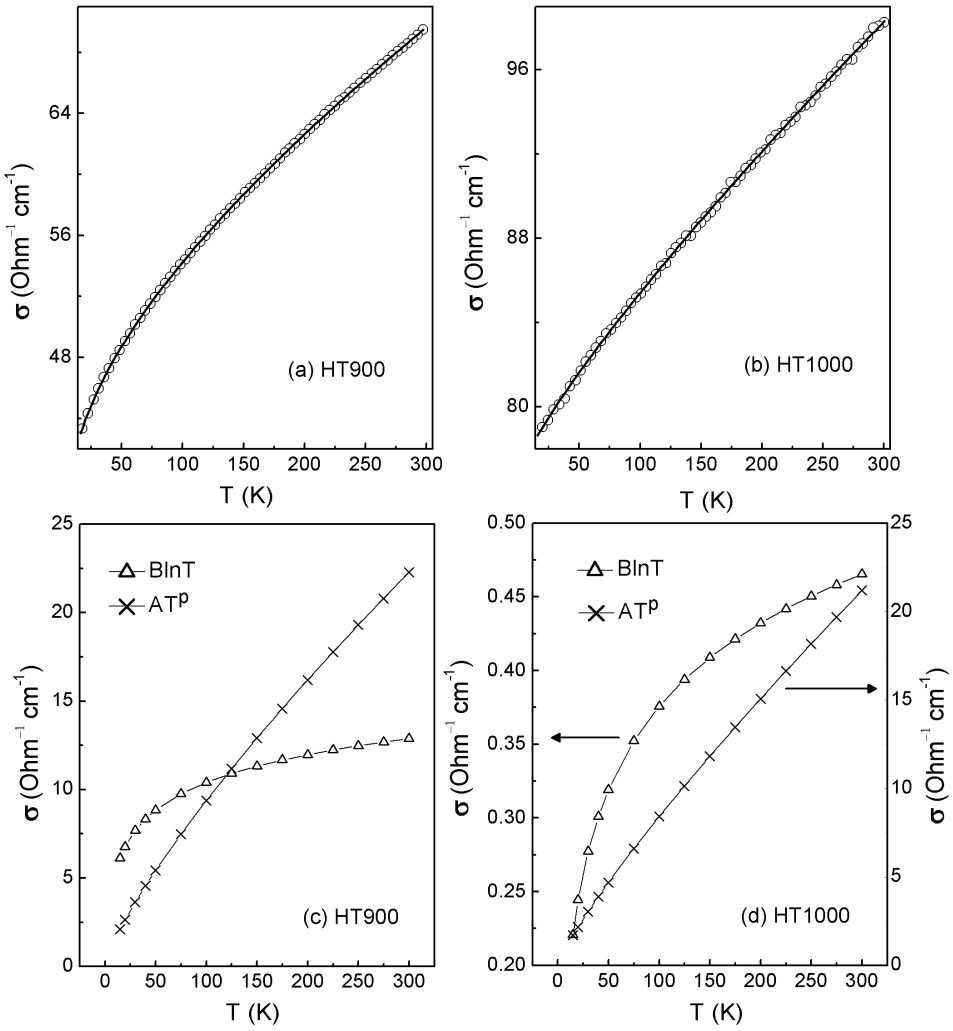

Figure 5.8: Fit (solid line) to the experimental data (open circles) using Equation 5.7 for (a) HT900 and (b) HT1000. Some points in the experimental data (a and b) are skipped for clarity. (c) and (d) show the changes in the different terms in Equation 5.7 with temperature.

Table 5.2: Least squares fitted parameters using Equation 5.6 and Equation 5.7 (values in brackets).

Sample code	σ_0 ($Ohm^{-1}cm^{-1}$)	A	p	B
HT800	0.64	2.05	0.45	-
HT900	37.80	1.04	0.60	-
	(34.40)	(0.25)	(0.79)	(2.26)
HT1000	77.50	0.12	0.90	-
	(76.60)	(0.18)	(0.84)	(0.08)

The exponent term (p) in Equation 5.7 for HT900 (p=0.79) and HT1000 (p=0.84) is greater than 0.5, and increases with the extent of graphitization, indicating the role of phonon-mediated scattering process along with the carrier–carrier interactions [22]. For HT900, at 300 K, along with the temperature independent term σ_0 (34.40 $Ohm^{-1}cm^{-1}$), T^p and $BlnT$ terms contribute 22.30 $Ohm^{-1}cm^{-1}$ and 12.89 $Ohm^{-1}cm^{-1}$, respectively, towards conductivity, whereas for HT1000, T^p and $BlnT$ terms contribute 21.18 $Ohm^{-1}cm^{-1}$ and 0.47 $Ohm^{-1}cm^{-1}$, respectively, along with the temperature independent term σ_0 (76.60 $Ohm^{-1}cm^{-1}$) (Table 5.2 and Figures 5.8 (c) and (d)). For both the samples, the contribution of the exponent term is comparable and decreases steadily nearly in the same magnitude as the temperature is decreased and hence forms more or less a straight line with nearly the same slope. However, the contribution from the 2D WL term is decreased by two order of magnitude while moving from HT900 to HT1000. This suppression of WL effect can be due to the decrease in the defect density in HT1000 when compared to that in HT900. For HT900, as the temperature is decreased below ∼120 K, the contribution from $BlnT$ term is higher than that from T^p. This indicates an apparent higher contribution from the 2D WL term over the carrier-carrier interaction term below ∼120 K. Because of this, even though Equation 5.7 is required to fit the experimental data in the entire temperature range, it

may be noted that the experimental data deviates only to a smaller extend from Equation 5.6 (Figure 5.6). However, in the case of HT1000, the contribution from the $BlnT$ term is always lower than that of the T^p term and it can also be noted that there is a considerable increase in $d(BlnT)/dT$ below ~50 K due to which the total conductivity decreases to a greater extend below this temperature when compared to the contribution at higher temperatures. Thus, the 2D WL mechanism is likely to be prominent than other scattering processes, thereby inducing a small additional resistivity, particularly at very low temperatures. Hence, with graphitic ordering, depending on the extent of graphitization, the 2D WL becomes important as observed previously in pre-graphitic carbon fibers [15].

Apart from 2D WL, magnetic impurity mediated scattering has also been observed to produce a similar decrease in the conductivity at low temperatures (Equation 5.7) [16,18]. Therefore, it is possible that this can be a possible conduction mechanism, since magnetic properties of heat-treated samples showed the presence of randomly distributed intrinsically magnetic nanographitic domains of variable strength giving rise to a spin-glass type disordered magnetic state, as described in Chapter 4. However, the low-temperature magnetization data (Figure 4.2, Chapter 4) showed a decrease in the magnetization at 60 kOe while moving from HT600 to HT1000. This indicates that, with heat-treatment, as the cluster size increases, the magnetization decreases due to the reduction in the number of graphitic clusters as two or more clusters tend to coalesce forming larger graphitic domains [29]. Therefore, the samples HT900 and HT1000 being considerably graphitic having lower magnetization than that of HT600, HT700 and HT800, the weak localization must be arising from the defect induced scattering at nanographitic edges rather than that arising from the scattering from magnetic impurities.

5.6 Sample-to-sample variation

Since the electrical properties of heat-treated samples are highly sensitive towards the microstructure, some sample-to-sample variations in the electrical properties

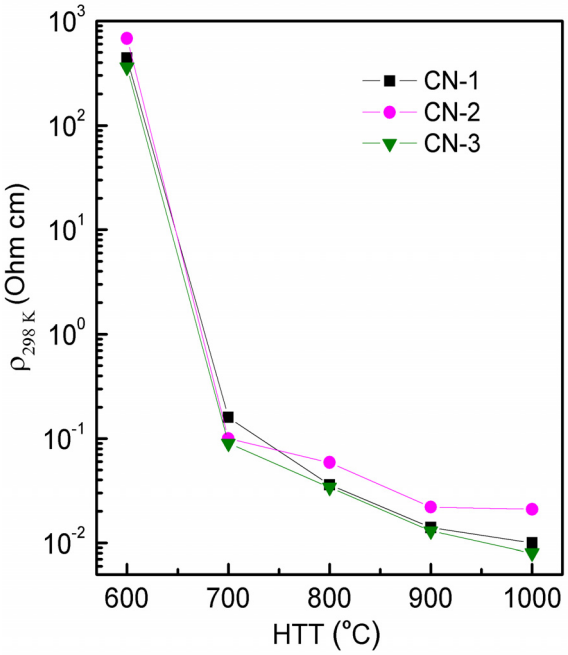

Figure 5.9: Variation of room temperature resistivity of CN-1, CN-2 and CN-3 with HTT. Solid lines are guide to the eyes.

are expected even if all the heat-treatment conditions are kept identical. This difference is likely to be arising from the factors like porosity, sintering of heat-treated carbon pellets, small differences in the extent of graphitization, etc. which are difficult to control while preparing carbon specimens from a natural source like CS. The ρ_{298K} of three samples (CN-1, CN-2 and CN-3) prepared from different pieces of CS by heat-treatment under identical conditions, from 600 to 1000 °C are compared in Figure 5.9 and Table 5.3 , in order to identify the range in which the ρ_{298K} may vary with the sample. From the table, it can be noted that the ρ_{298K} of three samples prepared from different pieces of CS are different. The ρ_{298K} of CN-2, after a heat-treatment at 600 °C, is 54% higher than that of CN-1, meanwhile the ρ_{298K} CN-3, after a heat-treatment at 600 °C, is 15% lower than that of CN-1. With an increase in HTT, the ρ_{298K} decreases (Figure 5.9) for all the samples, in a similar manner, keeping the difference between the individual ρ_{298K} at a particular HTT nearly same. This decrease in ρ_{298K} with an increase in HTT can be ascribed to the increase in the extent of graphitization. Barring

Table 5.3: ρ_{298K} (Ohm cm) of different CS pieces heat-treated under N_2 atmosphere from 600 to 1000 °C.

HTT (°C)	ρ_{298K} (Ohm cm)		
	CN-1	CN-2	CN-3
600	4.4×10^{2}	6.8×10^{2}	3.6×10^{2}
700	1.1×10^{-1}	1.6×10^{-1}	1.0×10^{-1}
800	3.6×10^{-2}	5.9×10^{-2}	3.4×10^{-2}
900	1.4×10^{-2}	2.2×10^{-2}	1.3×10^{-2}
1000	1.0×10^{-2}	2.1×10^{-2}	0.8×10^{-2}

the small differences in the resistivity at each HTT, the trend in the variation of ρ_{298K} with HTT is almost comparable for all these samples.

5.7 Effect of heat-treatment atmosphere

The possible effect of the gas atmosphere used for the heat-treatment on modifying the electrical properties is checked by comparing the ρ_{298K} of samples heat-treated under argon (sample code: CAr) and helium (sample code: CHe) atmospheres with that heat-treated under nitrogen atmosphere (sample code: CN-1). The comparison between the ρ_{298K} of CAr, CHe and CN-1 is given in Figure 5.10 and Table 5.4 .

The ρ_{298K} of CAr is larger than that of CN-1, which is in turn higher than that of CHe, irrespective of the heat-treatment temperature. Considering that the ρ_{298K} varies inversely with the extent of graphitization, the higher ρ_{298K} for samples heat-treated under argon and nitrogen when compared to those heat-treated under helium is likely to arise from the small difference in the extent of graphitization. Such small difference in the extent of graphitization can arise due to the difference in the thermal conductivity of the gases used during heat-treatment, where helium has the highest thermal conductivity (157 mW/mK at 300 °C and 0.1 MPa),

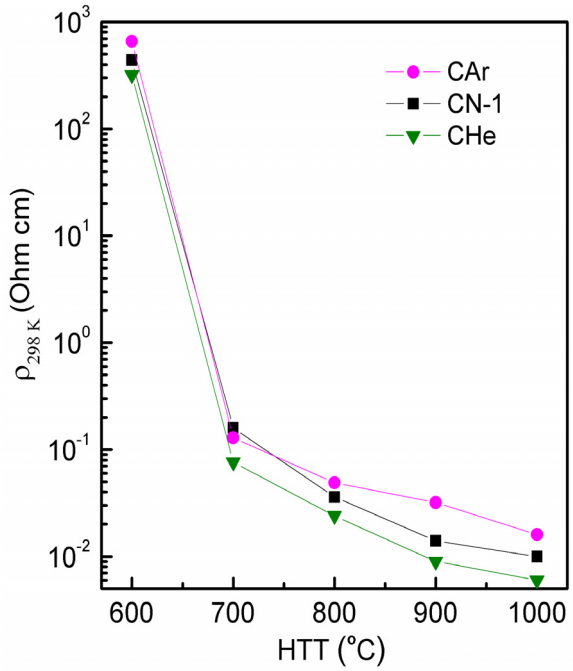

Figure 5.10: Variation of room temperature resistivity of CN-1, CAr and CHe with HTT. Solid lines are guide to the eyes.

Table 5.4: Room temperature resistivity of different CS pieces heat-treated from 600 to 1000 °C under different gas atmospheres.

HTT (°C)	ρ_{298K} (Ohm cm)		
	CAr	CN-1	CHe
600	6.6×10^{2}	4.4×10^{2}	3.2×10^{2}
700	1.3×10^{-1}	1.1×10^{-1}	0.8×10^{-1}
800	4.9×10^{-2}	3.6×10^{-2}	2.4×10^{-2}
900	3.2×10^{-2}	1.4×10^{-2}	0.9×10^{-2}
1000	1.6×10^{-2}	1.0×10^{-2}	0.6×10^{-2}

whereas argon (18 mW/mK at 300 °C and 0.1 MPa) and nitrogen (26 mW/mK at 300 °C and 0.1 MPa) have comparable thermal conductivity values [37]. With an increase in the thermal conductivity of the gas under which the heat-treatment is performed, the heat-treatment becomes effective and uniform making the sample more uniformly graphitic. Similar effect was observed in the magnetic properties also, where the low-temperature magnetization at 60 kOe for CS heat-treated under helium atmosphere was relatively lower (Figure 4.6, Chapter 4) than those heat-treated under other gas atmospheres at similar temperatures. However, the role of heat-treatment atmosphere on ρ_{298K} cannot be established beyond doubt because the ρ_{298K} can also vary when different samples from the same CS are heat-treated under identical conditions (Table 5.3).

5.8 Temperature variation of resistivity of samples heat-treated in different gas atmospheres

The ρ-T curves of three samples heat-treated under nitrogen along with those heat-treated in argon and helium atmospheres at 700 °C are shown in Figure 5.11 and the normalized resistivity curves are shown in Figure 5.12. All the samples heat-treated at 700 °C show large increase in the resistivity as the temperature is decreased. However, the magnitude to which the resistivity rises with decreasing temperature is different for each sample (Figure 5.12). The CS heat-treated under nitrogen (CN-2) atmosphere, which had the highest ρ_{298K} among the studied samples (Table 5.3), show the highest increase in the resistivity as the temperature is decreased. The other two samples heat-treated under nitrogen (CN-1 and CN-3) and the one heat-treated under argon atmosphere show an intermediate increase in the resistivity. The sample heat-treated under helium atmosphere has a smaller increase in resistivity as the temperature is decreased. However, it should be noted that the extent to which the resistivity increases at the lowest temperatures, for different samples heat-treated at 700 °C, falls between that of HT600 and HT800 (Figure 5.3).

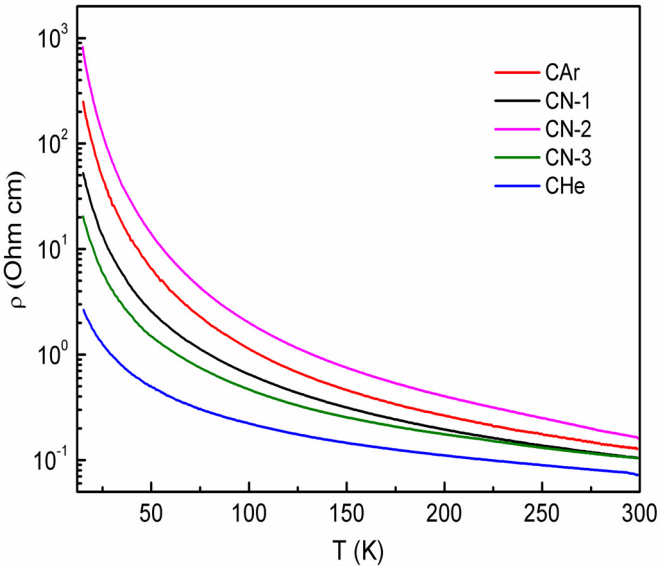

Figure 5.11: Temperature variation of the resistivity of samples heat-treated at 700 °C under nitrogen (CN-1, CN-2 and CN-3), argon (CAr) and helium (CHe) atmospheres.

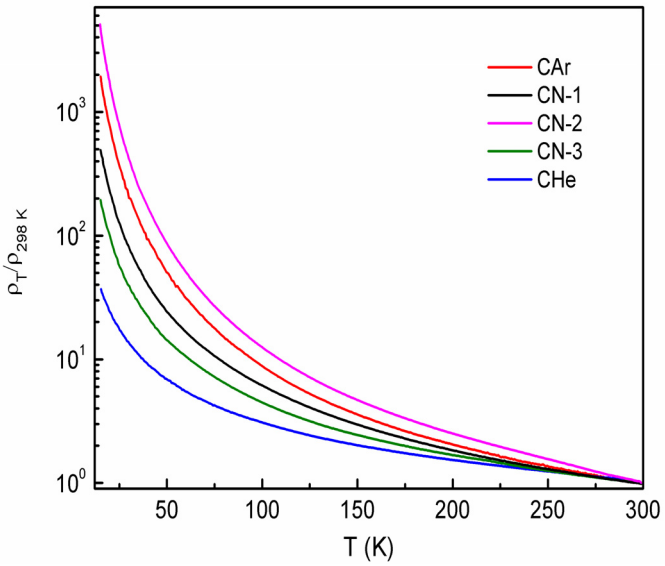

Figure 5.12: Normalized temperature variation of the resistivity of samples heat-treated at 700 °C under nitrogen (CN-1, CN-2 and CN-3), argon (CAr) and helium (CHe) atmospheres.

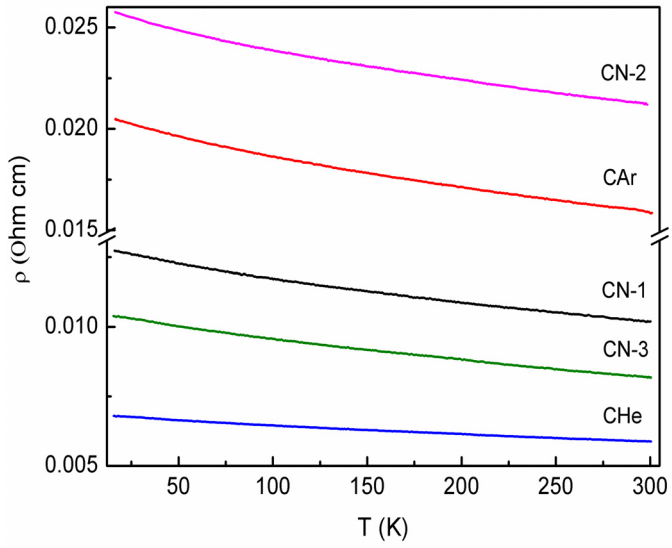

Figure 5.13: Temperature variation of the resistivity of samples heat-treated at 1000 °C under nitrogen (CN-1, CN-2 and CN-3), argon (CAr) and helium (CHe) atmospheres.

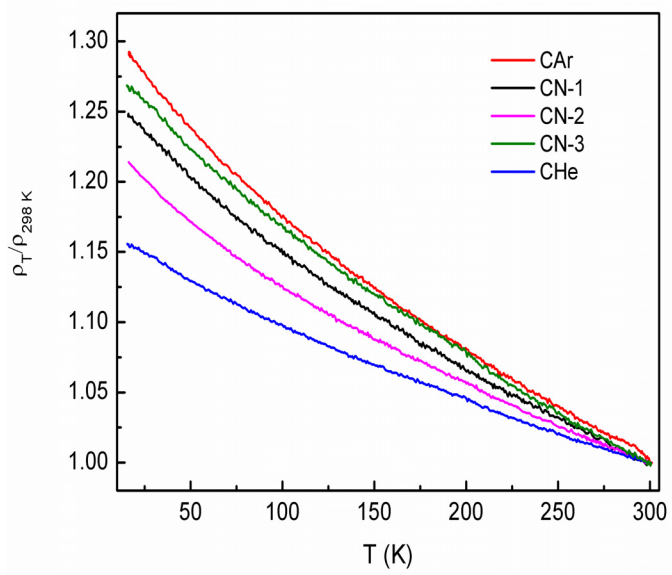

Figure 5.14: Normalized temperature variation of the resistivity of samples heat-treated at 1000 °C under nitrogen (CN-1, CN-2 and CN-3), argon (CAr) and helium (CHe) atmospheres.

Figure 5.13 shows the temperature variation of the resistivity of CN-1, CN-2, CN-3, CAr and CHe after heat-treating at 1000 °C. The ρ-T curves of all the samples heat-treated at 1000 °C are almost linear and less temperature dependent when compared to those samples heat-treated at 700 °C. Similar changes were observed for the samples HT700 and HT1000 (Figure 5.3) due to the increase in the extent of graphitization. For the samples heat-treated at 1000 °C, similar to those heat-treated at 700 °C, sample CN-2 and the sample CHe have the highest and lowest resistivity, respectively, at all measured temperatures. The normalized resistivity curves (Figure 5.14) do not show much variation in their ρ-T behavior. The resistivity curve of CHe shows a small increase when compared to that of other samples, as the temperature decreases.

5.8.1 Effect of heat-treatment atmosphere and sample-to-sample variation on conduction mechanism

Since the resistivity curves observed for the different samples have similar temperature dependence, depending on the HTT, the conduction mechanism is expected to be independent of the heat-treatment conditions as well as the CS samples used for heat-treatment. To ascertain this fact, the resistivity curves shown in Figure 5.11 and Figure 5.13 are analyzed with respect to the Mott 3D VRH (Equation 5.2) and 2D WL models (Equation 5.7), as described in Section 5.5, for samples heat-treated at 700 and 1000 °C. The ρ-T curves of the different samples heat-treated at 700 °C show good fit to the Mott 3D VRH law (Equation 5.2).

The fitting parameters and the fitted curves are shown in Figure 5.15. The ρ_0 and T_0 values obtained after curve fitting vary over nearly two orderers of magnitude. This indicates a difference in $N(E_F)$ (Equation 5.5) which might be arising due to the difference in the microstructures of these samples. Conduction mechanism remains the same for all samples heat-treated at 700 °C.

For the same set of samples, increase in the HTT from 700 °C to 1000 °C alters the conduction mechanism, where the low-temperature conductivity fits well to the 2D WL mechanism (Equation 5.7). The experimental data and fitted curves

for the samples heat-treated at 1000 °C, under different atmospheres are shown in Figure 5.16. The different parameters used for curve fitting are listed in the figure. It may be noted that in all the cases the value of p is above 0.5, which indicates that even though the ρ_{298K} value span over a small range, the conduction mechanism remains the same with the phonon-mediated scattering process dominating over

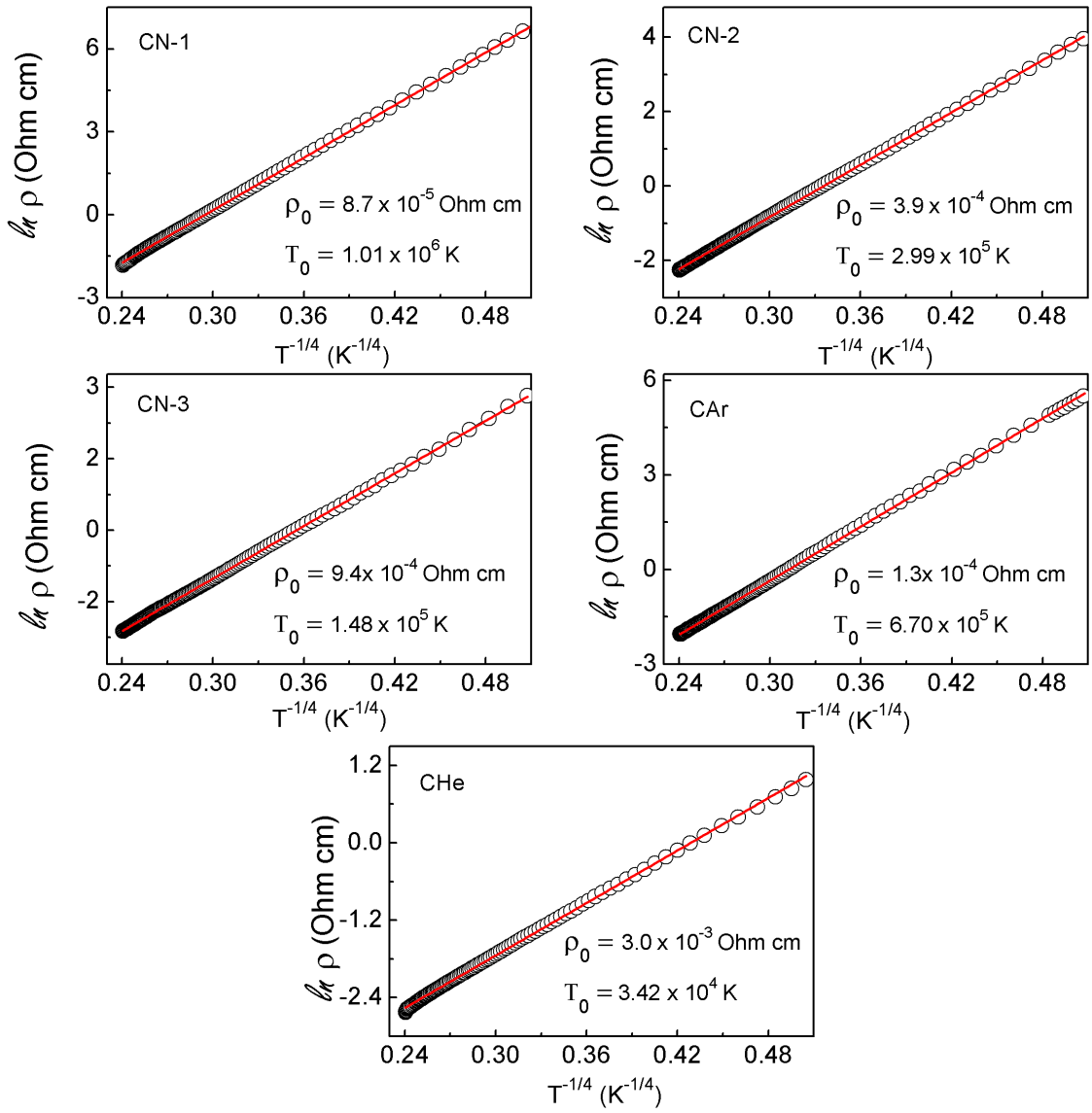

Figure 5.15: Fit (red line) to the experimental data (open circles) using Equation 5.2 for resistivity curves of the samples heat-treated at 700 °C under nitrogen (CN-1), argon (CAr) and helium (CHe) atmospheres. Some points in the experimental data are skipped for clarity.

carrier-carrier interaction after heat-treatment at 1000 °C. The fitting parameters vary for different samples heat-treated under nitrogen atmosphere and those heat-treated under other gas atmospheres like argon and helium. This is likely to be due to the small difference in the extent of localization owing to the variations in the extent of graphitization, porosity, electron density, etc. of the different carbon samples.

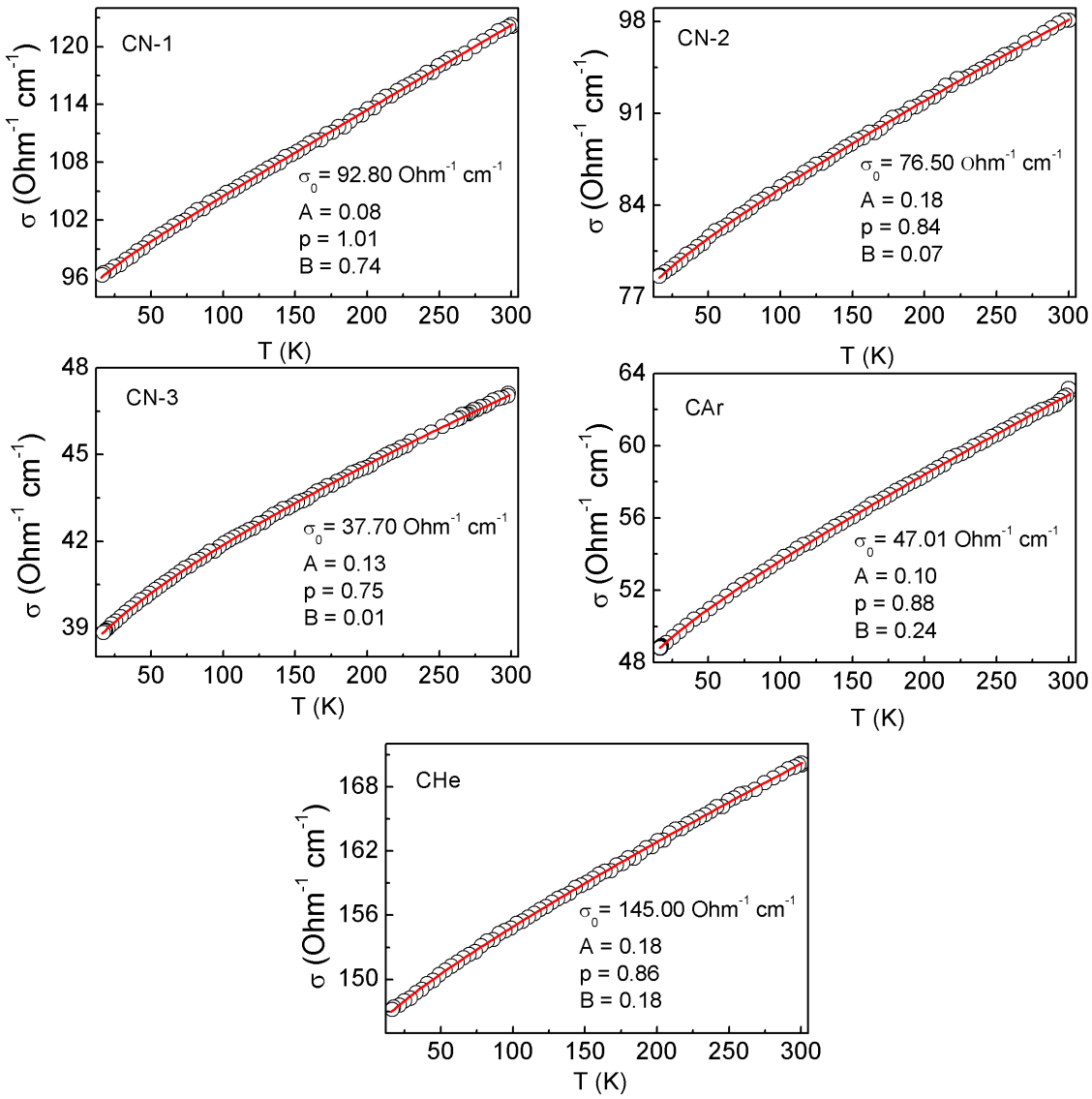

Figure 5.16: Fit (red line) to the experimental data (open circles) using Equation 5.7 for resistivity curves of the samples heat-treated at 1000 °C under nitrogen (CN-1), argon (CAr) and helium (CHe) atmospheres. Some points in the experimental data are skipped for clarity.

The results show that even though there is minor variation in the magnitude of room temperature resistivity of different samples heat-treated under the same or different gas atmospheres, under identical conditions, the mechanism of conduction remains the same for samples heat-treated at the same temperature. This indicates that the changes in the conduction mechanism are linked to the extent

of graphitization and not due to sample-to-sample variation. A detailed study related to the changes in conduction mechanism of samples heat-treated at different temperature under various gas atmospheres were not performed since the ρ_{298K} of the samples heat-treated under argon and helium is in the range expected for the precursor variation. Moreover, despite some differences in the ρ_{298K}, the conduction mechanism operating are similar in samples heat-treated at a particular HTT.

5.9 Conclusions

The changes in the electrical resistivity of the heat-treated disordered carbon, as a function of the extent of graphitization, has been studied. The heat-treatment induced structural ordering in the disordered carbon samples has been shown to change the conduction mechanism with the extent of graphitization. In samples heat-treated at lower temperatures ($<$ 800 °C), there is strong localization due to the smaller graphitic cluster size and their wide spatial distribution, leading to an exponential increase in the resistivity at low temperatures showing Mott 3D VRH conduction mechanism. On the other hand, those samples heat-treated at 900 and 1000 °C showed weak temperature dependence, showing a crossover of the conduction mechanism from 3D Mott VRH to 2D WL, due to the difference in the defect density and their spatial distribution. Thus, the extent to which different scattering mechanisms operate depends on the degree of graphitization. In the graphitic regime, the development of percolation conduction pathways, involving spatially correlated nanographitic regions, is likely to be responsible for the 2D weak localization. Magnetic impurity mediated scattering, another possible mechanism for the weak localization in the samples heat-treated at 900 and 1000 °C, is excluded because these samples are weakly magnetic when compared to those which followed activated hopping conduction. A high field magnetoresistance study is essential for completely ruling out the role of the magnetic impurity mediated scattering in the samples heat-treated at higher temperatures.

The small variation in the resistivity characteristics of heat-treated samples

derived from different pieces of CS indicates that a low-temperature impedance measurement can be more informative while studying the effect of heat-treatment atmosphere and sample-to-sample variation on the electrical properties. Thus, the present study provides details regarding the changes in the conduction mechanisms due to the changes in the extent of carrier localization in disordered carbons of varying crystallinity. A clear understanding on the evolution of defect induced localization can contribute towards the development of carbon-based electronic and spintronic devices, studies on graphene and CNT based ballistic conductors, etc. where structural defect plays a major role in the charge carrier scattering processes.

Bibliography

[1] J. Robertson and E. P. Oreilly, *Phys. Rev. B* 35 (1987) 2946.

[2] K. Takai, M. Oga, H. Sato, T. Enoki, Y. Ohki, A. Taomoto, K. Suenaga and S. Iijima, *Phys. Rev. B* 67 (2003) 214202.

[3] A. W. P. Fung, M. S. Dresselhaus and M. Endo, *Phys. Rev. B* 48 (1993) 14953.

[4] M. Theye and V. Paret, *Carbon* 40 (2002) 1153.

[5] E. Staryga and G.W. Bak, *Diamond Relat. Mater.* 14 (2005) 23.

[6] K. Sreedhar and P. A. Joy, *Solid State Commun* 99 (1996) 589.

[7] N. F. Mott, *Adv. Phys.* 61 (1967) 49.

[8] N. F. Mott and E. A. Davis, *Electronic Processes in Non-crystalline Materials* (Clarendon Press, 1979).

[9] P. P. Edwards, R. L. Johnston, C. N. R. Rao, D. P. Tunstall And F. Hensel, *Phil. Trans. R. Soc. Lond. A* 356 (1998) 5.

[10] C. Godet, *Philos. Mag. B* 81 (2001) 205.

[11] F. Carmona, P. Delhaes, G. Keryer and J. P. Manceau, *Solid State Commun.* 14 (1974) 1183.

[12] A. L. Efros and B. I. Shklovskii, *J. Phys. C: Solid State Phys.* 8 (1975) L49.

[13] K. Shimakawa and K. Miyake, *Phys. Rev. Lett.* 61 (1988) 994.

[14] B. L. Altshuler and A. G. Aronov, *Solid State Commun.* 30 (1979) 115.

[15] V. Bayot, L. Piraux, J. P. Michenaud and J. P. Issi, *Phys. Rev. B* 40 (1989) 3514.

[16] G. Bergmann, *Phys. Rep.* 107 (1984) 1.

[17] J. Ren, H. Guo, J. Pan, Y. Y. Zhang, X. Wu, H. G. Luo, S. Du, S. T. Pantelides and H. J. Gao, *Nano Lett.* 14 (2014) 4011.

[18] J. H. Chen, L. Li, W. G. Cullen, E. D. Williams and M. S. Fuhrer, *Nat. Phys.* 7 (2011) 535.

[19] C. L. Yang, X. Wang, X. Zhang, D. S. Wu, M. Liu, P. Zheng, J. Y. Yao, Z. Z. Li, Y. F. Yang, Y. G. Shi, J. L. Luo and N. L. Wang, *Phys. Rev. B* 91 (2015) 075120.

[20] V. H. Tran, R. Troc, Z. Bukowski, D. Badurski, and C. Sulkowski, *Phys. Rev. B* 71 (2005) 094428.

[21] S. Y. Hsu and J. M. Valles Jr, *Phys. Rev. Lett.* 74 (1995) 2331.

[22] P. A. Lee and T. V. Ramakrishnan, *Rev. Mod. Phys.* 57 (1985) 287.

[23] A. W. P. Pung, M. S. Dresselhaus and M. Endo, *Phys. Rev. B* 48 (1993) 14953.

[24] K. Shimakawa and K. Miyake, *Phys. Rev. B* 39 (1989) 7578.

[25] X. Y. Zhang, J. S. Chawla, B. M. Howe and D. Gall, *Phys. Rev. B* 83 (2011) 165205.

[26] C. Wood and D. Emin, *Phys. Rev. B* 29 (1984) 4582.

[27] H. E. Romero and M. Drndic, *Phys. Rev. Lett.* 95 (2005) 156801.

[28] Q. Guo and S. J. Poon, *Phys. Rev. B* 54 (1996) 12793.

[29] F. G. Emmerich, *Carbon* 33 (1995) 1709.

[30] M. J. Matthews, M. S. Dresselhaus, N. Kobayashi, T. Enoki, M. Endo and K. Nishimura, *Phys. Rev. B* 60 (1999) 4749.

[31] P. Vishwakarma and S. Subramanyam, *J. Appl. Phys.* 100 (2006) 113702.

[32] E. P. Sajitha, V. Prasad and S. V. Subramanyam, *J. Appl. Phys.* 105 (2009) 073708.

[33] P. W. Anderson, E. Abrahams and T. V. Ramakrishnan, *Phys. Rev. Lett.* 43 (1979) 718.

[34] F. V. Tikhonenko, D. W. Horsell, R. V. Gorbachev and A. K. Savchenko, *Phys. Rev. Lett.* 100 (2008) 056802.

[35] G. Bergmann, *Phys. Rev. Lett.* 28 (1983) 2914.

[36] P. E. Wolf and G. Maret, *Phys. Rev. Lett.* 55 (1985) 2696.

[37] N. B. Vargaftik, *Handbook of Thermal Conductivity of Liquids and Gases* (CRC Press, 1993).

Chapter 6

Structural, magnetic and electrical properties of catalytically graphitized activated carbon

6.1 Introduction

Activated carbon is of high commercial importance due to its effectiveness in water and air purification, gas storage and sequestration, sustainable and environmentally friendly energy storage devices, etc. [1–4]. Different types of activated carbonaceous materials such as amorphous carbon, carbon nanotubes, carbon nanofibers, graphene, etc. were found to be more efficient and effective for applications in energy storage devices such as in supercapacitors and battery electrodes, after performing a chemical or physical activation [5,6]. Even though the mounting interest in cost effective activated carbon-based energy storage devices has lead to a widespread interest in various activation methods and activated carbon nanostructures, the effect of activation on the modification of structural, magnetic and electrical properties of these materials are ignored and therefore remain unexplored.

Studies on the magnetic properties of carbon-only systems like graphene, GNR, fullerenes, graphene dots, graphene oxide, disordered carbon with mixed sp^2/sp^3 phase, etc. have attracted a considerable amount of attention from both experimental and theoretical scientists worldwide [7–11]. The magnetic properties of carbon-based materials arise from different structural contributions including the defects, dangling bonds, vacancies, zig-zag edges and edge termination [9]. The σ dangling bonds can be created by chemical modification of graphene edges and/or in any other carbon systems or by destroying the long scale hexagonal network of graphene and/or graphite [9,10]. The spins thus generated in a carbon-based system can interact among themselves bringing about different magnetic ordering in the material through various types of interactions which are described in Chapter 1 (Section 1.6) [12]. In an activated carbon system, some of the consequences of the activation process such as the large density of pores and defects, dangling bonds between the graphitic crystallites, a larger fraction of the carbons as surface atoms, crystalline disorder, etc. could be decisive enough to affect the magnetic properties of the materials.

The electrical properties of activated carbons are of particular importance con-

sidering that they have been widely used as electrode materials in batteries and supercapacitors, either in their native form or as composites with different metal oxides [13–16]. The electrical properties of carbonaceous materials are known to depend on their microstructure, imparting either metallic, semiconducting or insulating characteristics as discussed in Chapter 5. The heat-treatment induced graphitic ordering in different forms of disordered carbon has been found to be responsible for the development of conducting percolation pathways in the material, leading to a metallic state, where the resistivity shows weak temperature dependence [17–19]. A previous study on the boron-doped amorphous carbon by Subramanyam *et al.* was successful in identifying a crossover from Mott VRH (Equation 5.2) to ES VRH (Equation 5.3, $\beta = 1/2$) as the temperature is decreased [20]. This crossover was ascribed to the graphitic ordering induced during boron doping and the resulting changes in the π-electron density. Therefore, it may be expected that the structural ordering or disordering in carbon samples, after activation, might also modify the electrical properties of the material.

6.2 The carbon activation process

Activated carbon can be prepared by both physical and chemical methods. Physical activation involves heating of the carbonaceous precursor in the presence of gaseous oxidizing agents (like O_2, CO_2, etc.) and chemical activation involves a chemical pre-treatment of the precursor with suitable activating agent (like KOH, NaOH, $ZnCl_2$, H_3PO_4, etc.) followed by a heat-treatment at high temperatures ($\geq$600 °C) [21]. The chemical activation is preferred over physical methods due to the lower activation temperature and the resulting high surface area with large micropore volume of the activated carbon. Among the different chemical activating agents like KOH, NaOH, $ZnCl_2$ and H_3PO_4, KOH can form activated microporous carbon structures with a surface area up to 2500 m^2/g. Hence, KOH activated carbon have substantial commercial importance both as an adsorbent material and in electrochemical energy storage devices [1,5]. The final pore size distribution and surface area of the activated carbon depend on the activation temperature,

activation time, the amount of the activating agent used in the process and the microstructure of the precursor [22]. The microstructure of the precursor becomes particularly important because its porosity and adsorption capabilities determine the amount of activating agent that can be incorporated into the material before heat-treatment. Several precursors like polymers, coals, organic molecules, pitches, different nutshells, etc. have been reported to be suitable materials for preparing activated carbon [23].

The mechanism involved in the activation of carbon by using KOH was studied in detail by temperature programmed desorption experiments and surface area analysis [24]. Irrespective of the carbon form, the activation process involves a series of simultaneous redox reactions (Reactions 6.1 to 6.4) involving carbon and potassium along with their oxides. During the activation process, the formation of K_2CO_3 begins at about 400 °C and with an increase in the temperature to 600 °C, most of the KOH gets transformed to K_2CO_3. The main step in the activation process involves the transformation of K_2O into K_2CO_3 by CO_2 [5,24].

$$2\,KOH \longrightarrow K_2O + H_2O \tag{6.1}$$

$$C + H_2O \longrightarrow CO + H_2 \tag{6.2}$$

$$CO + H_2O \longrightarrow CO_2 + H_2 \tag{6.3}$$

$$CO_2 + K_2O \longrightarrow K_2CO_3 \tag{6.4}$$

By increasing the activation temperature above 700 °C, a large amount of metallic potassium is formed by the reactions 6.5 and 6.6 [5,24]. This influences the activation process considerably by the intercalation of potassium in to the ordered carbon structures or by mere incorporation of potassium in the amorphous carbon structure which results in the widening of carbon layers and formation of pores.

$$K_2O + H_2 \longrightarrow 2\,K + H_2O \tag{6.5}$$

$$K_2O + C \longrightarrow 2\,K + CO \tag{6.6}$$

The activation process at high temperatures always leads to significantly large surface area and porosity due to high efficiency of the gasification of carbon in

the presence CO_2 formed during the decomposition of K_2CO_3, along with the incorporation of potassium metal.

Interestingly, the inclusion of various chemical species, including the alkali metals, during the heat-treatment, is known to affect the carbon microstructure by catalytically transforming both graphitizing and non-graphitizing carbon to a partially crystallized form [25–27]. The graphitization process in disordered carbon is thermodynamically favorable due to a considerable decrease in the structural strain associated with a disordered lattice while relaxing to a graphitic structure. However, the kinetic barrier for crystallization is too large in non-graphitizing carbons and hence the thermally induced graphitization normally occurs above 2500 °C [26,28]. Depending on the metal and the carbonaceous material involved, the catalytic graphitization occurs at much lower temperatures in the range of 800 °C to 1500 °C [29]. A local graphitization at very low temperatures has been observed in carbon derived from alkali metal incorporated polyfurfuryl by microscopy experiments, where, alkali metals like Cs, Rb, K and Na were found to be effective whereas Li did not show any catalytic activity [26]. Many transition metals are also shown to be effective in inducing graphitization [29].

Even though the exact mechanism involved in the catalytic graphitization, using transition elements, borides of rare-earth elements, B_2O_3, CeO_2, etc. is unclear, the graphitization brought about by alkali metals is proposed to be either due to the intensive local heating or by the decomposition of metal carbides formed during the processes [25,29,30]. Hence, during KOH activation, additional structural modifications are expected due to the catalytic graphitization process along with the creation of defects and enhancement in the surface area. Therefore, the effect of KOH activation on the magnetic and electrical properties is worth studying. The present work is an attempt to relate the changes in the magnetic and electrical properties of KOH activated CS derived carbon to their microstructure.

6.3 Materials preparation

Small pieces of (10mm x 10mm) dried coconut shell was pyrolyzed at 500 °C in flowing nitrogen atmosphere, as described in Chapter 3 (Section 3.2.2). KOH and conc.HCl (37%) were purchased from Merck Chemicals and used as-received without any further purification. The amorphous carbon pellets were crushed and ground to fine powder using an agate mortar and pestle. Before proceeding to the chemical activation, this powder was subjected to a pre-treatment process with conc.HCl at 100 °C for 24 hours to remove any metal impurities present. The carbon powder was then recovered by filtration and subsequently washed several times with double distilled water and dried overnight in a hot air oven, at 60 °C.

For chemical activation, 0.5 g of the pre-treated carbon powder was soaked in 20 ml of a solution containing a fixed amount of KOH (0.5 g, 1 g, 1.5 g and 2 g). The amount of KOH was fixed in such a manner that the carbon to KOH weight ratios are maintained as 1:1, 1:2, 1:3 and 1:4. After 24 hours of soaking, the carbon-KOH mixture was dried to obtain a slurry. This slurry was transferred into a quartz boat and heat-treated at the desired temperatures in a horizontal tubular furnace under flowing nitrogen atmosphere. Three different temperatures (800 °C, 900 °C and 1000 °C) were tried for preparing activated carbon, for this study. The activation temperature was maintained for 3 hours and then the sample was allowed to cool down to room temperature. The activated carbon obtained after heat-treatment was washed several times with double distilled water till neutral pH and was used for further analysis after drying in an oven.

The activated samples are labeled as xACy, where 'x' denotes the activation temperature as 8 for 800 °C, 9 for 900 °C and 10 for 1000 °C. 'y' denotes the carbon to KOH ratio as 1 for 1:1, 2 for 1:2, 3 for 1:3 and 4 for 1:4. Control samples were also prepared at 800 °C, 900 °C and 1000 °C by following same procedures without adding any KOH and were labeled as 8AC0, 9AC0 and 10AC0, respectively.

6.4 Structure of activated carbon

6.4.1 X-ray diffraction

The XRD patterns of the different activated carbon samples show two peaks (Figure 6.1), an intense peak centered at ∼25° and a less prominent peak at ∼44° on the 2θ scale, corresponding respectively to the (*002*) and (*100*) reflections from a random layer structured disordered carbon lattice [31].

After activating at 800 °C, the broad (*002*) peak shows a small but constant shift towards higher angles with an increase in the KOH weight ratio. This observation is similar to the one previously reported for KOH activated carbon nanofibers and indicates a decrease in the inter-layer spacing and hence stacking of graphene layers to form nanographitic clusters [32]. However, the (*100*) peak position is not affected by the activation process. On increasing the activation temperature

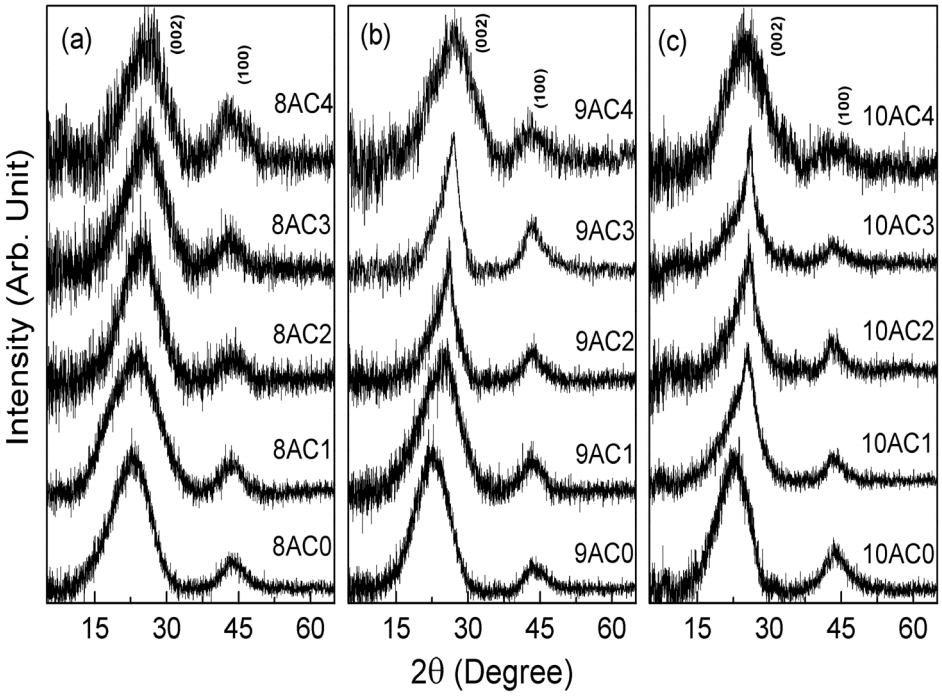

Figure 6.1: XRD patterns of samples activated at (a) 800 °C, (b) 900 °C and (c) 1000 °C along with that of the corresponding control samples, 8AC0, 9AC0 and 10AC0.

to 900 °C, for some samples, the XRD patterns show prominent changes in the (*002*) peak shape, with relatively sharper peak, indicating that the change in the activation mechanism at higher temperatures is critically affecting the microstructure of the activated carbon. These changes in the XRD patterns are similar to that observed after the calcium enhanced high temperature crystallization of carbon [33]. However, the control samples 9AC0 and 10AC0 show similar XRD patterns as that of 8AC0, characteristic of a defective random layer structure of disordered carbon [31]. The changes in the (*002*) peak shape, upon activation, can be clearly observed for 9AC2, 9AC3, 10AC1, 10AC2 and 10AC3. In addition to this change in the peak profiles, when compared to that of 9AC0, the (*002)* peak of 9AC1 shows a shift of ∼2 degrees on the 2θ scale towards higher angles. With further increase in the KOH ratio from 1:1 to 1:4 (samples 9AC1 to 9AC4), a small shift in the (*002*) peak position ($<$ 1 degree) persists. The shift in the (*002*) peak position is slightly larger when the activation temperature is increased to 1000 °C (∼3 degrees while moving from 10AC0 to 10AC1) indicating that the activation temperature plays a major role in determining the microstructure of the activated specimens along with the amount of KOH. However, the (*002*) peak remains static for 10AC2, 10AC3 and 10AC4. Moreover, for the samples with the highest amounts of KOH used, 9AC4 and 10AC4, the XRD patterns are different when compared to the ones activated with lower amounts of KOH, and resemble more to the control samples with broad peaks. Along with these variations, the less intense (*100*) peak also exhibits certain changes in its shape, for some samples.

To get better insights on the graphitization process with activation, the in-plane (L_a) and out-of-plane (L_c) coherence lengths are calculated by using the Scherrer type equation (Equation 2.2) with two different K values for calculating L_a (K=1.84) and L_c (K=0.89) [31], as described in Section 3.3.5. Disordered carbon has a strained carbon lattice due to the presence of both sp^2 and sp^3 hybridized carbon atoms [19,34]. In such a structure, with thermal assistance, the sp^2 carbons tend to form graphitic clusters, where the extent of clustering and hence the variations in L_a and L_c depends on the heat-treatment temperature [19].

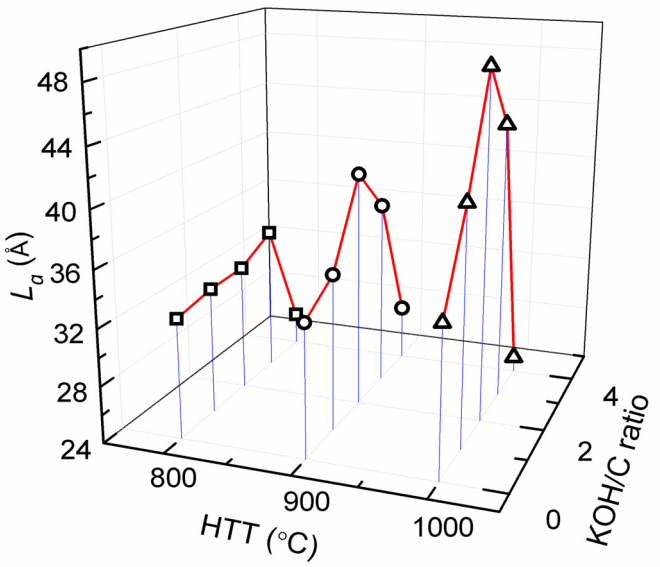

Figure 6.2: The in-plane coherence length (L_a) of activated carbon samples as a function of activation temperature and KOH/C ratio. The red and blue lines are guides to the eyes.

The increase in the value of L_a (Figure 6.2) and L_c (Figure 6.3) for the control samples, with an increase in the activation temperature from 800 °C to 1000 °C, is due to this thermally assisted graphitization process. However, after KOH activation, L_a is found to be increasing to much higher values than that expected after a simple heat-treatment induced ordering. With different amounts of KOH, for a given activation temperature, the L_a value exhibits a certain trend with an initial increase which reaches a maximum value and then dropping to a value which is even lower than that of the control samples. Among the 8AC series, maximum in-plane coherence length L_a is observed for 8AC3 (34.4 Å) after which the value drops to 26.3 Å for 8AC4. For 9AC and 10AC series the maximum value of L_a increases till a KOH weight ratio of 2 (40.7 Å for 9AC2 and 48.5 Å for 10AC2). On increasing the KOH weight ratio to 3 and further to 4, L_a shows a small decrease followed by a large drop to 28.0 Å and 25.1 Å for 9AC4 and 10AC4 respectively. Even though L_c is much lower in magnitude than L_a for the control samples as well as for samples activated at 800 °C, with an increase in activation temperature L_c shows a steep increase in magnitude for 9AC3 and 10AC3, whose

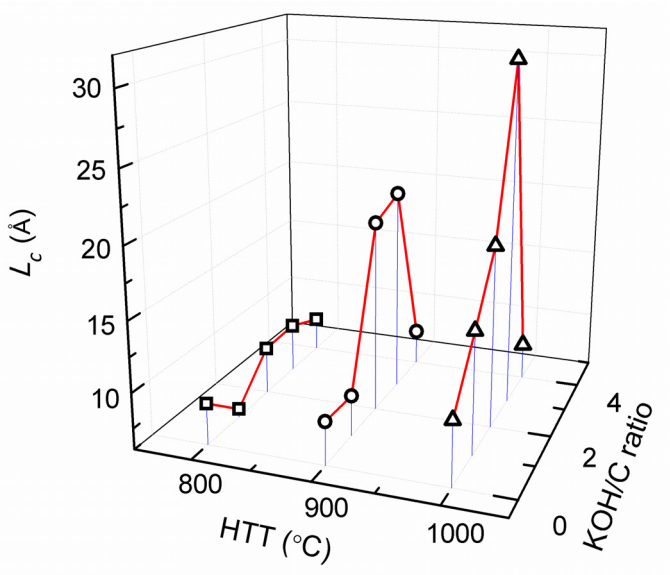

Figure 6.3: The out-of-plane coherence length (L_c) of activated carbon samples as a function of activation temperature and KOH/C ratio. The red and blue lines are guides to the eyes.

extent is much larger than that observed for L_a after the activation process. But on increasing the amount of KOH (for samples 9AC4 and 10AC4), the out-of-plane coherence length decreases drastically, even lower than 9AC0 and 10AC0. However the increase in L_c, reported by Mochida *et al.* after KOH activation of carbon nanofibers, was more regular, with a constant increase in L_c with an increase in the activation temperature, since the experiment was performed after using very low amount of KOH (0.25 g per 1 g nanofiber) [32]. Thus, a much more comprehensive information regarding the structural evolution was obtained here by varying both the amount of KOH and the activation temperature.

The increase in the values of both L_a and L_c suggests the ordering of graphitic phase, while the decrease in samples activated with KOH/C ratio 4 (for samples 8AC4, 9AC4 and 10AC4) suggests the disordering of the graphitic lattice. Thus, upon KOH activation, there is an ordering of graphitic clusters which is prominent in the case of samples activated at 900 and 1000 °C with intermediate KOH ratios. But more importantly, this ordering is suppressed on further increasing the amount of KOH to an extent where the structural disorder is even higher than

that in the control samples. The potassium metal incorporation during KOH activation at temperatures above 800 °C being known, the increase in the value of L_a and L_c can be attributed to the potassium mediated catalytic graphitization whose extent depends on the amount of potassium incorporated and the enhanced local heating experienced at the potassium metal incorporated sites [26]. The main disordering factor in KOH activated carbon should be the development of porosity by gasification of carbon (Reactions 6.5 and 6.6). Therefore, to verify the development of porosity, the pore size distribution and surface area of the control and activated samples are measured.

6.4.2 Surface area and pore size distribution

Nitrogen adsorption technique, which uses the nitrogen adsorption isotherms at 77 K, is an important method for characterizing the surface characteristics of activated carbonaceous materials. The surface area and porosity of all the activated carbon samples, along with that of the control samples, are analyzed using this method. As reported previously in carbon samples activated by a similar procedure, these parameters are found to be highly sensitive towards the amount of KOH and the activation temperature [22,35]. The surface areas of the control samples, 8AC0, 9AC0 and 10AC0 are obtained as 80, 230 and 360 m^2/g, respectively, which are too low when compared to that of the activated samples (Figure 6.4). The relatively small increase in the surface area of the carbon samples with an increase in the activation temperature is due to controlled conversion of nitrogen, sulphur, carbon and hydrogen present in the pre-treated samples to their respective oxides after a heat-treatment in nitrogen atmosphere [35]. This controlled expulsion of carbon, hydrogen and other hetero-elements from the carbonaceous material generates a small porosity in the carbon system which in turn increases the surface area nominally. A much more drastic enhancement in the surface area is observed when these samples are activated using different amounts of KOH, at a particular temperature (Figure 6.4), which points directly towards the role of the activating agent in determining the carbon microstructure. Similarly, the

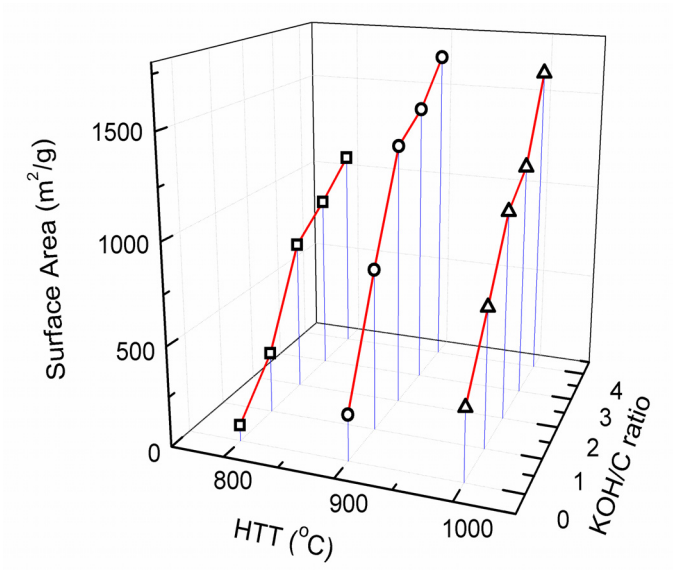

Figure 6.4: The BET surface area of carbon samples activated with different amounts of KOH at 800, 900 and 1000 °C. The red and blue lines are guides to the eyes.

surface area is also found to be varying an with increase in the activation temperature even though exactly the same amount of KOH is used for activation. This indicates that the surface area of the activated carbon is determined by both the amount of KOH and the activation temperature.

Even though the surface area increases with increase in the amount of KOH used, after activation at all three temperatures, the surface areas of the samples activated at 900 °C are always found to be larger than that of those activated at 1000 °C with the same amount of KOH. A similar decrease in the surface area with an increase in the activation temperature is previously reported in KOH activated corncob based carbon and was ascribed to the pore widening and subsequent formation of supra-nanometer (1-5 nm) pores at the expense of sub-nanometer (<1 nm) pores at extreme activation conditions [35,36]. In the present case also, this effect is confirmed from the pore size distribution curves (Figure 6.5). KOH activation at 800 °C generates large number of ∼6-7 Å wide pores. On increasing the activation temperature to 900 °C and further to 1000 °C, more number of supra-nanometer pores are generated at the expense of the sub-nanometer pores which are observed in the samples activated at 800 °C. The large increase in the

number of supra-nanometer pores in the samples activated at 1000 °C is likely to be due to the widening of sub-nanometer pores or by the coalescence of two or more adjacent sub-nanometer pores, with an increase in the carbon gasification as the activation temperature increases from 900 to 1000 °C. This kind of pore widening can in turn decreases the surface area of the activated carbon to a small extent, as shown in Figure 6.4.

6.4.3 Transmission electron microscopy

The TEM images of the samples activated at 900 °C (Figure 6.6) show the formation of nanographitc regions in different morphologies and to different extents. The TEM images of two different regions of the samples 9AC1 (images a and b), 9AC2 (images c and d), 9AC3 (images e and f) and 9AC4 (images g and h) are included the figure for comparison; the images clearly show that the graphitic clusters formed in the activated samples are heterogeneously distributed with different geometries and in-plane coherence lengths in each specimen. Moreover, in the graphitized structures, the morphology of the graphitic cluster is observed to be more like linear chains, similar to that observed after catalytic graphitization of templated mesoporous carbon after impregnating with the nitrates of Fe, Ni or Mn [37]. The TEM images of 9AC1 show very low graphitic ordering. However, the TEM images of 9AC2 show distinctly different features, with the formation of ordered graphitic channel with an amorphous background. For 9AC3, the clustering effects are observed to be more prominent than that in 9AC2. The extent of ordering in 9AC4 is found to be much higher than that observed in 9AC3, which shows that the local ordering increases even after activation with an excess amount of KOH. However, the TEM image of 9AC4 is in contrast with XRD characteristics; the information from the XRD data showed a large decrease in the value of L_a of 9AC4 when compared to the other carbon samples activated at 900 °C and the control sample.

To explain the difference in the observations from XRD and TEM studies, the nature of graphitization by KOH activation needs to be considered in detail.

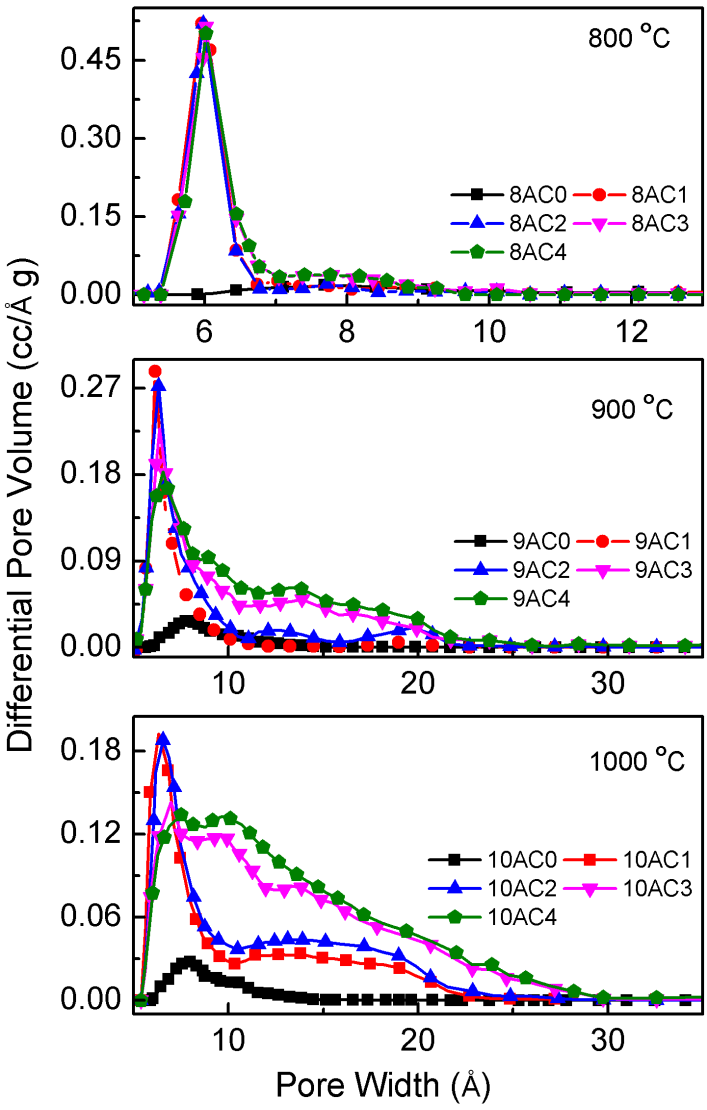

Figure 6.5: Changes in the porosity of activated carbon after activating with different amounts of KOH at 800 °C, 900 °C and 1000 °C, as indicated.

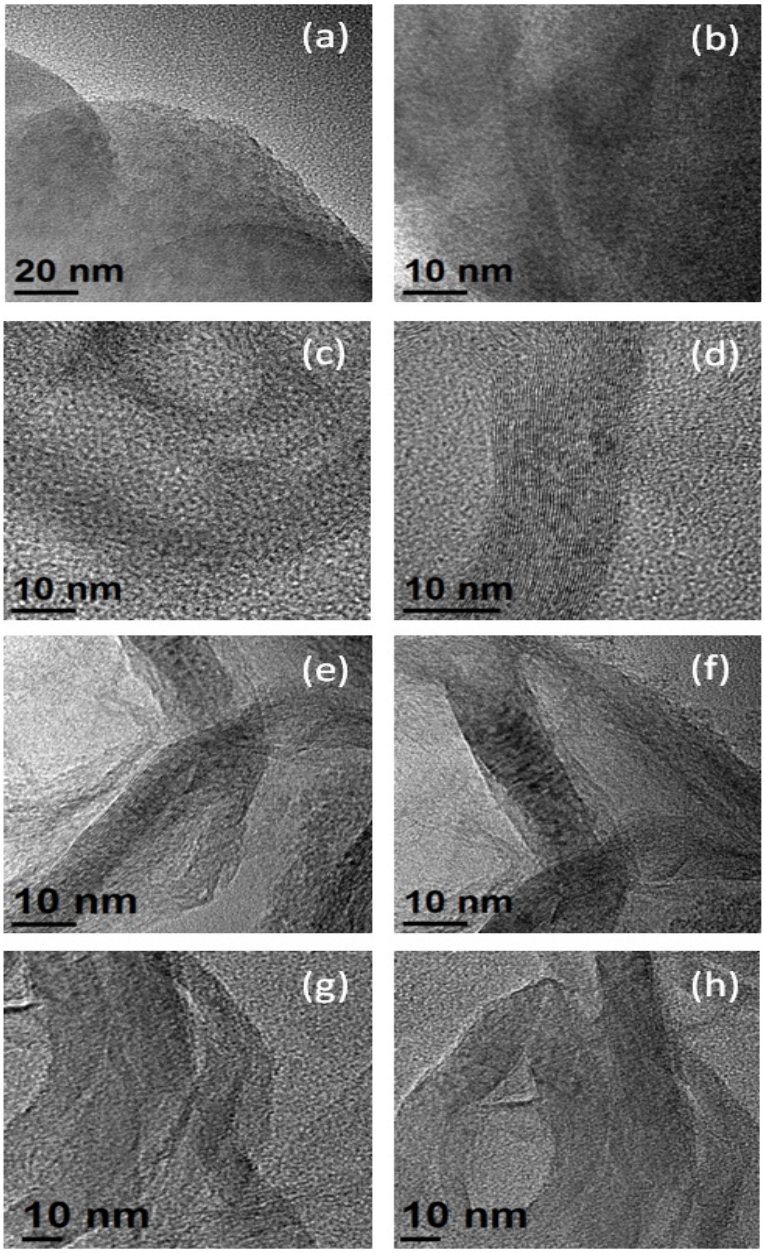

Figure 6.6: TEM images of two different regions of 9AC1 (a,b), 9AC2 (c,d), 9AC3 (e,f) and 9AC4 (g,h).

The heat-treatment-induced graphitization in disordered carbons is reported to be more or less uniform since the ordering is brought about by the thermal energy which is uniformly supplied to the material [34]. However, the catalytic graphitization by KOH activation occurs in a different manner. Here, the graphitization is triggered by metallic potassium and therefore occurs only at regions where metallic potassium is incorporated [26]. This limits the graphitization in KOH activated carbon to a localized phenomenon. In addition to the localized graphitization, a disordering effect also arises due to the formation of pores and oxidation reactions involving carbon and KOH as observed by nitrogen adsorption analysis [35]. Thus, during KOH activation, there is a competition between the ordering and disordering parameters which leaves the graphitization localized to a different extent as observed in the TEM images. Further, due to the localized graphitization, the coherence lengths calculated from XRD data can be only considered as the average values.

6.4.4 Raman spectroscopy

Raman spectra were recorded in order to obtain a more comprehensive information about the microstructure of the activated carbon. As mentioned in previous chapters, perfect graphite with sp^2 carbon networks shows a single sharp Raman band centered at 1580 cm^{-1} (G-peak) corresponding to the Raman active doubly degenerate phonon mode with E_{2g} symmetry at the Brillouin zone center. In highly disordered carbons with L_a less than 50 Å, like in charcoal, a distinctly different Raman spectrum is observed with two broad peaks, one centered around 1580 cm^{-1} corresponding to the graphitic G-peak of sp^2 carbon network and another broad peak centered around 1330 cm^{-1} called the D-peak [38]. However, in disordered carbon with micro- or even-nano sized graphitic regions, two additional features are observed in addition to the G- and D-peaks called the D′- and G′-peaks positioned around 1625 cm^{-1} and 2650 cm^{-1}, respectively [38,39]. The D- and D′-peaks emerge due to the breakage of crystal symmetry in the presence of disorder which activates certain vibrational modes which are otherwise forbidden

in a perfect sp^2 lattice [40]. The symmetry-allowed G′-peak corresponds to the overtone of the D-peak and appears in the second-order Raman spectra of crystalline graphite. G′-peak is very sensitive to the stacking order of the graphene sheets along the c-axis [39,41]. Irrespective of the excitation source, the L_a values can be estimated for nanographitic carbon from the D-peak to G-peak intensity ratio by using Equation 6.7, where λ is the laser line wavelength in nm units [42].

$$L_a(nm) = 2.4 \times 10^{-10} \lambda^4 \frac{I(D)}{I(G)}^{-1} \tag{6.7}$$

This relation connecting L_a and *I(D)/ I(G)* has (Equation 6.7) shown to be in good agreement with L_a calculated from XRD profile for less defective nanographites with uniform size distribution but shows large deviations for less uniformly graphitized specimens [43,44].

The Raman spectra of the control samples (8AC0, 9AC0 and 10AC0) and samples activated at 800 °C (8AC series) show similar features (Figure 6.7) with broad D- and G-peaks, as expected for carbonaceous materials a with low degree of crystallinity, with their L_a and L_c in angstrom range [38]. However, for 8AC4, an additional small peak is observed at ∼2650 cm^{-1}, which corresponds to the G′-peak normally observed in systems with higher crystallinity. On increasing the activation temperature to 900 °C and 1000 °C, D- and G-peaks become narrower with the appearance of the D′ feature, indicating a growth in the in-plane coherence lengths with activation and formation of graphitic regions with well defined boundaries and relatively narrow size distribution. Moreover, the G′-peak is also observed suggesting an ordering along c-axis in the KOH activated samples. It has been shown that the G′-peak profile depends critically on the number of graphene layers for graphenes, samples with less than 5 layers [45]. A single layer graphene gives a single G′-peak whereas in the case of bilayer and few-layer graphene the G′-peak has a shoulder and can be deconvoluted into two or more number of peaks due to the splitting of phonon branches or electronic bands on stacking [45].

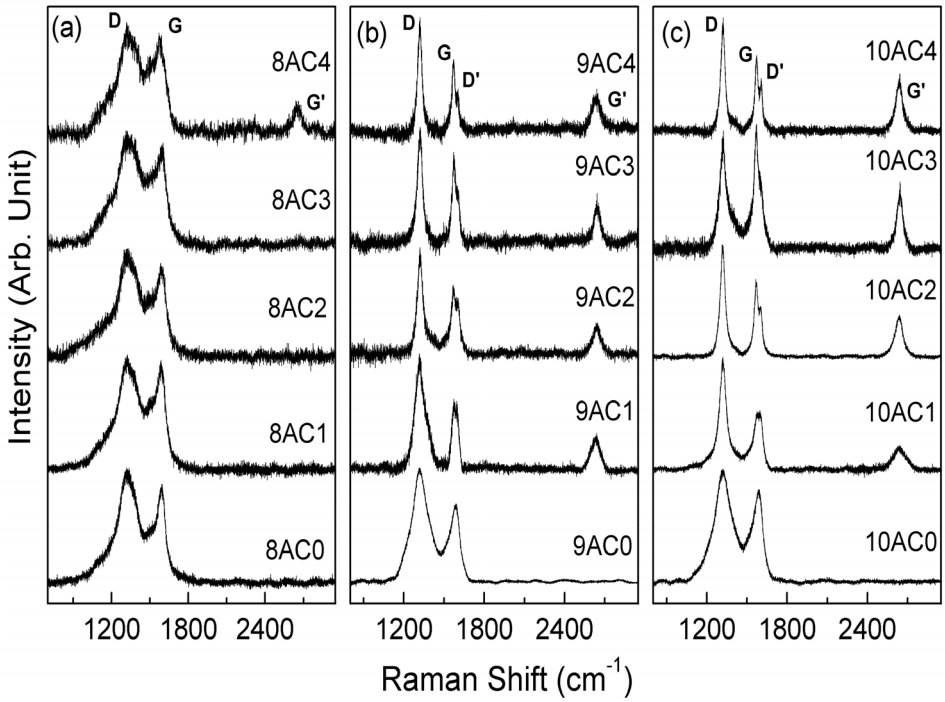

Figure 6.7: Raman spectra of control samples and carbon samples activated at (a) 800 °C, (b) 900 °C and (c) 1000 °C using different amounts of KOH. The spectra are normalized with respect to the intensity of the D-peak.

Similar difference in the G′-peak profile is observed while moving from turbostatic to crystalline graphite because of the increase in the interaction between the basal planes of graphitic clusters in crystalline graphite which results in splitting of π electrons dispersion energies giving several contributions to the G′-peak, similar to that of few-layer graphene [40,41,46]. The G′-peak profile of all the KOH activated samples show a single peak nature (Figure 6.7), similar to that reported for turbostatic graphite [47], where the interaction between the graphitic basal planes is much weaker and hence having a two-dimensional graphitic character. After activation, the G′-peak position remains more or less static but the peak intensity is found to be increasing with increase in the amount of KOH used for activation, for samples activated at 900 and 1000 °C. Casiraghi *et al.* had observed similar changes in the G′-peak intensity with the ordering of graphene while probing the disorder in oxidized graphene [48]. However on moving from samples 9AC3

to 9AC4 and 10AC3 to 10AC4, the peak intensity decreased slightly indicating that a further increase in the amount of KOH used for activation suppresses the stacking order of graphite. This shows good agreement with the variation trend in average L_c values calculated from XRD data which showed a regular increase while moving from samples 9AC0 to 9AC3 and 10AC0 to 10AC3 followed by a drop in L_c for 9AC4 and 10AC4 respectively. Table 6.1 summarizes the changes observed in different Raman parameters for the KOH activated samples.

The in-plane coherence length, L_a calculated from the *I(D)/I(G)* ratio, using Equation 6.7 is found to be varying arbitrarily after activation with their values being nearly ten times higher (∼30 nm) than those calculated from the XRD data (∼3 nm). This is rather unusual for thermally graphitized graphitic carbon, for which generally a better agreement between the L_a values calculated from XRD data and Raman spectra is expected [40,43,47]. To explain this large difference between the coherence lengths calculated from the Raman spectra and XRD profiles, one needs to consider the nature of graphitization process. The thermally induced graphitization should result in more or less uniformly graphitized specimen, since the ordering is due to thermal energy which is uniformly supplied to whole material. However in the KOH activated samples, the catalytic graphitization occurs only at regions where metallic potassium is incorporated and hence should be a localized phenomenon. Similarly, there is also a disordering effect arising due to the formation of pores and oxidation reactions (reactions 1 to 4) while using larger amounts of KOH which is independent of the amount of potassium metal incorporation. Therefore while probing the structure with XRD, which gives only average values, whereas Raman spectroscopy is very sensitive towards the clustering of sp^2 phase in the disordered carbon network. Therefore, the large difference in the calculated structural parameters should be the result of this highly localized graphitic ordering after KOH activation in an amorphous background containing different types of defects.

The Raman G-peak position of the activated carbons is very much sensitive towards the disorder present in the material along with the cluster dimensions of

Table 6.1: I(D)/I(G), L_a *calculated using Equation 6.7, G-Peak position, I(G′) and G′-Peak position of the KOH activated samples.*

Sample code	*I(D)/I(G)*	L_a (nm)	G-Peak Position (cm^{-1})	I(G′) (Arb. Unit)	G′-Peak Position (cm^{-1})
8AC0	1.24	31	1587	-	-
8AC1	1.07	36	1586	-	-
8AC2	1.22	32	1586	-	-
8AC3	1.16	33	1584	-	-
8AC4	1.04	37	1580	17	2646
9AC0	1.51	25	1587	-	-
9AC1	1.72	22	1575	122	2634
9AC2	1.58	24	1571	107	2644
9AC3	1.37	28	1572	158	2640
9AC4	1.64	23	1571	152	2637
10AC0	1.24	31	1588	-	-
10AC1	1.95	20	1574	90	2637
10AC2	1.55	25	1570	160	2637
10AC3	0.92	42	1568	232	2642
10AC4	1.48	26	1570	222	2637

the graphitized regions. For noncrystalline graphite, the G-peak position, shifts towards lower energy region as observed previously by Robertson *et al.*, indicating disordering of the carbon lattice [38]. After KOH activation, the major disordering factor that is observed is the introduction of sub-nanometer sized pores and their growth to supra-nanometer pores under extreme oxidation and carbon gasification conditions. For control samples (8AC0, 9AC0 and 10AC0) the G-peak is positioned at 1587 cm^{-1}. On comparing the G-peak position of the activated samples, as shown in Table 6.1, the shift in the G-peak position for samples activated at 800 °C (Figure 6.7) is much more gradual when compared to those samples activated at 900 and 1000 °C. Considering that the coherence lengths calculated from the XRD patterns are smaller and the G′-peak is absent in the Raman spectra for samples activated at 800 °C, it can be concluded that the potassium mediated catalytic graphitization does not occur in carbon samples activated at 800 °C. Therefore, in carbon samples activated at 800 °C, the extent of shift in the G-peak position can be assigned solely to the increase in the disorder. Since the gradual shift in the G-peak position coincides with the increase in the surface area after activation at 800 °C, the increase in the structural disorder for samples activated at 800 °C may be assumed to be due to the development of the surface area (Figure 6.4) and porosity (Figure 6.5). However, for KOH activation at 900 and 1000 °C, unlike at 800 °C, the structural ordering also occurs along with the large increase in the surface area and pore diameters. Here, there is a large shift in the G-peak position while moving from sample 9AC0 to 9AC1 and from sample 10AC0 to 10AC1, indicating that the disordering effect is more prominent when compared to the graphitization effect. This observation is in complete agreement with the development of microstructure observed from XRD and surface area analysis. However, as the KOH/C ratio increases, this shift becomes much more gradual for samples activated at 900 and 1000 °C (9AC1 to 9AC4 and 10AC1 to 10AC4). In highly activated samples, at a microscopic level, the ordering effect could be sufficiently high. In that case, the structural ordering will be overpowered only slightly by the large disordering effect induced due to

the highly porous structure, so that the effect of disordering is partially nullified by the catalytic graphitization.

6.5 Magnetic properties of the activated samples

Both low-temperature and room temperature magnetic measurements were performed on the activated carbon samples to show the changes in the magnetic properties. All the samples are diamagnetic at room temperature, similar to the heat-treated samples discussed in Chapter 4. The magnetization curves of all the activated samples, along with their respective control samples, measured at 2 K are presented in Figure 6.8(a-c). Figure 6.8d shows the initial magnetization curves for the control samples 8AC0, 9AC0 and 10AC0 along with their least squares fit to Brillouin function with J=1/2 (Equation 4.1) [49]. The Brillouin function fits well to the low magnetic field regions of the curves (below 40 kOe) and deviates at higher applied fields indicating that the spins are not more of a non-interacting type, as discussed in Section 4.3.

Since the magnetization curves of activated samples are not fitting to the Brillouin function with J=1/2, the value of J corresponding the best fit of magnetization curves to Brillouin function is calculated. The calculated value of J is (Table 6.2) lower than that is expected for a paramagnetic material (J=1/2), indicating that the individual magnetic moments in the activated samples are interacting. The magnetization of the control samples decreases with increase in the activation temperature (Figure 6.8d), which is consistent with that observed on the effect of heat-treatment induced graphitization on the magnetic properties, as discussed in Chapter 4 (Section 4.3). The magnetization (Figure 6.9) of activated samples increases with increase in the amount of KOH used for activation, except for those activated with the highest amount of KOH. This behavior is nearly similar to the variation in the surface area (Figure 6.4). This is probably due to the large increase in the number of edge states and defects in the activated carbons as the surface area increases. At high applied magnetic field, the edge state spins and the magnetic moment contributed by defects tend to align to the field resulting in

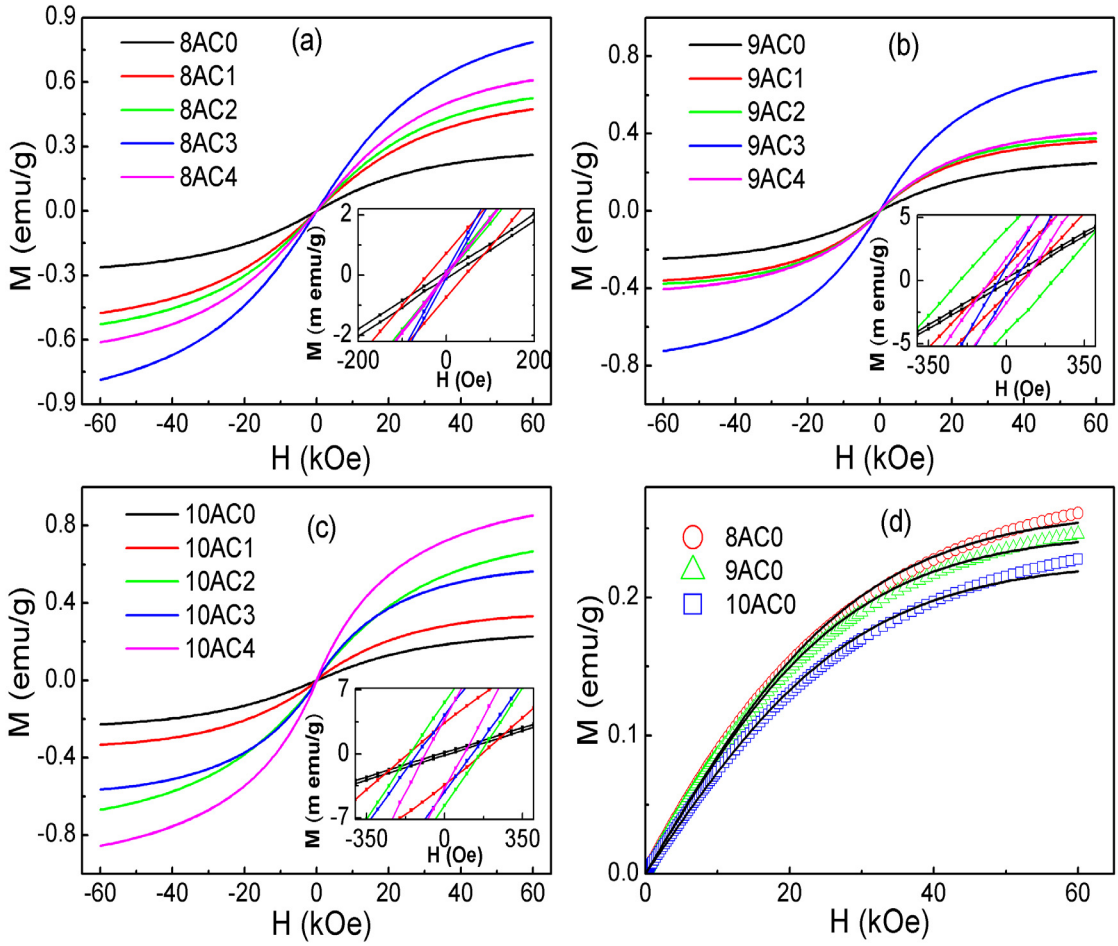

Figure 6.8: Magnetization curves for (a) 8AC series, (b) 9AC series and (c) 10AC series measured at 2 K. The insets show the zoomed curves at low fields. (d) Black solid lines are fit to initial magnetization curves (open circles) of control samples using Brillouin function with J=1/2.

an increase in the magnetization. This makes the changes in the magnetization (Figure 6.9) and surface area (Figure 6.4) of the activated samples comparable. The small discrepancy in the evolution of the magnetization with that of the surface area could be due to the inconsistent contributions from the edge state spins.

Along with the activated samples, the control samples also show a negligibly small coercivity (Figure 6.8a-c). This is similar to the coercivity observed in heat-treated carbons which result from the blocking of the spins in a disordered carbon

Table 6.2: The value of J obtained after fitting the initial magnetization curves of activated and control sample to Brillouin function.

Sample code	J	Sample	J	Sample	J
8AC0	0.489	9AC0	0.483	10AC0	0.421
8AC1	0.399	9AC1	0.912	10AC1	0.671
8AC2	0.420	9AC2	0.926	10AC2	0.456
8AC3	0.369	9AC3	0.734	10AC3	0.988
8AC4	0.394	9AC4	0.827	10AC4	0.889

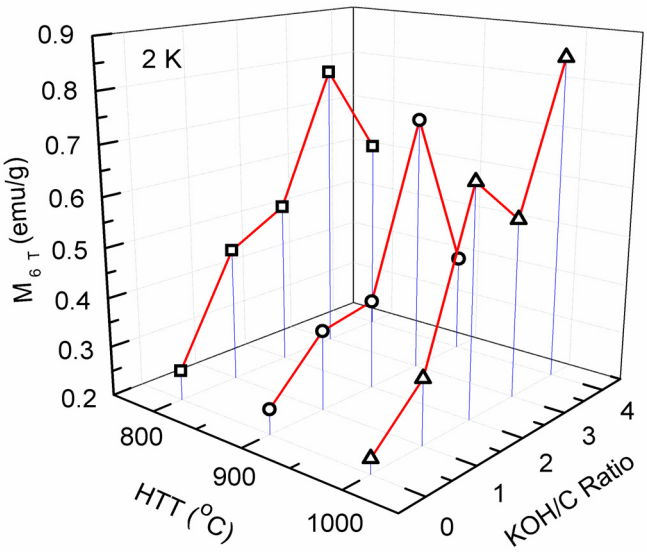

Figure 6.9: The magnetization of the samples activated at different activation conditions. The red and blue lines are guides to the eyes.

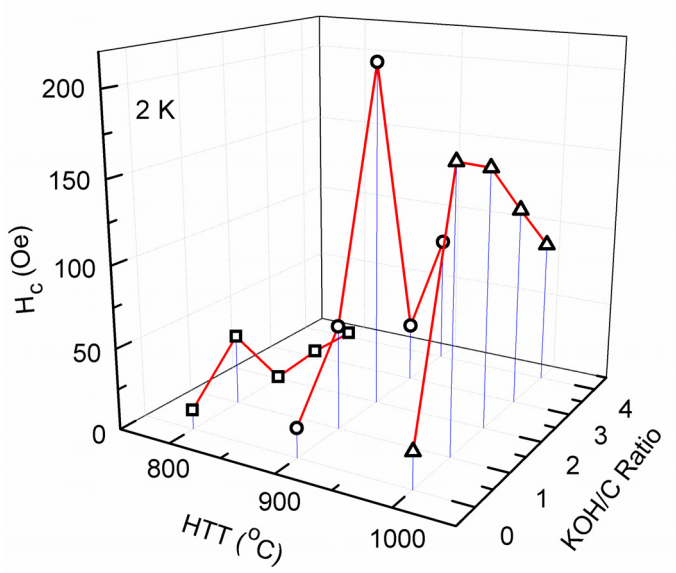

Figure 6.10: The coercivity of the samples activated at different activation conditions. The red and blue lines are guides to the eyes.

structure, as discussed in Chapter 4 (Section 4.3). A three dimensional plot of the magnetization at 60 kOe (M_{6T}), measured at 2 K, and the coercivity (H_c) of the activated samples against the activation temperature and the KOH to carbon weight ratio is shown in Figure 6.9 and Figure 6.10, respectively. The coercivity, which arises due to the blocking of the spins along random directions is known to depend on the microstructure of the materials as well as the magnetic anisotropy [49,50]. In the case of KOH activated carbon, the coercivity (Figure 6.10) varies in a similar manner as that of the coherence lengths calculated from the XRD data (Figure 6.2 and Figure 6.3). In a heterogeneously graphitized material, there can be considerable local magnetic anisotropy at the graphitic edges, which contributes towards the blockage of edge state spins among random directions resulting in an observable coercivity. Therefore, the total anisotropy contribution varies with the graphitic cluster size (microstructure) of the graphitized specimens. Another factor which likely has similar effect on both the magnetization and the coercivity is the different contributions from the various oxygen functionalities produced by the fundamental oxidation reactions occurring during KOH activation [24,50–52]. Experiments using graphene oxide have shown a change in the magnetization

values for different samples depending on the type of oxygen functionality present in the sample [50]. The uncompensated spins of many oxygen functionalities can be blocked in random directions, depending on the local environment, and hence can contribute towards the coercivity.

The temperature variation of magnetization is measured from 2 K to 300 K under an applied field of 10 kOe (1 T) under both FC and ZFC conditions (Figure 6.11). All the samples show a broad magnetic transition with a hump below

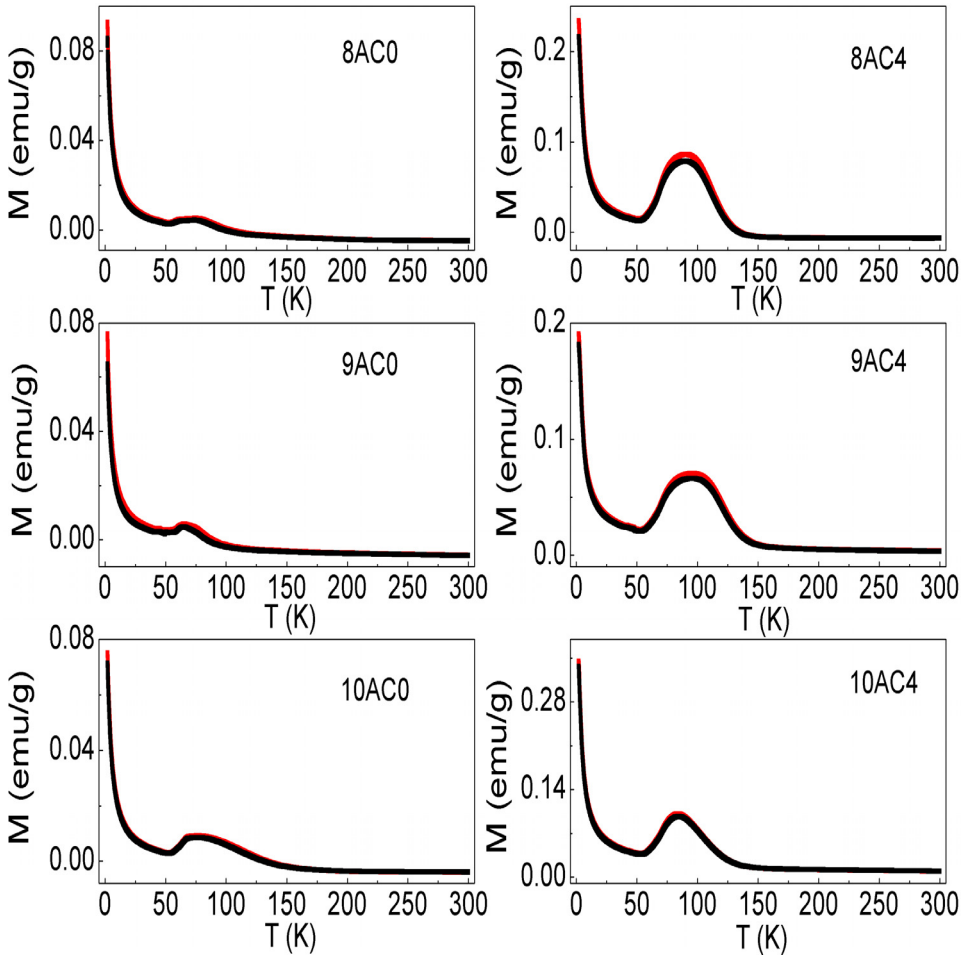

Figure 6.11: ZFC (black) and FC (Red) magnetization curves measured under 10 kOe magnetic field for control samples and those activated with highest amount KOH at 800 °C, 900 °C and 1000 °C.

150 K whose magnitude is larger for the activated samples than for control samples heat-treated at the same temperature. Similar magnetic transition with a

hump was observed in heat-treated and partially graphitized carbon samples, as discussed in Chapter 4 (Section 4.7). This magnetic transition is also similar that previously observed in thermally graphitized carbons which indicate the presence of a disordered magnetic state in the material [53]. This kind of disordered magnetism arises due to the complexity of the spin interactions when localized graphitic clusters having different magnetic strengths are present in the material [12,52,53].

In the activated samples, the broad maximum is centered around 100 K, unlike in the control samples where the maximum is centered around 60 K. Moreover, the maximum is more predominant after activation when compared to that in the control samples. These changes in the nature of the broad low-temperature magnetic transition could be due to the structural complexity arising from the local ordering and/or disordering factors in the activated samples. In the activated samples, the extent of graphitization is much higher when compared to that of the heat-treated samples discussed in Chapter 3 (Section 3.3). The highly heterogeneous structure of the activated carbon samples, with the localized graphitic regions, can lead to more complex inter-nanographene and intra-nanographite spin interactions when compared to that of the heat-treated samples (HT500–HT1000) discussed in Chapter 4 (Section 4.4) [12].

6.6 Electrical properties of the activated samples

The low-temperature electrical transport properties were measured using the Van der pauw method after compacting the activated carbon powders to hard pellets at 16 MPa pressure. One drop of 2% polyvinyl alcohol solution was used as the binder while preparing the pellets from 0.5 g of the powder.

In a disordered material, the electrical conductivity (σ) is determined by the extent of disorder [53]. For carbon materials, σ has been found to increase with an increase in the heat-treatment temperature due to the temperature assisted

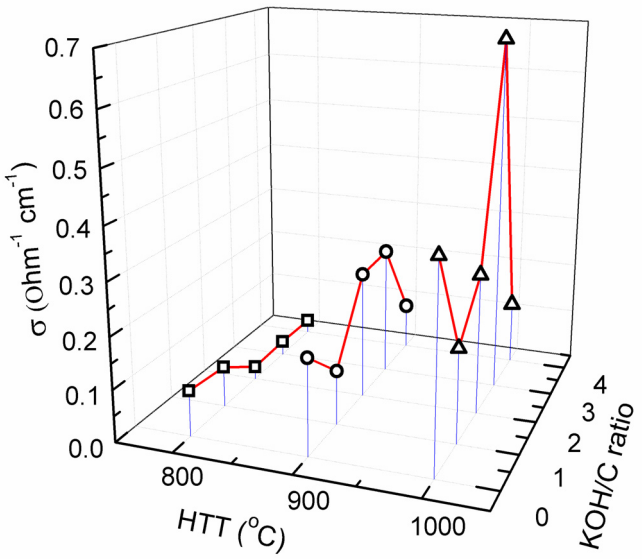

Figure 6.12: The room temperature electrical conductivity of the samples activated at different conditions. The red and blue lines are guides to the eyes.

structural ordering. [53] A similar increase in σ is observed with the increasing heat-treatment (Figure 6.12) temperature from 800 °C to 1000 °C for the control samples. This increase in the conductivity corresponds to the variation in coherence lengths calculated from XRD for these samples. A similar increase in conductivity was observed for the heat-treated carbon pellets with an increase in heat-treatment induced graphitization, as discussed in Chapter 5 (Section 5.3). Therefore, the changes in σ for the control samples with an increase in heat-treatment temperature can be considered as a resultant of the thermally induced structural ordering. However, for samples activated at 800 °C, conductivity decreases with increasing the amount of KOH. To account for this decrease in conductivity, the role of sub-nanometer pores generated needs to be considered. The XRD data showed that the samples activated at 800 °C have a poor graphitic ordering. Even 8AC4, which is activated with the highest amount of KOH, has a very weak G′ peak compared to those activated with much lower KOH to carbon weight ratio at 900 and 1000 °C, indicating a lower extent of graphitic character for 8AC4. Therefore, the increase in the defect-induced scattering of charge carriers in the activated samples is likely to reduce the conductivity by decreasing the

mean free path of the charge carriers. However, the conductivity of the samples activated at 900 and 1000 °C, shows large variations depending on the amount of the activating agent used. On comparing 9AC1 and 10AC1 with their respective control samples, the σ is decreased by 0.08 $Ohm^{-1}cm^{-1}$ and 0.21 $Ohm^{-1}cm^{-1}$, respectively. This drop in the conductivity is much higher when compared to that observed after activation at 800 °C and is likely to be due to the large increase in the number of pores and their widening without much enhancement in the crystallinity of the material. For the samples activated at 900 and 1000 °C, the conductivity almost follows the variation in the coherence lengths (Figure 6.2 and Figure 6.3) calculated from XRD data. This shows that the defect induced scattering in the disordered carbon depends on both the extent of graphitic ordering as well as the inter-nanographite percolation pathways created with the development of porosity. As the dimensions of the individual graphitic clusters increase, the resistive contributions from nanographite boundary scattering decreases since the number of graphitic clusters decreases and therefore the electronic transport becomes more efficient [53]. However, when the disorder becomes much larger, the transfer of electrons between the graphitic clusters may not be effective enough, due to which the conductivity diminishes in the case of 9AC4 and 10AC4.

Figure 6.13 shows the normalized temperature dependent resistivity of the samples activated at 800 °C. Figure 6.14 and Figure 6.15 present the normalized resistivity curves for the samples activated at 900 °C and 1000 °C, respectively. For all the samples, resistivity increases as the temperature is decreased indicating semiconducting nature of the materials. This increase in resistance points towards the localization of charge carriers in a disordered material, as discussed in Chapter 5 (Section 5.4). It can be noted that the increase in the resistivity is very small compared to that of the disordered carbons heat-treated at 600 °C and 700 °C (Figure 5.3, Chapter 5) and is comparable to those heat-treated at higher temperatures. This indicates that the disorder induced after KOH activation in the form of pores are not effective enough in bringing about large localization effects as observed in disordered carbons heat-treated at 600 °C and 700 °C. However,

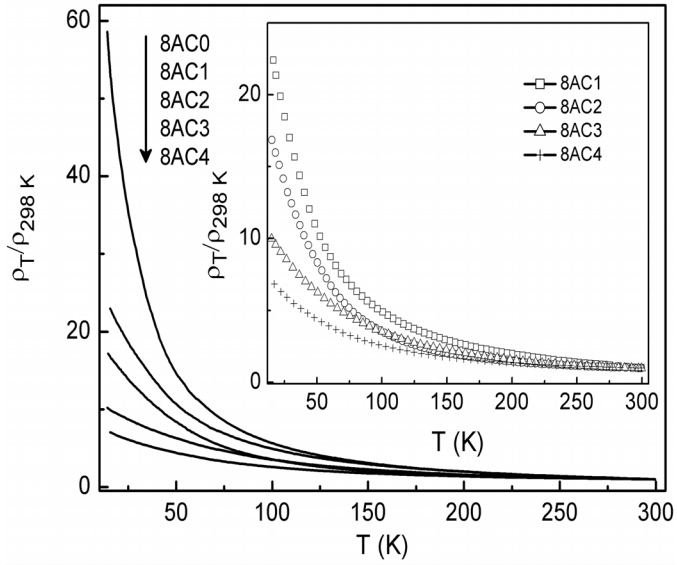

Figure 6.13: The temperature variation of resistivity of samples activated at 800 °C. Inset shows a zoomed view for 8AC1, 8AC2, 8AC3 and 8AC4.

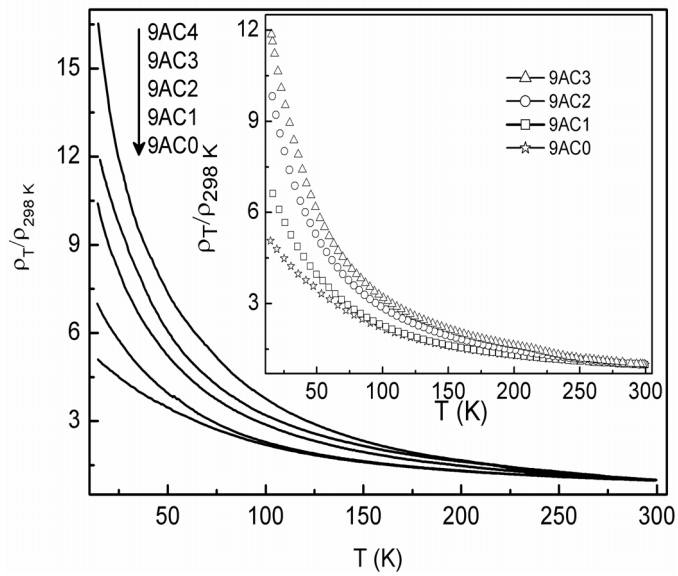

Figure 6.14: The temperature variation of resistivity of samples activated at 900 °C. Inset shows a zoomed view for 9AC0, 9AC1, 9AC2 and 9AC3.

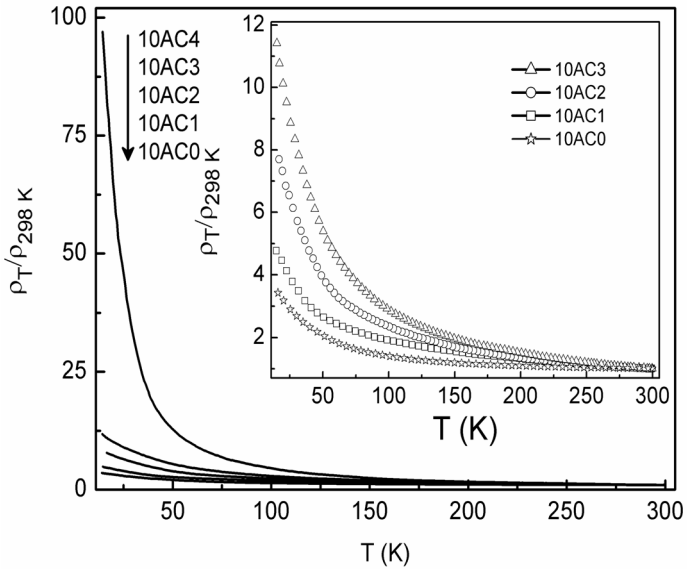

Figure 6.15: The temperature variation of resistivity of samples activated at 1000 °C. Inset shows a zoomed view for 10AC0, 10AC1, 10AC2 and 10AC3.

the increase in the resistivity with decreasing temperature for the control samples 8AC0, 9AC0 and 10AC0 is relatively large when compared to the carbon pellets heat-treated at 800, 900 and 1000 °C (Figure 5.3, Chapter 5). This variation must be arising from the difference in the processing conditions.

Figure 6.16 presents the low-temperature to room temperature resistivity ratio (ρ_{16K}/ρ_{298K}) of the activated samples, as a function of the KOH/C ration, which is a measure of the degree of disorder present in the materials [19]. The samples activated at 800 °C show a decrease in ρ_{16K}/ρ_{298K} when compared to that of 8AC0, with an increase in the amount of KOH used for activation (Figure 6.16a). This indicates that with an increase in the amount of KOH used for activation, the samples are undergoing structural ordering. However, for samples activated at 900 °C (Figure 6.16b) and 1000 °C (Figure 6.16c) this trend is reversed with an increase in the value of ρ_{16K}/ρ_{298K} with an increase in the amount of KOH, suggesting a disordering of the carbon lattice. This is consistent with the development of pore structure and catalytic graphitization observed in these samples. The KOH activation at 800 °C leads to the generation of sub-nanometer pores and does not considerably assist the pore widening process. At the same time, the broad (*100*)

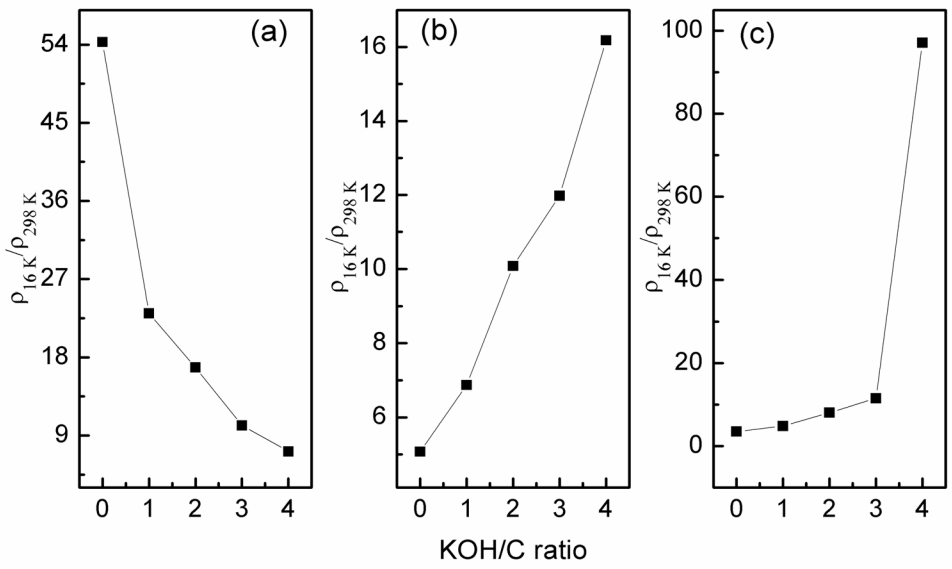

Figure 6.16: The low-temperature to room temperature resistivity ratio for samples activated at (a) 800 °C, (b) 900 °C and (c) 1000 °C. Solid lines are guide the to eyes.

and (*002*) peaks in the XRD patterns of the samples activated at 800 °C indicate (Figure 6.1) that the graphitization due to the incorporation of potassium metal is not occurring in these samples. However, the appearance of G′-peak in the Raman spectra of (Figure 6.7) 8AC4 indicate that the KOH activation is effective in bringing about local ordering on a microscopic scale. The comparatively lower downshift of G-peak for samples activated at 800 °C when compared to the others (Table 6.1) confirms that comparatively smaller disordering effect is operating in those samples. The reversal in the dependence of ρ_{16K}/ρ_{298K} on the amount of KOH used for samples activated at 900 °C and 1000 °C can be directly correlated to the pore widening observed in these samples which overpowers the structural ordering caused by catalytic graphitization, making these samples more disordered and thereby inducing a larger downshift of G′-peak.

The ρ-T curves of the activated samples were analyzed with respect to different conductivity models. As discussed in Chapter 5 for the heat-treated samples, different models like activated hopping (Equation 5.1) [54], Mott-VRH (Equation 5.2) [55], ES-VRH (Equation 5.3) [56], disorder induced scattering (Equation 5.6) [57] and 2D weak localization (Equation 5.7) [58], were considered for

the analysis. Figure 6.17 shows the fit of the resistivity curve to different theoretical models. The sample 8AC2 exhibited the lowest room temperature resistivity among all the activated samples, which is even lower than that of the carbon samples heat-treated above 900 °C (samples HT900 and HT1000, Chapter 5). However, the resistivity data of 8AC2 does not fit to the conduction mechanisms of samples with low resistivity, involving the weak localization mechanism (Equations 5.6 and 5.7) [19,58]. Similarly, an analyses based on activated hopping, Mott-VRH, ES-VRH or multiphonon tunneling conduction mechanisms were also found to be invalid for explaining the ρ-T curves in the entire measured temperature region. For other activated samples also the resistivity data did not fit to any of the conductivity models in the entire measured temperature region. During their study on the transport properties of self organized carbon networks, Govor *et al.* identified three distinctly different mechanisms operating in the same material below room temperature, which includes ES-VRH at low temperatures, Mott 3D-VRH at intermediate temperature and a combination of power law dependence and Mott VRH near to room temperature [59]. The existence these transport mechanisms were attributed to tails in the density of localized states, which are pulled out of the conduction and valence band, as a result of disorder and some overlap between these tails. Similarly, two different conduction regimes are identified in boron doped amorphous carbon films, where the temperature exponent in the VRH equation (Equation 5.3) was found to be changing from 0.25 to 0.5, as the temperature decreases, indicating a crossover from Mott-VRH to ES-VRH [20]. However, for the KOH activated samples, an attempt to fit specific regions of the resistivity curves to different exponents of temperature in Mott-VRH by plotting logρ against temperature on a log-log scale resulted in unrealistic exponential values with little physical significance. The microstructure of samples presented here are highly complex when compared to those studied previously [19,20,59]. This structural complexity involved due to the presence of both localized conducting graphitic regions along with the high amount of disordering factors can induce unique characteristics to the band structure. Therefore the temperature

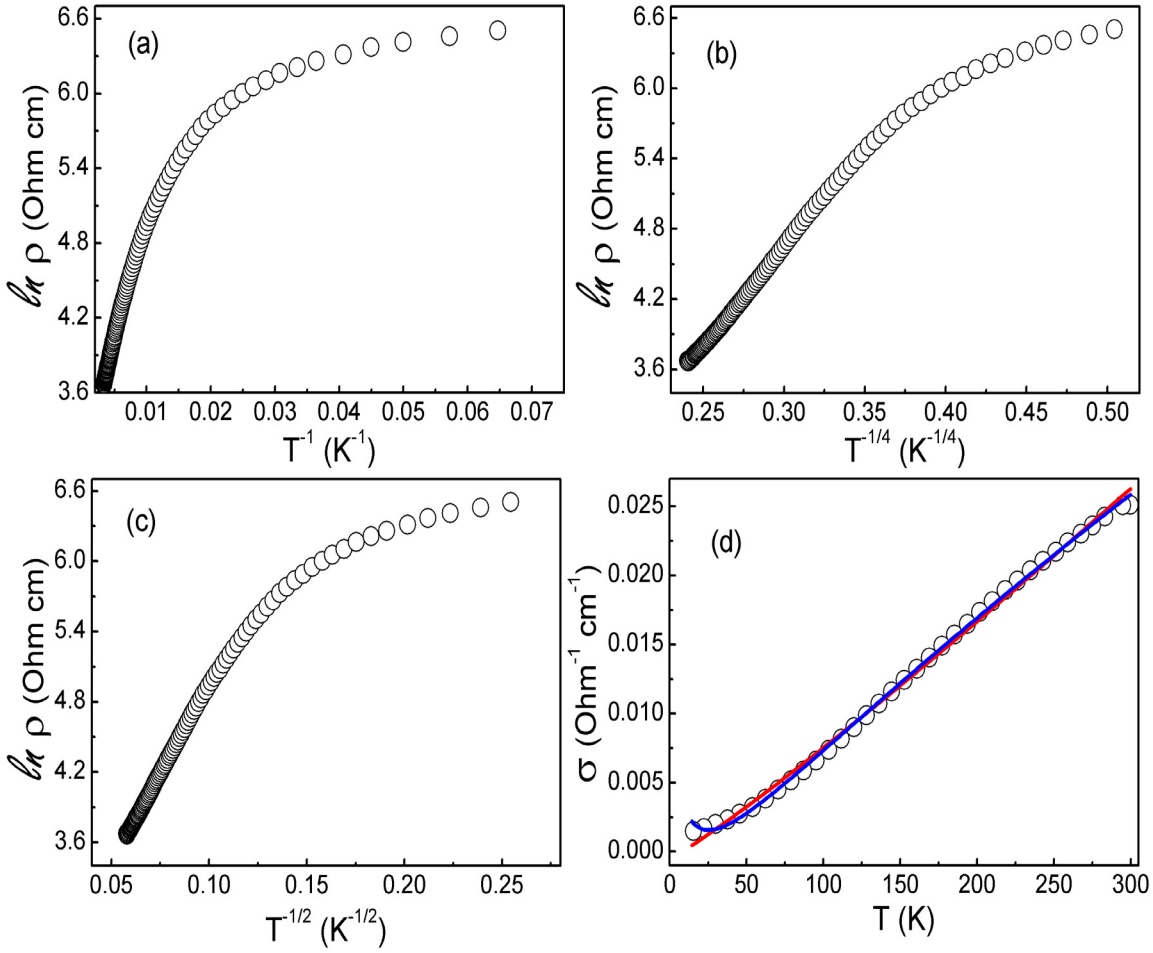

Figure 6.17: The measured resistivity curve of 8AC2 showing deviations from (a) activated hopping law, (b) Mott 3D VRH law and (c) ES VRH law. (d) The fits of the experimental data (open circles) to disorder induced scattering mechanism (red line) and 2D weak localization mechanism (blue line).

dependence of resistivity has contributions arising from combinations of different conduction mechanisms at unknown proportions. The unidentified parameters like the spatial correlation of graphitized regions, distribution of cluster size, the pore geometry, their distribution, etc. therefore becomes significant in relating conduction mechanism to the microstructure. Moreover, unlike the dense heat-treated carbon pellets studied in Chapter 5, the activated carbon pellets used for electrical measurements are compacted from powders and not sintered. Therefore, the low density pellets contain loose grains and pores in them. The additional electrical resistance contributions due to the grain boundary and pores also needs to be considered while explaining the conduction mechanism in the KOH activated carbon materials and this is beyond the scope of present work.

6.7 Conclusions

A detailed investigation on the structural, magnetic and electrical properties of activated carbon, a material which is of huge commercial importance due to its surface characteristics in applications like adsorption, gas storage and as an electrode material is presented in this chapter. The structural characterization of the KOH activated carbons using X-ray diffraction, Raman spectroscopy and Transmission electron microscopy revealed the occurrence of a localized graphitization in the materials. The changes in surface area and porosity, after activation, were determined by nitrogen adsorption technique. Results showed that the activated samples are highly porous and have a large specific surface area when compared to the control specimens. With the increase in the activation temperature, the adjacent pores merge together to produce wider pores, which in turn decrease the specific surface area. This observation is in line with previous reports on KOH activated carbon. A detailed study using X-ray diffraction technique pointed towards the development of graphitic clusters in the activated samples. The in-plane and the out-of-plane coherence lengths increased as the activation temperature and the amount of KOH used for activation are increased. However, it was observed that at extreme activation conditions, when a large amount of KOH was used for

activation, the coherence lengths dropped to very low values. Raman spectroscopy was employed in order to obtain better insights on the activation dependent developments in the microstructure. The *I(D)/I(G)* ratio and G-peak position in the Raman spectra, which are sensitive towards the in-plane and out-of-plane ordering of graphitic cluster indicated arbitrary variation in the in-plane ordering with activation, while the out-of-plane ordering was in agreement with that observed from XRD studies. This suggested that the graphitic clusters have nearly the same out-of-plane dimension, whereas the in-plane dimensions are quite different. These facts further confirmed from TEM studies, which showed the presence of inhomogeneity distributed assemblies of graphitic chains forming regions with different morphologies.

The magnetic and electrical properties of the KOH activated samples were studied. The KOH activated carbons showed interesting magnetic properties, with increased coercivity and low-temperature magnetization than that of the control samples. The presence of dangling bonds as well as magnetic edge states in the zig-zag graphene edges are ascribed to be responsible for the magnetic properties of the carbon-only systems. Here, both the factors contribute to the magnetic properties since the samples contain isolated graphitic clusters as well as dangling bonds due to the porous structure. The magnetization curves were not fitting to Brillouin function with J=1/2, indicating that the samples are not paramagnetic. Further, the changes in the low-temperature magnetization at 60 kOe and the coercivity of the activated carbon samples could be correlated respectively to the development of the specific surface area and the coherence lengths calculated from the XRD data. The observation of a pronounced broad feature below 150 K, in the temperature variation of magnetization, for activated samples confirm the presence of a disordered magnetic state as in the case of spin-glasses arising from different magnetic exchange interactions of variable strengths.

The room temperature resistivity and the ρ_{16K}/ρ_{298K} ratio showed typical variations that could be correlated with the structural evolution after KOH activation. A comparison between the changes in the room temperature conductivity and the

coherence lengths calculated from XRD showed that the conductivity is directly varying with the graphitic cluster dimension. For samples activated at 800 °C, ρ_{16K}/ρ_{298K} decreases with increase in the amount of KOH used for activation, indicating the ordering of carbon atoms with activation, whereas for samples activated at 900 and 1000 °C, the trend was opposite, indicating disordering. These change could be explained on the basis of development in porosity with activation at these temperatures which competes with the clustering of the graphitic phase. The control sample heated at 1000 °C showed the highest low-temperature to room temperature resistance ratio, typical of the electronic systems with a large structural disorder, which induces the localization of charge carriers. However, the elucidation of exact conduction mechanism operating below room temperature was difficult due to the complexity of the system, where many different mechanisms like activated hopping, Mott-VRH, ES-VRH, weak localization, etc. might be operating at different proportions depending on the temperature range.

Bibliography

[1] C. Brasquet and P. Le Cloirec, *Carbon* 35 (1997) 1307.

[2] T. Otowa, R. Tanibata and M. Itoh, *Gas Sep. Purif.* 7 (1993) 241.

[3] J. P. Marco-Lozar, M. Kunowsky, F. Surez-Garca, J. D. Carruthers and A. Linares-Solano, *Energy Environ. Sci.* 5 (2012) 9833.

[4] H. Wang, Q. Gao and J. Hu, *J. Am. Chem. Soc.* 131 (2009) 7016.

[5] J Wang and S. Kaskel, *J. Mater. Chem.* 22 (2012) 23710.

[6] Y. Zhu, S. Murali, M. D. Stoller, K. J. Ganesh, W. Cai, P. J. Ferreira and A. Pirkle, *Science* 332 (2011) 1537.

[7] P. Stamenov and J. M. D. Coey, *J. Magn. Magn. Mater.* 290 (2005) 279.

[8] M. M. Ugeda,I. Brihuega, F. Guinea, and J. M. Gomez-Rodryguez, *Phys. Rev. Lett.* 104 (2010) 096804.

[9] T. L. Makarova, *Semiconductors* 38 (2004) 615.

[10] O. V. Yazyev and L. Helm, *Phys. Rev. B* 75 (2007) 125408.

[11] L. R. Radovicand B. Bockrath, *J. Am. Chem. Soc.* 127 (2005) 5917.

[12] T. Enoki and K. Takai, *Solid State Commun.* 149 (2009) 1144.

[13] J. Wang and S. Kaskel, *J. Mater. Chem.* 22 (2012) 23710.

[14] L. L. Zhang and X. S. Zhao, *Chem. Soc. Rev.* 38 (2009) 2520.

[15] J. Gamby, P. L. Taberna, P. Simon, J. F. Fauvarque and M. Chesneau, *J. Power Sources* 101 (2001) 109.

[16] X. Du, C. Wang, M. Chen, Y. Jiao and J. Wang, *J. Phys. Chem. C* 113 (2009) 2643.

[17] P. A. Lee and T. V. Ramakrishnan, *Rev. Mod. Phys.* 57 (1985) 287.

[18] N. F. Mott, *Adv. Phys.* 61 (1967) 49.

[19] K. Takai, M. Oga, H. Sato, T. Enoki, Y. Ohki, A. Taomoto, K. Suenaga and S. Iijima, *Phys. Rev. B* 67 (2003) 214202.

[20] P. N. Vishwakarma and S. V. Subramanyam, *J. Appl. Phys.* 100 (2006) 113702.

[21] J. A. Macia-Agullo, B. C. Moore, D. Cazorla-Amoros and A. Linares-Solano, *Carbon* 42 (2004) 1367.

[22] Z. Hu and M. P. Srinivasan, *Microporous Mesoporous Mater.* 27 (1999) 11.

[23] O. Ioannidou and A. Zabaniotou, *Renewable Sustainable Energy Rev.* 11 (2007) 1966.

[24] D. Lozano-Castello, J. M. Calo, D. Cazorla-Amors and A. Linares-Solano, *Carbon* 45 (2007) 2529.

[25] A. Oya and S. Otani, *Carbon* 17 (1979) 131.

[26] K. W. McNamara, P. Ayyappan, R. Rajagopalan, G. J. Chen and H. C. Foley, *Carbon* 56 (2013) 109.

[27] I. Mochida, R. Ohtsubo, K. Takeshita and H. Marsh, *Carbon* 18 (1980) 117.

[28] R. E. Franklin, *Proc. R. Soc. London* A209 (1951) 196.

[29] A. Oya and A. Marsh, *J. Mater. Sci.* 17 (1982) 309.

[30] A. S. Schwartz and J. C. Bokros, *Carbon* 5 (1967) 325.

[31] B. E. Warren, *Phys. Rev.* 59 (1941) 693.

[32] S. H. Yoon, S. Lim, Y. Song, Y. Ota, W. Qiao, A. Tanaka and I. Mochida, *Carbon* 42 (2004) 1723.

[33] N. Tsubouchi, C. Xu and Y. Ohtsuka, *Energy Fuels* 17 (2003) 1119.

[34] F. G. Emmerich, *Carbon* 33 (1995) 1709.

[35] J. Romanos, M. Beckner, T. Rash, L. Firlej, B. Kuchta, P. Yu, G. Suppes, C. Wexler and P. Pfeifer, *Nanotechnology* 23 (2012) 015401.

[36] J. Hayashi, A. Kazehaya, K. Muroyama and A. P. Watkinson, *Carbon* 38 (2000) 1873.

[37] M. Sevilla and A. B. Fuertes, *Carbon* 44 (2006) 468.

[38] A. C. Ferrari and J. Robertson, *Phys. Rev. B* 61 (2000) 14095.

[39] P. Lespade, R. Al-Jishi and M. S. Dresselhaus, *Carbon* 20 (1982) 427.

[40] L. G. Cancado, K. Takai, T. Enoki, M. Endo, Y. A. Kim, H. Mizusaki, N. L. Speziali, A. Jorio and M. A. Pimenta, *Carbon* 46 (2008) 272.

[41] H. Wilhelm, M. Lelausian, E. McRae and B. Humbert B, *J. Appl. Phys.* 84 (1998) 6552.

[42] L. G. Canado, K. Takai, T. Enoki, M. Endo, Y. A. Kim, H. Mizusaki, A. Jorio, L. N. Coelho, R. Magalhaes-Paniago and M. A. Pimenta, *Appl. Phys. Lett.* 88 (2206) 163106.

[43] M. R. Baldan, E. C. Almeida, A. F. Azevedo, E. S. Goncalves, M. C. Rezende and N. G. Ferreira, *Appl. Surf. Sci.* 254 (2007) 600.

[44] A. C. Ferrari, *Solid State Commun.* 143 (2007) 47.

[45] A. C. Ferrari, J. C. Meyer, V. Scardaci, C. Casiraghi, M. Lazzeri, F. Mauri, S. Piscanec, D. Jiang, K. S. Novoselov, S. Roth and A. K. Geim, *Phys. Rev. Lett.* 97 (2006) 187401.

[46] R. J. Nemanich and S. A. Solin, *Phys. Rev. B* 20 (1979) 392.

[47] M. A. Pimenta, G. Dresselhaus, M. S. Dresselhaus, L. G. Canado, A. Jorio and R. Saito, *Phys. Chem. Chem. Phys.* 9 (2007) 1276.

[48] A. Eckmann, A. Felten, A. Mishchenko, L. Britnell, R. Krupke, K. S. Novoselov and C. Casiraghi, *Nano Lett.* 12 (2012) 3925.

[49] B. D. Cullity and C. D. Graham, *Introduction to Magnetic Materials* (John Wiley & Sons, 2011).

[50] K. Bagani, A. Bhattacharya, J. Kaur, A. Rai Chowdhury, B. Ghosh, M. Sardar and S. Banerjee, *J. Appl. Phys.* 115 (2014) 023902.

[51] S. S. Rao, S. N. Jammalamadaka, A. Stesmans, V. V. Moshchalkov, J. V. Tol, D. V. Kosynkin, A. H. Duque and J. M. Tour, *Nano Lett.* 12 (2012) 1210.

[52] K. G. Raj and P. A. Joy, *Solid State Commun.* 177 (2014) 89.

[53] Y. Shibayama, H. Sato and T. Enoki, *Phys. Rev. Lett.* 84 (2000) 1744.

[54] D. Dasgupta, F. Demichelis and A. Tagliaferro, *Philos. Mag. B* 63 (1991) 1255.

[55] N. F. Mott and E. A. Davis, *Electronic Processes in Non-crystalline Materials* (Clarendon Press Oxford, 1979).

[56] A. L. Efros and B. I. Shklovskii, *J. Phys. C: Solid State Phys.* 8 (1975) L49.

[57] R. Rosenbaum, *Phys. Rev. B* 44 (1991) 3599.

[58] V. Bayot, L. Piraux, J. P. Michenaud and J. P. Issi, *Phys. Rev. B* 40 (1989) 3514.

[59] L. V. Govor, I. A. Bashmakov, K. Boehme, M. Pientka and J. Parisi, *J. Appl. Phys.* 90 (2001) 1307.

Chapter 7

Activated carbon - iron oxide composite for cleaning of oil spills

7.1 Introduction

The increasing demand for energy and fuels around the world after the industrial revolution has contributed much towards the use of difference types of oils and fuels. As a result of the heterogeneous distribution of petroleum in earth's crust, the transportation of petroleum-based products from one region to another became inevitable. The most used transport route for oil tankers is through seas and therefore, over the years, the marine ecosystem have been badly affected by the spillage of oil from the carrier ships [1,2]. The unforeseen accidental explosions from oil wells also release a large amount of oil to the aquatic bodies [1,2]. Both these contributions create momentary oil spills which spread throughout the affected system quite instantaneously. Apart from these, a slow and steady contribution of oil, which accumulates in the aquatic system with time, originates from industrial effluents or from oil leakage from machineries and pipelines [3]. The oil which reaches in the aquatic systems, by whatever means, tends to decrease the dissolved oxygen content thereby affecting the microorganisms and other aquatic flora and fauna. Birds are also badly effected by oil spillage as they get trapped in oils while fishing in such waters, which destroys the texture of their feathers after which their flying ability gets hampered.

Different techniques like skimmers, floating barriers, synthetic organophilic sorbent materials like polypropylene, polyethylene terephthalate, silica aerogels, zeolites, organophilic clays, exfoliated graphite, graphene frameworks, cellulose fiber, collagen fibers, etc. have been employed in cleaning up the oil spills [3–7]. The most important criteria that should be met by any material to be used on large scale for such an environmental application are the efficiency, recyclability and biocompatibility. Here, biocompatibility is of particular importance since the cleaning agent should not produce any additional harm to the aquatic system under consideration. Even though many of the currently available sorbent materials satisfy these three criteria, they suffer a major disadvantage that the removal of sorbent materials along with the adsorbed oil from the aquatic system after the oil adsorption process is a tedious and time consuming task, considering that

large quantity of oil has to be removed quite quickly and efficiently to prevent further spreading. This posts a serious challenge in applying these materials for any practical application. However, this disadvantage can be surpassed by adding a magnetic functionality to the sorbent material. With an additional magnetic property along with good sorption properties, the material can be of great advantage since the magnetic sorbent material can be quickly recovered in the presence of a magnet [7,8]. Such a multifunctional material can simplify the whole oil removal process and hence can increase the total efficiency of the process considerably. Ideal multifunctional candidates can be prepared by making a composite of the adsorbent material with magnetic nanoparticles having sufficiently high magnetization so that the nanoparticles can drag the whole oil adsorbed material with it in the presence of a magnetic field. The use of nanoparticles facilitates the preparation of a stable composite with an adsorbent material. However, the composite as a whole and especially the magnetic material should be biocompatible to avoid any secondary pollution in the aquatic systems by the adsorbent/composite material. The cost effectiveness of the whole process and ease of preparation of the composite materials in bulk quantities can considerably improve their practical applications since tonnes of such material are required for removal of oil from large aquatic systems like oceans.

Superparamagnetic iron oxide nanoparticles, SPIONs (Fe_3O_4 and γ-Fe_2O_3), due to their good magnetic properties, biocompatibility and low cytotoxicity, find applications in targeted drug delivery, magnetic hyperthermia, as MRI contrast enhancement agent, etc. They have also been studied as the magnetic part of the sorbent material [8,9]. Different types of magnetic sorbents such as collagen fiber-SPION composites [7], Fe_2O_3@C core-shell nanoparticles [8], Fe-carbon nanocomposites [10], magnetic floating foams [11], iron incorporated carbon nanotube sponges [12], metal-organic framework (MOF) derived porous carbon-iron oxide nanocomposite [13], magnetic exfoliated graphite [14], epoxidized natural rubber-magnetite nanocomposites [15], polystyrene-iron oxide nanocomposites [16] and palm shell based activated carbon-iron oxide composite [17] have been studied

for the removal of oil spill by magnetic separation. Many of these materials such as the macroporous carbon nanotubes, magnetic floating foams, magnetic exfoliated graphite, MOF-derived porous carbon-iron oxide composite and polystyrene-iron oxide composite are good in terms of their oil retention capacity. However, the synthesis of these materials includes relatively complex procedures and costly chemicals, with low yield, so that a cost effective bulk production for real time applications is impossible [11–14,16]. Comparatively cheaper natural sorbent materials like collagen fibers [7], epoxidized natural rubber [15] and palm shell based chemically activated carbon [17] have been proposed to overcome the major issues, after incorporating with different magnetic nanoparticles. However, they also suffer from either a low oil retention capacity or a very slow response time which reduces the efficiency of the whole process. Therefore, search for a cheap and efficient material which can actually be used for immediate containment and/or sudden removal of large oil spills is still an open area of research.

The search for a cheap adsorbent always leads to carbon-based materials prepared from different natural resources like nut shells, husks, leaves, tree bark, etc., with the characteristics like high adsorption capacity, considerable mechanical strength and low ash content [18]. They are widely studied and found productive for applications such as removal of metal ions and organic dyes from water [19]. Between the different natural resources, nut shells are known to produce granular activated carbons with good adsorption properties. Amongst the nut shells, coconut shell has special importance since it can be used to produce activated carbon in bulk quantities due to their size and availability as an agricultural and household waste material [17]. The sorption properties of activated carbon derived from any resource is known to depend on the surface area and porosity which in turn are determined by the inherent porosity of the carbon precursor, activating agent used, the amount of activating agent used for activation, activation temperature, etc. [20,21]. Among different activating agents like KOH, $ZnCl_2$, H_3PO_4, CO_2, steam, etc., KOH is known to enhance porosity and surface area considerably by creating microporous structure at activation temperatures below 800

°C [22]. Above 900 °C, the pores get wider by increased gasification of carbon in the form of gaseous oxides [22], through a series of oxidation reactions, as discussed in Chapter 6 (Section 6.2). The KOH activation also generates a large number of oxygen functionalities at the carbon surface similar to those produced during surface activation with HNO_3 or HNO_3/H_2SO_4 mixture [23].

From the insights obtained while studying the KOH activation process in detail, as discussed in Chapter 6 (Section 6.4.2), the KOH activated CS derived carbon was applied for the removal of oil spills from water. Since oil consists of macromolecules, the study presented in this chapter was performed using activated carbon with wider pores by activating with large amounts of KOH at 1000 °C and after making a composite with biocompatible superparamagnetic iron oxide nanoparticles.

7.2 Preparation of materials

7.2.1 Preparation of activated carbon

Locally available coconut shell was used as the carbon source. Dried coconut shell was pyrolyzed at 1000 °C in a horizontal tubular furnace under flowing nitrogen atmosphere. The pyrolyzed carbon obtained was crushed and ground to fine powder using an agate mortar and pestle. Analytical grade conc.H_2SO_4 (98%), conc.HNO_3 (69%) and KOH were purchased from Merck Chemicals and were used as-received without any further purification. For solution based activation, 10 g of the pyrolyzed carbon powder was refluxed with a mixture of 125 ml of 20% (v/v) HNO_3 and 125 ml of 20% (v/v) H_2SO_4 at 110 °C for 90 minutes [23]. The activated sample was washed several times with double distilled water till neutral pH and then dried in an oven at 60 °C (sample code AAC).

The KOH activation was carried out by a liquid state KOH impregnation of the pyrolyzed carbon. In the present work, 1:3 carbon (5 g) to KOH (15 g) weight ratio was used after fixing the maximum possible high temperature (1000 °C) The KOH impregnation was carried out for 24 hours, by immersing the carbon

powder in KOH solution, followed by drying and heating at 1000 °C under argon atmosphere in a tubular furnace [21]. The activated sample was washed with double distilled water till neutral pH and then dried in an oven at 60 °C (sample code KAC).

7.2.2 Preparation of the magnetic composite

Activated carbon/iron oxide composite was prepared by *in situ* co-precipitation of Fe_3O_4 in the presence of AAC or KAC [24]. Analytical grade iron (II) chloride tetrahydrate ($FeCl_2 \cdot 4\,H_2O$), iron (III) chloride hexahydrate ($FeCl_3 \cdot 6\,H_2O$) and 25% ammonia solution were purchased from Merck Chemicals and were used as-received without any further purification. The activated carbon to iron oxide weight ratio in the final composite material was fixed as 1:1. For the preparation of the composite, 0.5 g of AAC was first dispersed in water to which a 2:1 molar mixture of $FeCl_3.6\,H_2O$ (11.6770 g) and $FeCl_2.4\,H_2O$ (4.2943 g) was added and stirred for 2 hours, after de-aerating with argon gas. The argon flow was maintained and the pH was then adjusted to 12 using 25% ammonia solution to precipitate the iron oxide nanoparticles. The precipitate was then heated in the mother liquor at 80 °C for 1 hour to facilitate the binding of the nanoparticles to the surface functionalities of activated carbon [24]. The magnetite-carbon composite formed was magnetically separated the supernatant solution and then washed several times till neutral pH. A small fraction of light weight nonmagnetic part was discarded so that the weight of the discarded light-weight portion was less than 0.5% of the weight of KAC or AAC used for the synthesis. Hence, the quantity of this small portion lost during the preparation of the composite was ignored for calculating the oil retention capacity of the composite materials with respect to the amount of activated carbon present in the material. The washed product was then dried in an oven 60 °C to obtain AAC-iron oxide composite material (sample code: ACF). KAC-iron oxide composite material was prepared by a similar procedure using the similar amounts of KAC and iron oxide precursors (sample code: KCF).

All the materials were characterized using powder X-ray diffraction (XRD), in-

frared (IR) spectroscopy, transmission electron microscopy (TEM), BET surface area analysis using isothermal N_2 adsorption method and magnetic measurement were performed using a SQUID VSM. Temperature dependent oil adsorption studies were also performed after maintaining the temperature using a refrigerated circulating water bath.

7.3 Material characterization

7.3.1 Surface area analysis

BET surface area analysis was carried out to identify the surface characteristics of both ACF and KCF. The acid activated sample, ACF, and base activated sample, KCF, exhibited a surface area of 580 m^2g^{-1} and 1650 m^2g^{-1}, respectively. The pore size distribution of ACF and KCF are distinctly different, as expected, with ACF consisting of smaller pores with pore diameter ranging from 6 to 14 Å. Among these, majority of the pores are 8 Å wide, as shown in Figure 7.1. On the other hand, KCF shows a different pore size distribution with a large increase in the porosity with two distinct types of pores, a large number of 7 Å and 10 Å wide

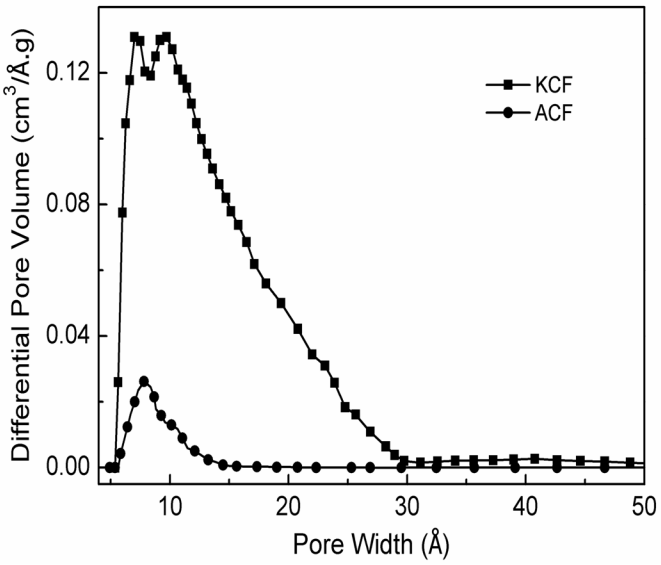

Figure 7.1: Pore size distribution in KCF and ACF.

pores along with comparatively less number of wider pores of size in the range 15–25 Å. A similar pattern of the pore size distribution has been previously reported for KOH activated carbon prepared from coconut shell [21,22]. Previous studies by Hu and Srinivasan using coconut shell based carbon shows that the increase in the microporosity is characteristic of KOH activation at low KOH to carbon ratio (1:2 KOH to carbon), whereas the increased gasification of carbon at high KOH to carbon ratio (≥1.5:2 KOH to carbon) induces some amount of wider pores by the coalescence of the nearby micropores [21].

7.3.2 Transmission electron microscopy

The TEM images of ACF and KCF (Figure 7.2) confirm the granular and porous nature of both composites. The overall grain size of KCF is found to be much smaller than that in ACF which directly points towards the difference in the activation mechanism involved during the synthesis of these materials. The acid

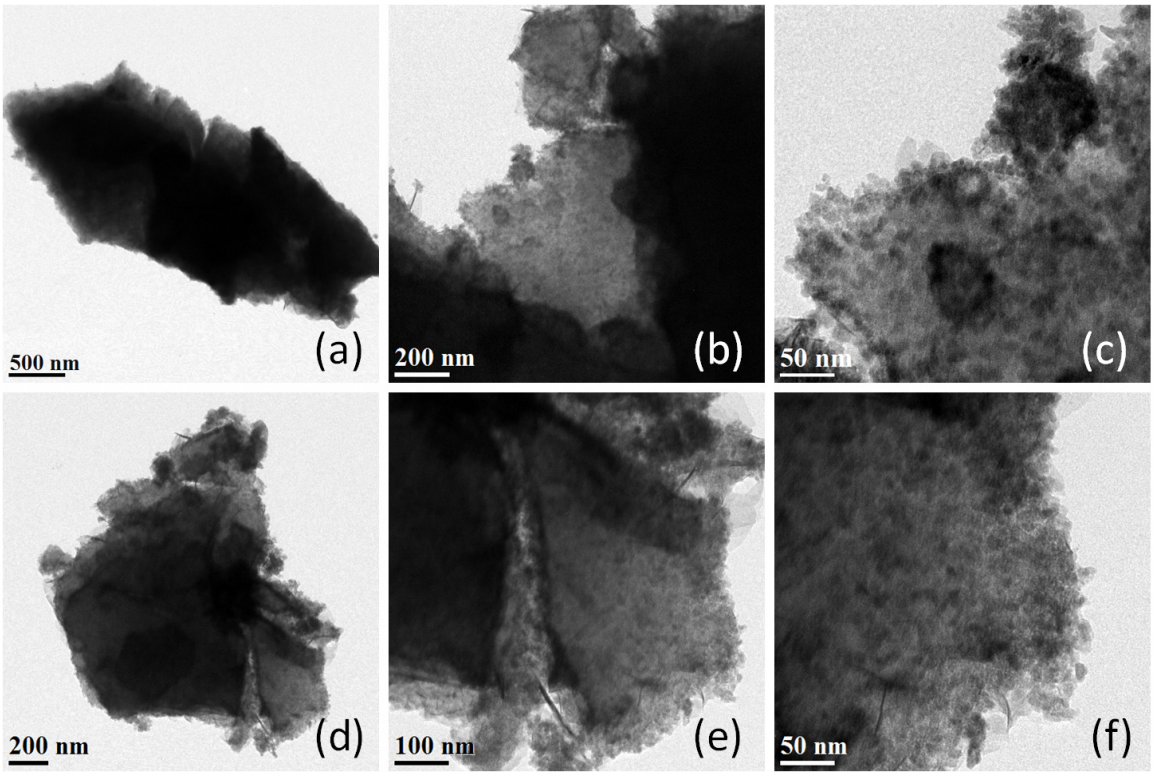

Figure 7.2: TEM images of (a-c) ACF and (d-f) KCF.

activation process does not affect the microstructure of the activated carbon and results only in the development of surface functional groups. However, potassium mediated activation in KAC proceeds through extreme oxidation conditions which result in intense gasification because of which activated carbon with smaller grain size is produced [22].

7.3.3 X-ray diffraction

The activated carbons show two broad peaks in the XRD patterns, a relatively intense and broad peak at ∼24° and a small hump at ∼44° on the 2θ scale, which are typical of the (*002*) and (*100*) reflections from amorphous carbon (Figure 7.3), as discussed in Chapter 3 (Section 3.3.5). For KAC, the (002) peak is having larger width and the (100) peak is less pronounced than that of AAC. This indicates that the KOH activation reduces carbon grain size and induces more structural disorder and the coherence length gets reduced in all three dimensions. This size reduction of carbon grains is also observed in the TEM images (Figure 7.2). For the composite materials ACF and KCF, apart from the (002) reflection from activated carbon, many other peaks are also observed in the XRD pattern.

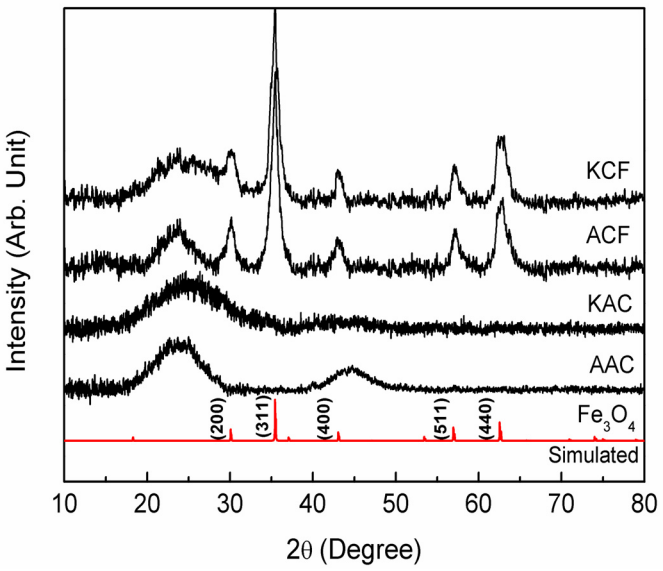

Figure 7.3: XRD pattern of AAC, KAC, ACF and KCF along with the simulated pattern of Fe_3O_4 (PDF#190629).

All of the extra peaks correspond to the peaks of Fe_3O_4 as evidenced by the comparison with the simulated pattern of Fe_3O_4, shown in the figure. The average crystallite size of Fe_3O_4 in the composite material is calculated as ∼8 nm from XRD pattern by using the Scherrer formula, $t = 0.9\lambda/BCos\theta$ (Equation 2.2), where t is the crystallite size, λ is the wavelength of the Cu Kα radiation (1.542 Å), B is the peak width (FWHM) corrected for instrumental broadening and θ is the Bragg angle.

7.3.4 IR spectroscopy

Both acid (HNO_3/H_2SO_4) and base (KOH) activations are known to introduce different types of oxygen functionalities like carboxylic acid, carbonyl or alcoholic functional groups on the carbon surface by partial oxidation of carbon [25,26]. Infrared (IR) spectroscopy was employed to identify the surface functional groups in the activated carbons and to study the bonding interaction between the activated carbon and iron oxide nanoparticles. The IR spectra of AAC, KAC, ACF and KCF are compared in Figure 7.4. The broad band at 3420 cm^{-1} for AAC indicates the presence of bonded O-H groups of phenols or alcohols. In the spectra of KAC and KCF, a broad band at 3170 cm^{-1} indicates that large number of -COOH groups are also present in KAC along with -OH groups [27]. The band at 1640 cm^{-1} present in both the spectra of AAC and KAC corresponds to the C=O stretching vibration of the carboxylic anion and this band shows a shift to 1630 cm^{-1} in both the spectra of ACF and KCF (Figure 7.4). However, the sharp band at 1085 cm^{-1} corresponding to the C-O stretching in alcohols and phenols does not show any shift [27]. This indicates the weakening of C=O group present in the acid functionalities and development of a partial single bond character. Both ACF and KCF show two additional IR bands at 562 cm^{-1} and 617 cm^{-1} when compared to that of AAC and KAC (Figure 7.4), which correspond to the Fe-O vibrations in Fe_3O_4 nanocrystals. However, there is a considerable decrease in the vibrational frequency of these two bands from that of bare Fe_3O_4 in which these vibrations are observed at 585 and 632 cm^{-1} [28]. Thus, in the spectra of ACF and KCF,

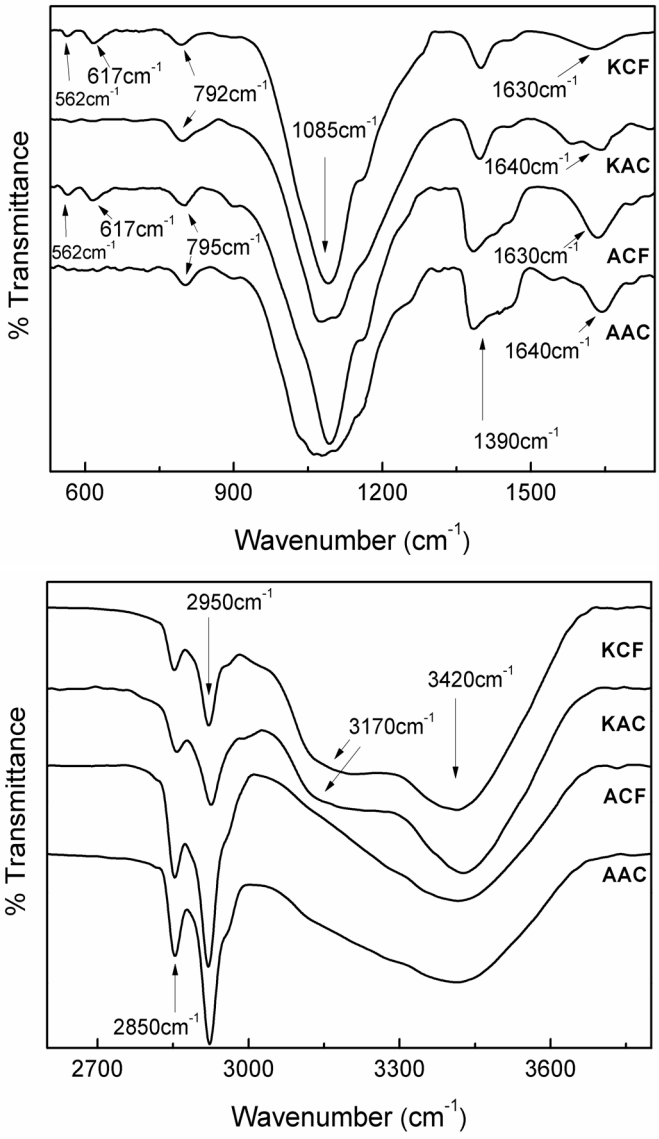

Figure 7.4: Different regions of the infrared spectra of AAC, ACF, KAC and KCF.

the Fe-O vibrations in Fe_3O_4 nanocrystals are shifted by 15 to 20 cm^{-1} towards the lower energy region. The synergetic decrease in the vibrational frequency of Fe-O and C=O vibrations indicates a bond formation between the Fe atoms on the surface of the Fe_3O_4 nanocrystals and the surface carboxylic acid groups of the activated carbons, resembling the capping action of organic molecules like oleic acid on Fe_3O_4 [29].

7.3.5 Magnetic measurements

The composite samples ACF and KCF show comparable room temperature magnetization measured up to a field of 3 T, as shown in Figure 7.5. The magnetization curves of both ACF and KCF exhibit zero coercivity. Also, the magnetization is increased with increasing magnetic filed strength and at higher fields the magnetization increased almost linearly with increasing field. This indicates superparamagnetic nature of the iron oxide nanoparticles incorporated in the composite materials. The magnetization at 0.5 T for ACF and KCF is ∼15 emu/g, which is sufficiently high so that the whole material can be easily attracted towards a laboratory magnet. The small difference in the magnetization of ACF and KCF is likely to be due to the size distribution of iron oxide nanoparticles. During the *in situ* co-precipitation more number of smaller iron oxide nanoparticles can form in the pores of microporous ACF when compared to that of mesoporous KCF.

Therefore, the incorporation of the magnetic nanoparticles in the activated carbon facilitate the removal of oil adsorbed on the carbon particles in the composite material through the application of an external magnetic field. Further, since the magnetization depends on the size and number of the nanoparticles, the magnetic action can be easily tuned by manipulating the size and amount of the nanoparticles attached on the surface of activated carbon. However, there will always be a maximum limit determined by the coverage of nanoparticles on the adsorbent surface, since the higher coverage may hamper the adsorption capacity by blocking the adsorption sites on carbon surface and interior of the pores.

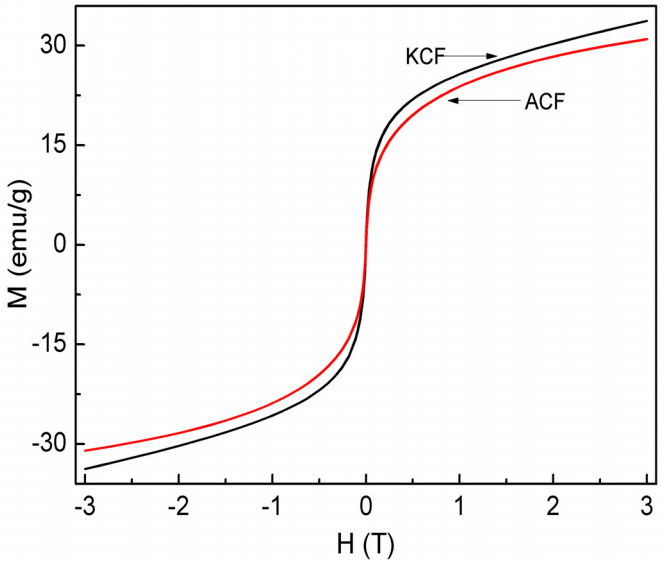

Figure 7.5: M-H curves of ACF and KCF

7.4 Oil removal studies

7.4.1 Determination of oil adsorption capacity

For the oil removal studies, a red colored new premium oil (Veedol lubricants Ltd.) and black colored used oil collected from a local motor workshop were used to create an artificial oil spillage in the laboratory. The black colored used motor oil is found to be highly viscous due to the presence of dispersed fine carbon particles. The oil adsorption capacity of the materials was determined at room temperature (30 °C) by using weight measurements. For the oil removal studies, 2 g oil was poured on top of 10 ml water taken in a petri dish to create an artificial oil spill. A weighed amount of the composite material is smeared over the oil and then waited for a specific time before the oil adsorbed material is separated from the artificial spill. On performing the experiment with the magnetic composites ACF and KCF, the oil adsorbed composite was recovered using a permanent magnet and then dried overnight at 100 °C to remove water. However, in the control experiment, when AAC and KAC were used to remove oil from artificial spillage, the separation of the oil adsorbed material was performed using filtration technique, which was then dried under similar conditions as in the case of ACF and KCF. The oil

retention capacity (k) of ACF, KCF, AAC and KAC was determined by using Equation 7.1, where 'a' is the weight (in gram) of the adsorbent material smeared on top of the oil layer and 'b' is the weight (in gram) of the oil adsorbed material recovered from the artificial oil spill, after drying.

$$k = \frac{(b-a)}{a} \tag{7.1}$$

The retention capacity (k) was then normalized with respect to the weight of carbon in the case of ACF and KCF in order to compare the results with that using AAC and KAC, considering that 1:1 composites are obtained.

7.4.2 Oil removal

One gram of AAC is found to adsorb 2.22 g of premium oil and 5.64 g of used oil almost instantaneously as showed in Figure 7.6, on the other hand, one gram the of the high surface area carbon, KAC adsorbs 9.33 g of premium oil and 5.54 g of used oil (Figure 7.6). In the case of ACF and KCF the normalized oil retention ability with respect to the weight of activated carbon present in them is calculated. A plot of the normalized oil retention ability of ACF and KCF as a function of time, using the premium and used oils, are shown in Figure 7.7a and Figure 7.7b respectively. One gram of carbon (AAC) when used in the form of composite material ACF retains 3.01 g of premium oil and 7.59 g of used oil almost instantaneously. KCF, having large surface area and wide pores, similar to that of KAC, shows a large increase in the retention capacity of premium oil, nearly by 420%. One gram of carbon (KAC) in KCF is found to retain 12.93 g of premium oil and 7.65 gm of used oil. The retention capacities of the present coconut shell based carbon composites are high when compared to that of palm shell based activated carbon, whose maximum retention capacity was limited to 99 mg oil per gram of carbon even after activation [17]. The snapshots of different steps during the oil removal process (premium and used oils), using the nanocomposite KCF, are shown in Figure 7.8.

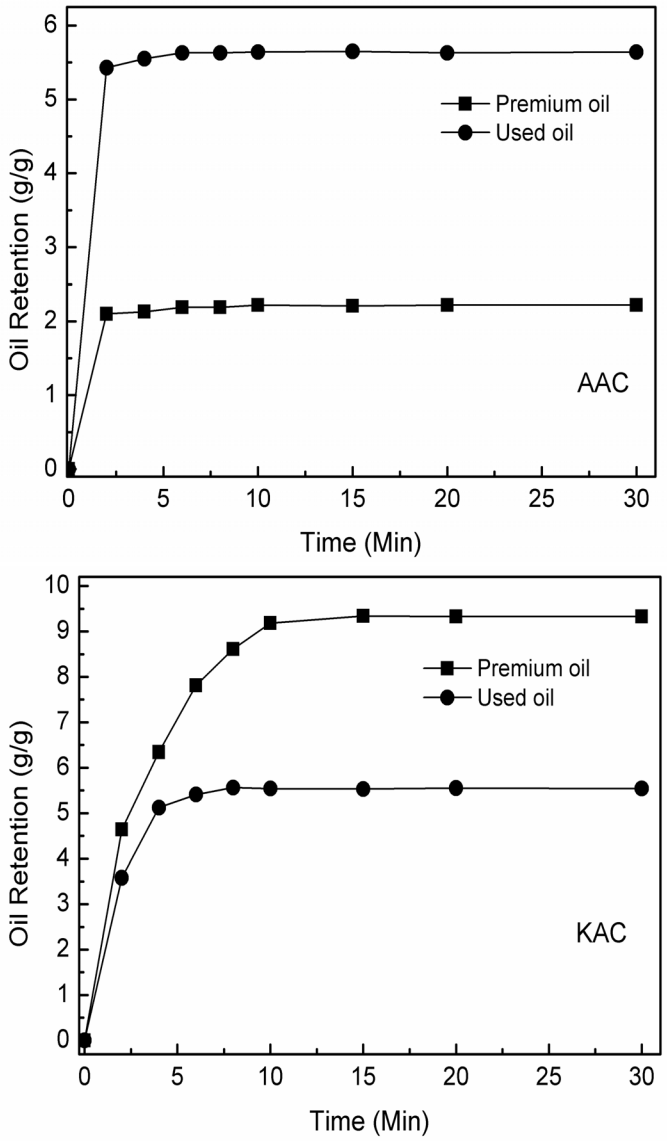

Figure 7.6: Oil retention capacity of AAC and KAC, normalized with respect to their weight, as a function of time, using premium and used motor oils.

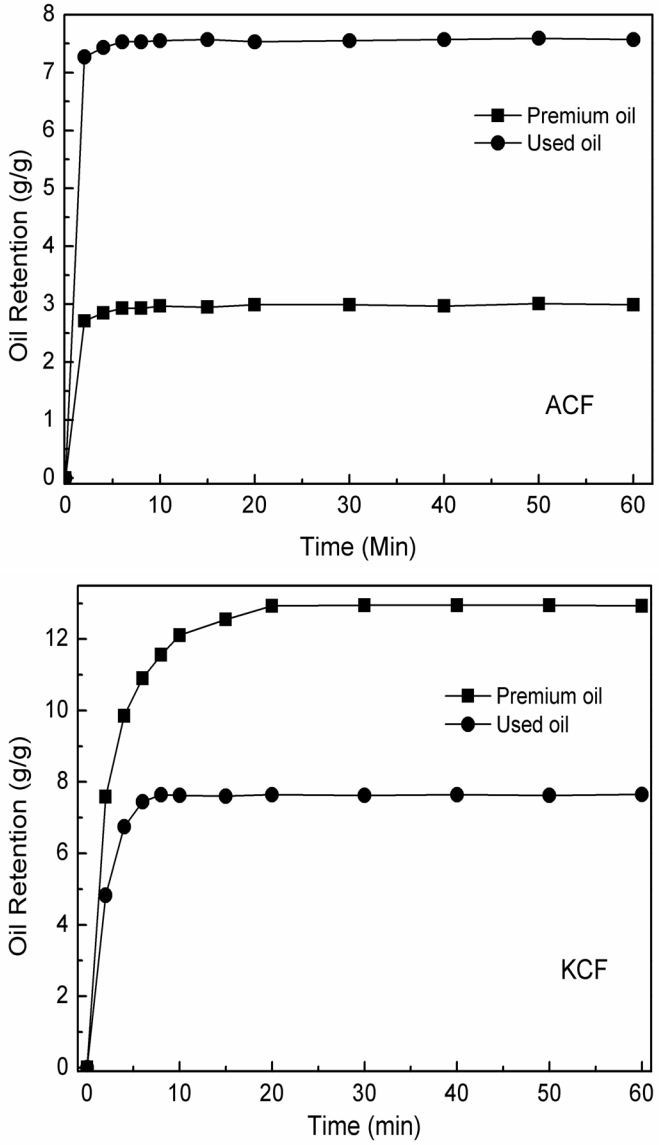

Figure 7.7: Oil retention capacity of ACF and KCF, normalized with respect to the weight of activated carbon present in the materials, as a function of time, using premium and used motor oils.

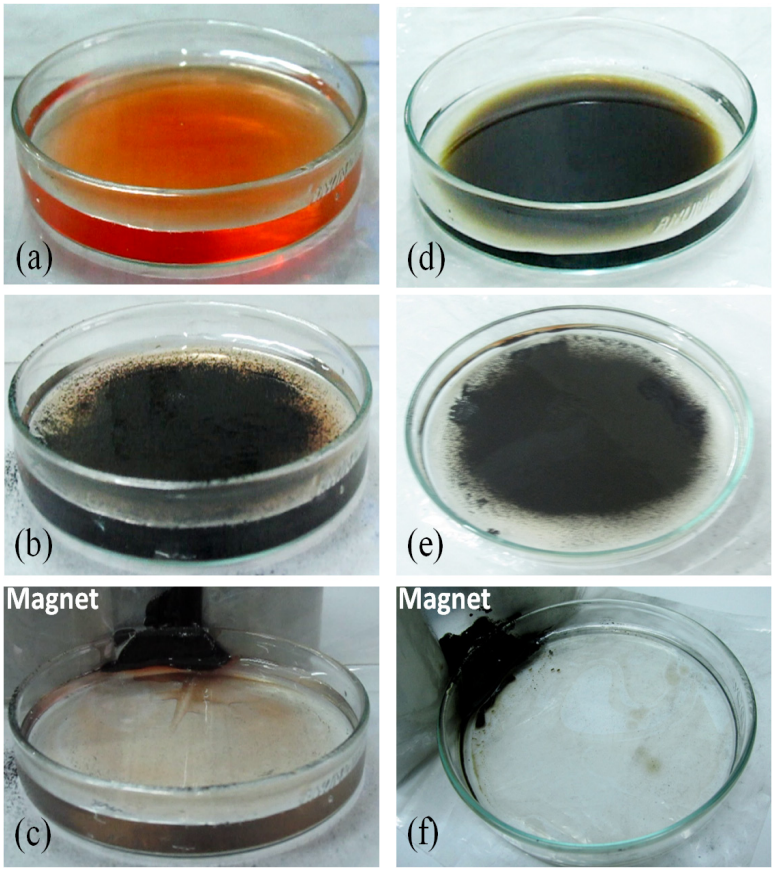

Figure 7.8: Snapshots of different stages of oil removal process using premium oil (a,b,c) and used motor oil (d,e,f). Oil spilled over water (a and d), the activated carbon-iron oxide composite (KCF) smeared over the spilled oil (b and e), the adsorbent along with the oil is separated by an external magnet (c and f).

The oil removal process using AAC and KAC was time consuming and tedious due to filtration process involved in the recovery of the adsorbent. However, this serious disability can be overpowered by using the magnetic composite ACF and KCF instead of AAC and KAC. Here, the recovery of oil adsorbed material from the artificial spill was quite instantaneous when an external magnet was used. Moreover, this instantaneous pulling action of the magnetic nanocomposite facilitates an increased oil retention capacity of activated carbon by dragging more oil with the oil adsorbed material when used as the magnetic composite. The adsorption kinetics appear to be similar for activated carbon and the composite material indicating the crucial role of porosity and surface area of the adsorbent in determining the oil adsorption capacity. The large increase in the uptake of used oil by AAC and ACF could be due to the fine carbon particles dispersed in it, which enhances the hydrophobic interaction between the used oil molecules and the adsorbent when compared to that of premium oil. However, when using KAC and KCF, the adsorption is not that instantaneous when compared to that by AAC and ACF. This is a direct consequence of the role played by the pores in retaining the oil. The oil retention in the pores of the adsorbent is a slow process since a finite time is required for viscous fluids like oil to penetrate into the pores by capillary action [30]. However, the maximum retention capacity is achieved by KCF in 20 minutes which is much faster when compared to the previously reported magnetic adsorbent composites like the epoxidized natural rubber based composite, where maximum retention was achieved after 2 hours [15]. The used oil retention capacity and sorption characteristics exhibited by KAC and KCF are similar to that exhibited by AAC and ACF respectively, indicating that the pores in KAC and KCF are not effective in containing used oil since it does not get into the pores due to the high viscous nature and the oil retention is solely due to hydrophobic interactions.

7.4.3 Adsorption kinetics

The oil retention kinetics of both ACF and KCF are tested using pseudo-first-order (Equation 7.2) and pseudo-second-order (Equation 7.3) kinetic models [19] to calculate the equilibrium oil adsorption capacity of these materials.

$$log(q_e - q_t) = logq_e - \frac{k_1}{2.303}t \tag{7.2}$$

$$\frac{t}{q_t} = \frac{1}{k_2 q_e^2} + \frac{t}{q_e} \tag{7.3}$$

Here, q_t (g of oil/g of activated carbon in activated carbon composite) is the amount of oil adsorbed at time t (in minute), k_1 and k_2 are the first (1/Min) and second order (g/g Min) rate constants and q_e is the equilibrium oil retention capacity of the material and have same units as that of q_t.

Among the two kinetic models, the experimental data were found to fit well to the pseudo-second-order model (Figure 7.9) given by Equation 7.3, as reported previously for adsorption of dyes and metal ions from aqueous solutions [19]. The equilibrium adsorption capacity, q_t, and the second order rate constant for both ACF and KCF when used for removal of premium and used motor oils are calculated from the slope and intercept of t/q_t versus t plot (Figure 7.9). Table 7.1 shows the slope, intercept, equilibrium oil retention capacity and the rate constant obtained after a least square fitting of t/q_t versus t plot. The q_e values obtained are comparable to the saturation values observed in figure 7.7. The pseudo-second-order rate constant is much higher for ACF when compared to that obtained for KCF which confirms the sluggish kinetics of the latter composite. Therefore, the oil sorption inside the carbon pores could be considered as the rate limiting step.

7.4.4 Temperature dependence

To study the effectiveness of the composites for oil removal at different temperatures, oil removal studies are performed at 10 °C and 50 °C, using the premium

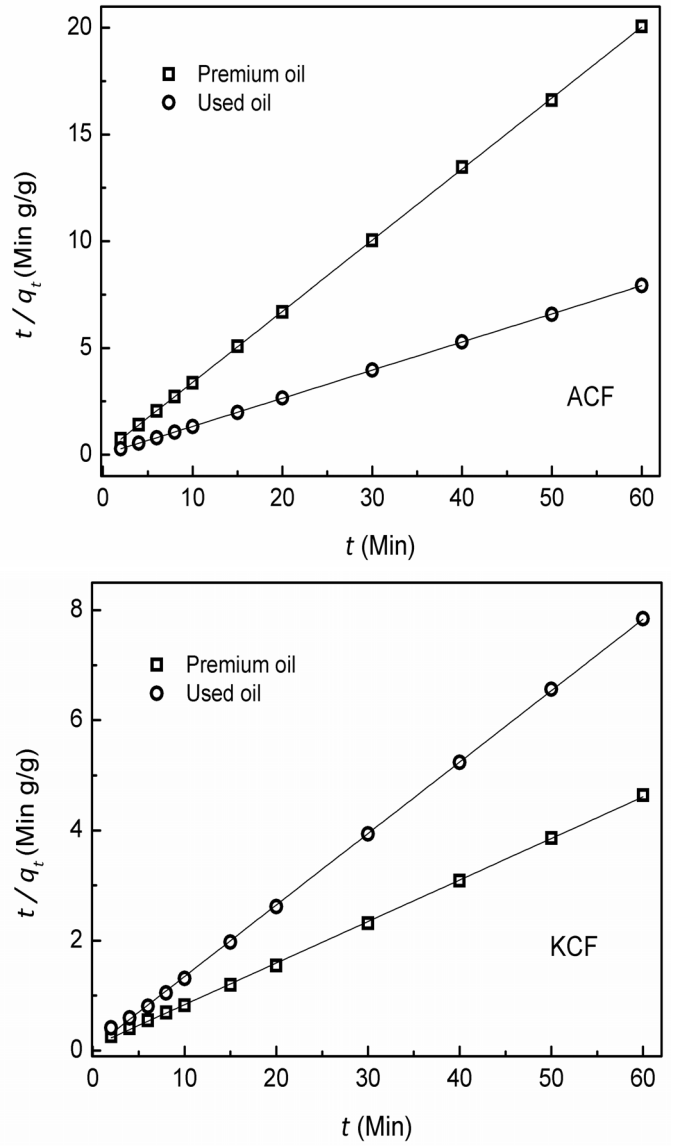

Figure 7.9: Pseudo-second-order fit for the oil retention curves of ACF and KCF. Symbols show the experimental data and solid lines are fit to Equation 7.3.

Table 7.1: Results of the analysis of the adsorption kinetics using Equation 7.3 for ACF and KCF using premium (P) and used (U) motor oils.

Sample code	Oil	Slope	Intercept	q_e (g oil/g carbon)	k_2 (g/g Min)
ACF	P	0.3330	0.0625	3.03	1.7427
	U	0.1320	0.0095	7.57	1.8369
KCF	P	0.0754	0.0824	13.26	0.0690
	U	0.1300	0.0509	7.69	0.3339

oil, in addition to the study carried out at room temperature (30 °C). The petri dish containing the premium oil was kept in a circulating water bath for sufficient time (30 minutes) to establish thermal equilibrium. Then the composite material which showed highest oil retention capacity (KCF) was smeared on top of the oil layer and then separated magnetically after waiting for different time intervals. Figure 7.10 shows the amount of oil separated as a function of time at the three different temperatures. As the temperature is decreased to 10 °C, the oil retention capacity of KCF increases to 15.42 g premium oil per g of carbon compared to 12.93 g at 30 °C. When the temperature is increased to 50 °C, the retention capacity of the same composite is decreased to 10.11 g premium oil/ per g of carbon. Thus, when compared to the result at room temperature, the oil retention capacity is increased by nearly 20% at 10 °C and decreased by nearly 22% at 50 °C, showing a linear variation of the retention capacity with temperature, as shown in the inset of Figure 7.10. The decrease in the oil retention with increasing temperature can be due to the weakening of the strength of physisorption, mediated by hydrophobic interactions. However, despite the decrease in the retention capacity with an increase in the temperature, the retention value at 50 °C is much higher than the values reported previously for different composites at room temperature [7,8] and hence, the present composite is more efficient and effective.

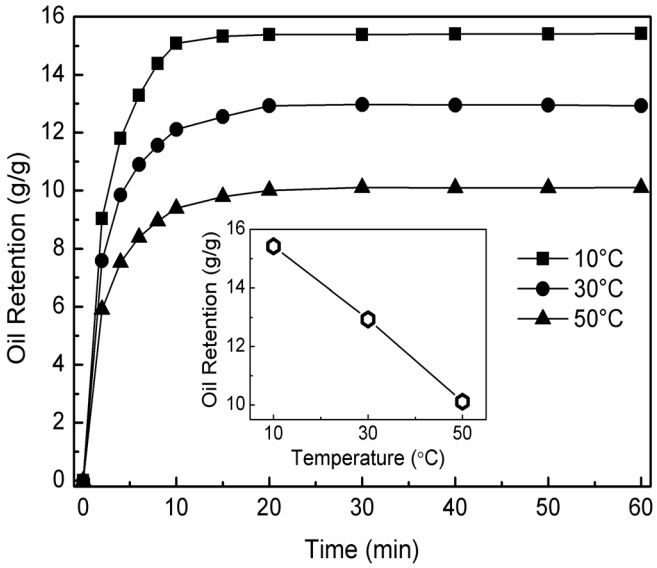

Figure 7.10: Oil retention capacity of KCF with respect to the weight of activated carbon, measured at different temperatures, as a function of time, using premium oil. Inset shows the variation of maximum oil retention capacity as a function of temperature.

7.4.5 Recyclability

The recyclability of the magnetic adsorbent material for oil removal is checked by two different approaches. In the first approach, the composite material KCF is recycled, at the expense of the oil retained, by heating the magnetically recovered oil adsorbed composite in a tubular furnace at 500 °C, for 1 hour, under nitrogen gas atmosphere. This method is previously reported as a disposal technique for oil adsorbed collagen-based magnetic composite which was converted to Fe_3O_4 incorporated graphitic carbon on heating [7]. Since the weight percentage of carbon in the composite material increases on heating due to the pyrolysis of adsorbed oil, the values presented in this section is normalized with respect to the weight of the composite considering that fresh KCF showed an oil retention capacity of 12.93 g premium oil per gram of carbon which is equivalent to 6.45 g oil per gram of KCF. The heat-treated recovered material after cooling to room temperature is again used for removal of premium oil and showed an oil retention capacity of 4.26 g premium oil per g of the material at room temperature. This observed retention capacity is 34% less than that of fresh KCF. The experiment was repeated for

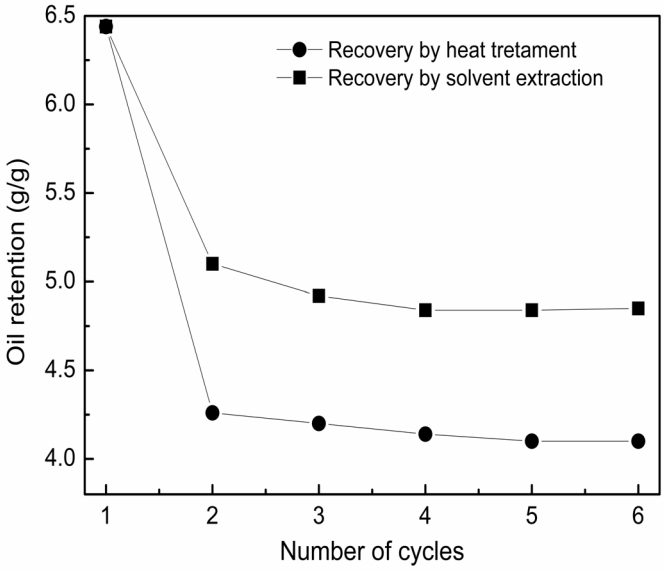

Figure 7.11: Variation in the adsorption capacity of KCF (per gram of KCF) on recycling by heat-treatment and solvent extraction methods.

five more cycles with the recovered oil adsorbed composite material obtained from the previous cycle. Figure 7.11 shows the changes in the oil retention capacity of the composite material up to 6 cycles. Even though the retention capacity is decreased after the first cycle, the retention value remains almost constant from the second cycle onwards and the value is still good enough when compared to the previous reports on other carbon-based materials [15–17]. The decrease in the oil retention capacity after the first cycle could be due to charring of oil molecules inside the carbon pores which in turn decreases the porosity of the adsorbent after the first cycle.

In the second approach, the adsorbed premium oil is separated from the adsorbent material by solvent extraction. 5 ml petroleum ether was added to 0.5 g of KCF containing the recovered oil, sonicated for 10 minutes, and centrifuged at 3000 rpm for 5 minutes. The supernatant liquid was collected and the extraction process was repeated two more times. Then the solvent was evaporated to recover the oil which was then weighed on an electronic balance. By this process, at laboratory conditions, 40% of the premium oil could be recovered from the magnetically collected, oil-adsorbed, KCF. The solid adsorbent part, when reused for

oil removal, showed superior performance than the adsorbent recovered by heat-treatment, with an oil retention capacity of 4.89 g premium oil per g of material (24% decrease in retention capacity than that of fresh KCF). The variation of the oil retention capacity of the material recovered by solvent extraction up to six cycles is shown in Figure 7.11. After the first cycle, the retention capacity remains almost the same around 4.8 g/g, larger than the retention capacity of ACF in the first cycle (Figure 7.7). Thus, the recovery by solvent extraction is quite promising since the efficiency of oil recovery and recyclability can be manipulated by changing the solvent and optimizing the extraction conditions there by recovering the oil, the adsorbent and the solvent with minimal loss.

7.5 conclusions

carbon-based magnetic nanocomposites were prepared using coconut shell based activated carbon and superparamagnetic iron oxide nanoparticles by *in situ* co-precipitation technique. IR spectroscopic studies showed that the composite material is not a loose physical mixture of the two components and rather is chemically attached through interaction between the cations on the surface of nanoparticles and surface functional groups of the activated carbon. The magnetization of the composite materials was found to be sufficiently high enough for the removal of the material by a permanent magnet. This allowed a fast and effective separation of the oil adsorbed material from water by mere application of a laboratory magnet after oil adsorption process. The magnetic separation technique is very fast and less tedious when compared to the conventional separation techniques. A detailed study showed that the amount of oil retained by the composite is determined by the microstructure of the composite material which in turn is determined by the activation process involved during the preparation of activated carbon. The KOH activated carbon with mesoporous structure and high specific surface area showed superior oil adsorption properties when compared to acid activated carbon with narrower pores and low specific surface area. However, the oil adsorption by the acid activated carbon was instantaneous when compared to KOH activated car-

bon due to the difference in the pore structure. During magnetic separation, the composite material was found to be dragging more oil with it due to the combined effect of viscous drag and hydrophobic interaction. Therefore, the amount of oil removed by the composite material is much larger when compared to that by using the activated carbon alone which was used for the preparation of the composite, due to the dragging effect of the composite. This is an additional advantage that the composite material exhibited apart from the ease of synthesis and separation of adsorbed oil, which makes it superior to the other materials reported in the literature previously for oil removal.

The study of the oil removal process indicated that the composite material may also be suitable for containment of oil immediately after the spill to prevent further spreading because of its moderately large oil uptake and fast separation. To extend the applicability of the composite material, its recyclability and temperature dependent performance were monitored. The composite material can be regenerated either by heat-treatment or after solvent extraction of the adsorbed oil. The first method is cheaper and quite fast, but works at the expense of the adsorbed oil. However, by solvent extraction, the adsorbed oil can also be regenerated along with the adsorbent material for further use. The additional advantages like cost effectiveness, the simplicity of the process and easily scalable synthesis procedure along with superior sorption capacity can enable the material to be used for oil remediation in conjugation with the currently available technologies.

Bibliography

[1] F. R. William and R. Gramling, *Blowout in the Gulf: The BP Oil Spill Disaster and the Future of Energy in America* (MIT Press, 2011).

[2] C. H. Peterson, S. D. Rice, J. W. Short, D. Esler, J. L. Bodkin, B. E. Ballachey and D. B. Irons, *Science* 302 (2003) 2082.

[3] M.O. Adebajo, R.L. Frost, J.T. Kloprogge, O. Carmody and S. Kokot, *J. Porous Mater.* 10 (2003) 159.

[4] M. Toyoda , Y. Nishib, N. Iwashitab and M. Inagaki, *Desalination* 151 (2003) 139.

[5] Y. Zhao, C. Hu, Y. Hu, H. Cheng, G. Shi and L. Qu, *Angew. Chem. Int. Ed.* 51 (2012) 11371.

[6] G. Deschamps, H. Caruel, M. Borredon, C. Bonnin and C. Vignoles, *Environ. Sci. Technol.* 37 (2003) 1013.

[7] P. Thanikaivelan, N.T. Narayanan, B.K. Pradhan and P.M. Ajayan, *Sci. Rep.* 2 (2012) 230.

[8] Q. Zhu, F. Tao and Q. Pan, *ACS Appl. Mater. Interfaces* 2 (2010) 3141.

[9] L.H. Reddy, J.L. Arias, J. Nicolas and P. Couvreur, *Chem. Rev.* 112 (2012) 5818.

[10] Y. Chu and Q. Pan, *ACS Appl. Mater. Interfaces* 4 (2012) 2420.

[11] P. Calcagnile, D. Fragouli, I.S. Bayer, G.C. Anyfantis, L. Martiradonna, P. D. Cozzoli, R. Cingolani and A. Athanassiou, *ACS Nano.* 6 (2012) 5413.

[12] X. Gui, Z. Zeng, Z. Lin, Q. Gan, R. Xiang, Y. Zhu, A. Cao and Z. Tang,*ACS Appl. Mater. Interfaces* 5 (2013) 5845.

[13] A. Banerjee, R. Gokhale, S. Bhatnagar, J. Jog, M. Bhardwaj, B. Lefez, B. Hannoyerc and S. Ogale, *J. Mater. Chem.* 22(2012) 19694.

[14] G. Wang, Q. Sun, Y. Zhang, J. Fan and L. Ma, *Desalination* 263 (2010) 183.

[15] S. Venkatanarasimhan and D. Raghavachari, *J. Mater. Chem. A* 1 (2013) 868.

[16] P. Tempesti, M. Bonini, F. Ridi and P. Baglioni, *J. Mater. Chem. A* 2 (2014) 1980.

[17] W. Ngarmkam, C. Sirisathitkul and C. Phalakornkule, *J. Environ. Manage.* 92 (2011) 472.

[18] O. Ioannidou and A. Zabaniotou, *Renewable Sustainable Energy Rev.* 11 (2007) 1966.

[19] F. C. Wu, R. L. Tseng and R. S. Juang, *Wat. Res.* 35 (2001) 613.

[20] O.W. Achaw and G. Afrane, *Micropor. Mesopor. Mater.* 112 (2008) 284.

[21] Z. Hu and M. P. Srinivasan, *Micropor. Mesopor. Mater.* 27 (1999) 11.

[22] J. Romanos, M. Beckner, T. Rash, L. Firlej, B. Kuchta, P. Yu, G. Suppes, C. Wexler and P. Pfeifer, *Nanotechnology* 23 (2012) 015401.

[23] P. Thakuria and P.A. Joy, *Nanosci. Nanotechnol. Lett.* 1 (2009) 171.

[24] L. C. A. Oliveira, R. V. R. A. Rios, J. D. Fabris, V. Garg, K. Sapag and R. M. Lago, *Carbon* 40 (2002) 2177.

[25] T. G. Ros, A. J. Van Dillen, J. W. Geus and D. C. Koningsberger, *Chem. Eur. J.* 8 (2002) 1151.

[26] S. J. Park and W. Y. Jung, *J. Colloid Interface Sci.* 250 (2002) 93.

[27] S. Biniak, G. Szymanski, J. Siedlewski and A. Swiatkowski, *Carbon* 35 (1997) 1799.

[28] J. L. Zhang, R. S. Srivastava and R. D. K. *Langmuir* 23 (2007) 6342.

[29] W. Wu, Q. He and C. Jiang, *Nanoscale Res. Lett.* 3 (2008) 397.

[30] V. Meshko, L. Markovska, M. Mincheva and A. E. Rodrigues, *Water Res.* 35 (2001) 3357.

Chapter 8

Conclusions and future perspectives

8.1 Conclusions

Carbon-based materials are of particular importance due to their unique catenation property, which enables the formation of a wide variety of structures with peculiar physical properties. Differences in the physical properties due to difference in the bonding characteristics in bulk carbon systems like diamond and graphite, is very well known. The ordered carbon-based nanomaterials like fullerenes, carbon nanotube, graphene, graphene oxide, graphene nanoribbons, nanodiamond, nanographite, etc. have been extensively studied in the recent years. The particular electronic environment prevailing in each of these materials, due to the difference in the bonding characteristics of carbon atoms, gives them interesting electronic, magnetic, optical and mechanical properties. The differences in the bonding characteristics mainly arise due to the sp^2 and sp^3 hybridization of the constituent carbon atoms, structural defects, the tendency of sp^2 carbon atoms to form localized clusters, dangling bonds, etc. The disordered form of carbon is known to show contrasting physical properties when compared to the ordered allotropes because of the complex electronic band structure created by the short range ordering and defects.

The investigations on the structural, magnetic and electrical properties of disordered carbon are reported in this thesis. For this study, the disordered carbon was prepared by the pyrolysis of coconut shell (CS), which is an important precursor for the industrial preparation of activated carbon. The laboratory preparation of disordered carbon ensured that the thermal history of the material is completely known, unlike the commercially available carbonaceous materials. Structure and microstructure of the disordered carbon are tuned by heat-treatment as well as by chemical activation, which enabled detailed studies and the correlation between the microstructure and the electrical and magnetic properties of the materials. The possibilities of a porous, cheap activated carbon material as a sustainable solution for the cleaning of oil spills, with the aid of an external magnetic field, after combining the advantages of superparamagnetic iron oxide nanoparticles along with activated carbon prepared from CS, is also studied and discussed.

To obtain disordered carbon with different microstructure, heat-treatment was carried out from 500 to 1000 °C under an inert atmosphere. The carbon structure was studied using different characterization techniques such as surface area analysis, X-ray diffraction, Raman spectroscopy, TEM and SEM. The XRD patterns were analyzed according to the random layer structure model for disordered carbon and the Raman spectra were analyzed according to the three-stage model of graphitization. The heat-treated carbon prepared from different pieces of CS, heat-treated at the same temperature, under nitrogen atmosphere, have slightly different extent of graphitization, as expected for the disordered carbon derived from a natural source like CS. The effect of the gas atmosphere used during heat-treatment on the microstructure was analyzed after heat-treatment under different gas atmospheres like helium, argon and nitrogen. The XRD and Raman spectra of these samples heat-treated under different gas atmosphere does not show any considerable difference, indicating that the gas atmosphere did not have any crucial effect in modifying the microstructure of the heat-treated carbons. A quantitative analysis of the metal ion impurities present in the heat-treated carbon, using ICP-OES, showed the presence of different impurities in ppm level.

The in-plane and out-of-plane coherence length of disordered carbon, L_a and L_c, calculated from the XRD spectra of the heat-treated carbons are found to be increasing with increasing the heat-treatment temperature (HTT) from 500 to 1000 °C. The ratio of the intensity of the D-peak and G-peak in the Raman spectra, *I(D)/I(G)*, and the G-peak position when plotted as a function of HTT, showed a peculiar trend, consistent with the three-stage model of graphitization reported in the literature. According to the three-stage model, the nanographitic carbon samples occupy stage-1 and the more disordered structures, with low sp^3 content, are placed under stage-2. The analysis of the Raman spectral parameters, according to the three-stage model identified two distinctly different stages in which the samples heat-treated at 500 and 600 °C (HT500 and HT600) can be placed under stage-2, whereas the samples heat-treated at 800, 900 and 1000 °C (HT800, HT900 and HT1000) belongs to stage-1. The sample heat-treated at

700 °C (HT700) occupies the border separating stage-1 and stage-2. The large increase in both the coherence lengths for samples heat-treated above 800 °C is in line with the above mentioned changes in the Raman spectral parameters, confirming a structural ordering of disordered carbon to a nanographitic structure, with an increase in HTT. All the samples were found to be porous with the surface area increasing from 35 to 350 m^2/g with increasing HTT from 500 to 1000 °C. No notable difference in the surface morphology is observed in the SEM and TEM studies. The heat-treated samples were treated with conc. HCl to remove the metal impurities. A comparison between the XRD patterns and Raman spectra of HT500 before and after acid-treatment confirmed that the microstructures of the carbon samples are not affected by the acid-treatment. The modifications in the magnetic and electrical properties of the heat-treated samples, as a function of the extent of graphitization, are studied using these samples.

All the carbon samples are found to be diamagnetic at room temperature. However, as the temperature is decreased to 2 K, all the samples showed an 'S'-shaped magnetization curve. The magnetization measured at 60 kOe (6 T), at 2 K, decreased with increasing HTT. HT500 and HT1000 showed the highest and the lowest magnetization, respectively. The maximum possible magnetization that ferromagnetic metals can contribute, when present in ppm levels, as impurities, as estimated in each sample, is calculated theoretically using the mass magnetization values of bulk ferromagnetic Fe, Co and Ni, at 0 K. The measured magnetization was much higher than this calculated contribution and therefore the presence of impurities are not the origin of magnetism in the heat-treated samples. The magnetization at 60 kOe, when plotted as a function of HTT, decreased in a particular manner, with a small decrease in the magnetization initially from HT500 to HT600, followed by a sudden drop for HT700. With further increase in HTT to 800, 900 and 1000 °C, the decrease in the magnetization becomes more gradual. This trend could be correlated to the increase in the extent of graphitization observed from XRD and Raman studies. The low magnetization of HT1000, with larger nanographitic domains, is ascribed to the decrease in number of edge

states, defects and dangling bonds which contributes towards magnetic moment. HT800 and HT900, for which the extent of graphitization is lower, consists of smaller nanographitic domains because of which the magnetic contribution from edge states should be more prominent than in HT1000. The much higher magnetization of lower HTT samples are explained based on their highly disordered structure, where the major magnetic contributions come from defects and dangling bonds. The acid-treated samples showed similar magnetization curves as that of the heat-treated samples, but with lower magnetization values. The lower magnetization of the acid-treated samples might be due to the chemical modification of the edge states and dangling bonds during the acid treatment, as observed in some previous reports on different carbon forms. The zero field cooled and field cooled magnetization curves, when measured from 2 K to 300 K, showed a broad hump around 150 K. This broad transition might be resulting from the complex magnetic interactions with variable strength due to the low dimensionality of the system. The regenerating nature of this magnetic transition on repeated acid and heat-treatment further confirmed the intrinsic nature of magnetic properties of the materials and the presence of disordered magnetic states in the heat-treated samples.

The low-temperature electrical resistivity (ρ) of heat-treated samples were measured using the Van der pauw method. The low HTT samples showed high values of ρ at 298 K (ρ_{298K}) when compared to the high HTT samples. The variation of ρ_{298K} when plotted against HTT was similar to that observed for the variation of magnetization as a function of HTT, at 60 kOe, measured at 2 K. This similarity pointed towards the reduction of structural defects and the increase in the extent of graphitization as the reason for the decrease in ρ_{298K} with HTT. The ρ_{15K}/ρ_{298K} ratio, which is considered to be a parameter which increases exponentially with disorder also showed a similar trend as that of ρ_{298K}, with an increase in HTT. This confirmed that the decrease in the disorder with the associated structural ordering owing to an increase in HTT was responsible for the decrease in ρ_{298K}. A detailed analysis of the conduction mechanism based on the fitting of the ρ-T

curves to well known theoretical models indicated the strong localization in samples heat-treated at low temperatures. The strong localization arises due to the large disorder, which results in wide spatial distribution of hopping sites due to which the resistivity followed Mott three-dimensional variable range hopping (3D VRH) law, with an exponential increase in the resistivity as the temperature is decreased. As the HTT increases, in the case of HT900 and HT1000, due to the relatively more ordered nanographitic structure, the resistivity showed weak temperature dependence. The ρ-T curves of HT900 and HT1000 could be fitted to the weak localization models. The development of percolation conduction pathways through the spatially correlated nanographitic regions might be responsible for the two-dimensional weak localization (2D WL) effect in these samples. Similar ρ-T curves could also originate from the magnetic impurity scattering, which is unlikely to occur in HT900 and HT1000 since these samples are weakly magnetic when compared to those which followed Mott 3D VRH type conduction. Therefore, the crossover of the mechanism of conduction from Mott 3D VRH to 2D WL in disordered carbon, with an increase in the heat-treatment temperature, is due to the structural change from disordered to nanographitic carbon.

After the detailed studies on the heat-treatment effects on disordered carbon, the structural modification of disordered carbon after KOH activation and the resulting changes in the magnetic and electrical properties are investigated. The industrially important KOH activated carbon has never been studied for its microstructure or the associated changes in the magnetic and the electrical properties. Heterogeneously distributed localized graphitic regions in the KOH activated carbon are observed in TEM images. The XRD and Raman spectroscopic analyses gave interesting results regarding the catalytic transformation of disordered carbon to the graphitic carbon. The L_a and L_c of the activated carbons increased with activation temperature and the amount of KOH used for activation. However, at the extreme activation conditions, involving a large amount of KOH, the coherence lengths dropped to very low values. This has been explained based on the increase in the surface area and porosity which occurs during the extreme activation con-

ditions owing to the pore widening at the expense of two or more subnanometer pores. Therefore, the drop in the coherence length might be a cumulative effect, involving the increase in the structural disorder due to the increase in the porosity and the ordering due to the catalytic graphitization effect. The changes in the values of *I(D)/I(G)* and the G-peak position in the activated samples confirmed this competition between ordering and disordering factors and heterogeneous in-plane graphitization in activated carbon. The changes in the magnetic and the electrical properties after activation are also studied. The changes in the magnetization at 60 kOe, measured at 2 K, and the coercivity of the activated carbon are correlated respectively with the development in the specific surface area and the coherence lengths calculated from XRD data. The observation of a pronounced broad feature below 150 K, in the temperature variation of magnetization for activated samples, confirmed the presence of a disordered magnetic state as in the case of spin-glasses arising from different magnetic exchange interactions of variable strengths. The room temperature electrical conductivity and the coherence lengths calculated from XRD changed in a similar manner with the extent of activation, indicating that the conductivity is directly varying with the graphitic cluster dimension. This effect was observed in the case of heat-treated samples also. The detailed analysis of the exact conduction mechanism operating in the activated sample was too difficult to perform due to the structural complexity of the samples.

As an extension of the work, the activated carbon sample was applied to the removal of oil spills after making a composite with superparamagnetic iron oxide nanoparticle. The presence of the magnetic nanoparticles along with the activated carbon as the adsorbent made the recovery of oil adsorbed material easy, using an external magnet, thereby avoiding the tedious filtration steps. The adsorbent was activated through a solid state KOH impregnation and liquid state acid activation, for comparison. The preparation of composite is through a simple *in situ* co-precipitation method, which may be used for the preparation of the composite in large quantities with out any specialized experimental setup. The composite

material was characterized using XRD, IR spectroscopy, porosity analysis and TEM. The oil recovery experiments were performed using premium oil and used oils. The magnetic composite material showed high oil retention capacity than the parent adsorbent material, due to the viscous drag created during the magnetic recovery of the material. The uptake of premium oil was higher for KOH activated carbon- magnetite composite since the pores are effective enough in containing the oil. The oil recovery using the composite is quite instantaneous and therefore very effective. The kinetic studies showed that the oil adsorption process obeys pseudo-second-order model. The material shows good temperature stability and can be reused without much loss in efficiency either after a heat-treatment or a solvent extraction process.

8.2 Future perspectives

The heat-treatment in the present work is limited to 1000 °C due to the limitation of the tubular furnace used. A further increase in the heat-treatment temperature may lead to a rapid relaxation in the carbon structure to a nearly graphitic arrangement which might further modify the magnetic and electrical properties. This study could be of paramount importance for tuning, controlling and finally producing high-quality carbon-based devices suitable for electronics applications. A high field magnetoresistance study can be highly informative while considering this material for any electronic applications. Nuclear magnetic resonance study can give more information regarding the localized defects and the clustering effects in disordered carbon. Similarly, more information on the electronic structure of the materials can be obtained from electron paramagnetic resonance studies.

The elucidation of the conduction mechanism in activated carbon is highly complex and needs to be performed in detail. Such a study requires more details on the changes in the structural characteristics in KOH activated samples. Here also, the activation with larger quantities of KOH, at temperature above 1000 °C, may give interesting results. Such an activation condition is difficult to use because of the corroding and highly oxidizing nature of potassium and its

oxides generated during heat-treatment. Carbon-based materials with sufficiently high magnetic moment can revolutionize many industries including the biomedical industry and information technology. The disordered two-dimensional materials from graphene family like the graphene oxide can also be a potential system for investigating magnetic and electronic properties. The functionalization possibilities in aqueous media give innumerable options in modifying the carbon structure for developing better carbon-based systems. To sum up, the studies on disordered carbon structure and its magnetic and electrical properties can be extended to a wide range of carbon-based systems because the extent and type of order/disorder in each system which can be different and will lead to distinctly different properties. The oil removal studies can be extended to activated carbon prepared from other cheap biological wastes like nutshell husks.

List of Publications

1. Synthesis and Reactivity of Magnetically Diverse Au@Ni CoreShell Nanostructures, V. A. Bharathan, **K. Govind Raj**, P. A. Joy and C. P. Vinod, *Part. Part. Syst. Charact.* 31 (2014) 236-244.

2. Magnetism in disordered carbon as a function of the extent of graphitization, **K. Govind Raj** and P. A. Joy, *Solid State Commun.* 177 (2014) 89-94.

3. Ferromagnetism at room temperature in activated graphene oxide, **K. Govind Raj** and P. A. Joy, *Chem. Phys. Lett.* 605-606 (2014) 89-92.

4. Coconut shell based activated carbon-iron oxide magnetic nanocomposite for fast and efficient removal of oil spills, **K. Govind Raj** and P. A. Joy, *J. Environ. Chem. Eng.* 3 (2015) 20682075.

5. Cross over from 3D variable range hopping to 2D weak localization conduction mechanism in disordered carbon with the extent of graphitization, **K. Govind Raj** and P. A. Joy, *Phys. Chem. Chem. Phys.* 17 (2015) 16178-16185.

List of Patents

6. **K. Govind Raj** and P. A. Joy, "Process for cleaning up oil spills", Provisional application filed (Application number: 3483/DEL/2014).